BULGARIAN ACADEMY of SCIENCES 1869

INSTITUTE OF ORGANIC CHEMISTRY
WITH CENTRE OF PHYTOCHEMISTRY
BULGARIAN ACADEMY OF SCIENCES

IOCCP BAS

Margarita Dimitrova Popova

NOVEL APPROACHES IN THE PREPARATION OF NANOPOROUS MATERIALS WITH APPLICATION AS CATALYSTS OR DRUG CARRIERS

ABSTRACT

A thesis submitted for the degree of Doctor of Science
Professional Field: 4.2. Chemical Sciences
Scientific Specialty: Organic Chemistry

Sofia, 2021

The DSc thesis is written on 215 pages and contains 173 figures, 53 tables, 18 schemes and 272 references. The thesis summarizes 28 scientific papers (27 in Q1 and 1 in Q2 (Scopus/WoS), 1 paper is Q1, top in ranking list) and in 18 papers Margarita Popova is a corresponding author. The results are presented in 37 oral or poster presentations at scientific conferences in Bulgaria and abroad.

The results included in the thesis were obtained during the implementation of research projects financed under contracts funded by the Bulgarian Science Fund (ВУ–Х–305/07, DO02-295 2008, Bulgaria-Slovenia bilateral project 01/6, ДН 09/18, ДН 17/18), project for establishment of a Center of excellence „National Centre for Mechatronics and Clean Technologies“ (BG05M2OP001-1.001-0008), National Scientific Program „Low-carbon energy for transport and domestic use“ (E^+) and 3 projects for Inter-academic exchange between the Bulgarian academy of sciences and the Hungarian academy of sciences.

The thesis was discussed and proposed for defense at a meeting of the Colloquium "Functional Materials, Computer Modeling and Technology" at the Institute of Organic Chemistry with Centre for Phytochemistry – Bulgarian academy of sciences (Minutes № 32 from 05.07.2021).

Scientific jury:
1. Prof. PhD Antoaneta Trendafilova
2. Prof. PhD Denitsa Pantaleeva
3. Prof. DSc Konstantin Hadjiivanov
4. Prof. PhD Tatyana Tabakova
5. Prof. PhD Silvia Todorova
6. Assoc. Prof. DSc Georgi Yordanov
7. Assoc. Prof. PhD Ivanka Spassova

The defense of the dissertation will take place on 20.10.2021 from 11 h on the web platform MS Teams.
All materials included in dissertation are available in the office of IOCCP-BAS, Acad. Georgi Bonchev str., bl. 9, room 206.

NOTES AND ACKNOWLEDGMENTS:

The presented scientific results were obtained from 2007 to 2020 and they are part of my scientific publications from this period. I included two main research areas: development of catalysts for processes related to environmental protection and development of new drug delivery systems. The articles presented in the dissertation for the development of drug delivery systems based on modified mesoporous silicates are the first publications on this topic by Bulgarian authors and currently only in IOCCP-BAS are developed new modified nanoporous silica-based carriers for drug formulations.

I express my sincere thanks for the common work, for the friendly support and valuable advice of the colleagues:
Institute of Organic Chemistry with Centre of Phytochemistry – Bulgarian academy of sciences
Assoc. Prof. PhD Vesselina Mavrodinova **Assoc. Prof. PhD Momchil Dimitrov**
Prof. PhD Pavletta Shestakova **Assist. Prof. PhD Ivalina Trendafilova**
Prof. DSc. Tania Tsoncheva **Asistant Hristina Lazarova**

Institute of Materials and Environmental Chemistry, Budapest, Hungary
Assoc. Prof. PhD Ágnes Szegedi **Assoc. Prof. PhD Judith Mihály**

Centre for Energy Research, Budapest, Hungary
Assoc. Prof. PhD Károly Lázár

Institute of catalysis, Bulgarian academy of sciences
Prof. PhD Ivan Mitov **Prof. PhD Zara Cherkezova-Zheleva**

Institute of polymers – Bulgarian academy of sciences
Prof. PhD Neli Koseva **Assoc. Prof. PhD Violeta Mitova**

Faculty of Pharmacy, Medical University of Sofia
Prof. PhD Denitsa Momekova **Prof. PhD Georgi Momekov**
Prof. PhD Krassimira Yoncheva **Prof. PhD Spiro Konstantinov**

National Institute of Chemistry, Ljubliana
Prof. PhD Natasa Novak Tušar **Assoc. Prof. PhD Alenka Ristić**

Faculty of Chemistry and Pharmacy, Sofia University „St. Kliment Ohridski“
Prof. DSc Georgi N. Vayssilov **Prof. PhD Hristiyan Aleksandrov**

Technical University of Sofia
Assoc. Prof. PhD Silviya Boicheva

I dedicate this thesis to my family with infinite gratitude and love.

Table of Contents

1. INTRODUCTION

The concept of nanotechnology was introduced for the first time in 1959 by the physicist and Nobel laureate Richard Feynman, who said in his speech at the American Physical Society, "There's Plenty of Room at the Bottom". In his famous speech, Feynman talked about the problem of manipulating and controlling things on a small scale. This "problem" has nowadays become the foundation for the powerful and widely spread nanotechnologies. Nanotechnologies have attracted intense research interest due to their application potential for production of novel materials and devices with new extraordinary properties (OECD, 2014). Nanomaterials fall in between single atoms and bulk materials and generally exhibit unique and significantly improved but sometimes unpredictable physical, chemical, and biological properties, different from their bulk analogs. Today's scientists are able to produce diverse materials at the nanoscale level with more prominent physico-chemical properties. Nanotechnologies are a merging of multiple scientific disciplines including biology, physics, chemistry, medicine, and engineering. The innovative and revolutionary nature of nanotechnologies is attributed to quantum mechanics principles. The behavior of the material is now under the control of quantum laws rather than classical physics. This fact gives the nanostructured material new abilities and properties that may be more favorable than those of the bulk material version.

Nanotechnology is considered to be one of the most rapidly developing sciences of the last decade (nano.DE-Report, 2013). The enormous potential of this new technology was immediately recognized by both academia and industry. The impact of nanotechnology on the various fields of human life is far-reaching. It is considered one of the most relevant technologies of the 21st century due to both its economic potential in new or optimized products, and its expected contributions to the effort to minimize ecological stress and consumption of resources. There are also upcoming discussions about the potential risks, fears, and arguments regarding application of nanotechnology. Proper use of the technology will bring miraculous achievements in the field of medicine, industry, electronics, and other essentials. The Green Chemistry perspective in catalysis is related to the replacement of conventional homogeneous catalysts by heterogeneous ones, which are easy to handle and usually recyclable since they can be readily recovered. In this regard, zeolites, modified mesoporous silicas or mesoporous metal oxides or nanomaretials in general have received increasing attention owing to their efficiency and selectivity in organic transformations, as a consequence of their attractive properties, i.e. tunable acidity and pore size; still, an important feature of such materials is the possibility of inserting additional metals into their framework. Other important factors associated with the development of greener processes are atom economy, efficiency, elimination of toxic intermediates/products and generation of as little waste as possible. Because of the potential for increased efficiency and selectivity, along with the advantages of environmentally benign synthetic procedures and catalyst reusability, it becomes clear that heterogeneous catalysis with application of nanomaterials opens windows of opportunity.

Intensive research on the synthesis procedure allows the production of nanoporous materials with the desired morphology, particle size and textural characteristics, which predetermines the prospect of their application in various fields of catalysis for important chemicals' production and medicine for treatment and diagnosis. The development of appropriate procedures for the modification of the mesoporous silicate with metal/metal oxides or organic functional groups is a prerequisite for their successful application.

Modified mesoporous silicas are promising catalysts for many processes because of some of their beneficial structural and compositional characteristics. The large pores and the tunable pore architecture ensure fine and stable deposition of different active sites (metal/metal oxides or organic functional groups) and ensure their resistance to agglomeration and leaching processes. The optimization of the synthesis and modification procedure can provide the perfect catalyst for many catalytic processes with strong environmental impact. The next key challenge is to better control the distribution of multicomponent active centers on the mesoporous surface, which would result in the formation of new improved active sites.

Globally, the control and elimination of volatile organic compounds (VOCs) is central to environmental protection. In recent years, European legislation has set strict requirements for the permissible levels of VOCs due to their direct toxic effect and contribution to the greenhouse effect due to their participation in secondary photochemical reactions related to ozone generation. A number of EC directives are aimed at limiting VOC emissions: Directive 1999/13/EC; Directive 2004/42/EC, Directive 2009/125/EC, NEC Directive. In 2013, the EC adopted a program for clean air. The long-term European strategy for the period 2020-2050 is to invest in low-carbon technologies to triple the reduction of greenhouse gas emissions compared to their 1990 levels. The "Green Deal" proposed by the EC in 2019 as a strategic plan for environmental development includes a number of measures in the field of ecology. The first target by 2030 is to reduce greenhouse gas emissions by at least 40% (from 1990 levels), increase the share of energy from renewable sources to at least 32% and improve energy efficiency by at least 32.5%. VOCs are emitted during waste incineration, production and use of organic solvents, petrochemistry, metallurgy, printing, diesel engines and others. Catalytic processes for their complete oxidation (combustion) are an area of intensive research with respect to developing highly active, selective,

stable and inexpensive catalysts. Depending on their chemical nature, VOCs can be divided into several groups: (i) chlor-containing hydrocarbons, (ii) aromatic hydrocarbons, (iii) mono- and polyalcohols, (iv) ketones and (v) alkenes/alkanes. The EC envisages limiting the concentrations for VOCs to 50 - 100 mgC/Nm^3, and for some representatives such as benzene they are even stricter (5 $\mu g/m^3$ for one calendar year).

The development of drug delivery systems based on mesoporous silicate materials began in 2001 with the first publication by the group of Prof. Maria Vallet-Regi, marking rapid development, and currently the articles in the scientific literature in this area are over 11000. Mesoporous silicates provide opportunities for the development of systems for controlled delivery and release of medicinal substances. Additionally, these systems can solve the problem of low water solubility of some drugs by finely dispersing them in the pores of the silicate carrier. A number of approaches have been developed to obtain drug delivery systems with modified release based on mesoporous materials, which provide sustained release of the drug substance and maintain its therapeutic concentration in the target functional area for a long period, which allows the reduction of both the frequency of administration and the possibility of adverse reactions. The ability to surface functionalize and control the morphology and particle size of mesoporous silica materials makes them extremely attractive for various applications in nanomedicine and can solve the problems associated with low load efficiency and rapid initial release of the included drug from the starting silicates. By appropriate modification of the surface of the particles with targeting ligands, active delivery of the drugs to target organs, tissues or subcellular functional areas can be achieved, which significantly reduces the systemic toxic effects in healthy tissues. Targeted drug release from mesoporous silicate carriers can provide maintenance of therapeutic concentrations in target tissues for an extended period of time. Due to their small size, mesoporous silicate nanoparticles have the ability to overcome biological barriers and thus can enter cells, which allows the efficient delivery of the drug substance to cellular organelles. Another strategy for developing sustained release delivery systems is based on the use of polymers to coat drug-laden carriers. A new impetus in the development of drug-delivery systems for antitumor drugs is provided by magnetic iron oxide/silicate mesoporous nanocomposites with different structure, the development of which as carriers for drugs and diagnostics began in 2011. By incorporating magnetic nanocrystals into mesoporous silicate structures, original drug delivery systems can be obtained that allow the drug to be selectively delivered to a desired organ or tissue in the body, using an external magnetic field and simultaneously monitoring in vivo behavior using magnetic-resonance technique for image diagnostics. In order to achieve high efficiency of these systems, it is necessary for the magnetic nanoparticles to have a relatively small size, high crystallinity and high value of magnetic saturation to provide maximum signal. Much exploration has taken place for evaluating the properties of mesoporous silica nanoparticles for their suitability in drug delivery as well as biomedical applications. A wide range of anti-inflammatory and anticancer drugs, biologicals, diagnostic agents have been satisfactorily delivered to the target regions for effective therapeutic action. Additionally, despite the promising advantages of mesoporous silica nanoparticles as carriers in drug delivery systems for anticancer therapy, the real-time achievement lies with meaningful clinical application to provide patients with the benefits. Thus, adequate clinical evidences on the biocompatibility and safety of the mesoporous silica nanoparticles as per the regulatory requirements proposed by US Food and Drug Administration are still currently needed. Finally, our efforts should focus not only on the laboratory synthesis/functionalization but also on the further improvement of the targeting ability of mesoporous silica nanocarriers for treatment. Evidently, there is plenty of work ahead for the scientific community in order to successfully translate this new family of drug delivery systems from laboratory research into practical clinical and therapeutic methods, and eventually marketable healthcare products.

2. AIM AND TASKS OF THE THESIS

The aim of the present thesis is is to present the novel approaches in the development of new nanosized materials with tailored properties benefitting their application in two main directions:

- **as catalysts for processes related to the protection of clean air**
- **as drug carriers ensuring the controlled delivery of drugs in oral, dermal or parenteral systems**

The following tasks have been set for the realization of the stated aim:

A. Development of catalysts for total oxidation of volatile organic compounds (VOCs) as an ecological process for the protection of clean air

- Monocomponent metal oxide modified mesoporous silicas and zeolite catalysts, obtained by applying different synthesis and postsynthesis approaches
- Twocomponent metal oxide modified mesoporous silicas and zeolite catalysts, obtained by applying different synthesis and postsynthesis approaches

B. Nanoporous materials for the preparation of drug delivery systems

- Development of new procedures for synthesis and modification of mesoporous silicas and zeolites with predetermined structural and surface properties and their application for the preparation of drug delivery systems
- Development of hybrid mesoporous silica-polymer carriers in order to prevent premature release of the applied drug before reaching the target organ or tissue.
- The synthesis of nanoscale magnetic iron oxide/silica composites for simultenous delivery of anti-tumor and anti-inflammatory drugs

3. RESULTS

3.1. Development of catalysts for complete oxidation of volatile organic compounds

Catalytic oxidation of VOCs is one of the promising approaches for their elimination, since it takes place at much lower temperatures (670-770 K) than their corresponding thermal destruction (above 870 K). Catalytic oxidation is particularly advantageous at low VOCs concentrations of 0.1 to 10 g/Nm^3. Aromatic hydrocarbons are one of the main representatives of VOCs, which are emitted from a number of industries such as petrochemicals, paint and steel, with the most common being benzene and toluene. The average annual health standard for benzene is up to 5 μg/m^3 for 1 calendar year. In most of our studies, toluene was chosen as the model compound for VOCs. Catalysts containing transition metal oxides (Co, Cu, Fe, Cr, etc.) are a promising alternative to costly noble metal-based catalysts to eliminate toxic emissions. The modification of mesoporous supports enables the production of fine oxide species showing high catalytic activity. Despite intensive research in recent years, the issue of creating a low-temperature aromatic hydrocarbon catalyst to reduce fuel consumption in the process remains open. In the present dissertation different approaches for obtaining active, selective and stable catalysts are presented. For this purpose, mesoporous silicas and zeolites were used as carriers with a high specific surface area, for their modification different methods were used (direct synthesis, impregnation, reaction in solid phase), amount of modifier, type of modifying salts, modification medium, use of two or more metals, etc. Catalysts are divided into two main groups: monocomponent catalytic systems and bicomponent catalytic systems. In the monocomponent catalytic systems, through the interaction between the metal oxide nanoparticles and the mesoporous silicate or zeolite, the nature and dispersion of the formed metal oxide particles can be controlled. The development of two-component metal oxide supported catalysts leads to the formation of mixed metal oxides with new physicochemical properties, which could influence their catalytic activity.

3.1.1. Monocomponent catalytic systems

3.1.1.1. Cobalt-containing MCM-41, SBA-15 and KIL-2 catalysts

The influence of pH of the impregnation solution on the formation of cobalt oxide species with different nature, reducibility, and dispersion on MCM-41 and SBA-15 silica materials was studied. The effect of the impregnation of disordered silica KIL-2 with different cobalt salts on the formation of cobalt oxide species of various nature, reducibility and dispersion was compared with its ordered silicate analog SBA-15.

Cobalt was supported on KIL-2 and SBA-15 by incipient wetness impregnation with different salt solutions of cobalt nitrate, cobalt acetate and cobalt acetylacetonate designated as Co(N), Co(Ac) and Co(AcAc), respectively. The cobalt loading for all catalysts was 3–4 wt%. Wet impregnation with 0.028 M Co-nitrate was applied for loading 5.5 wt% Co at various pH values (1.5-5) on SBA-15 and the samples were denoted as

Co/SBA-15(1.5) Co/SBA-15(3) Co/SBA-15(5.5). The salt decomposition occurred during calcination in air at 673 K for 2 h.

The low-angle powder XRD patterns of KIL-2, MCM-41 and SBA-15 indicate that KIL-2 has a disordered mesoporous structure, while the SBA-15 and MCM-41 have an ordered 2D-hexagonal pore arrangement (not shown). Diffraction peaks of Co_3O_4 at higher diffraction angles cannot be detected by in situ XRD of the Co/MCM-41 samples after the salt decomposition (data not shown). Very broad reflections with low intensity, typical of Co_3O_4, are evident for Co/SBA-15(3) and Co/SBA-15(5) samples. The XRD patterns of Co/KIL-2 and Co/SBA-15 prepared recorded at the wide-angle range confirm that spinel Co_3O_4 (JCPDF file 01-073-1701, is present in both samples after calcination independently on the salt precursor used (not shown). The formed Co_3O_4 particles are highly (finely) dispersed on both supports. The crystallite size of Co/SBA-15 samples are calculated using Scherrer's equation based on the selected diffraction peaks of the corresponding XRD pattern and it was found to be 70, 52 and 26 nm for Co(Ac)/SBA-15, Co(AcAc)/SBA-15 and Co(N)/SBA-15, respectively, while Co_3O_4 with particle size of about 70, 42 and 46 nm was determined for Co(Ac)/KIL-2, Co(AcAc)/KIL-2 and Co(N)/KIL-2, respectively.

The nitrogen adsorption and desorption isotherms of the parent and modified MCM-41 are reversible and do not show any hysteresis loop, whereas the isotherms of the parent and modified SBA-15 exhibit a H2-type hysteresis loop, which is a typical feature of this type of mesoporous material. The calculations by NLDFT method show that Co/MCM-41 and Co/SBA-15 samples have narrow pore size distribution with a maximum at about 4 and 7 nm, respectively (Table1). The specific surface area of the modified Co/MCM-41 and Co/SBA-15 mesoporous materials (S_{BET}) is slightly lower than that of the parent ones. The pore diameter of MCM-41 and SBA-15 samples has not changed after the impregnation procedure.

Table 1 Physico-chemical characteristics of the parent and the cobalt-modified samples

Samples	pH	S_{BET} (m^2/g)	pore volume (m^3/g)	pore diameter (nm)	H_2 uptake (mmol/g)	extent of reduction (%)
MCM-41	-	1023	0.90	4.2	-	-
Co/MCM-41(5)	1.5	861	0.70	4.2	0.06	5.2
Co/MCM-41(3)	3.0	892	0.80	4.1	0.18	14.7
Co/MCM-41(1.5)	5.0	902	0.81	4.1	0.15	12.3
SBA-15	-	856	1.10	7.0	-	-
Co/SBA-15(5)	1.5	794	1.00	7.0	0.19	15.4
Co/SBA-15(3)	3.0	787	1.00	7.0	0.13	10.5
Co/SBA-15(1.5)	5.0	763	0.93	7.0	0.12	9.7

The specific surface area of the Co-modified materials is lower than that of the parent ones. The loading of Co_3O_4 nanoparticles into KIL-2 and SBA-15 supports led to a decrease in the specific surface area, pore volume and pore diameter. Therefore, it can be concluded that the Co_3O_4 nanoparticles have been dispersed inside the KIL-2 and SBA-15 matrix during the Co-salt decomposition step. Some decrease in the structural ordering during the cobalt salt decomposition cannot be excluded as well. The only exception is the Co(AcAc)/SBA-15 sample, where the average pore size increased. This effect could be due to the interaction of cobalt(II) acetyl acetonate complex with the silica matrix, a partial dissociation of silanol groups as a result, and accompanying formation of cobalt silicate as a separate phase.

The DR UV-Vis spectra of Co/MCM-41 and Co/SBA-15 (Fig. 1) show the presence of a triplet at 540, 585, and 630 nm can be assigned to the electronic ligand-field $^4A_2(F) \rightarrow {}^4T_1(P)$ transition for tetrahedrally coordinated Co^{2+}, whereas the absorption band around 420 nm can be attributed to octahedrally coordinated Co^{3+} in the mixed spinel oxide Co_3O_4. The DR UV-Vis spectrum of Co/MCM-41(3) displays a more intensive absorption band at 420 nm, typical of the octahedrally coordinated Co^{3+} in Co_3O_4 in comparison to that of the Co/MCM-41(5) (Fig. 1). In the case of cobalt-containing SBA-15 samples this band is the most intensive for the Co/SBA-15(5) sample. The differences in the nature of the cobalt oxide species, registered by DR UV-Vis spectroscopy, can be correlated well with the color of the samples, for example Co/MCM-41(3) is black (octahedrally coordinated Co^{3+} in Co_3O_4), whereas the Co/MCM-41(5) sample is blue (tetrahedrally coordinated Co^{2+}).

The UV-Vis spectra of Co/KIL-2 and Co/SBA-15 samples (not shown) reveal two broad peaks at 420-440 nm and around 700 nm that could respectively be attributed to the Co^{3+} centers in the octahedral sublattice in the Co_3O_4 spinel and to the Co^{2+} centers in the tetrahedral sublattice in the Co_3O_4 spinel, indicating the presence of Co_3O_4 spinel whereas triplet at 540, 585 and 630 nm, typical for tetrahedrally coordinated Co^{2+} was not registered in any of the spectra.

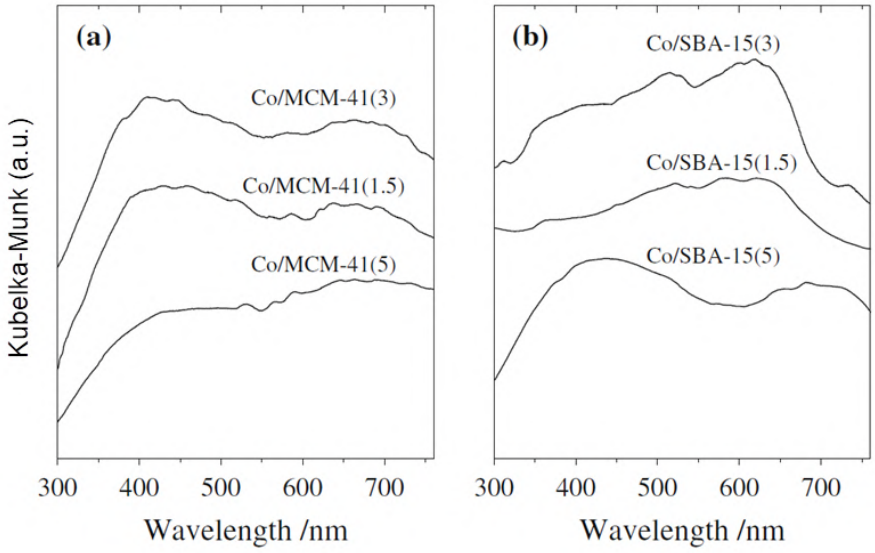

Figure 1 DR UV-Vis spectra of cobalt-modified MCM-41 (a) and SBA-15 materials (b)

An experimental approach has been applied in order to reveal the variety of cobalt oxide species that has been formed during the salt decomposition step upon the catalysts preparation. It consisted of a reduction procedure (TPR) in H_2 carried out for both mesoporous silicas modified with the different salt precursors (Table 1). Two main reduction intervals, a lower one at 500-600 K and a higher one at 773-873 K could be differentiated. The former one is indicative for the reduction of the finely dispersed Co_3O_4 to Co, the presence of which was revealed by our XRD results. Both samples prepared from nitrate precursor, as well as the Co(Ac)/SBA-15 one, exhibit a higher extent of reduction up to 703 K. The modification with cobalt(II) acetyl acetonate had an adverse effect especially on KIL-2, showing the lowest degree of reduction in both temperature intervals. The remaining unreduced up to 873 K cobalt oxide species should exist as Co^{2+} and Co-silicate-like species which are considered not participating in the redox cycles of the studied reaction.

The TPR data of the Co/MCM-41 and Co/SBA-15 samples prepared with nitrate salt precursor impregnation at different pH values show the presence of cobalt oxide species reducible at different temperature intervals and different extents, up to 923 K (Table 1). The TPR curve of Co/MCM-41(3) exhibits four peaks: the first peak is centered at 470 K and three overlapping peaks in the range of 520 to 650 K. These reduction peaks can be ascribed to the reduction of Co_3O_4 particles in a two-step process. Obviously, these reduction features indicate that during the calcination easily reducible Co_3O_4 particles have been obtained. They are most probably formed as a result of weak interaction between the cobalt aqueous complexes and the support at pH = 3 and as a consequence the major part of them is reducible at low temperature. The TPR curves of Co/MCM-41(5) and Co/MCM-41(1.5) samples show one reduction peak at about 550 K. Considering the amount of consumed H_2 (Table 1) a higher extent of reduction was achieved for Co/MCM-41 sample prepared at pH = 3 in comparison with other Co/MCM-41 samples. The TPR curves of the Co/SBA-15 samples show one highly intensive peak at 580 K and one small peak at about 700 K (Fig. 3b). In this case pH = 5 of the impregnation solution is proved to be the most appropriate value for the formation of higher amount of easily reducible cobalt oxide species. The metal ion deposition during the impregnation process of the silica support with an ionic solution is strongly affected by the pH value of the impregnation solution. Strong cobalt support interaction could occur at pH = 5 when MCM-41 is used as a support, which is probably a reason for the lower reducibility of Co/MCM-41(5). However, in the case of Co/SBA-15, the impregnation at pH = 5 leads to weaker cobalt-support interaction.

To explain the differences in the cobalt precursor-support interactions, the surface active centers were investigated by means of FT-IR spectroscopy. The spectra of the parent materials possess a highly intensive band at 3740 cm^{-1} and a broad band in the 3690-3450 cm^{-1} region (data not shown) which is typical for the isolated silanol groups and the silanol groups involved in hydrogen bonding in mesoporous silicas, respectively (Suvanto et al., 2000). The comparison of the spectra for the parent MCM-41 and SBA-15 materials shows significantly higher amount of SiOH groups on SBA-15. The intensity of SiOH bands is decreased in a different extent after the modification with cobalt. These differences could be due to the different participation of the surface silanol groups in the impregnation process, depending on the pH value of the impregnation solution. The FT-IR spectra of the adsorbed pyridine on the modified samples can be used for more detailed characterization of the cobalt oxide species interacting with the silica supports (Fig. 2). The bands at 1450/1610 cm^{-1} can be attributed to pyridine, coordinatively bound to Lewis acid sites, for example, coordinatively unsaturated cobalt oxide species connected to the silica support. The intensity of these bands is higher in the case of Co/MCM-41(5) than that of Co/MCM-41(3). This effect can probably be due to the more intensive cobalt-support interactions during impregnation at pH = 5 in contrast to the impregnation at pH = 3. Co/MCM-41(3) sample shows the highest extent of reduction as a result of the less intensive cobalt-support interactions. The spectrum of Co/SBA-15(5) also shows higher intensity of the

bands at 1450/1610 cm^{-1} in comparison to the spectrum of Co/SBA-15(3). The higher amount of SiOH groups in SBA-15 (Fig. 2) probably favors the formation of higher amount of tetrahedrally coordinated Co^{2+} ions, interacting with the silica support. When the silica support is impregnated by an ionic solution, the adsorption of ions is strongly affected by the surface charge of the support. Silanol groups possess amphoteric character and can exist in the form of SiOH, SiO^-, or $SiOH_2^+$ species, depending on the pH of the be embedded in the silica walls and therefore it cannot be detected by FT-IR method using adsorbed pyridine as a probe molecule. The Co^{2+} species are reducible at lower temperature in comparison to cobalt silicate. It was found tht different interactions of the cobalt oxide species with the silanol groups of the support depending on the pH value of the impregnation solution resulted in different reducibility of the samples. The formed cobalt oxide species (Co_3O_4, Co^{2+}, and Co-silicate like species) possess diverse reducibility and dispersion as the TPR data show. The highest amount of Co_3O_4 particles are obtained in the case of Co/MCM-41(3) prepared at pH = 3, whereas the highest amount of cobalt silicate could be formed in the Co/MCM-41(5) sample, impregnated at pH = 5. The presence of a larger quantity of silanols in SBA-15 leads to the formation of a higher amount of surface bound Co^{2+} ions, resulting in an intensive Lewis acidic band (coordinatively unsaturated cobalt oxide species) in the FT-IR spectra of Co/SBA-15(5).

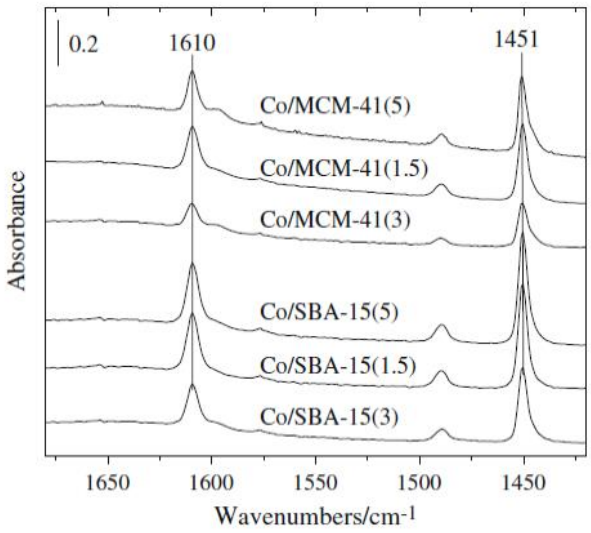

Figure 2 FT-IR spectra of adsorbed pyridine on cobalt modified MCM- 41 and SBA-15 samples

The Co/KIL-2 and Co/SBA-15 samples prepared by impregnation with cobalt nitrate show higher catalytic activity than their analogs prepared with cobalt acetylacetonate salt precursors (Fig. 3a) in accordance with their reducibility. It seems that in this case the nature of the mesoporous support does not have any effect on the catalytic activity. However, the application of conventional SiO_2 as a support and cobalt nitrate for modification leads to lower catalytic activity in comparison to mesoporous supported analogs prepared from the same cobalt salt (Fig. 3a). When acetate and acetylacetonate salt precursors are used, however, the formation of cobalt oxide species is strongly influenced by the peculiarities of the support according to the strongly distinguished reducibility and respectively catalytic activity (Fig. 3) of these modifications. The predominant formation of Co_3O_4 as finely dispersed oxide phase, providing easier oxygen release, is an essential step in VOC oxidation, and can be an explanation for the higher catalytic activity of Co-acetate and Co-acetylacetonate supported SBA-15.
Indeed, the UV-Vis spectra of the spent Co(Ac)/KIL-2 and Co(AcAc)/KIL-2 catalysts show, in contrast to SBA-15 supported analogs, an appearance of a triplet at 540, 585 and 630 nm which is indicative for the transformation, and actually loss of the active Co_3O_4 oxide phase during the catalytic reaction and its transformation into tetrahedrally coordinated Co^{2+}. In the presence of the modifying nitrate salt precursor, however, the new KIL-2 support provides very high catalytic stability which is its main advantage in the reaction of total toluene oxidation. It can be suggested that the application of $Co(NO_3)_2$ ensures the formation of Co_3O_4 with optimal dispersion, reducibility and stabilization in the voids between the KIL-2 nanoparticles.

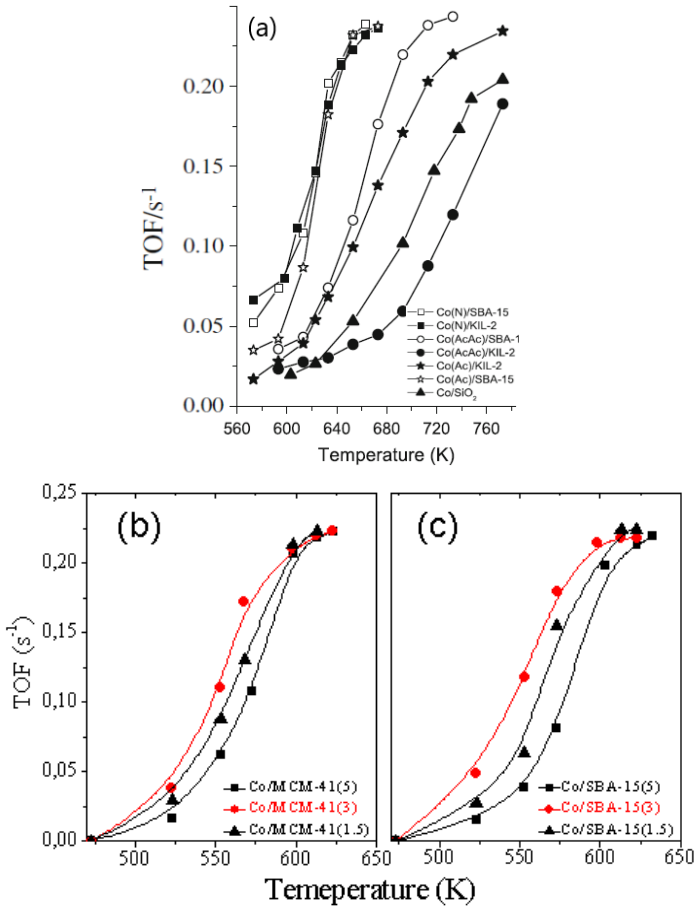

Figure 3 Catalytic activity of the Co/KIL-2, Co/MCM-41 и Co/SBA-15 samples

In Fig. 4 the results of the catalytic oxidation of toluene as a function of reaction temperature (450-620 K) on the Co/MCM-41 and Co/SBA-15 samples pretreated at 673 K in air are shown. The samples, prepared at pH = 3 of the impregnation solution, show the highest catalytic activity in toluene oxidation for both supports. The shift of the conversion curve for the Co/MCM-41 and Co/SBA-15 samples, prepared at pH = 5 and pH = 1.5 to the higher temperature, is an evidence for their lower catalytic activity in comparison to their analogs, prepared at pH = 3.
The temperature of the oxidative pretreatment has a notable influence on the nature and dispersion of the cobalt oxide species formed upon the precursor decomposition. The catalytic activity of the selected samples oxidized at 673 and 573 K is compared in Fig. 4 a,b.

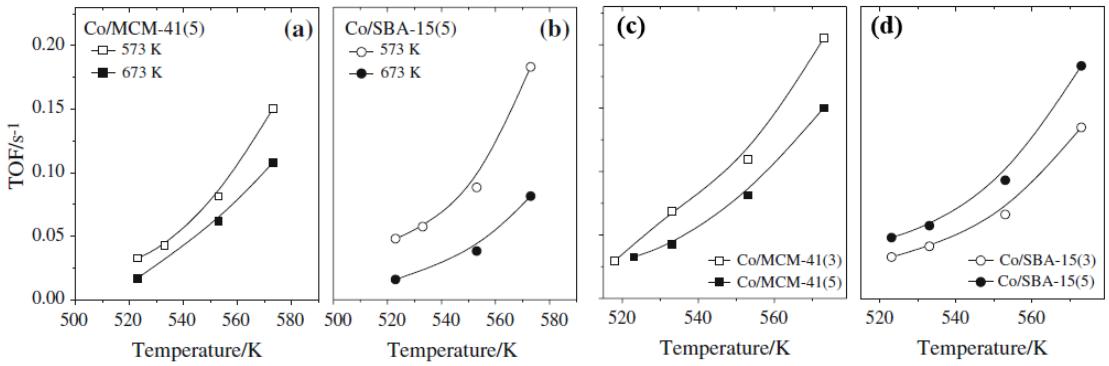

Figure 4 Effect of the pretreatment temperature (a, b) and the pH values of the impregnation solution (c, d) on the catalytic activity of cobalt-modified MCM-41 and SBA-15

Mild oxidative pretreatment at 573 K has a favorable effect on the formation of catalytically active cobalt oxide species for both types of mesoporous supports. Besides, this influence is stronger when SBA-15 is used as a support. Summarizing the catalytic performance and the physicochemical characterization of the modified materials, we could conclude that the samples containing higher amount of easily reducible Co_3O_4 particles show higher catalytic activity. According to the Mars-van Krevelen mechanism, which is usually realized during the toluene oxidation, participation of oxygen from the solid catalyst is of key importance. The higher catalytic activity of Co/MCM-41(3) and Co/SBA-15(3) could be assigned to the easier release of oxygen from the Co-

oxide species. However, in the case of Co/SBA-15(5) the higher extent of reduction does not lead to higher catalytic activity, more probably due to the simultaneous presence of Co_3O_4 and Co^{2+}, latter being less active in toluene oxidation. In Fig. 4c,d, the results of the catalytic oxidation of toluene as a function of temperature on both supports prepared at pH = 3 and pH = 5 and oxidized at 573 K are presented.
In this case the mild oxidative treatment resulted in higher catalytic activity for Co/SBA-15(5). The higher oxidation temperature probably leads to further transformation of finely dispersed Co_3O_4 particles to cobalt silicate. The effect of the post-synthesis modification with cobalt *via* wet impregnation of mesoporous MCM-41 and SBA-15 materials at different pH values of the impregnation solution was studied. The mechanism of cobalt deposition depends on the pH of the impregnation solution. Cobalt oxide species with different nature (Co_3O_4, Co^{2+}, and Co-silicate like species) are formed as a result of different interactions with the support. These species possess diverse reducibility and dispersion. The highest catalytic activity is observed for both type of samples prepared at pH = 3 due to the presence of easily reducible and finely dispersed Co_3O_4 particles. Mild oxidative pretreatment has a favorable effect on the formation of easily reducible and finely dispersed cobalt oxide species active in total toluene oxidation for both supports. The low price of the preparation of KIL-2, if compared to SBA-15, and its high and stable catalytic activity in total toluene oxidation make this type of silica a perspective support for catalytically active Co-oxide species.

3.1.1.2. Iron-functionalized silica nanoparticles with textural mesoporosity

On the basis of the above results obtained with Co-modified KIL-2 materials iron-functionalized KIL-2 silicas were studied as highly efficient adsorbents and catalysts for toluene elimination. Heterogeneous iron *KIL-2 catalysts with various iron concentrations (Fe/Si ratios ranging from 0.005 to 0.05) were prepared through direct two-step solvothermal synthesis. The samples were denoted as 005FeKIL-2, 01FeKIL-2, 02FeKIL-2 u 05FeKIL-2.*

We have prepared the heterogeneous catalysts through the incorporation of iron into the silicate nanoparticles of the disordered mesoporous KIL-2 structure with interparticle porosity. Heterogeneous iron catalysts with various iron concentrations (Fe/Si ratios ranging from 0.005 to 0.05) were prepared through direct two-step solvothermal synthesis. The XRD patterns of FeKIL-2 samples at high angles do not show detectable diffraction peaks that could be assigned to iron oxide phases. Structural parameters for FeKIL-2 materials based on the nitrogen adsorption isotherms are shown are listed in Table 2. BET specific surface areas of 005FeKIL-2 and 01FeKIL-2 materials increase with a higher amount of iron, whereas the specific surface areas of 02FeKIL-2 and 05FeKIL-2 materials decrease significantly. The pore size distribution determined from adsorption isotherms shows one distinguished maximum for 005FeKIL-2 and 01FeKIL-2 samples. 02FeKIL-2 and 05FeKIL-2 samples show very broad pore size distributions with no apparent maximum because of the technique limits of the nitrogen adsorption-desorption apparatus.

Table 2 Physicochemical properties of the studied samples

Samples	Fe/Si	Fe (wt. %)	S_{BET} (m^2/g)	w_{BJH} (nm)	V_{me} (cm^3/g)	V_t (cm^3/g)	V_{mi} (cm^3/g)	S_{me} (m^2/g)	S_{ex} (m^2/g)
KIL-2	-	-	545	19.9	1.39	1.48	0.05	370	38
005FeKIL-2	0.005	0.47	472	27.0	1.15	1.29	0.08	246	37
01FeKIL-2	0.01	0.92	556	21.6	1.33	1.46	0.07	332	39
02FeKIL-2	0.02	2.91	213	-	0.55	0.98	-	143	73
05FeKIL-2	0.05	3.84	366	-	0.37	0.64	0.07	136	70

S_{BET} - specific surface area; S_{ex} - external surface; S_{me} - mesoporous surface area; V_{me} - mesopore volume; V_{mi} - micropore volume; V_t - total pore volume; w_{BJH} - mesopore diameter.

The catalytic activity increases with the increase in the iron content (up to 0.9 wt. %) but a further increase in the iron content (02FeKIL-2 and 05FeKIL-2) leads to lower catalytic activity. Of the modified materials, 005FeKIL-2 and 01FeKIL-2 possess the best catalytic stability at 380°C (Fig. 5b) and the conversion remains approximately constant over 3 h. The catalysts maintain their catalytic activity in three reaction cycles. A well-defined trend of catalytic activity decrease is observed for 02FeKIL-2. The stable activity of 05FeKIL-2 could be related to the low activity of this sample. The formation of Si-O-Fe species results in easier oxygen release, which is an essential step in the oxidation reaction according to the Mars-van Krevelen mechanism. The mechanism of oxidation assumes the adsorption of the VOC molecule on the catalyst's surface and its oxidation with lattice oxygen following the oxidation of the reduced catalysts. The surface properties (acidic and basic) of the catalyst affect the sorption of organic molecules and therefore its conversion in the oxidation reaction. The activity in the total oxidation of toluene is connected to the interaction of aromatic electrons with acidic centers of the catalyst, which increases the possibility of the electrophilic attack of adsorbed oxygen and the combustion of toluene molecules. Iron ions could act as Lewis acid sites, which facilitates the interaction of toluene molecules with the support and

thus increases the catalytic activity. The reduction properties of the samples can be used for the interpretation of their catalytic performance as well (see the TPR data below).

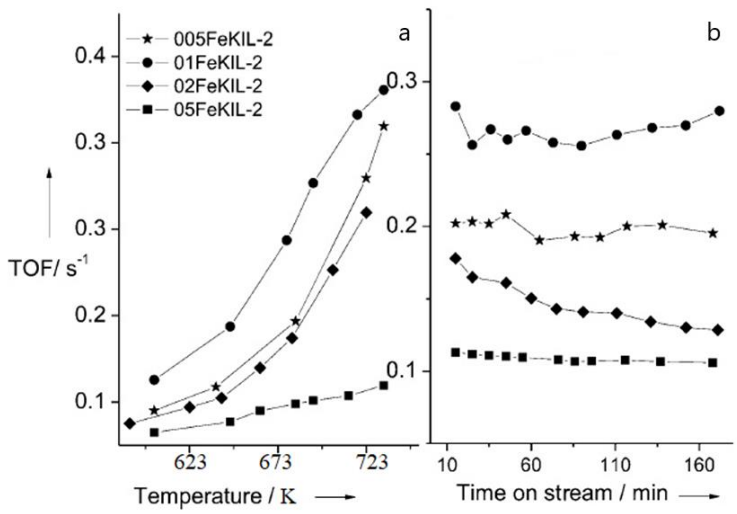

Figure 5 a) Catalytic activity versus temperature and b) catalytic activity versus time on stream at 380 °C on the iron-containing silicate nanoparticles with Fe/Si molar ratios 0.005 (denoted as 005FeKIL-2), 0.01 (denoted as 01FeKIL-2), 0.02 (denoted as 02FeKIL-2), and 0.05 (denoted as 05FeKIL-2)

The information on the local environment of iron is obtained through FTIR, UV/Vis, Mossbauer, and temperature-programmed reduction (TPR) experiments.
The TPR thermogravimetric (TG) profiles (Fig. 6) show different reduction behaviors of the modified materials in terms of dependence of iron content.

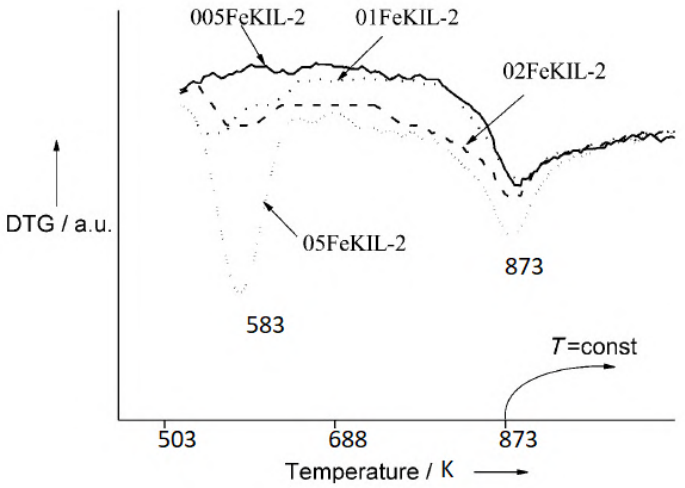

Figure 6 TPR-TG profiles of the iron-modified samples

02FeKIL-2 and 05FeKIL-2 samples are characterized with two reduction peaks at low temperatures in the intervals 523-653 K and 753-873 K, whereas 005FeKIL-2 and 01FeKIL-2 samples possess a single reduction peak at high temperatures (753-873 K). The reduction peak at low temperatures is attributed to the presence of oligonuclear iron clusters, which are formed mainly in the samples with high iron content (02FeKIL-2 and 05FeKIL-2). The reduction of iron ions incorporated into the silica matrix of 005FeKIL-2 and 01FeKIL-2 is observed at high temperatures. This assumption is also supported by the FTIR and UV/Vis data of the samples, and the presence of tetrahedrally coordinated Fe^{3+} ions can be observed in the latter case. The TPR data of 02FeKIL-2 and 05FeKIL-2 samples show a peak at a low temperature and possess lower reduction ability compared with those in 005FeKIL-2 and 01FeKIL-2 samples (Table 2).
To obtain specific information on the local environment of iron, in situ Mössbauer spectra were recorded for 01FeKIL-2, 02FeKIL-2, and 05FeKIL-2 samples under different conditions (after calcination and subsequent treatments at 640-650 K, i.e., evacuation and reduction in hydrogen, respectively). The spectra are shown in Figure 7.

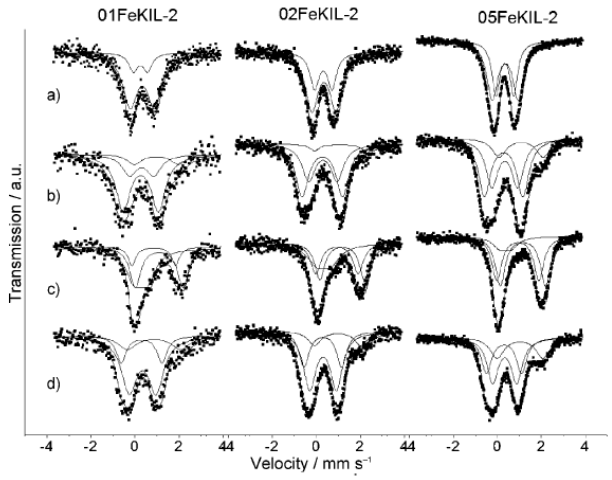

Figure 7 *In situ* Mössbauer spectra recorded for 01FeKIL-2, 02FeKIL-2, and 05FeKIL-2 samples a) as received, b) after evacuation at 633 K, c) after reduction in H_2 at 623 K, and d) after 2nd evacuation at 633 K.

The signal of the tetrahedrally coordinated isolated Fe^{3+} ions can be easily identified in the spectra. These ions demonstrate a characteristic Fe^{3+} doublet with large quadrupole splitting (quadrupole splitting = 1.8-2.0 mm/s and isomer shift = 0.26-0.30 mm/s) in the spectra recorded after evacuation. Notably, the proportion of this component decreases with the increase in the iron content and the corresponding relative intensity value is 67 % for 01FeKIL-2, whereas it is only 44% for 05FeKIL-2 in the first series of evacuations. The other characteristic observation in the analysis of spectra is that a large amount of iron participates in the reversible $Fe^{3+} \rightleftharpoons Fe^{2+}$ process. In microporous ferrisilicates, this process is not prevailing and in their rigid crystalline structure, the Fe^{3+} to Fe^{2+} reduction is not allowed for the framework-substituted tetrahedral Fe^{3+} ions, or if the Fe^{3+} to Fe^{2+} reduction proceeds, then the reduced Fe^{2+} irons are expelled from the tetrahedral framework site to the extraframework position.

In contrast, in mesoporous materials, the reversible $Fe^{3+} \rightleftharpoons Fe^{2+}$ reduction proceeds on isolated iron ions because the structure is more flexible and the crystallinity is less strict. In comparison to the formation of silanolic Si-OH groups, Fe^{2+}–OH groups form during the reduction of Fe^{3+}-O bonds. This reversibility plays a role during the oxidation reaction by transferring of oxygen atoms. Furthermore, the Fe^{3+}/Fe^{2+} reduction also proceeds on the mentioned polyferrate Fe-O-Fe-O- chains through the simple extraction of oxygen. However, this latter process is not reversible when the hydrogen treatment is reverted to the repeated evacuation. The Fe^{2+} component formed upon the extraction of oxygen starts to form oligomeric separate Fe_xO_y species, which does not participate in further reversible $Fe^{3}+ \rightleftharpoons Fe^{2+}$ process, that is, in transferring oxygen. The proportion of this "immobilized" iron in agglomerates increases with the iron content, as demonstrated by the increase in the remaining Fe^{2+} part after the hydrogen treatment and the subsequent second evacuation. Thus, the Mössbauer studies demonstrate the concentration dependence of the proportions of tetrahedrally coordinated single Fe^{3+} ions, and they also prove that a large proportion of tetrahedrally coordinated iron ions can participate in the reversible Fe^{3+}/Fe^{2+} redox process.

The results from physicochemical studies of the local iron environment indicate that iron is incorporated into the framework for materials with a Fe/Si ratio up to 0.01. If the iron concentration exceeds this value, iron deposits in the form of an oligonuclear iron complex. The iron ions incorporated into the silica matrix can participate in Fe^{3+}/Fe^{2+} redox cycles more easily, which is an essential step in the oxidation process according to the Mars-van Krevelen mechanism. We assume that, in the case of samples with lower iron content (005FeKIL-2 and 01FeKIL-2), iron is incorporated predominantly as stable Fe^{3+} ions into the silica structure, whereas the oligonuclear iron complexes formed in samples with higher iron content (02FeKIL-2 and 05FeKIL-2) are more prone to the agglomeration process.

3.1.1.3. Titanium modified MCM-41 catalysts

The comparison of the state of titanium species, introduced into MCM-41 silica either by direct synthesis technique at ambient temperature or by conventional impregnation procedure, and their catalytic performance in total oxidation of toluene were studied.

Sol-gel synthesis of Ti-containing samples in the presence of ethanol or propan-2-ol is performed. The samples were designated TiMCM-41 (e) and TiMCM-41 (p), corresponding to both alcohols. A sample impregnated with titanium iso-propoxide was also obtained to achieve 25 wt. % of TiO_2. The sample was designated Ti/MCM-41.

All titanium modified materials represent small angle X-ray diffraction patterns typical of good quality MCM-41 type materials, with hexagonal symmetry. The calculated values for the cell parameter (a_0) of the modified materials (Table 3) decrease in comparison to those of the initial sample due to the titanium incorporation into the silica matrix. In case of directly synthesized samples no reflections of crystalline titania phases appear at

higher angles, while in the case of impregnated material the very broad and weak (101) reflection of anatase at 25.3° 2 Theta indicates the presence of small (<20 nm) nanoparticles as a separate phase.

Table 3 Physico-chemial properties of the studied samples

Samples	S_{BET} (m^2/g)	pore diameter (nm)	pore volume (cm^3/g)	a_0[a] (nm)
MCM-41	1198	2.3	0.99	4.28
Ti/MCM-41	1053	2.3	0.77	4.05
TiMCM-41(p) (Si/Ti=10)	957	2.5	0.99	3.95
TiMCM-41(e) (Si/Ti=10)	907	2.6	0.89	4.06

[a] cell parameter ($a_o=2d_{100}(3)^{-1/2}$)

The slight decrease in the BET surface area and pore volume of Ti/MCM-41 could be evidence for their predominant location on the external silica surface. In the case of both directly synthesized TiMCM-41(n) materials, a simultaneous decrease in the BET surface area and an increase in the pore diameter are registered (Table 3). Summarizing these observations and the data from the XRD measurements, titanium incorporation into the silica framework position could be assumed.

More information about the state of titanium species is obtained by TPR-TG experiments (Fig. 8). A well-defined increase of TG signal is registered for both directly synthesized materials in the temperature interval between 473 and 723 K. We ascribe this effect to the scission of Ti-O-Si bonds in the silica framework, followed by the formation of additional silanol groups. A simultaneous Ti^{4+}/Ti^{3+} transition probably occurs as well. The weight loss above 723 K could be attributed to the water release during their further reduction to metallic Ti as well as to the partial reduction of various TiO_x species, supported on the silica matrix. The reduction changes are more pronounced for TiMCM-41(p) in comparison with Ti/MCM-41, which is well illustrated with the higher hydrogen consumption registered in this case. The amount of consumed H_2 corresponds to 3-7.9% extent of reduction for Ti/MCM-41 and TiMCM-41(p), respectively (Fig. 8).

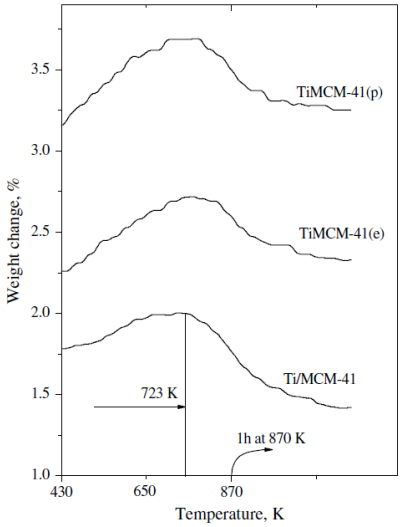

Figure 8 TPR-TG profiles of various titanium modified samples

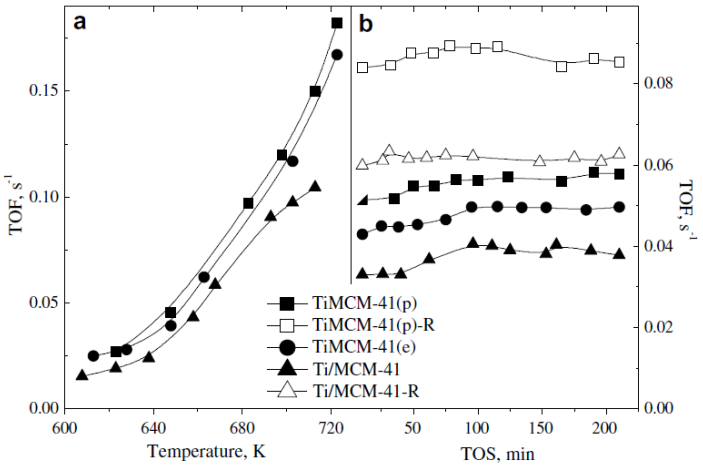

Figure 9 Catalytic activityvs. temperature (a) and time on stream at 673 K (b) on titanium modified materials. The samples after reduction in hydrogen at 723 K, TiMCM-41(p)-R and Ti/MCM-41-R, are also presented (b)

Data on the catalytic activity of toluene oxidation *vs* temperature for all titanium modifications are presented in Fig.9a. The shift of the conversion curve for Ti/MCM-41 to the higher temperature is evidence for its significantly lower catalytic activity in comparison with both directly synthesized materials. Among them, TiMCM-41(p), the sample synthesized in propan-2-ol medium, exhibits higher catalytic activity. These results are more clearly pronounced in the catalytic experiments under isothermal conditions (Fig. 9b). Comparing the catalytic data with the physicochemical ones, it could be assumed that the catalytic process is facilitated by the tetrahedrally incorporated in the silica framework titanium ions. Moreover, the presence of reduced Ti^{3+} ions leads to a significant increase in the catalytic activity and this is well illustrated by comparing the catalytic behavior of the samples pretreated in air or in hydrogen at 723 K (Fig. 9b), the effect being more pronounced for TiMCM-41(n) in comparison with Ti/MCM-41. In this aspect, we could assume the participation of catalytic active centres type Ti^{4+}-Ti^{3+}, where easier release of oxygen from the catalyst lattice is realized. The latter is well known as a crucial step in the Mars-van-Krevelen mechanism, widely accepted in the case of toluene oxidation reaction. The higher amount of such catalytic active sites is probably formed in the case of directly synthesized materials, where Ti^{4+}/Ti^{3+} transition is easily realized and this assumption correlates well

with the TPR data (Fig. 9).
The method of modification of mesoporous silica materials strongly influences the state of the incorporated titanium species. In contrast to the wet impregnation procedure, the direct synthesis of titanium modified MCM-41 material facilitates the formation of titanium ions incorporated into the silica host matrix, providing higher catalytic activity in toluene total oxidation. This effect is more pronounced when the preparation procedure is carried out in propan-2-ol medium.

3.1.1.4. Silver nanoparticles confined in nanoporous silica catalysts

In order to insert silver nanoparticles in nanoporous silica MCM-41 and SBA-15 chemical routes (direct synthesis and template ion-exchange method) and ultra-short pulsed laser ablation in liquid were employed.

Synthesis of Ag/MCM-41 by template ion-exchange method (TIE), Ag/SBA-15 by hydrothermal method and Ag/SBA-15 by laser ablation method were performed. The samples were denoted as Ag/MCM-41TIE, Ag/SBA-15DS and xAg/SBA-15LA (x=5 and 8 % Ag), respectively.

Small and wide angle XRD powder patterns of the silver-containing SBA-15 and MCM-41 silica materials are shown in Fig. 10. XRD patterns of Ag/SBA-15 and Ag/MCM-41 samples at low 2 Theta region show the formation of well-ordered 2D hexagonal structure with the intense (100) reflection and the appearance of the higher indexed (110) and (200) peaks.

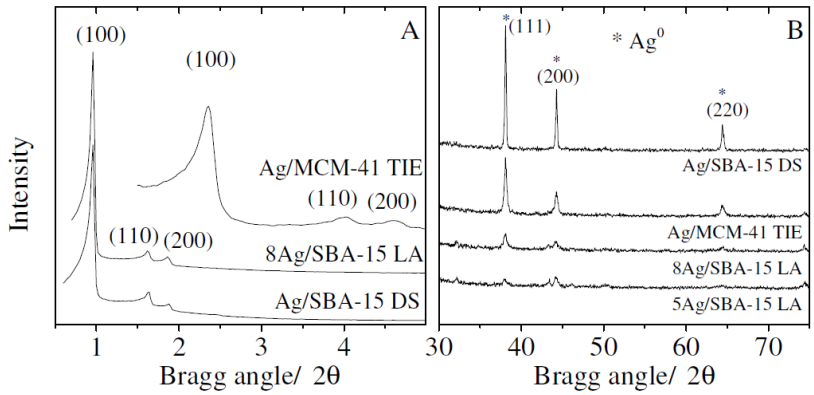

Figure 10 Small angle (A) and wide angle (B) XRD patterns

Compared to the pure silica SBA-15 and MCM-41 varieties some intensity decrease and unit cell size changes can be observed due to the chemical and physical modification of the mesoporous materials (Table 4).

Table 4 Textural properties and silver content of the studied samples

Samples	Ag content (wt. %)	a_0 [a] (nm)	S_{BET} (m^2/g)	pore diameter (nm)	pore volume (cm^3/g)
MCM-41	-	4.4	1175	2.7	0.97
Ag/MCM-41 TIE	5.6	4.3	927	2.6	0.76
SBA-15	-	10.2	1012	6.0	1.20
Ag/SBA-15 DS	7.2	10.6	698	6.6	1.08
5Ag/SBA-15 LA	4.7	10.2	880	6.0	1.02
8Ag/SBA-15 LA	8.0	10.2	865	6.0	1.01

[a] cell parameter ($a_o=2d_{100}(3)^{-1/2}$)

Only a small decrease can be observed in the unit cell parameter and pore size of Ag/MCM-41 TIE sample relative to the corresponding pure silica material. This can be due to the deteriorating effect of the ion exchange procedure. Heating the sample in water solution at 353 K for 20 h could induce a less ordered honeycomb-like structure. Incorporation of Ag into the structure of SBA-15 by direct synthesis is associated with more significant changes. The unit cell and the pore sizes increased, which can be due to either the isomorphous substitution of silicon atoms by larger silver ions, or to the changing of the synthesis medium from HCl to HNO_3. The Ag/SBA-15 samples, prepared by laser ablation method, have shown a unit cell and pore size similar to the parent SBA-15 material, indicating that the procedure did not affect the initial silica structure.
At higher angles the XRD pattern of each sample shows the presence of metallic silver phase. The Ag^0 reflections indicate the formation of silver particles larger than 5 nm. These particles can be either bound or not bound to the outer surface of the silica particles. The most intensive reflections can be observed on the XRD pattern of the Ag/SBA-15 DS sample; whereas the Ag/SBA-15 LA samples having silver contents in the same range show weaker and broader lines. In general, the intensity of these Ag^0 reflections are lower than the expected ones considering the silver content. This can be explained by the confinement of silver nanoparticles smaller than 5 nm

size inside the channels of the hosting silica structure. Also, the incorporation of silver ions into mesopore walls of the silica cannot be excluded. However, in contrast to two- and trivalent transition metals (Cu, Ni, Co, Fe) the monovalent Ag ions cannot strongly interact with silanol groups, *i.e*., there is not a strong interaction between the silver ions and the silica support. The average crystallite size of the metallic silver, determined by the Sherrer method, was about 45 nm for the Ag/MCM-41TIE and Ag/SBA-15 LA samples, whereas it was slightly over 1μm for the Ag/SBA-15 DS sample.

The textural parameters of the preparations together with the evaluated specific surface area by BET method are summarized in Table 4. Compared to parent silica material, the specific surface area and the total pore volume of the Ag/MCM-41 TIE sample are slightly lower, suggesting partial structural destruction. The type IV N_2 adsorption isotherms of the Ag/SBA-15 samples show type H1 hysteresis loop, characteristic for the SBA-15 structures. The specific surface area and pore volume of the Ag/SBA-15 samples, prepared either by direct synthesis or by laser ablation, are hardly lower than the corresponding ones of the bare silica SBA-15. The minor changes may reflect some pore blocking by small silver nanoparticles present within the channels.

Modification by silver does not influence the original morphology of MCM-41 and SBA-15 materials as evidenced by TEM pictures (Figs. 11, 12).

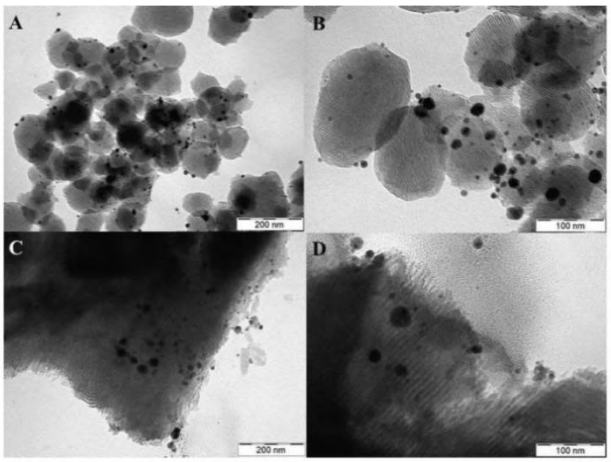

Figure 11 TEM images of Ag/MCM-41 TIE (A, B), and Ag/SBA-15 DS (C, D) samples

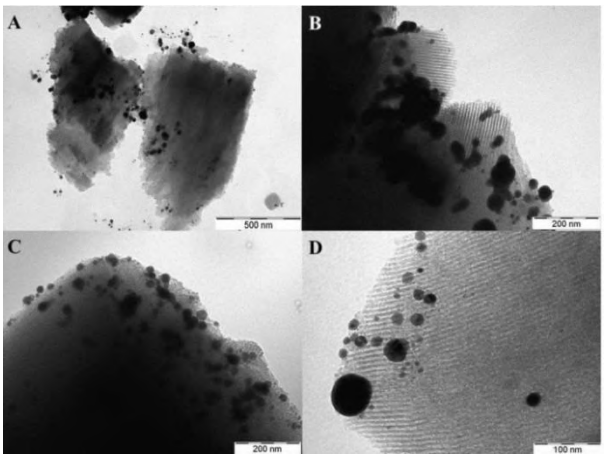

Figure 12 TEM images of 5Ag/SBA-15 LA (A, B) and 8Ag/SBA-15 LA (C, D) samples

The channel system of the Ag/MCM-41 TIE sample, having spherical particles of about 100 nm diameter, is well preserved. Silver nanoparticles of different sizes from 5 to 20 nm can be observed in the images of Figs. 11 A, B. These findings are in accordance with the XRD results showing the presence of a separate silver phase placed outside the spherical silica particles. The TEM images of the Ag/SBA-15 DS sample exhibits slightly different pictures (Fig. 11 C, D). There are larger 5-50-nm size silver nanoparticles on the external surface of the silica particles, and smaller 5 nm particles inside the silica mesopores. The TEM images of Ag/SBA-15 samples prepared by laser ablation method (Fig. 12) show similar features. Silver particles of 5-50-nm size can be observed on the outer surface of the silica carrier, and also smaller particles can be discerned to have penetrated into the channels. No large silver particles, neither separated nor attached to silica particles, have been detected. This is in accordance with the XRD results, showing, on the contrary of Ag/MCM-41, a small amount of silver phase with broadened reflections. The laser ablation seems to give smaller and more uniform size metallic silver nanoparticles adhered to the surface of the silica support than the procedure of direct synthesis. During high temperature template removal the silver ions incorporated into the silica mesoporous structure can leave the framework and agglomerate to larger particles. The narrower pores of the MCM-41 silica can hinder this agglomeration process, as opposed to the larger pores of the SBA-15 support.

Diffuse reflectance UV-Vis spectra of various silver mesoporous silica materials are shown in Fig. 13 A, B.

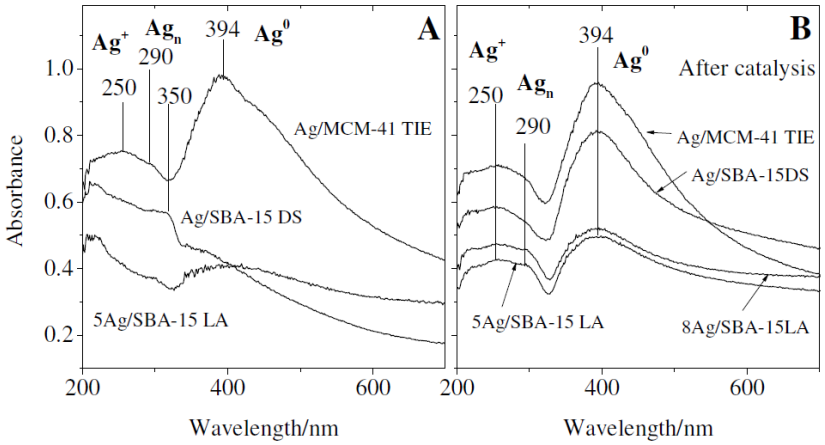

Figure 13 DR UV-vis spectra of silver supported onto nanostructured silica materials before and after catalytic experiments

Three main features can be identified: the peaks between 210-250 nm, attributed to the $4d^{10}$ to $4d^9s^1$ transition of Ag^+ ions, the bands at 290 and 350 nm, assigned to the presence of Agn nanoclusters and the wide band around 400 nm that comes from surface plasmon resonance (SPR) of metallic silver nanoparticles. The spectrum of the Ag/MCM-41 TIE sample shows a very intense and asymmetric SPR band, indicating a high amount of metallic silver nanoparticles in the diameter range of 5-45 nm with different morphologies (spherical and elongated). The UV-Vis spectra of the Ag/SBA-15 samples exhibit, in general, lower intensity SPR band, especially the spectrum of the Ag/SBA-15 DS sample and, in agreement with XRD and TEM data, these display even the presence of larger silver particles. For both Ag/SBA-15 systems the Ag cluster and ionic components of the UV-Vis spectra are greater than the SPR band.

Comparing the catalytic activities of the obtained samples (Fig. 14 A), it is clear that higher catalytic conversion is provided by the Ag/MCM-41 catalyst than by silver SBA-15 samples. Consequently, the MCM-41 mesoporous silica seems to be a more suitable support for the formation of metallic silver species with favorable catalytic properties for toluene oxidation.

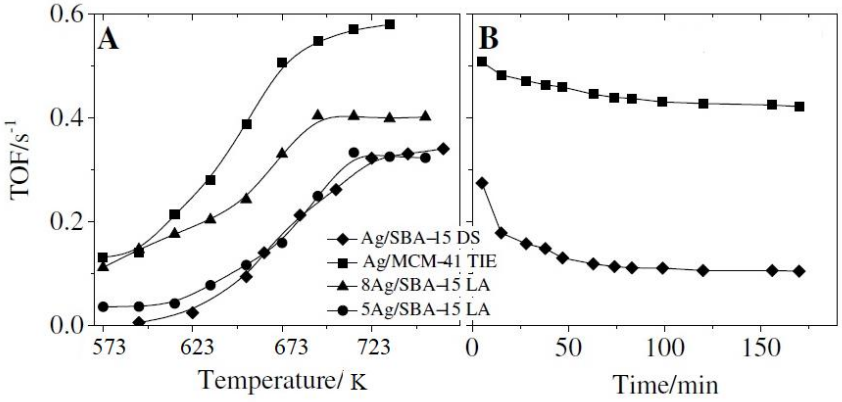

Figure 14 Catalytic activity vs. temperature (A) and time on stream experiments at 673K (B)

The Ag/SBA-15 samples show lower oxidation activities than the Ag/MCM-41 catalyst. Among these, the 8Ag/SBA-15 LA catalyst is more active than both the 5Ag/SBA-15 LA and Ag/SBA-15 DS samples. Investigating the time on stream behavior of the catalysts, the Ag/SBA-15 DS catalyst showed fast deactivation, whereas the Ag/MCM-41 TIE one was more stable (Fig. 14 B). The lower activity of the 5Ag/SBA-15 LA sample can be related to its lower metal content, whereas the unfavorable metal dispersion could be responsible for the poor performance of the chemically synthesized Ag/SBA-15 sample.

The fresh and spent catalysts investigated by DR UV-Vis spectroscopy (Fig. 13 A, B) show that the distribution of silver ions and particles in the Ag/MCM-41TIE catalyst hardly changed upon use. For such a sample the asymmetry of the SPR band slightly decreased after its use, indicating that some restructuring of the larger elongated nanoparticles could have taken place. In contrast, the silver particles in the Ag/SBA-15 DS catalyst became totally redispersed after reaction. The UV-Vis spectrum, in fact, shows that the fresh catalyst contains mainly ionic and nanoclustered silver, whereas the SPR band is negligible. In accordance with these findings the XRD results showed that the fresh catalyst contains larger than nanosize silver particles. However, after catalytic reaction an intense SPR band appeared at 394 nm in the spectrum of the spent catalyst, evidencing that the metal particles became redistributed on the surface of SBA-15 support. The adsorption interaction between the particles and the reactants weakens the metal-metal bond and mobilizes the metal atoms at the elevated reaction temperature. This phenomenon can be discussed in terms of adsorbate-induced reduction of the surface-free energy. Oxygen adsorption is known to result in a reduction of the surface-free energy of solids. This might be the

reason for the lower catalytic stability of the Ag/SBA-15DS sample. The Ag/SBA-15 catalysts prepared by laser ablation showed less significant restructuring. The SPR band of the catalyst became somewhat stronger upon use. In any case, the homogeneously dispersed small metallic nanoparticles were quite efficiently stabilized by the silica surface and, therefore, showing favorable catalytic properties.
Comparing the dispersion of metallic silver particles on different supports prepared by laser ablation or chemical methods it has been found that smaller and more homogeneously dispersed nanoparticles can be fabricated by the former. It is shown that nanostructured silica supporting metallic silver nanoparticles are suitable catalysts for the oxidation reaction of toluene. For this outcome the dispersion of the metal nanoparticles plays a key role in the catalytic activity. Since 8Ag/SBA-15 LA shows better catalytic performance than chemically synthesized Ag/SBA-15 DS, it can be concluded that finely and uniformly dispersed nanoparticles confined in small nanopores or stabilized on the surface of silica support.

3.1.2. Bicomponent catalytic systems

3.1.2.1.Chromium- and copper-modified SiO_2 and SBA-15 catalysts

The effects of silica-based support materials (SiO_2 and SBA-15) on the state of the loaded chromium and copper oxide species and the effect of the Cu:Cr ratio on their hydrophobic surface properties and their catalytic activity are studied.

Two series of chromium and/or copper modified SBA-15 and catalysts containing 10 wt. % metal oxides were obtained. Monocomponent modifications are designated Cu10 / SBA-15 and Cr10 / SBA-15, and bicomponent materials are designated CrxCuy/SBA-15, where x and y are the weight percentages of the loaded metal oxides.

In the higher angle XRD region, reflections typical of CuO are registered for both monocomponent ($Cu10/SiO_2$ and Cu10/SBA-15) samples (Fig. 15).

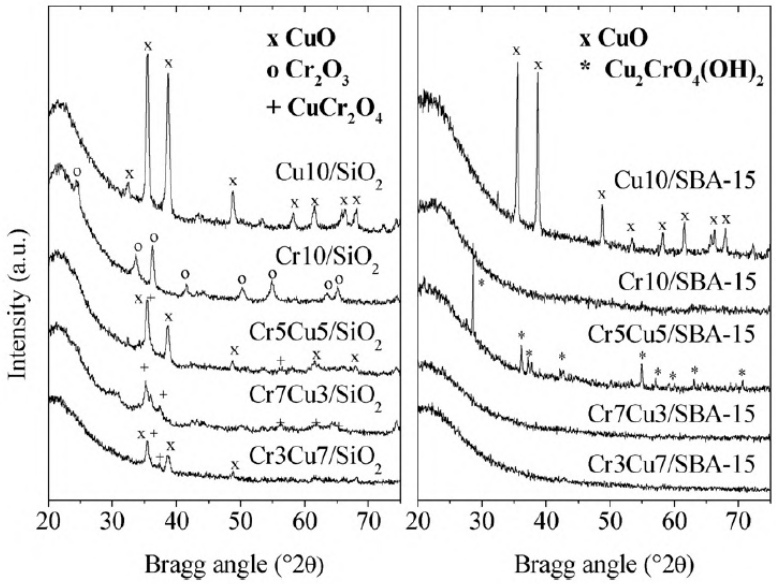

Figure 15 XRD patterns of copper- and chromium-impregnated SiO_2 and SBA-15 samples

Formation of Cr_2O_3 is only found for monocomponent catalysts on SiO_2 support. The bi-component SiO_2-supported materials possess weak and broad reflections (Fig. 15) due to the presence of CuO and spinel phases. Note that significant amount of $CuCr_2O_4$ spinel phase can be observed only on $Cr7Cu3/SiO_2$ sample. On SBA-15-based bicomponent materials (with the exception of Cr5Cu5/SBA-15) no reflections of crystalline metal phases appear in connection with the formation of finely dispersed copper and chromium oxide species (<5 nm). However, crystalline $Cu_2CrO_4(OH)_2$ phase can be detected on Cr5Cu5/SBA-15 (Fig. 15). Higher degree of copper and chromium incorporation could be concluded mainly in the case of the SBA-15-supported samples, whereas on the SiO_2 modifications, formation of metal oxides as separate phases is predominantly registered.
The BET surface area and the pore volume of all the modified SBA-15 materials slightly decreased in comparison with the parent SBA-15 support. No changes in the pore size of the modified SBA-15 materials (except Cr5Cu5/SBA-15 sample) could be observed as a result of metal incorporation. This can be explained by the formation of finely dispersed metal oxide species on the SBA-15 support. The slight decrease of the pore size, observed for the Cr5Cu5/SBA-15 catalyst (5.1 nm), is in accordance with XRD data, indicating the presence of crystalline metal oxide particles. Since the metal oxides can be detected by XRD (particle size is over 5 nm) and the pore diameter of the mesoporous support has not been changed significantly, they are most probably disposed on the external surface of the support.
The chromium and copper oxide species present in these materials were reduced in different temperature ranges

and to various extents during the TPR measurements up to 773 K. The reducibility of these oxide species also depended on the support material used. All copper-containing samples possess a clearly defined reduction peak with a maximum at about 475-500 K attributed to the Cu(II) → Cu(0) reduction. The highest extent of reduction (100 %) is calculated for Cu10/SiO_2, whereas for Cu10/SBA-15 it is 70%. Probably, copper in Cu10/SiO_2 exists mainly in the form of easily reducible, large copper oxide species, as was detected by XRD. The Cu10/SBA-15 sample also contains large copper oxide particles (detectable by XRD), as well as hardly reducible, finely dispersed copper oxide species. The intensity of the reduction peak at 475-500 K decreases with decreasing of copper content. The TPR curves of the monocomponent Cr-containing SiO_2 and SBA-15 samples indicate their weak reducibility. A low intensity reduction peak is registered only for Cr10/SBA-15 at about 640 K, whereas chromium oxide species reducible up to 773 K cannot be observed in Cr10/SiO_2 sample. Calculations show that weight changes during the reduction of Cr10/SBA-15 correspond to the total reduction of Cr^{6+} to Cr^{3+}.

The interpretation of the TPR data of the bicomponent samples is even more complex. Taking into account our former observations we can assume that the reduction at low temperature is mainly due to the reduction of copper oxide species. In addition, a well-defined shift of the low temperature reduction peak to higher temperature can also be observed for the bicomponent SBA-15-supported samples in comparison to Cu/SBA-15. Probably, the formation of finely dispersed, Cr-O-Cu-type oxide species is responsible for these changes. This assumption is also supported by the XRD and DR UV-Vis data of the bi-component SBA-15-supported samples, where the formation of tetrahedrally incorporated metal species can be observed.

FT-IR spectroscopy of adsorbed probe molecules is generally used for the characterization of Lewis and Bronsted acid sites. However, in the case of mesoporous silica-based catalyst this method is suitable for the detection of metal ions connected to the silica matrix as Lewis acid sites. FT-IR spectra of pyridine (Py) adsorbed on the monocomponent SBA-15-supported samples proved the formation of metal ions, interacting with the mesoporous matrix. In Fig. 16 the spectra recorded for monocomponent Cu10/SBA-15 and Cr10/SBA-15 samples are compared after different pretreatment conditions.

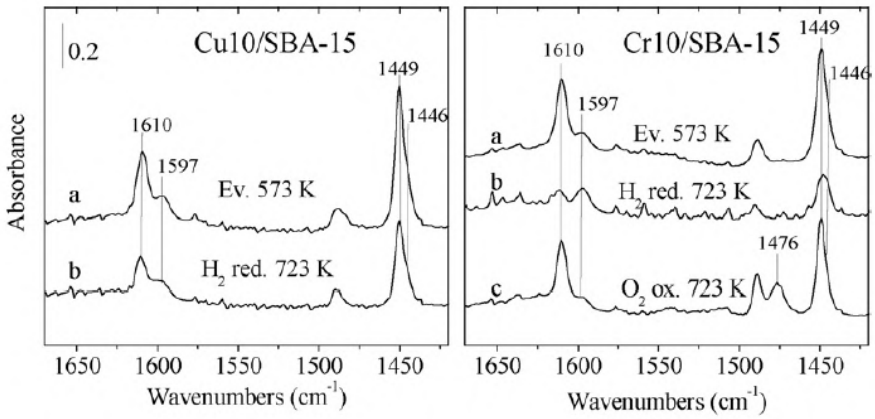

Figure 16 FT-IR spectra of adsorbed pyridine on Cu10/SBA-15 and Cr10/SBA-15 samples, evacuated at 573 K (a), reduced at 723 K in H_2 (b) and reoxidized in O_2 at 723 K (c)

The spectra of both samples after evacuation at 573K contain bands at 1449/1610 cm^{-1}, assigned to pyridine coordinatively bound to Lewis acid sites (Cu^{2+} and Cr^{6+} species, respectively), while the band pair at 1446/1597 cm^{-1} can be associated with Py connected to SiOH groups. Samples reduced at 723 K behaved differently. In accordance with the TPR data, part of the copper ions cannot be reduced in Cu10/SBA-15 and they can react with Py, whereas in chromium-containing sample the bands of pyridine coordinatively bound to ionic species disappeared completely. This latter phenomenon can be explained by the formation of a separate, finely dispersed Cr_2O_3 phase which can react with the silanol groups of the support during reoxidation at 723 K. This was evidenced by the reappearance of Lewis bands in the spectrum (Fig. 16c).

NO adsorption at room temperature results in the appearance of an intensive band at 1890 cm^{-1} on the bicomponent SBA-15-supported samples. This band can be assigned to NO attached to Cu^{2+} and/or Cr^{n+} species. Thus, the appearance of this band in the spectra of SBA-15-supported catalysts indicates the preferential formation of Cu^{2+} and Cr^{n+} species. The spectra of Cr3Cu7/SiO_2 and Cr7Cu3/SiO_2 samples do not show any band associated with adsorbed NO. The result is indicative of the formation of separate copper and chromium oxide phases, not interacting with the support, and it is also supported by the XRD and UV-Vis results discussed above. Note that with increasing the copper content the intensity of the 1890 cm^{-1} band increases (see sample Cr3Cu7/SBA-15). Obviously, the intensity of this band is related mainly to the presence of Cu^{2+} species.

Toluene oxidation was investigated in the temperature interval of 550-660 K. All samples show catalytic activity above 550 K and CO_2 is the main carbon-containing product. The catalytic activity (calculated as turn-over-frequency (TOF) per metal site) as a function of temperature is shown in Fig. 21.

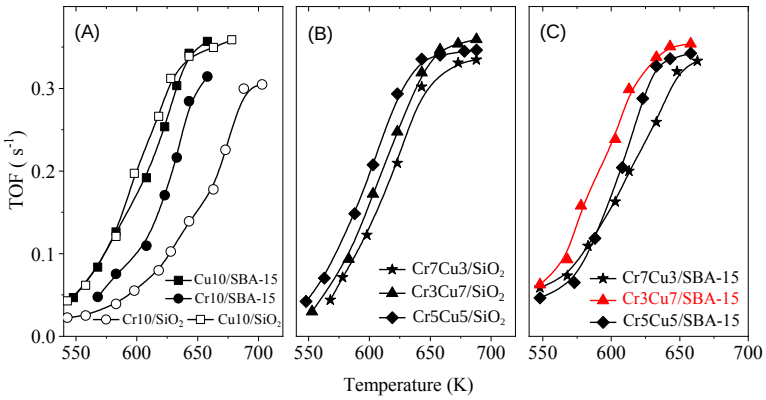

Figure 17 Catalytic activity vs. temperature of the mono- and bi-component SiO_2 and SBA-15 materials: catalyst weight - 0.03 g, toluene - 0.69 mmol/h, air flow rate 30 ml/min

For the monocomponent materials much higher catalytic activity is observed when copper is the modifier (Fig. 17A). In the case of copper-modified catalysts, the silica support does not show any significant effect on the catalytic activity, while it is just the opposite for the chromium-modified ones. This fact is in agreement with the XRD and UV-vis results, where the confinement effect of the porous structure is stronger for the Cr10/SBA-15 sample. Among the bicomponent SiO_2 modifications, $Cr5Cu5/SiO_2$ shows the highest catalytic activity (Fig. 17B), whereas in the case of the bicomponent SBA-15 modifications, Cr3Cu7/SBA-15 is the most active catalyst (Fig. 17C). The use of SBA-15 as a support has a positive effect on the catalytic performances of all bicomponent samples. The physico-chemical characteristics (UV-Vis and FT-IR spectra) of the bicomponent mesoporous catalysts show strong interaction between the metals and supports, leading to the formation of very finely dispersed metal oxide phases, probably chromate and bichromate species determining the higher catalytic activity. Kim (Kim et al., 2002) also found that the presence of highly dispersed copper species had a positive effect on the catalytic activity in toluene oxidation. To achieve the highest catalytic activity the optimum metal oxide content is 3 wt.% chromium and 7 wt.% copper supported on SBA-15. Most probably, the higher amount of copper, more active in the reaction, and the presence of chromium in such an amount that it is able to stabilize the copper species in Cu-O-Cr form, are the reason for the best catalytic performance.
The catalytic activity as a function of time on stream is presented in Fig. 18.

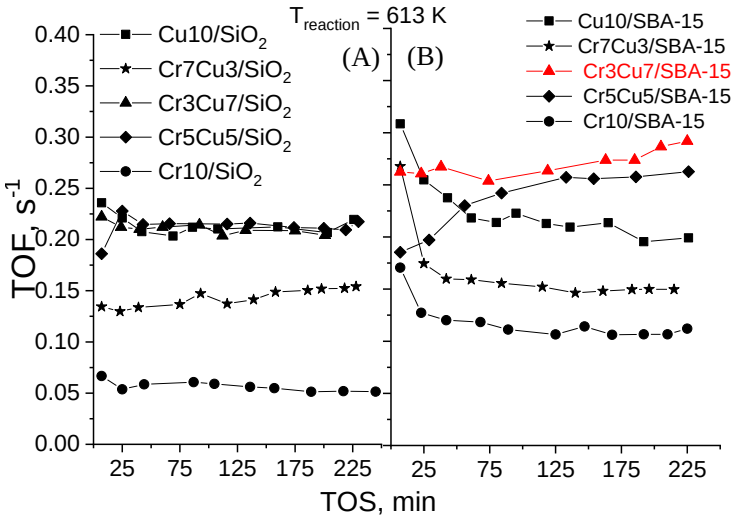

Figure 18 Catalytic activity vs. time on stream at 613 K on the copper- and chromium-modified SiO_2 and SBA-15 materials: catalyst weight - 0.03 g, toluene - 0.69 mmol/h, air flow rate 30 ml/min

The high catalytic activity of Cu10/SBA-15 at the beginning of the catalytic reaction (Fig. 18 B) is followed by a well-defined trend to activity decrease. This effect is most probably due to the agglomeration of the metal. Determination of the crystallite size by XRD showed increased size of the copper oxide particles after the catalytic experiment (20 nm before and 30 nm after the catalytic experiment). The highest and most stable catalytic activity is registered for Cr3Cu7/SBA-15 catalyst. In this case, formation of copper chromate and bichromate species can be suggested in accordance with the physico-chemical characterizations. The catalytic activity is related mainly to the presence of the latter species. Note, that the Cr5Cu5/SBA-15 sample also showed increasing catalytic activity with time on stream (Fig. 22). This can be due to the redistribution of copper on the sample. Formation of additional Cu-O-Cr species during the catalytic test is also accompanied by the redistribution of the crystalline phases of the parent material detected by XRD (Fig. 15). The latter is evidenced by the XRD pattern of the spent catalyst (not shown) indicating the lack of any crystalline metal phase. The higher

Cu-O-Cr bond polarization in copper chromate species results in easier oxygen release which is an essential step in oxidation reaction according to the Mars-van-Krevelen mechanism. Apparently, the higher dispersion of the metal oxide species supported on the mesoporous silica favors the formation of such mixed oxide species. The mechanism of oxidation suggests the adsorption of a VOC molecule on the catalyst's surface, its oxidation with lattice oxygen following the oxidation of the reduced catalysts. The surface properties (acidic and basic) of the catalyst affect the sorption of organic molecules and therefore its conversion in the oxidation reaction. Activity in total oxidation of VOC is connected with the interaction of the aromatic electrons with the acidic centers of the catalyst, increasing the possibility of an electrophilic attack of adsorbed oxygen and combustion of the toluene molecules. Additional FT-IR spectra of adsorbed pyridine on bicomponent SiO_2 and SBA-15-supported samples (Fig. 23) are made in order to illustrate the influence of acid sites on the catalytic activity.

The presence of highly intensive bands at 1449/1610 cm^{-1} (Fig. 23), assigned to pyridine coordinatively bound to Lewis acid sites (ionic Cu^{2+} and Cr^{6+} species bound to silica structure), is observed on the spectrum of Cr7Cu3/SBA-15. These Lewis acid sites could facilitate the interaction of toluene molecules with the support and lead to higher activity in toluene oxidation in comparison to the SiO_2-supported analog (Figs. 21 and 22). The reduction properties of the samples can be used for the interpretation of their catalytic performance. The TPR data of bicomponent SBA-15-supported samples show the shift of TPR peak to higher temperature as well as a lower reduction ability. The higher extent of reduction observed for Cu10/SBA-15 could be ascribed to the reduction of Cu^{2+} to Cu^0, followed by easier agglomeration (see the text above) and as a result catalytic activity decrease. Despite the lower reducibility of the bi-component SBA-15-supported samples, they show higher catalytic activity. Moste probably the extent of reduction measured by hydrogen uptake does not correspond directly to the reduction by a reactant. Additional TPO-DTG experiments of the spent catalysts were applied to indicate the changes of the oxidation state of metal oxide species during the reaction. TPO-DTG peaks were observed only for Cr10/SBA-15 and Cr7Cu3/SBA-15 samples and the effect is more pronounced for Cr10/SBA-15. The weight losses correspond to Cr^{3+} oxidation to Cr^{6+}. The change of sample color also substantiates the oxidation state transformation of chromium oxide species, the sample was orange before the catalytic experiment and became green. These conclusions are further supported by the EPR study of the catalysts before and after catalysis (Fig. 24). The EPR spectrum of Cr10/SBA-15 before the catalytic test possesses a strong axially symmetric peak with a g =1.97 and AH =1.4 mT which is correspond to Cr^{5+} species. In the EPR spectrum of the sample after the catalytic test the appearance of a broad peak corresponding to Cr^{3}+ (g =1.95, AH =53.5 mT) in Cr_2O_3 phase was registered (Fig. 24A).

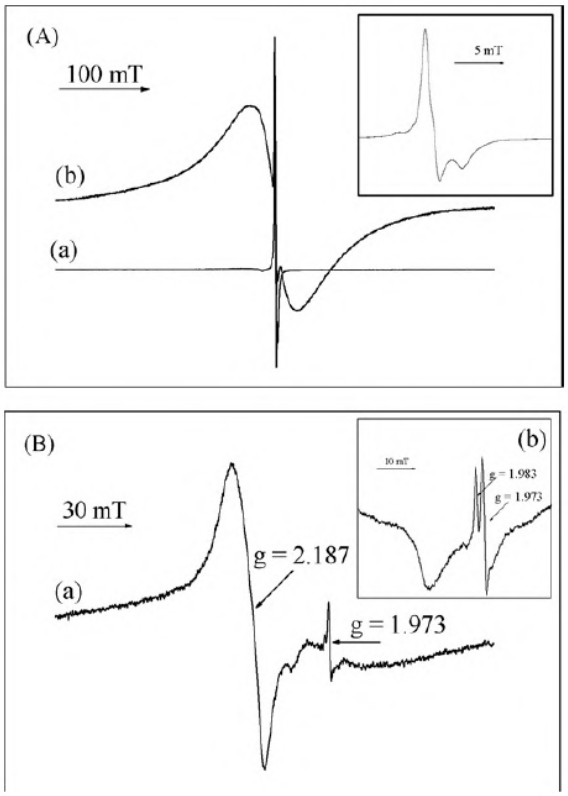

Figure 19 EPR spectra at room temperature of Cr10/SBA-15 (A) and Cr3Cu7/SBA-15 (B) before (a) and after (b) catalytic test

The reduction of chromium oxide species can lead to activity decrease (Fig. 18B) owing to the loss of active sites, probably being chromium in higher oxidation state. It was also found (Oliveira et al., 2007) that the deactivation of the chromium catalyst in reaction of aromatics oxidation is due to the loss of Cr^{6+} active species. The small

TPO effect for the Cr7Cu3/SBA-15 sample can be most probably associated with the inappropriate ratio of metals not able to avoid the loss of active sites during the reaction. Its catalytic activity decreases with time on stream (Fig. 18B). The suitable ratio of metals can stabilize the formed metal oxide species into the mesoporous support and influence the catalytic performance positively (Fig. 22B). This is also supported by TPO-TGA data of other samples (Cr5Cu5/SBA-15 and Cr3Cu7/SBA-15), which do not show any weight loss associated with the change of oxidation state of metal oxide species after the catalytic test. The EPR spectra of Cr3Cu7/SBA-15 before and after the catalytic test are presented in Fig. 19 B. The presence of Cu^{2+} (g = 2.18) and Cr^{5}+ (g =1.97) as finely dispersed oxide species is registered in the EPR spectrum of the Cr3Cu7/SBA-15 sample before the catalytic test (Fig. 24 B, curve a). The EPR spectrum of the sample after the catalytic test possesses peaks, characteristic for the presence of finely dispersed copper oxide species (g =2.18) and two forms of chromium species (g =1.97 and 1.98) (Fig. 19 B, inset). The latter peaks are due to the presence of Cr^{5+} and $(Cr^{6+}\text{-}O^{2-}\text{-}Cr^{3+}\text{-}O^{2-}\text{-}Cr^{6+})_x$ clusters. Peaks corresponding to Cr^{3+} in Cr_2O_3 crystallites are not observed, which supports our assimtion that the copper and chromium oxide species are stabilized in the mesoporous support and they do not transform to separate oxide phase during the catalytic test.
Compared to their SBA-15-supported analogs, the SiO_2-supported catalysts exhibit lower catalytic activity and it remains almost unchanged with time on stream (Fig. 18 A). This can be related with the presence of metal oxides as a separate phase and their lower dispersion in comparison to the SBA-15-supported analogs. The absence of TPO peak related to the phase transformation, can be observed in the TPO-DTG curve of the spent $Cr10/SiO_2$ catalyst. Formation of Cr_2O_3 phase (see physico-chemical data above) can be responsible for it and also for the lower catalytic activity in comparison to Cr10/SBA-15 catalyst (Figs. 17 and 18). The bi-component SiO_2-supported samples also show lower catalytic activities in comparison to their SBA-15-supported analogs. The FT-IR spectrum of adsorbed pyridine on $Cr7Cu3/SiO_2$ sample shows low intensity bands at 1449/1610 cm^{-1}, assigned to pyridine coordinatively bound to Lewis acid sites. The absence of a sufficient amount of acidic sites influences the catalytic activity negatively. Other physico-chemical characteristics (XRD, UV-vis and FT-IR spectra of adsorbed NO) also support that copper and chromium mainly exist as a separate oxide phase on SiO_2 catalysts.
Our catalytic results on copper- and chromium-modified silica materials can be summarized as follows: (i) copper oxide species formed in mesoporous support possess higher catalytic activity in comparison to chromium ones; (ii) the presence of chromium stabilizes the copper species and leads to the formation of a new type of Cu-O-Cr sites, more active in toluene oxidation.

3.1.2.2. Copper- and iron-containing SBA-15 and SBA-16 materials

The influence of structure peculiarities of SBA-15 and SBA-16 materials on the formation of copper and iron oxide nanoparticles during the incipient wetness impregnation and their catalytic behavior in total oxidation of toluene were investigated.

The parent silica SBA-15 and SBA-16 materials were modified by incipient wetness impregnation technique with copper and iron nitrates for loading of 9 wt. % of copper and 3 wt. or 4.5 wt. % of iron.

XRD data of the copper and iron modified silica materials in the low two theta region (not shown) confirm the preservation of the mesopore structure after the impregnation process. In the higher two theta region, reflections with low intensity, characteristic for CuO were detected on all the studied materials. No reflections typical of iron oxide species could be observed on bicomponent materials for both supports. Crystallite size of copper oxide particles determined by the Scherrer method can be found in Table 5. Significant differences can be found in crystallite sizes between the different supports, the average crystallite size is about 100-120 nm for SBA-15 support, whereas 200-300 nm for SBA-16. Formation of a smaller amount of metal oxide was detected in the case of SBA-15 support compared to SBA-16 support. These observations can be explained by the easier penetration of the impregnating salt into the straight channels of SBA-15 materials. The calculated parameters based on the nitrogen physisorption isotherms of metal-containing silica materials are listed in Table 5. Compared to parent supports a 20-30 % decrease in specific surface area and pore volume can be observed on metal oxide modified samples. Pore diameters are reduced from 6 to 5 nm in SBA-15 supported samples, whereas no significant pore size reduction can be observed in SBA-16 supported catalysts either in the spherical pores (~8 nm) or in the interconnecting channels (2.5 nm).
These data support the assumption that a part of metal oxides penetrated into the channels and cavities of mesoporous supports, but no significant pore blocking occurred.
In the DR UV-Vis spectrum of copper loaded SBA-15 sample the bands characteristic for mononuclear Cu^{2+} as well as $[Cu\text{-}O\text{-}Cu]_n$ cluster species can be observed at 250, and at 300 nm, respectively. A band associated with the d-d transition of Cu^{2+} in octahedral environment, e.g. in a separate CuO phase can also be identified between 670 and 740 nm. For bimetallic samples two intensive bands at about 500 nm and 720 nm can be observed. The former one can be associated with the formation of copper ferrite ($CuFe_2O_4$) phase, the latter one can be attributed to the presence of oligomeric FeO_x clusters and finely dispersed hematite like nanoparticles, respectively. For

9CuSBA-16 sample an intensive band for mononuclear Cu^{2+} can be observed at 240 nm and in contrast to SBA-15 support not oligomeric species were detected. This fact is in accordance with our former TEM results showing the absence of metal-oxide nanoparticles inside the channels. The formation of crystalline copper oxide phase is also evidenced between 670 and 740 nm. Addition of the iron component resulted in the appearance of FeOx species at lower wavelength than in the case of SBA-15 support, at about 350 nm. The presence of finely dispersed, crystalline CuO and Fe_2O_3 nanoparticles can be detected over 600 nm. Increasing the iron content to 4.5 wt. % a clear shift can be seen to higher wavelength for both supports over 400 nm, more pronounced for SBA-16. This is an indication for the formation of a higher amount of oligomeric FeO_x clusters with increasing iron content. The absence of intensive 500 nm band characteristic for copper ferrite phase on SBA-16 support is also remarkable. Formation of copper ferrite phase on bimetallic SBA-15 materials was not evidenced by XRD, which can be explained by its fine dispersion, i.e. the crystallites are smaller than 5 nm. Also the color of the samples is very different, bimetallic SBA-15 samples are black, whereas SBA-16 ones are brownish. Direct evidence for the formation of finely dispersed copper oxide phase can be accumulated by means of *in situ* high temperature XRD measurements. 9Cu4.5Fe/SBA-15 and SBA-16 samples were heat treated at 873 and 973 K in O_2/He gas in order to increase the crystallite size of ferrite phase by agglomeration. The existence of a small amount of copper ferrite phase following the 973 K heat treatment can be observed on SBA-15 support, whereas on SBA-16 support the appearance of separate Fe_2O_3 phase can be detected. Our XRD profile fitting calculations on ferrite containing sample showed that the amounts of copper ferrite and copper-oxide phases are almost equal (7-6.5 %), and the crystallite size of the ferrite phase is about 7 nm. Reduction behavior of the metal-oxide modified samples was characterized by temperature programmed reduction (TPR) method.

Table 5 Physico-chemical properties of the studied samples

Samples	S_{BET} (m^2/g)	pore diameter (nm)	pore volume (cm^3/g)	CuO crist. size[a] (nm)	extent of reduction[b] (calc. 773 K) (%)
SBA-15	756	6.0	1.0	-	-
9Cu/SBA-15	615	4.71	0.75	100±30	100
9Cu3Fe/SBA-15	609	5.05	0.76	120±30	100
9Cu4.5/SBA-15	602	5.05	0.75	120±30	92
SBA-16	1128	7.90(2.5)	0.64	-	-
9CuSBA-16	705	3.53(2.5)	0.43	330±90	100
9Cu3FeSBA-16	611	3.57(2.5)	0.40	200±60	90
9Cu4.5Fe/SBA-16	570	3.52(2.5)	0.37	200±60	85

[a] determined by XRD method using Sherrer equation, [b] determined from TPR data.

In all samples reduction of finely dispersed separate copper oxide phase can be observed with the appearance of an intensive peak at 523 K. This reduction temperature is lower than that of bulk commercial CuO between 523 and 623 K, and it is probably due to the smaller crystallite size. During the impregnation procedure a part of copper can react with the silanol groups of the support and these copper silicate species can be reduced to metallic state at higher temperatures, up to 673-773 K (Popova et al., 2010). Therefore in copper-containing samples a second reduction peak can be observed at 673-773 K. The latter one is more pronounced and shifted to higher temperature for 9Cu/SBA-16 sample. The extent of reduction is 100 % for both monocomponent catalysts, copper oxide on both supports can be totally reduced up to 723 K (Table 5). In iron and copper containing SBA-15 samples the first 523 K peak is broadened and the second reduction peak appears at about 623 K. With increasing amount of iron the intensity of the 623 K peak is slightly decreased and the 523 K peak increased. These changes are indicating that in the presence of iron higher amount of CuO phase is formed because the interaction of copper with the silica wall is hindered. However, on iron containing catalysts total reduction cannot be achieved up to 873 K. This can be explained by the stabilization of a part of Fe^{3+} species in the silica matrix by the reaction with silanol groups. These kinds of Fe^{3+} can be reduced up to 873 K only to Fe^{2+} state and their total reduction to metallic state proceeds only over 1073 K. Consequently, on iron containing samples the higher temperature peaks (623-673 K) can be associated with the reduction of iron containing phases in different forms, such as small Fe_2O_3 nanoclusters, copper ferrite, and ionic iron species connected to silica wall. On all iron containing samples a wide peak can be observed between 970-1073 K, which can be associated with the reduction of the latter ionic iron species to metallic state. These observations are in accordance with out XRD result, showing the lack of highly crystalline iron oxide phase in the channels or on the outer surface of the supports. Reduction of iron containing phases on SBA-16 supported bimetallic catalysts proceeds in two steps between 573 and 673 K. The lower temperature peak can probably be associated with the reduction of finely dispersed Fe_2O_3 phase, and the higher one with the ionic iron silicate species. Due to the strong interaction of iron with the support, primarily iron oxide

nanoclusters can be formed in the channels of the mesoporous materials. If the size of the channels allows it, they can react with the finely dispersed copper ions to form a ferrite phase.

In situ Mossbauer spectroscopy was applied to access complementary information on the various local environments of iron in the samples. Measurements were performed at ambient temperature in a three-step procedure. Spectra were first recorded on the samples containing adsorbed water. In the next stage samples were evacuated at 663 K for 2 h. Finally, the samples were treated in hydrogen at 663 K for 2 h. Spectra were collected in two velocity ranges, ± 12 mm/s, and ± 4 mm/s. The former, broad range provides information on the total amount of iron, whereas the narrow ± 4 mm/s range displays only the central part of spectra in improved resolution. ± 12 mm/s spectra collected on SBA-15 and SBA-16 samples are displayed in Figs. 20 A, B. The parent samples containing adsorbed water show a typical doublet characteristic for iron oxide phase with Fe^{3+} oxidation state and octahedral coordination. In the higher resolution spectra this doublet can be decomposed to two types of components with different QS values (0.6 and 1.05 mm/s) indicating different coordination symmetries. These parameters are characteristic for finely dispersed iron- oxide species and ionic iron species connected to the silica matrix through oxygen atoms, respectively. Besides, the appearance of a magnetic sextet on the SBA-16 support and the absence of it on the SBA-15 spectra are apparent (Figs. 20 A, B, top).The detected magnetic splitting is ca. 50 Tesla, characteristic of antiferromagnetic oxides.

The difference in the appearance is correlated with the size of agglomerated oxidic Fe entities with Fe-O-Fe chains. The sextet component appears if the size of the oxidic particles exceeds 10-20 nm. Thus, 24-26 % of iron in the SBA-16 samples form particles with diameter exceeding this size.

These observations support our former XRD results with the formation of iron oxide phase on SBA-16 support. In contrast, the mean diameter of the dominant part of iron-oxidic particles is smaller on the SBA-15 support. Because of the similarity of Mossbauer parameters of iron-oxide and ferrite nanoclusters a separate ferrite phase cannot be distinguished on SBA-support. Our results show that the dominant part of iron in both supports is distributed evenly in high dispersion. Simple evacuation has a detectable effect - namely the quadrupole splitting increases and even Fe^{3+} => Fe^{2+} (auto) reduction proceeds in a small extent. The removal of the adsorbed water from the proximity of the Fe^{3}+ ions decreases the charge symmetry around them as reflected in the increase of QS values (not shown). This phenomenon may proceed only with those iron ions that are connected to the support in very high dispersion. Reducing the samples at 663 K in hydrogen a doublet characteristic for Fe^{2+} species can be registered. The amount of divalent iron is about 50-70 %, and it is in good accordance with our TPR data showing the partial reduction of Fe^{3+} to Fe^{0}. Iron and copper are in close vicinity of each other. In spectra recorded after the 663 K reduction in hydrogen also a ferromagnetic sextet appears with 33 Tesla internal magnetic field. This value is primarily characteristic for metallic iron. The reduction of Fe_2O_3 without copper in hydrogen to metallic iron proceeds only at higher temperatures. Furthermore, another, single-line component is also present in these spectra at isomer shift ~ 0.0 mm/s, which can be attributed to copper-iron bimetallic component.

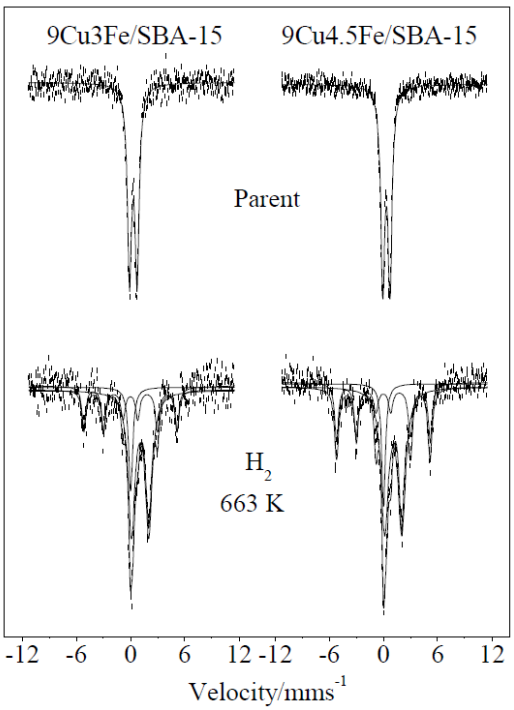

Figure 20A ^{57}Fe Mössbauer spectra of the copper and iron modified SBA-15 materials

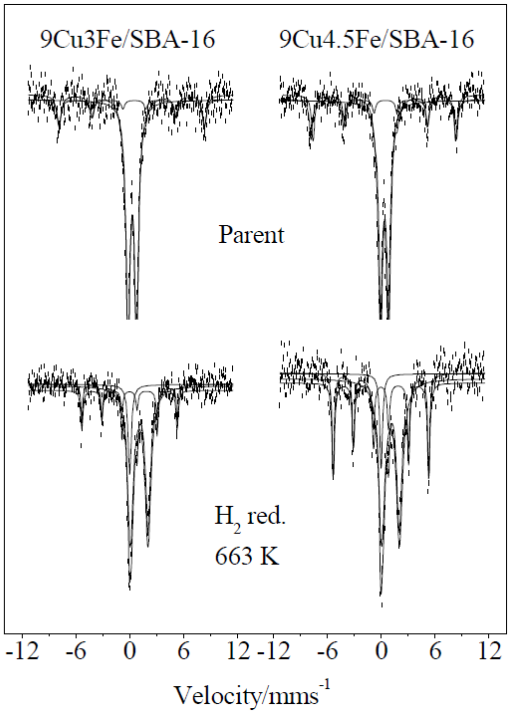

Figure 20B ^{57}Fe Mössbauer spectra of the copper and iron modified SBA-16 materials

High temperature *in situ* XRD measurements carried out in H_2 atmosphere up to 873 K on 9Cu4.5Fe/SBA-15 and SBA-16 samples confirmed our Mossbauer and TPR results. On both supports reduction of CuO to copper starts at a low temperature. At 473 both CuO and Cu phases can be observed. However, total reduction to metallic copper proceeds up to 573 K and at higher temperatures only the agglomeration of metallic particles can be observed as evidenced by the decrease of FWMH values of the reflections. According to the Sherrer equation, after 873 K reduction the crystallite size of metallic copper particles is 55 nm for SBA-15 and 165 nm for SBA-16 support. Reduction of iron oxide species to metallic iron begins at 573 K, but more pronounced from 673 K. It can be observed that on SBA-16 support iron is formed in bigger crystallites owing to the lower FWMH values. Reflections of metallic iron on SBA-15 support are broadened even at 873 K, indicating very finely dispersed species.

These results support our former observations, that ferrite phase can be found in the channels of SBA-15 and their agglomeration during reduction is restricted, whereas bigger metal crystallites can be formed during the reduction of iron oxide particles on the outer surface of SBA-16.

The temperature dependencies of catalytic activities in toluene oxidation on the modified SBA-15 and SBA-16 materials are presented in Fig. 21. Prior to the catalytic tests samples were calcined ex situ at 573 K for 2 h in air. Comparing the catalytic activities of the copper containing monocomponent SBA-15 and SBA-16 catalysts, it can be seen that on SBA-15 support higher conversion can be achieved. It seems that SBA-15 is a more appropriate support for the formation of catalytically active copper oxide species. Our XRD data confirmed that more finely dispersed copper oxide phase is formed on this catalyst. Introduction of the second metal resulted in the shift of conversion curves to lower temperatures. With lower amount of iron also SBA-15 shows higher catalytic activity, whereas this advantage of the support structure disappears with the addition of higher amount of iron. With 4.5 % iron content about 5 % lower conversion can be achieved. The change of catalytic activity in dependence of time on stream at 653 K is presented in Fig. 22. The high catalytic activity of monocomponent copper catalysts at the beginning of the reaction is followed by a well-defined deactivation, more pronounced for SBA-16 sample. Our XRD results confirm that a higher amount of separate CuO phase can be found in SBA-sample, so its agglomeration during catalytic reaction can be the explanation for the fast deactivation of this sample. According to UV-Vis data copper can be found in the SBA-15 catalyst in the form of isolated copper ions, oligomeric Cu-O-Cu species in the channels, and also as a separate CuO and $CuFe_2O_4$ spinel phase on the outer surface. Whereas, on SBA-16 support only isolated copper ions and separate copper oxide phase are formed.

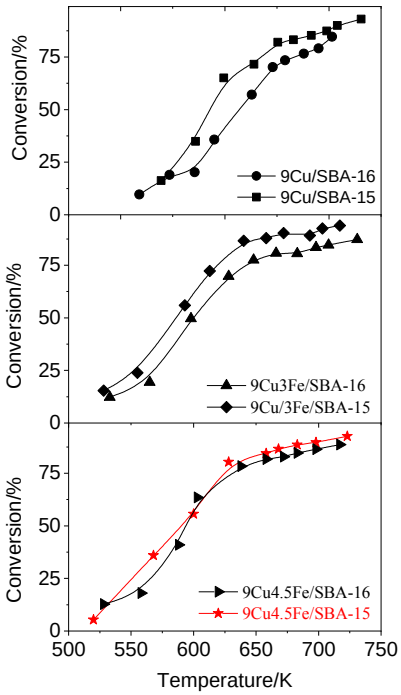

Figure 21 Toluene conversion *vs.* reaction temperature on the studied samples

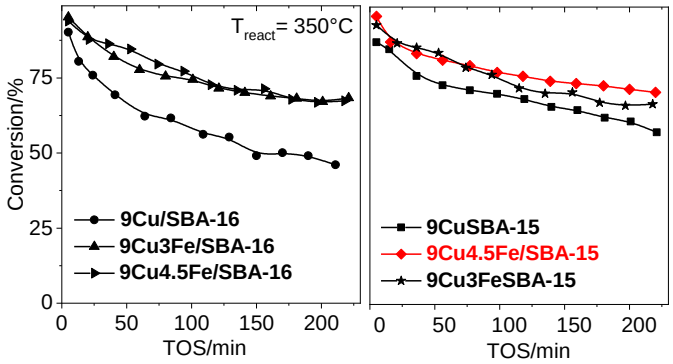

Figure 22 Toluene conversion vs. time on stream on the studied samples

The presence of oligomeric Cu- O-Cu species is more favorable from the point of oxygen release ability. Additionally, higher amount of finely dispersed copper oxide phase is formed in the channels of SBA-15 in contrast to SBA-16 support, where the copper oxide phase can be found mainly on the outer surface of the silica particles. Addition of iron resulted in a more stable catalytic behavior for both supports and for both iron

concentrations. This can be explained by the formation of the mixed CuFe oxide, e.g. ferrite phase, which is in good accordance with the appearance of a CuFe alloy upon reduction, evidenced by Mossbauer spectroscopy. The simultaneous presence of Cu^{2+}/Fe^{3+} pairs in the catalysts leads to higher catalytic activity for all bicomponent samples due to the easier oxygen release.

3.1.2.3. CuO nanocrystals and Cu-oxo-Fe clusters on silica support

The nature and reduction properties of copper oxide species are influenced by the peculiarity of the silica nanoparticles with interparticle mesoporosity (KIL-2 structure) and the presence of a second metal (iron) in the silica matrix were demonstrated for the first time.

Cu containing (6 wt. %) mesoporous disordered silica CuKIL-2 with different sizes of CuO nanoparticles (100, 30 and 5 nm) were prepared. In the sample name CuxFeKIL(y), x=Fe/Si molar ratio is represented as the number before Fe, while the average CuO crystallite size in nanometers (y) is given in the parentheses at the end of the sample names.

XRD patterns show reflections that are typical of copper oxide for Cu/KIL-2, but not for the Cu/FeKIL-2 sample, probably because of the formation of small copper oxide nanoparticles. Copper oxide with a particle size of approximately 100 nm is determined for Cu/KIL-2 with calculations from the Scherrer equation, which is based on the selected diffraction peaks of the corresponding XRD pattern.

The structural parameters calculated from nitrogen adsorption isotherms for KIL-2, FeKIL-2 and Cu/FeKIL-2 materials are listed in Table 6. KIL-2 and FeKIL-2 samples exhibit adsorption isotherms typical for KIL-2 and FeKIL-2 materials with relatively narrow hysteresis loops of type IV. The FeKIL-2 sample undergoes a capillary condensation step at higher relative pressures than the KIL-2 sample, which indicates that larger mesopores are present in the FeKIL-2 material compared to the KIL-2 support. It can be clearly observed that the presence of copper oxide nanoparticles in KIL-2 and FeKIL-2 supports leads to a marked change in the shape of the hysteresis loop. The loading of copper oxide nanoparticles into KIL-2 and FeKIL-2 supports also leads to a decreased specific surface area, pore volume and pore diameter (Table 6).

Table 6 Structural parameters of the catalysts determined from nitrogen adsorption isotherms

Samples	S_{BET} (m_2/g)	pore volume (cm^3/g)	mesopore volume (cm^3/g)	mesopore diameter (nm)
KIL-2	545	1.48	1.39	19.9
Cu/KIL-2	359	0.73	0.65	14.8
FeKIL-2	556	1.46	1.33	21.6
Cu/KIL-2	407	1.11	1.00	16.1

Therefore, it can be concluded that the copper oxide nanoparticles are dispersed inside the KIL-2 and FeKIL-2 matrices. Pore size distribution of the different mesoporous materials was determined by using the Barrett-Joyner-Halenda (BJH) model, which is widely used for this type of samples. The average pore diameters of 19.9 and 21.6 nm were determined for KIL-2 and FeKIL-2 supports, respectively. The maxima characteristics of copper oxide impregnated materials are shifted to lower pore size values (14.8 nm for Cu/KIL-2 and 16.1 nm for Cu/FeKIL-2).

A TEM micrograph of the Cu/KIL-2 sample shows a porous texture with interparticle porosity typical for KIL-2 silica materials. Agglomerated silica nanoparticles with an estimated size of 10 nm form voids and cavities with a broad size distribution. The porous silica matrix contains individual crystallites of copper oxide. The relatively large thickness of the crystallites makes the TEM observation somewhat difficult, however an approximate size of 100 nm could be estimated. This is in agreement with the calculations from the Scherrer equation, which is based on the selected diffraction peaks of the corresponding XRD pattern. The presence of the monoclinic copper oxide phase in the CuKIL-2 sample, which is already indicated by XRD analysis, is finally confirmed by the selected area electron diffraction method (SAED). The sizes of the copper oxide crystallites indicate that they are located exclusively on the surface of the KIL-2 silica matrix. The observations at higher magnification did not reveal the presence of any smaller metal oxide nanoparticles that could be located within the voids. TEM analysis of the Cu/FeKIL-2 sample shows similar textural properties as for the Cu/KIL-2 sample. The FeKIL-2 silica matrix is inhomogenously covered with the copper oxide phase, however individual metal oxide nanoparticles are somewhat smaller (100 nm) and appear to be agglomerated into larger clusters. Similarly, as in the case of the Cu/KIL-2 sample, the observations at higher magnification do not reveal the presence of any smaller metal oxide nanoparticles. More information on the oxidation state of copper oxide species and their reducibility was obtained by temperature-programmed oxidation-reduction thermogravimetric analysis (TPO/TPR-TG) experiments (Fig. 23). Pretreatment in different media (air and argon) was applied before the TPR experiments. The samples showed different behavior during the pretreatment procedure, which depended on the pretreatment media and the used support (Fig. 23).

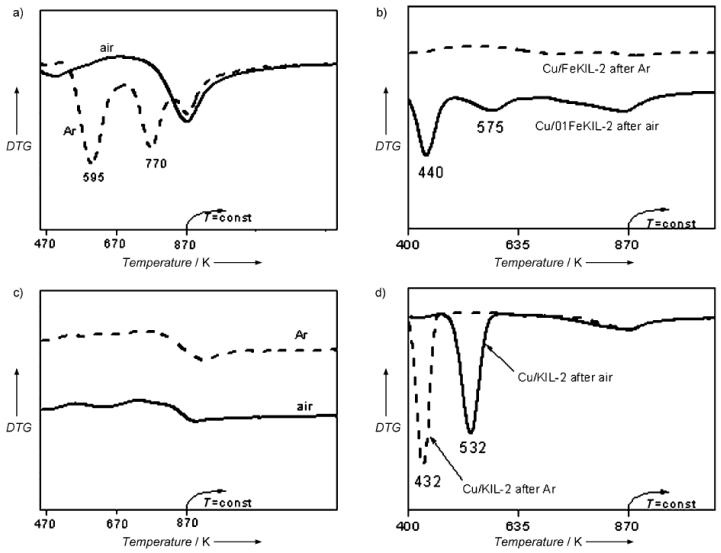

Figure 23 TPO/TPR-DTG profiles of a, b) Cu/FeKIL-2 and c, d) Cu/KIL-2 samples

There were no significant changes in the weight of both samples Cu/KIL-2 and Cu/FeKIL-2 during the pretreatment in air. A low intensity peak is registered at 870 K for both samples; this probably owes to silica matrix dehydroxylation. In contrast, the pretreatment in argon results in significant weight changes, which correspond to 100% reduction of copper(II) ions to metallic copper on the FeKIL-2 sample. Reduction peaks at 595 and 770 K are registered for Cu/FeKIL-2 pretreated in argon. For the first time the copper autoreduction process is determined on mesoporous materials. We ascribe the copper autoreduction process to the influence of iron(III) ions and the formation of weak Brönsted acid sites in the sample as a result of iron incorporation into the silica structure. The predominant formation of copper(II) ions on this sample owes to the presence of Broensted acid sites in the iron-containing KIL-2 support and their interaction with the copper precursor during the impregnation process. These copper(II) species can be easily reduced to metallic copper during evacuation at high temperature or under an inert atmosphere. The reduction profiles of the copper-containing catalysts depend on the support material used and the pretreatment procedure. The copper-containing KIL-2 and FeKIL-2 samples pretreated in air possess clearly defined low-temperature reduction peaks at 530 and 440 K, respectively, which can be attributed to copper(II) to metallic copper reduction. The extent of reduction is 89.33% for Cu/KIL-2 and 100% for Cu/FeKIL-2. The narrow reduction peak with a maximum at 430 K, registered for Cu/KIL-2 after pretreatment in argon (Fig. 23d), is related to the more homogenous distribution of copper oxide species on the supports. There are no peaks in the TPR-TG profile of the Cu/KIL-2 sample after pretreatment in argon at 773 K (Fig. 23c), which owes to total copper autoreduction during the pretreatment under an inert atmosphere.

The catalytic activities versus the temperature and versus the time on a stream of copper-containing materials that were pretreated in an inert gas or air at 723 K in total toluene oxidation are presented in Fig. 24. The pretreatment in different media (air or argon) does not lead to different catalytic activity with a temperature increase for Cu/FeKIL-2 (Fig. 24b). It is the opposite for Cu/KIL-2, the increase in the temperature leads to higher catalytic activity in toluene oxidation for this sample after the pretreatment in air at 773 K (Fig. 35a). The use of KIL-2 as a support has a positive effect on the catalytic performances of the Cu/KIL-2 sample. The Cu/FeKIL-2 catalyst shows stable catalytic activity at 653 K after pretreatment in different reaction media (air and argon) (Fig. 35d), whereas the Cu/KIL-2 sample shows stable catalytic activity only in the pretreatment with air, and a trend towards deactivation in the pretreatment with argon (Fig. 24c). The physicochemical characteristics (UV-Vis and TPR data) of the catalysts show the formation of finely dispersed copper oxide species on both supports, which determine their high catalytic activities.

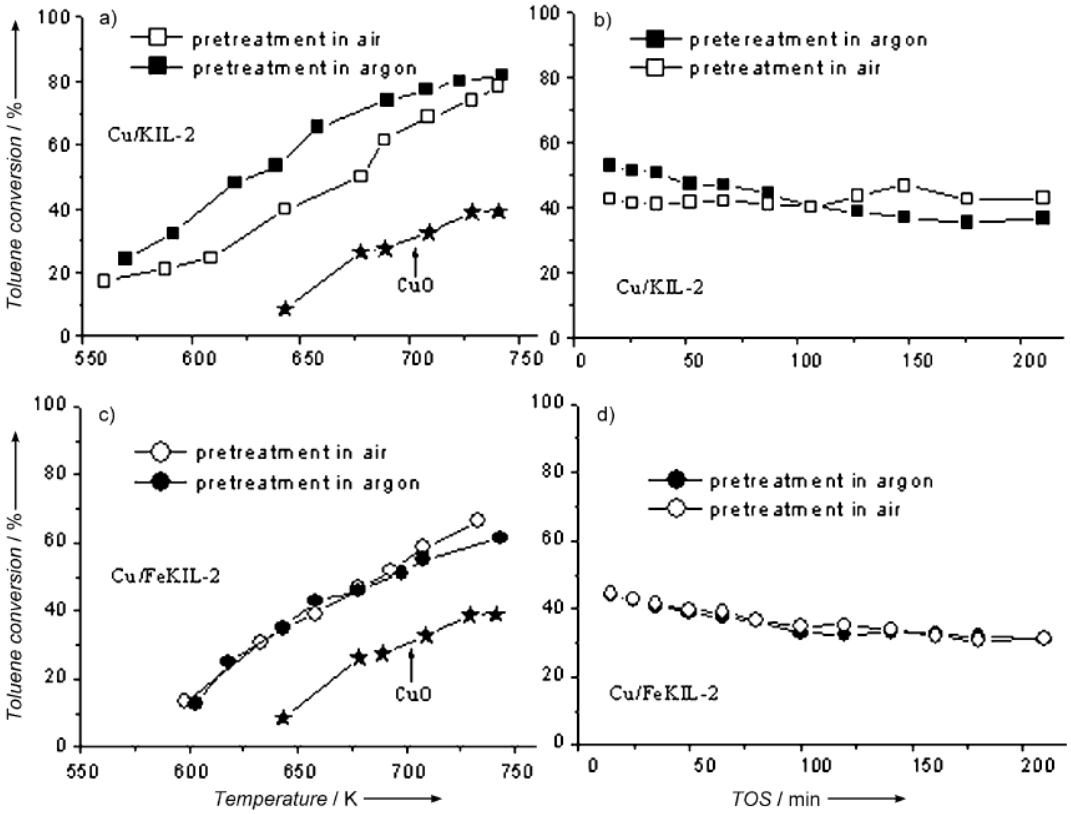

Figure 24 Catalytic activity versus temperature on a) Cu/KIL-2 and b) Cu/FeKIL-2 samples and versus time on stream at 653 K on c) Cu/KIL-2 and d) Cu/FeKIL-2 samples after pretreatment in argon or air

Additional experiments were performed on the KIL-2 supported catalysts with different CuO sizes, different Fe/Si and Fe/Cu ratio in order to obtain highly active and stable catalyst (Fig. 25). Catalytic tests were performed on the monometallic CuKIL catalysts with different size of CuO (CuKIL(30) and CuKIL(100)) and bimetallic catalysts containing small amounts of iron (Fe/Si = 0.005, Fe:Cu = 1:11) (Fig. 25). The coexistence of CuO nanocrystals and Cu-oxo-Fe clusters (confirmed by TEM-EDX and XANES analyses) significantly improves the catalytic performance, compared to the monometallic CuKIL(30) analogue (97 and 76 % toluene conversion, Fig. 25 b). The difference in toluene conversion is present also at 603K (40 vs. 33 % for Cu005FeKIL(30) and CuKIL(30), respectively). At this temperature, the reaction rates and consequently toluene conversions were much less influenced by mass transport. A further increase in the Fe content (Fe/Si > 0.01), however, continuously decreases the catalytic activity of the CuFeKIL materials. With increasing Fe content, the fraction of CuO phase quickly decreases and diminishes completely (Cu02FeKIL), resulting only in the presence of only finely dispersed Cu-oxo-Fe clusters. The catalytic activity of Cu005- FeKIL(30) is also much higher compared to the monometallic 01FeKIL catalyst. It appears that a synergy between the CuO nanocrystals and the Cu-oxo-Fe clusters plays a crucial role in providing high catalytic activity for toluene oxidation. Considering the co-existence of CuO nanocrystals and Cu-oxo-Fe clusters is a prerequisite for high activity, the interface between both oxide phases likely provides the majority of catalytic activity, i.e. represents the reactive perimeter. The highest gain in catalytic activity over bimetallic CuFe catalysts was about twofold (calculated as a ratio of toluene conversion achieved at 603 K over Cu005FeKIL(30) and Cu05FeKIL samples: 40/19 = 2.1).

The stability of bimetallic (CuFeKIL) and 01FeKIL catalysts is much higher compared to monometallic CuKIL samples. The CuKIL samples, irrespective of the CuO crystal size, show 9-23 % toluene conversion loss in the initial 75 min of reaction. Over the CuFe bimetallic catalysts, this value is much lower (2-8 %). Presence of strongly anchored Fe^{3+} species in the silica matrix seems highly favorable for the increase in catalytic stability, as it acts as surface anchoring sites for the Cu-oxo-Fe phase. Sintering of CuO cannot be reliably studied with XAS technique, as the average Cu coordination number change will be observable only in the CuO crystallites smaller than ~3 nm.

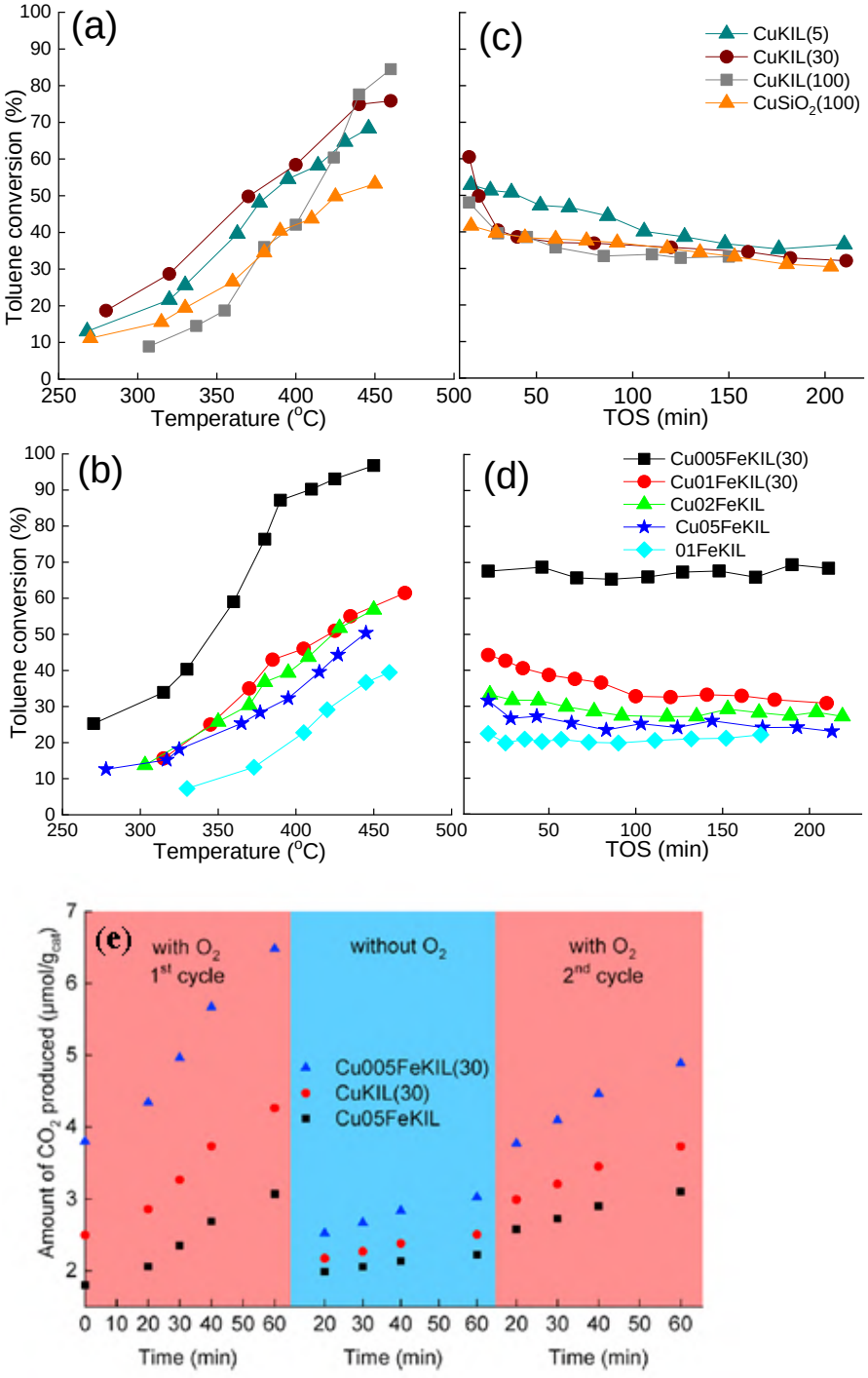

Figure 25 Catalytic activity as a function of temperature (a, b) and time on stream at 653 K (c, d) for bimetallic (CuFeKIL) as well as monometallic (CuKIL) and (FeKIL) catalysts and effect of oxygen on the amount of CO_2 produced during catalytic pulse toluene oxidation experiments over CuKIL(30), Cu05FeKIL and Cu005FeKIL (30) samples at 673 K (e)

The amount of deposited carbon was the lowest (0.09 wt. %) on the Cu(30)KIL sample, which deactivated to the highest extent. Over both bimetallic catalysts, the carbon amounts were different, but notably higher compared to the monometallic one: 1.4 in 4.1 wt. % for Cu005(30)FeKIL and Cu02FeKIL, respectively. In addition, the deactivation of bimetallic catalysts was negligible. Lack of any positive correlation between the accumulated carbon and the extent of deactivation suggests that the carbon deposition is not the cause for the observed decline of the catalytic activity.

The TEM-EDXS analysis on the Cu005(30)FeKIL catalyst after the toluene oxidation reaction revealed sintering of the CuO crystals and their growth to about 100 nm. It was observed previously that CuO is prone to sintering when exposed to temperatures above 573 K.

Quantitative estimation of the extent of reduction was performed based on the total amounts of H_2 consumed and actual content of Cu and Fe, which are initially present as Cu^{2+} and Fe^{3+} as it was proven by XAS. In the case of CuKIL(30) sample, quantitative reduction of CuO to metallic copper took place, which is in line of CuO crystals decorating the outer surface of silica. In case of FeKIL sample, 58 % of Fe^{3+} was reduced to Fe°, which supports dispersion of Fe in the silica matrix and only partial availability of the Fe^{3+} for contact with the gas phase. In the bimetallic Cu02FeKIL and Cu005FeKIL(30) samples, actual H_2 consumption reached 68 and 79 % of the theoretical values, resulting in incomplete reduction. The latter is likely related to Fe^{3+} cations remaining in the

silica matrix, inaccessible to H_2. The lower reduction temperature of Cu and especially CuFe containing samples compared to Fe confirms higher strength of Fe-O bond compared to Cu-O or Cu-Fe-O. The isothermal transient reduction experiments were performed to reveal differences in the rates of surface and lattice oxygen abstraction when exposed to H_2 at 673 K. This could shed light onto the origins of the observed differences in catalytic activity. Over the analyzed CuKIL(30), Cu02FeKIL and Cu005FeKIL(30) samples, very similar peak oxygen abstraction rates (0.27-0.28 mmol $H_2 gcat^{-1} s^{-1}$) were calculated, which are related to surface reduction (initial 20 s of reduction), indicating no measurable differences in the kinetics of surface reduction among these samples. The rate of bulk oxygen removal (20-200 s of reduction) of the Cu005FeKIL(30) was superior compared to CuKIL(30) and Cu02FeKIL lies above the blue and green which overlay), which is likely connected to an electronic metal-support interaction. This phenomenon is well known during reduction of CuO dispersed over reducible oxides. Namely, in the case of Cu005FeKIL(30), CuO is deposited over a partly reduced Cu-oxo-Fe layer, whereas in monometallic CuKIL(30), CuO sits on inert silica. The excess electrons in the partly reduced surface Cu-oxo-Fe layer can influence the electron distribution on the adjacent CuO crystals, thus altering their reactivity.

No correlation was found between the catalytic activity and the total removable lattice oxygen (H_2-TPR), nor calculated oxygen abstraction rates (isothermal reduction). This suggests the lattice oxygen reacting with adsorbed toluene is fast and not the rate determining step in the investigated oxidation reaction. As a result, toluene oxidation could proceed through the Mars van Krevelen mechanism, which is often reported in the literature as crucial in the VOC total oxidation mechanism.

Pulsing of toluene over the catalysts in air atmosphere at 673 K (1st cycle, Fig. 25) resulted in a progressively increasing amount of CO_2 formed in the following order: Cu05FeKIL < CuKIL(30) < Cu005FeKIL(30). With four consecutive toluene pulses injected to the catalysts in inert He atmosphere (Fig. 25), the trend of increasing CO_2 formation was identical to the one in air atmosphere. The formed CO_2 amounts represent a small fraction of lattice oxygen (2-3 %), contained in the reducible copper and iron containing phases that reacted with toluene. This indicates the pulse experiment results are not influenced by lack of available lattice oxygen. This experiment confirmed the lattice oxygen species (O_L) participation in the total toluene oxidation reaction ($C_7H_8(g) + 18O_L \rightarrow 7CO_2(g) + 4H_2O(g)$). In the 2nd cycle experiment (toluene was injected into the air stream over the catalyst), the trend of increasing catalytic activity was identical to the 1st cycle, while the amounts of formed CO_2 were lower (Fig. 36e). This was most evident for the most active Cu005FeKIL(30) sample and could be due to coke formation and blocking of the active sites. The amounts of CO_2 formed in air were 22-65 % higher compared to experiments in inert atmosphere. This provides solid evidence that besides lattice oxygen, adsorbed oxygen species participate in the catalytic toluene oxidation reaction and their contribution to toluene oxidation activity is dominant especially for Cu005FeKIL(30) sample. The surface defect sites are usually considered as energetically favorable binding sites for any adsorbate, because of lower degree of bond saturation compared to atoms on ideal crystalline planes. The interface between the crystalline CuO and the amorphous Cu-oxo-Fe layer represents an intrinsically defect-rich area. Molecular oxygen is electrophilic and preferentially adsorbs on electron rich sites. The facile reduction of Cu-oxo-Fe clusters, which occurs at ~ 343 K and is considerably lower compared to FeO_x (~ 443 K) or bulk CuO (~393 K) (inset Fig. 37a) favors presence of reduced, electron rich Cu^{d+} (d < 2) in the catalyst containing Cu-oxo-Fe phase, which serves as active site for the activation of molecular oxygen.

3.1.2.4. Ferrite-containing MCM-41 and SBA-15 catalysts

The formation of finely dispersed ferrite nanoparticles on mesoporous MCM-41 and SBA-15 silicate carriers is an opportunity to create active centers for complete oxidation of toluene.

An incipient wetness impregnation technique with cobalt and iron nitrates was applied for loading of 15 and 23 wt.% metals on SBA-15 and MCM-41 with Co:Fe = 1:2.

XRD data of the cobalt and iron modified silica materials in the low two theta region (not shown) confirm the preservation of the hexagonal structure after the impregnation process. In the higher two theta region, wide reflections with low intensity, typical of Co_3O_4 and $CoFe_2O_4$ on 23CoFe/MCM-41, whereas only reflections of $CoFe_2O_4$ can be observed on the SBA-15 support (15CoFe/SBA-15 and 23CoFe/SBA-15 samples), after calcination at 773 K (Fig. 26A).

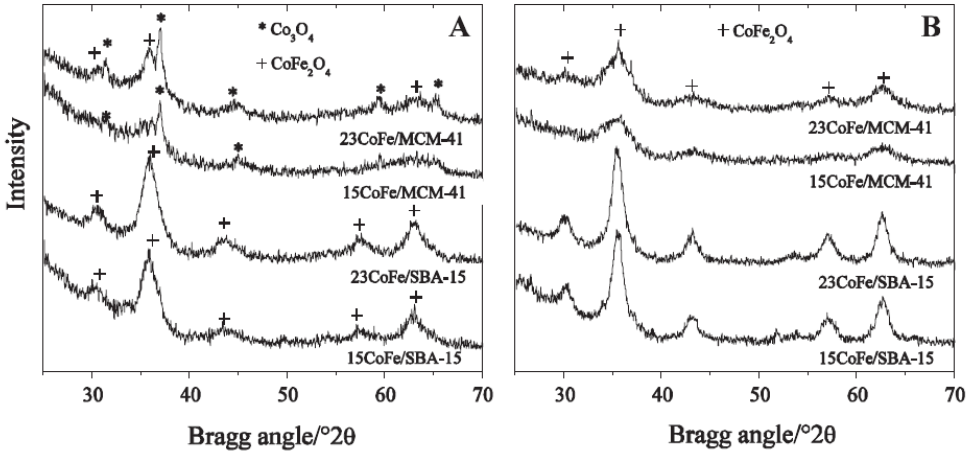

Figure 26 XRD patterns of the studied samples calcined at 773 K (A) and at 973 K (B)

Thermal treatment at 973 K resulted exclusively in the formation of cobalt ferrite phase on both supports (Fig. 26 B). Crystallite size of ferrite and cobalt oxide particles determined by the Scherrer method can be found in Table 7.

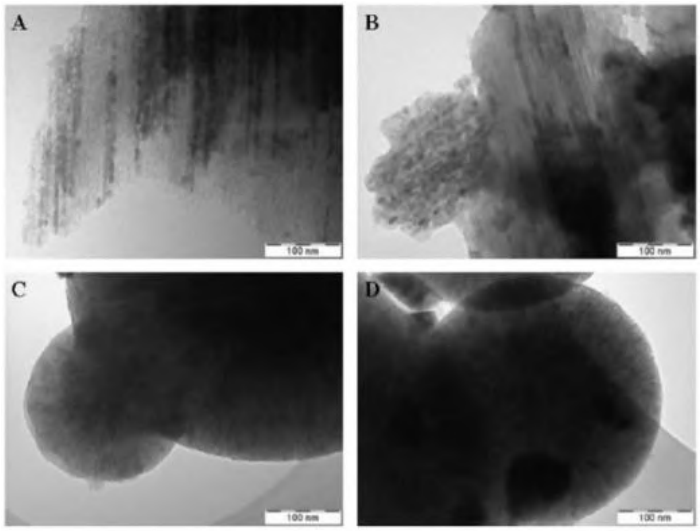

Figure 27 TEM images of 15CoFe/SBA-15 (A), 23CoFe/SBA-15 (B), 15CoFe/MCM-41 (C), and 23CoFe/MCM-41 (D) samples, calcined at 773 K

Our data show that the particle size of ferrite phase on 773 K treated samples is similar (below 10 nm), but the amount of crystalline ferrite phase (crystallite size ≥5 nm) is higher on the SBA-15 support. Salt decomposition at 973 K increased the particle size of ferrite phase on SBA-15 and decreased on the MCM-41 sample. The latter can be explained by the stronger metal-support interaction, most of the metal ions form cobalt and iron silicates with the silanol groups of the silica matrix.

Table 7 Physico-chemical properties of the studied samples

Samples	S_{BET} (m^2/g)	pore diameter (nm)	Co_3O_4 cryst. size[a] (nm)	$CoFe_2O_4$ crystal size[a] (калц. 773 K) (nm)	$CoFe_2O_4$ crystal size[a] (calc. 973 K) (nm)	extent of reduction[b] (calc. 773 K) (%)	extent of reduction[b] (calc. 973 K) (%)
MCM-41	970	2.4	-	-	-	-	
15CoFe/MCM-41	709	2.36	43	7	4.3	58.9	26.8
23CoFe/MCM-41	623	2.30	30	10	5.9	79.1	38.4
SBA-15	756	6	-	-	-	-	
15CoFe/SBA-15	644	6/4.7	-	9.1	10.1	69.1	43.0
23CoFe/SBA-15	571	6/4.4	-	7.7	11.2	83.4	37.5

[a] determined by XRD method using Sherrer equation, [b] determined from TPR data.

The calculated parameters based on nitrogen physisorption isotherms are listed in 72. The isotherms are of type IV (IUPAC classification), with a sharp capillary condensation step at about 0.25 and 0.6 relative pressures, characteristic of MCM-41 and SBA-15 type mesoporous materials, respectively. MCM-41 samples do not show

any hysteresis, whereas on SBA-15 catalysts a parallel, H1 type hysteresis loop can be observed. This is characteristic for narrow pore size distribution indicating the preservation of the mesoporous structure. Impregnation procedure results in a decreased BET surface area of the modified MCM-41 and SBA-15 materials (Table 7). With increasing amount of metal content surface area is also decreasing. Upon impregnation in MCM-41 samples the average pore diameter slightly decreases, whereas in SBA-15 a bimodal pore structure is formed with 6 and 4.7-4.4 nm pore diameters (Fig. 56, inset). This means that some pores were not affected by the impregnation procedure, but some other pores are partly blocked by the ferrite nanocrystals.
TEM investigations (Fig. 27) support the XRD and nitrogen physisorption results. On SBA-15 support one can clearly observe the channels filled with ferrite nanocrystals (Fig. 39A, B). The size of the crystals is below 10 nm, which is in good accordance with the XRD results. On MCM-41 samples we can differentiate very small particles in the channel system of MCM-41 and big crystals on the outer silica surface (Fig. 27 C, D). According to XRD the latter ones can be associated with Co_3O_4 particles. The smaller ones can probably be finely dispersed ferrite crystals.
Characterization of the iron component in samples calcined at 773 K and reduced in hydrogen at 653 K was performed by *in situ* Mossbauer spectroscopy. The Mossbauer spectra recorded on the two supports are distinctly different (Figs. 28 a, b).

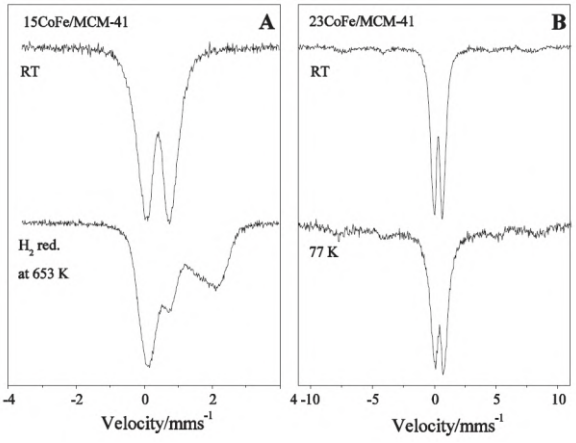

Figure 28a Mössbauer spectra of MCM-41 supported samples recorded at ambient (300 K – RT) and at liquid nitrogen (77 K) temperatures. Sample 15CoFe/MCM-41 calcined at 773 K and reduced at 653 K (A), sample 23CoFe/MCM-41 calcined at 773 K (B)

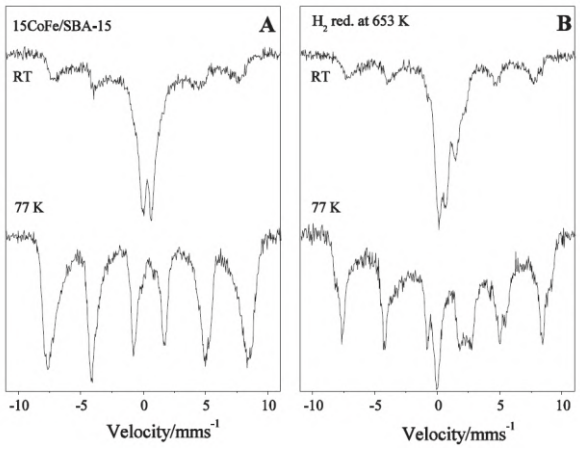

Figure 28b Mossbauer spectra of 15CoFe/SBA-15 sample recorded at ambient (300 K - RT) and at liquid nitrogen (77 K) temperatures. Sample calcined at 773 K (A), and treated in hydrogen at 653 K (B)

Spectra of MCM-41 supported samples are predominantly characteristic for iron incorporated into the silica matrix and forming small oxide ensembles - the presence of $CoFe_2O_4$ spinel phase is hardly detected, mostly the superparamagnetic component is seen in Fig. 28a. The spectrum of 23CoFe/MCM-41, recorded at the liquid nitrogen temperature (77 K - Fig. 28a), exhibits antiferromagnetically ordered component (sextet) only in smaller proportion (~40 %), which may be attributed either to small iron oxide or the formed Co-ferrite spinel phase with less than 10 nm size. Treatment of the 15CoFe/MCM- 41 sample in hydrogen at 653 K converts most of the Fe^{3+} component to Fe^{2+} displaying simple doublets (ca. 80% - see 16). This $Fe^{3+} \Rightarrow Fe^{2+}$ conversion upon hydrogen treatment at 653 K is characteristic to isomorphously substituted Fe-MCM-41 samples, thus it can be assumed that this component is not connected to cobalt ions. The remaining mixed valent Fe^{2+}/Fe^{3+} component can be assigned to the CoFe mixed ferrite phase (present only in ca. 20%).
In contrast, spectra recorded on the SBA-15 impregnated sample attest for the expressed presence of $CoFe_2O_4$ spinel phase. The antiferromagnetic ordering is almost complete in the 77 K spectrum of the calcined sample (Fig. 28b). After reduction in hydrogen both Fe^{2+} and Fe^{3+} components can be found in the antiferro- magnetically ordered ferrite phase. Only a minor part of Fe^{3+} is reduced to Fe^{2+} component exhibiting the non-magnetic Fe^{2+} doublet. Consequently most of the iron in the SBA-15 supported sample is interacting with cobalt in the Co-ferrite phase.
In summary, we can conclude that on MCM-41 support most of the iron oxide and cobalt oxide phases are separated and only a minor amount of CoFe mixed spinel phase forms. Interaction of transition metals with the silanol groups of the silica support is significant, whereas on the SBA-15 support the mixed spinel phase is dominant.
TPR-TG profiles of the metal modified materials are used for calculation of their reduction rates (58-83%, Table 7) which are lower than the theoretically needed and can be also explained by the formation of hardly reducible iron and cobalt silicates. According to our former investigations these types of species can be reduced only at

much higher temperatures (over 1000 K). SBA-15 supported ferrite samples exhibit a wide peak between 500 and 773 K. According to XRD data, this reduction step corresponds to the reduction of cobalt-ferrite phase to metallic state. This step is more pronounced with a higher amount of metal loading and shifted to lower temperatures compared to MCM-41 samples due to the formation of bigger ferrite particles (Table 7). The extent of reduction is higher (70-83%) compared to MCM-41 varieties, which is an indication of weaker metal support interaction. Higher temperature salt decomposition results in the formation of a higher amount of ferrite phase in MCM-41 sample but the crystallite size is not increasing. Because of the wider channels of the SBA-15 support, crystallization procedure of ferrite is more complete at this higher temperature and bigger crystallite sizes can be observed (Table 7). However, a stronger metal support interaction is also evidenced by the shift of the TPR peaks to higher temperatures and the lower reducibility of the samples (26-47%, Table 7).

High temperature in situ XRD measurements fully support our TPR results. The main reduction product of all the cobalt and iron modified catalysts, detectable by XRD method, is metallic iron (α-Fe). Formation of metallic iron on 23CoFe/MCM-41 and SBA-15 catalysts begins even at 623 K (not shown). The samples with the lower amount of transition metals behave differently. First traces of metallic iron on 15CoFe/MCM-41 can be observed only after reduction with hydrogen at 773 K. Reducing 15CoFe/SBA-15 at 623 K only the presence of FeO phase can be observed, but two-valent iron is readily reduced to zero-valent state up to 673 K. The presence of cobalt(II) oxide or metallic cobalt cannot be observed by in situ XRD investigations. It is highly probable, that the lower amount of cobalt released from spinel structure is reacting with the silanol groups on the surface of the silica support and cannot form a separate metallic cobalt phase, detectable by XRD. These results are also in accordance with our Mossbauer investigations. Upon reduction in 15CoFe/MCM-41 only the formation of Fe^{2+} species, incorporated into the silica matrix, can be observed. In the case of the 15CoFe/SBA-15 sample formation of a two-valent iron oxide phase is evidenced.

In Fig. 29 the temperature dependence of catalytic activity in toluene oxidation on the modified MCM-41 and SBA-15 materials is presented.

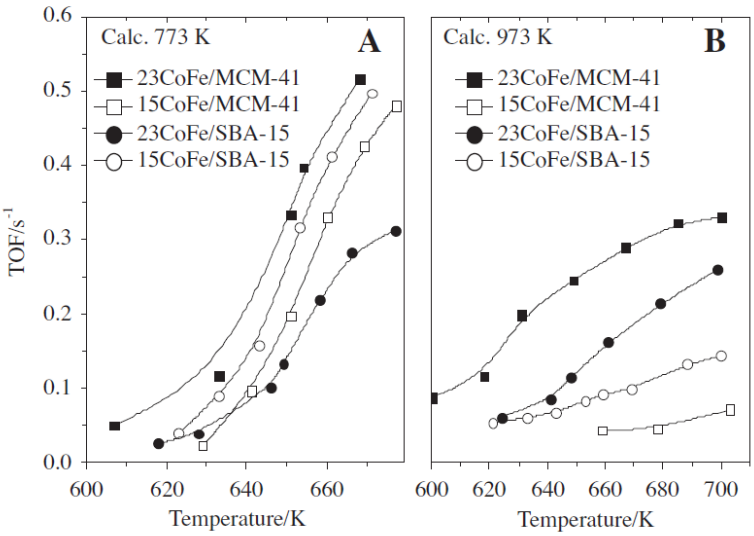

Figure 29 Toluene conversion vs. reaction temperature on the studied samples calcined at 773 (A) and 973 K (B)

Prior to the catalytic tests the catalysts calcined *ex situ* at different temperatures (779, 973 K) were pretreated in nitrogen at 623 K for 1 h. Precursor decomposition at 773 K resulted in high catalytic activity for all studied samples, whereas decomposition at higher temperature – in significant activity decrease (Fig. 29). This can be explained by the stronger silica-metal interaction at high calcination temperature and consequently by the lower amount of separate oxide phase, active in the catalytic reaction. In our previous work it was found (Szegedi et al., 2008) that the temperature for precursor decomposition has decisive influence on the nature of the formed cobalt oxide species. Mild oxidative pretreatment has a favorable effect on the formation of Co_3O_4, whereas precursor decomposition at higher temperature leads to stronger metal-support interaction and formation of mostly Co^{2+} ions and Co-silicate like species. These facts are also supported by the much lower reducibility of the samples, calcined at 973 K. Also the dispersion of ferrite phase is decreased, evidenced by the XRD results. Comparing the different preparations at 773 K precursor decomposition temperature, the highest catalytic activity was achieved by the 23CoFe/MCM-41 sample. This effect can be explained by the simultaneous presence of Co^{2+}/Co^{3+} and Co^{2+}/Fe^{3+} species in the catalyst, providing easier oxygen release, essential for Mars-van Krevelen mechanism, widely accepted in the literature for this type of reaction. According to the mechanism of oxidation, after the adsorption of VOC molecule on the catalyst surface, its oxidation with lattice oxygen takes place, followed by the oxidation of the reduced catalysts. The process of adsorption of organic molecules can be affected by the surface properties of the catalysts. Activity in total oxidation of VOC is connected with the interaction of aromatic electrons with metal ions in tetrahedral position, acting as Lewis acid sites, increasing the possibility of

electrophilic attack of adsorbed oxygen and combustion of toluene molecules. The lowest catalytic activity was observed for the 23CoFe/SBA-15 catalyst. Our XRD data show that the crystallite size of ferrite particles is similar to the channel diameter of SBA-15 host. TEM images revealed that ferrite particles (7.7 nm) are mainly located in the channel system (6 nm) filling them like pearls, preventing the reactant from accessing the oxide phase. This phenomenon was also supported by N_2 physisorption measurement where some pore blocking effects were detected. Both 15% metal-containing catalysts show medium activity between the former two samples. The lower reducibility of the 15CoFe/MCM-41 sample can be an explanation for its lower catalytic activity in comparison to 23CoFe/MCM-41. However, despite its lower reducibility 15CoFe/SBA-15 shows higher catalytic activity in comparison to its SBA-15 supported analog with higher metal content. More probably the extent of reduction of the catalysts by hydrogen does not correspond directly to that of by a reactant. It was also found (Jiratova et al., 2009) that the enhancement of the reducibility of the K-modified Co-Mn-Al mixed oxide is reflected in lower activity in toluene oxidation.

Salt decomposition at 973 K not only reduced the catalytic activity, but the behavior of the different catalysts has also changed. The most active catalysts became those with higher amount of metals. The extremely low catalytic activity of 15CoFe/MCM- 41 can be explained by the stronger metal-support interaction at this high temperature resulting in very low reducibility (27%), which is a clearly indicating the lack of sufficient amount of separate oxide phase active in the reaction. The higher oxidation temperature probably leads to further transformation of finely dispersed Co_3O_4 particles to cobalt silicate which are mainly formed on MCM-41 support. Our XRD and TPR data for the samples calcined at 973 K are indicative for the formation of very finely dispersed cobalt oxide phase, strongly connected with the silica support. Such transformation of cobalt supported samples, depending on the calcination temperature, has been reported also by Van Steen.

Our catalytic results on cobalt ferrite-modified silica materials can be summarized as follows: (i) salt decomposition at 773 K leads to metal oxide species formation on mesoporous support possessing higher catalytic activity in comparison to the ones formed by calcination at 973 K; (ii) in MCM-41 support the reaction of metal precursors with the silanol groups is more favorable and formation of Co^{2+}/Co^{3+} and Co^{2+}/Fe^{3+} species, more active in toluene oxidation, can be observed; (iii) in SBA-15 the formed well-crystallized separate ferrite phase fills the pores and hinders the access of the reactant molecules to the active sites.

3.1.2.5. Titanium- and iron-modified MCM-41 catalysts

Substituted with iron and titanium mesoporous MCM-41 were obtained by impregnation and sol-gel synthesis in order to form active centers of mixed metal oxide species.

The silica MCM-41, the monosubstituted TiMCM-41 and FeMCM-41 materials and the bisubstituted titanium- and ironcontaining sample (TiFeMCM-41) were prepared at room temperature. For comparison a sample with higher amount of Ti (Si/Ti = 2) was synthesized by the same procedure. It was denoted as Ti(2)FeMCM-41. Titania impregnated FeMCM-41 sample (Ti/FeMCM-41) was prepared to achieve 25 wt.% TiO_2 loading.

Small angle XRD patterns of parent silica material exhibit reflections typical of hexagonally arranged pore structure, which is almost preserved after the modification. The shift of the position of the (100) reflection for the modified materials in comparison with the parent one could be assigned to the incorporation of the metal ions in the silica framework. Higher degree of titanium incorporation could be concluded in the case of bisubstituted directly synthesized material, where more distinguished shift of the SAXS reflection to smaller 2 Theta, in comparison with pure MCM-41, is observed. Partial silica matrix collapse can be assumed only for Ti(2)FeMCM-41, where the disappearance of the (100) reflection confirms the long range ordering decrease of the structure. In the wide-angles region no characteristic reflections of any iron and/or titanium containing species are registered, which suggests their predominant incorporation into the MCM-41 silica framework. Only in the case of Ti/FeMCM-41 wide reflections of anatase phase are observed.

The nitrogen physisorption isotherms of parent MCM-41 silica are of type IV (IUPAC classification), with a sharp capillary condensation step at about 0.25 p/p_0, characteristic of mesoporous materials with narrow pore size distribution. After the modification, the isotherms preserve their shape, indicating the mesoporous structure preservation. Only in the case of the sample with the highest titanium content, Ti(2)FeMCM-41, a partial structure collapse (Table 8) could be assumed, which is in accordance with the XRD measurements. The impregnated sample, Ti/FeMCM-41, exhibits a simultaneous decrease in the pore volume and average pore diameter, indicating a partial pore blocking due to the deposition of anatase particles.

Table 8 Phisico-chemical properties of the studied samples

Samples	Si/Fe	Si/Ti	content of Fe[a] (mmol/g)	S_{BET} (m^2/g)	pore diameter (nm)	pore volume (cm^3/g)	a_o[b]
SiMCM-41	-	-	-	1198	2.3	1.00	3.94
FeMCM-41	20	-	0.78	984	2.3	0.92	3.95
Ti/FeMCM-41	20	4	0.62	880	2.2	0.62	3.83
TiFeMCM-41	20	10	0.68	852	2.5	0.91	3.95
Ti(2)FeMCM-41	20	2	0.48	573	2.3	0.71	-
TiMCM-41	-	10	-	907	2.6	0.90	4.06

[a] related to 1 g calcined at 1273 K; [b] cell parameter ($a_o=2d_{100}(3)^{-1/2}$

Mössbauer spectroscopy is applied for more detailed characterization of the iron species. The spectra of all studied materials consist only of doublet-lines. Their optimal mathematical treatment represents two doublet components with different relative weight. The determined hyperfine parameters of the two sets of doublets show the presence of high spin Fe^{3+} ions in tetrahedral (Dbl 1) and octahedral (Dbl 2) oxygen coordination, respectively. Dbl 1 can be assigned to iron species isomorphously incorporated into the silica framework. The interpretation of Dbl 2 is more complicated. On one hand, its parameters could be indicative for the presence of finely dispersed iron oxide nanoparticles (D<10nm) with superparamagnetic behavior. On the other hand, Dbl 2 could also be assigned to Fe^{3+} ions incorporated into the silica framework, completing their coordination spheres to octahedral with adsorbed water molecules.

All iron containing samples show a well pronounced TPR peak between 500 and 870 K. The calculated hydrogen uptake (Table 9) for FeMCM-41 corresponds to one electron transfer, i.e. Fe^{3+} ions could be reduced only to Fe^{2+} state up to 870 K. The lower hydrogen uptake, which is registered for bisubstituted directly synthesised materials in comparison with FeMCM-41, could be assigned to the more difficult reduction of the iron species in the case of the former materials (Table 9). Changes of the iron environment, probably due to the formation of -Ti-O-Fe- type species, can be responsible for this decreased reducibility. The hydrogen uptake at lower temperature and higher degree of reduction (about 100%) that is found for Ti/FeMCM-41 could be assigned to the presence of easily reducible iron oxide species in it. This effect confirms the limited formation of -Ti-O-Fe- type species during the impregnation technique.

Table 9 Redox properties of titanium- and iron-modified MCM-41 materials

Samples	H_2 uptake[a] (mmol/g)	extent of reduction[b] (%)	C[c] (wt. %)
FeMCM-41	0.42	100.0	1.11
Ti/FeMCM-41	0.31	100.0	0.00
TiFeMCM-41	0.21	62.0	6.60
Ti(2)FeMCM-41	0.19	79.7	8.83
TiMCM-41	0.05	7.9	4.65

[a] calculated from the area of TPR curves in the range of 373-1073 K,
[b] calculated from the H_2 uptake related to the total amount of iron and titanium,
[c] amount of coke formed during the 240 min reaction at 613 K.

For the monosubstituted samples, the titanium containing one exhibits lower catalytic activity and it remains almost unchanged with time on stream (Fig. 30). In contrast to that, a well-defined trend to catalytic activity decrease is registered for FeMCM-41 (Fig. 30 B). Among the modified materials, Ti/FeMCM-41 possesses the best catalytic activity and stability. Lower catalytic activity but higher stability in comparison with FeMCM-41 is observed for bisubstituted materials, prepared by direct synthesis. A well-pronounced increase in the catalytic activity with time on stream is registered for these samples as well. The catalytic activity significantly decreases with the increase of the titanium content, which could be due to the lower BET surface area and the high degree of structure collapse in this case (see XRD, N_2 physisorption data). The hydrogen pretreatment at 723 K leads to an increase in the catalytic activity of TiMCM-41 and to its decrease for the iron containing materials (Fig. 30 B). Only in the case of Ti/FeMCM-41 a negligible effect of preliminary reduction is observed.

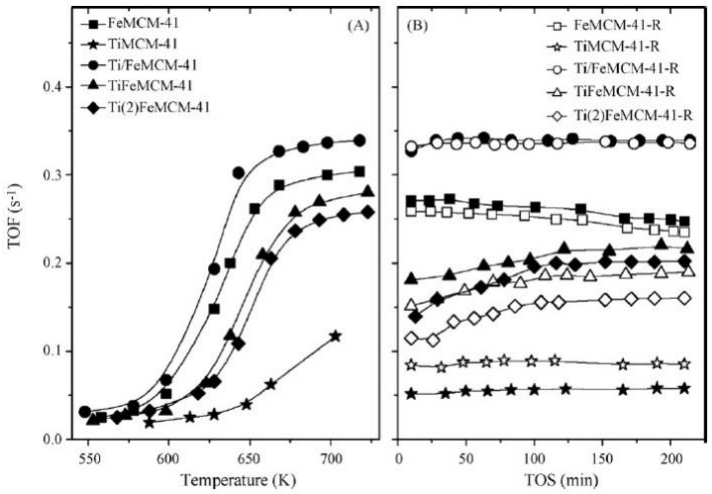

Figure 30 Catalytic activity vs. temperature (A) and time on stream at 673K (B) on the modified materials before and after pretreatment in hydrogen at 723K

After the catalytic tests some structural changes of the samples could be observed. The Mössbauer spectra exhibited increasing relative part of the octahedrally coordinated iron ions, which could be ascribed to their partial release from framework positions. These changes are negligible for TiFeMCM-41 that confirms the favorable effect of titanium incorporation for the stabilization of iron ions in framework positions. The appearance of a new doublet component with a higher isomer shift, that is registered only for the sample with a partial structure collapse, Ti(2)FeMCM-41, could be ascribed to Fe^{2+} ions. The DTG analysis in air of the materials used in catalytic tests, point to the presence of non-desorbed products, which can be found in higher amount on the samples possessing lower catalytic activity. Formation of coke precursors, probably due to the oligomerization of intermediate products of the total toluene oxidation is expected. This coke deposition could be considered a reason for the reduction transformations of the samples during the catalytic tests.

Summarizing the catalytic performance and physicochemical analysis of the modified materials, the simultaneous participation of different catalytically active sites could be assumed. The activity of Fe^{3+}-Fe^{2+} and Ti^{3+}-Ti^{4+} redox ion couples is expected in the case of FeMCM-41 and TiMCM-41, respectively. According to Mars-van-Krevelen mechanism, which is usually realized during the toluene oxidation, the participation of oxygen from the solid catalyst is of key importance. In this aspect, the higher catalytic activity of FeMCM-41 could be assigned to the easier release of oxygen from the modified silica lattice, probably due to the higher polarization of the Fe-O-Si bond in comparison to the Ti-O-Si one. This assumption is supported by the easier reducibility of the iron-modified MCM-41 (see TPR data). The intermediate catalytic activity that was observed for the directly modified bisubstituted materials in comparison to their monosubstituted analogues could be ascribed to the presence of hardly reducible active sites, probably type Fe-O-Ti (see TPR data). The electron transitions types of Fe^{2+}-Ti^{4+} and Fe^{3+}-Ti^{3+} could be suggested in them during the redox process. These transitions seem to be favored for the hydrogen pretreated materials (Fig. 30 B). The facilitated effect of the formed Fe-O-Ti species on the catalytic stability should also be stressed (Fig. 30 B). In the case of monosubstituted iron containing material (FeMCM-41) the catalytic activity decrease could be assigned to the partial iron release from the tetrahedral position, most probably with the formation of hematite like nanoparticles. Such hematite like nanoparticles seem to be also formed in the impregnated sample, Ti/FeMCM41, and this is confirmed by the decreased relative part of the tetrahedrally coordinated iron species in the Mössbauer spectra after the catalytic test. These transformations could be due to the influence of the reaction and pretreatment media or the water formed in the reaction, leading to the formation of hematite like nanoparticles. Their deposition on the anatase phase could be a reason for the increased catalytic activity. Here, the titania support effect on the hematite like nanoparticles resulted in facilitated oxygen release from the iron oxide species, could be assumed and it is confirmed by the sample's easier reducibility.

3.1.2.6. Cobalt- and iron-containing Ti-MCM-41 catalysts

Substituted with iron and titanium mesoporous MCM-41 were obtained by impregnation and sol-gel synthesis in order to form active centers of mixed metal oxide species.

The starting Ti-MCM-41 (Si/Ti = 10 or 20) was synthesized and designated Ti-MCM-41(x), where x is the Si/Ti ratio. Modified monocomponent materials (Co/Ti-MCM-41(x) and Fe/Ti-MCM-41(x)) and two-component materials (CoFe/Ti-MCM-41(x)) were obtained, where x is 10 wt. % of the metal content in the monocomponent catalysts and 5 wt. % for each metal oxide for the two-component catalysts.

XRD patterns of the modified samples in the higher angle region, reflections typical of Co_3O_4 can be observed for cobalt-containing samples. However, no characteristic reflections of any iron or titanium containing species are registered, which suggests their low dispersion (<5 nm) or their incorporation into the MCM-41 silica framework.

Formation of larger Co_3O_4 particles is found for the sample with lower titanium content, Co/Ti-MCM-41(20) (Table 10).

Table 10 Physico-chemical properties of the studied samples

Samples	S_{BET} (m^2/g)	pore diameter (nm)	Co_3O_4 crist. size[a] (nm)	extent of reduction[b] (%)
Ti-MCM-41(20)	1109	2.6	-	-
Co/Ti-MCM-41(20)	804	2.4	40	81.4
CoFe/Ti-MCM-41(20)	809	2.4	15	95.4
Fe/Ti-MCM-41(20)	798	2.4	-	24.4
Ti-MCM-41(10)	1032	2.6	-	-
Co/Ti-FeMCM-41(10)	716	2.4	28	53.7
CoFe/Ti-FeMCM-41(10)	751	2.4	14	90.2
Fe/Ti-MCM-41(10)	851	2.4	-	22.2

[a] determined by XRD, using the Sherrer equation, [b] calculated from the TPR experiment related to the calculated theoretical weight loss for the reduction of the corresponding ion to metallic state.

The bicomponent CoFe/Ti-MCM-41 material possesses very weak and broad reflections due to the presence of finely dispersed Co_3O_4 particles (Table 10). Consequently, incorporation of cobalt into the silica structure can be assumed in these bicomponent samples as well.

The BET surface area and the average pore diameter of the modified Ti-MCM- 41 materials slightly decreased after the impregnation process (Table 10). These results can be explained by the formation of finely dispersed metal oxide species inside the channels of Ti-MCM-41 supports.

DR UV-Vis spectra (Fig. 31) recorded at room temperature are used for the characterization of oxidation and coordination state of cobalt and iron oxide species of the modified MCM-41 samples. The presence of a triplet at 540, 585 and 630 nm can be assigned to the electronic ligand-field $^4A_2(F) \rightarrow {}^4T_1(P)$ transition for tetrahedrally coordinated Co^{2+}, whereas the absorption band around 420 and 730 nm can be attributed to octahedrally coordinated Co^{3+} in the mixed spinel oxide phase Co_3O_4 (Kotsoulidis et al., 2006). Co/Ti-MCM-41(20) sample displays more intense absorption bands at 420 and 730 nm, typical of octahedrally coordinated Co^{3+} in Co_3O_4, in comparison to Co/Ti-MCM-41(10). The UV-Vis spectra (Fig. 31) of both monocomponent iron-containing Ti-MCM-41 materials exhibit an absorption band in the 210-290 nm region attributable to isolated, tetrahedrally coordinated iron and titanium species. The bands over 300 nm, detected for both iron-containing materials, most probably arise from the presence of oligomeric FeO_x species and finely dispersed hematite-like nanoparticles. In the case of the bicomponent cobalt- and iron-containing Ti-MCM-41 samples both bands at 210-290 nm, characteristic for the isolated iron species, and the bands at 420 and 730 nm, associated with octahedrally coordinated Co^{3+} in Co_3O_4, can be detected. A more intense 420 and 730 nm band can be observed for CoFe/Ti-MCM-41(20). We can conclude that the formation of Co_3O_4 phase occurs predominantly on the Ti-MCM-41(20) support.

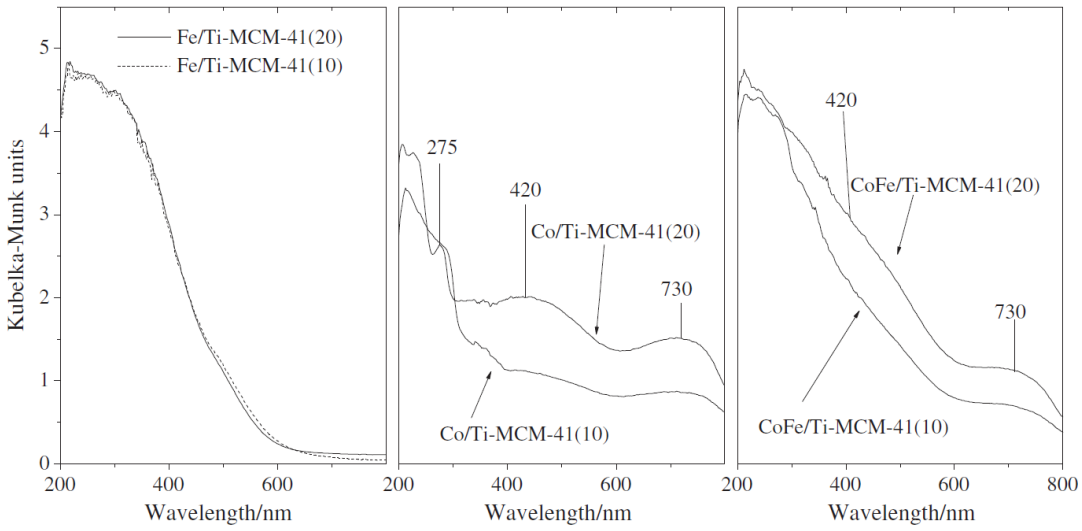

Figure 31 UV-Vis spectra of the cobalt- and/or iron-containing Ti-MCM-41 materials

TPR profiles of the metal modified materials are shown in Fig. 32. TPR curve of Co/Ti-MCM-41(20) sample has two overlapping reduction peaks with a maximum at 550 K and a shoulder at 613 K, attributed to the reduction of

Co_3O_4 to Co^0 in a two-step process. The extent of reduction of this sample is 81.4%, assuming that 2.66 electrons/Co are needed for the total reduction of Co_3O_4 to Co^0. This reduction behavior indicates that salt decomposition in air at 773 K results in the formation of relatively large, easily reducible Co_3O_4 particles, observed also by XRD. The TPR profile of Co/Ti-MCM-41(10) shows an intense reduction peak at 565 K. The extent of reduction is 53.7%. Probably, the higher amount of titania in the Ti-MCM-41(10) support favors the stabilization of cobalt ions as Co-O-Ti species, reducible only at higher temperatures (over 1000 K). The TPR curves of iron-containing monocomponent samples show reduction peaks at 615 K and 590 K for Fe/Ti-MCM- 41(20) and Fe/Ti-MCM-41(10), respectively. The calculated extent of reduction is 24.4% and 22.2%, which correspond to the reduction of hematite-like nanoparticles to magnetite type mixed oxide phase (Fe_3O_4). A relatively narrow reduction peak at 600 K can be observed for the bicomponent CoFe/Ti-MCM-41 samples. Reduction behavior of the bicomponent catalysts seems to have both characteristics of the monocomponent ones, however the presence of iron favors the formation of very finely dispersed Co_3O_4 supported by the XRD data.

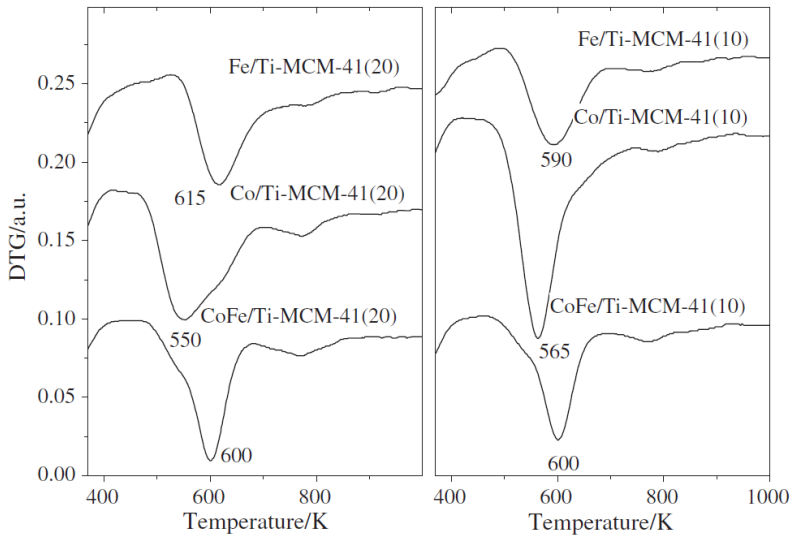

Figure 32 TPR profiles of the modified samples

Mössbauer spectroscopy was also applied for the characterization of iron species. Spectra consist only of doublet-lines with similar relative weights. The determined hyperfine parameters of two sets of doublet-lines (Dbl 1 and Dbl 2) can be assigned to ultradisperse hematite-like nanoparticles (D <10 nm) with superparamagnetic (SPM) behavior. In accordance with the calculated core/shell ratios, almost similar iron particle dispersion could be assumed for both samples. These results are in good accordance with the XRD and TPR data, assuming the formation of finely dispersed iron oxide species and almost equal extent of reduction for both iron containing samples (Table 10). In the EPR spectra of Co/Ti-MCM-41 catalysts a signal at about g = 2.2, corresponding to Co_3O_4, can be observed (Makshina et al., 2008), with lower intensity for Co/Ti-MCM-41(10). Detection of Co_3O_4 particles in Co/TiMCM-41 catalysts is in good accordance with their XRD and UV-Vis spectroscopic data. Moreover, the higher intensity of Co_3O_4 EPR signal of Co/MCM-41(20) sample is in accordance with its higher reducibility (81.4%, Table 10) and the formation of larger particles (40 nm, Table 10) in comparison to Co/Ti-MCM-41(10) sample. The EPR spectra of both iron-containing MCM-41 samples show the presence of EPR signal at about g = 2.0.

The EPR spectra of the bicomponent mesoporous materials possess EPR signal at g = 4.3 with very low intensity and two overlapping signals at about g = 2.2 and about g = 2.0. The signal at g = 4.3 corresponds to Fe^{3+} species with distorted tetrahedral coordination. The other two signals can be interpreted as a combination of cobalt and iron oxides, probably more finely dispersed in comparison to the monocomponent ones. The shift of g values to higher magnetic field of bicomponent samples compared to the theoretically calculated spectra assuming the combination of monocomponent samples is due to the predominant formation of cobalt oxide species in spinel oxide. The appearance of the signals at g = 4.3 and g = 2.2 can be interpreted as the formation of iron species with different coordination states compared to the monocomponent ones. These facts are also supported by the higher extent of reduction of the bicomponent catalysts (Table 10). On the basis of the EPR data we can conclude that in the bicomponent mesoporous MCM-41 modifications metal oxides are formed after salt decomposition rather than metallic ions connected to the mesoporous support.

In Fig. 33 the temperature dependence of catalytic activity in total oxidation of toluene on various cobalt and iron modified Ti-MCM-41 materials is shown.

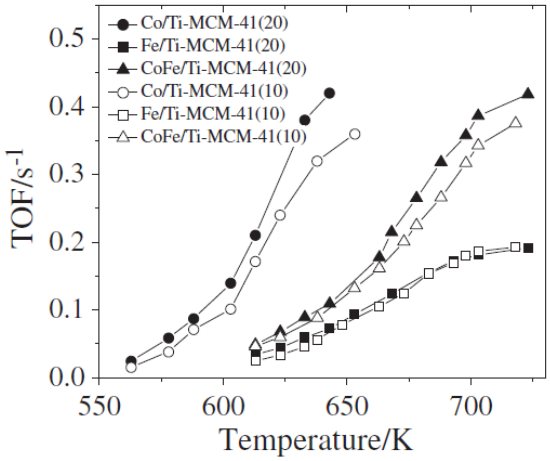

Figure 33 Toluene conversion vs. reaction temperature on the studied samples, pretreated in air at 773 K

Prior to the catalytic tests the catalysts were pretreated in air at 773 K for 2 h in order to ensure the salt decomposition. The shift of the conversion curves of Fe/Ti-MCM-41 and CoFe/Ti-MCM-41 materials to higher temperatures compared to Co/Ti-MCM-41 is an evidence for their lower catalytic activity. The higher catalytic activity of Co/Ti-MCM-41 catalysts is related to the presence of Co^{3+}/Co^{2+} type catalytic active centers in Co_3O_4 phase, where easier release of oxygen can be realized. The latter is well known as a crucial step in the Mars-van-Krevelen mechanism, widely accepted in the case of toluene oxidation reaction. Higher catalytic activity was achieved by Co/Ti-MCM-41(20) sample, despite of the larger Co_3O_4 particles of the catalyst. The higher extent of reduction compared to Co/Ti-MCM-41(10) can explain this positive effect on the catalytic behavior. Higher extent of reduction can be associated with the presence of higher amount of Co_3O_4 as a separate phase essential for the easier redox transformations of the catalyst during the reaction.

The catalytic activities of Co/Ti-MCM-41, CoFe/Ti-MCM-41 and Fe/Ti-MCM-41 catalysts, pretreated in different media and temperatures with time on stream, are presented in Fig. 34. Both monocomponent cobalt-containing catalysts show steady and slightly increasing catalytic activity with time on stream. The bicomponent samples possess also stable activity during the investigated period. The pretreatment in air and subsequently in hydrogen at 773 K leads to higher catalytic activity for both types of (mono- and bicomponent) cobalt-containing samples (Fig. 34). High and stable catalytic activity is observed for cobalt-containing samples, more pronounced for Co/Ti-MCM-41(10) material.

Comparing the catalytic results with the physico-chemical investigations, it could be assumed that the catalytic process is facilitated mainly by the presence of finely dispersed Co_3O_4 particles. Reductive treatment can lead to the release of additional amount of cobalt species formerly connected to the mesoporous matrix (on the surface of the channels) and during the oxidative reaction to the formation of finely and homogeneously dispersed cobalt oxide. The higher catalytic activity increase of Co/Ti-MCM-41(10) catalyst is most probably due to the formation of the above mentioned highly dispersed Co_3O_4 particles in higher amount by the reaction conditions, because of the lower initial reducibility of this catalyst. This is supported by our XRD data showing the formation of Co_3O_4 particles with 21 nm crystallite size of the spent catalyst. The relatively lower activity increase of Co/Ti-MCM-41(20) can be explained also by the formation of CoO stabilized on the support at the applied reaction conditions, detectable by XRD. However, in this case we also can not exclude the formation of finely dispersed Co_3O_4 phase, not detectable by XRD. According to the EPR spectrum of the latter sample formation of different types of cobalt oxides (Co_3O_4, CoO) is supported by the signal at g = 2.1 and the appearance of a signal at g = 2.4. The most significant influence of the pretreatment conditions (air and subsequently hydrogen at 773 K) on catalytic activity can be observed by the bicomponent samples. They show about five times higher catalytic activity than the only air-pretreated varieties. A well-defined trend to activity drop can also be observed for both bicomponent catalysts in the first 25 min. The latter can be associated with the transformation of the initially formed magnetite (Fe_3O_4) to hematite (Fe_2O_3) in the oxidative reaction media. The Mössbauer spectra of the air and hydrogen pretreated CoFe/Ti-MCM-41 samples indicate that a part of Fe^{3+} is reduced to Fe^{2+} and besides also an α-FeCo alloy phase is formed. In EPR spectrum of the catalyst a sharp and characteristic signal at g = 2.0 shows (Vaidyanathan et al., 2008) that highly dispersed cobalt ferrite particles can be found in the spent catalysts after the oxidation reaction. The presence of Fe_2CoO_4 phase was also evidenced by the XRD investigation of the used catalyst.

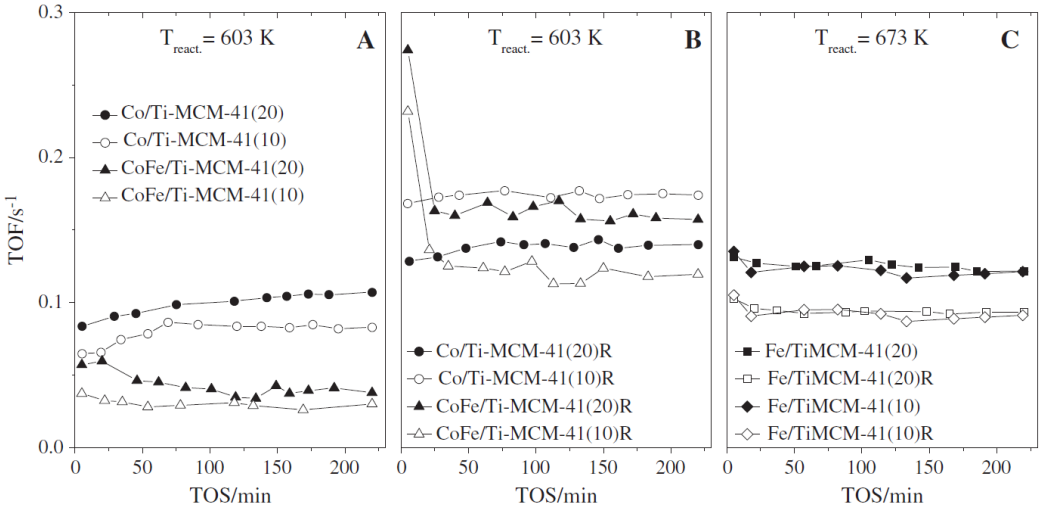

Figure 34 Toluene conversion vs. time on stream at 603 K on Co/Ti-MCM-41 and CoFe/Ti-MCM-41 samples, pretreated in air at 773 K (A), pretreated in air and subsequently in hydrogen at 773 K denoted as (R) (B) and at 673 K on Fe/Ti-MCM-41, pretreated in air at 773 K or in air and hydrogen at 773 K (C)

The Fe/Ti-MCM-41(20) sample shows lower catalytic activity after pretreatment in air and subsequently in hydrogen at 773 K comparing to the one pretreated only in air at the same temperature (Fig. 34 C). Time on stream investigations were carried out at 673 K because of the lower catalyst activity. This result could be explained by the formation of agglomerated iron oxide clusters on the reoxidation process, possessing lower catalytic activity. This assumption was supported by EPR data of the used Fe/Ti-MCM-41(20) sample showing the intensive EPR signal at g = 2.2 which is associated with the formation of Fe^{3+} species in non-framework positions.

3.1.2.7. Copper- and cobalt-modified coal ash zeolites

The fly ash zeolite (FAZ) and copper- or cobalt-modified FAZ materials were studied as VOCs oxidation catalysts that are expected to be a low-cost alternative of the existing catalysts and to reveal another valuable utilization approach of coal ash residues.

Fly ash generated by combustion of lignite coal from the major energy source of Bulgaria, "Maritza East" basin, was used as a raw material for synthesis of FAZ. FA was sampled from the electrostatic precipitators of three different Thermal Power Plants (TPP), namely TPP "Maritza East 2" (ME 2), TPP "AES Galabovo" (AES) and TPP "Contour Global" (CG). FAZ samples were obtained by alkaline conversion of FA applying three different procedures: double-stage fusion-hydrothermal activation (FHA), double-stage fusion-atmospheric crystallization (FAC) and atmospheric ageing (AA). An incipient wetness impregnation technique was used for the preparation of Cu- and Co-modified FAZ catalysts, containing 5 wt. % Cu and 6 wt. % of Co (Cu-FAZ and Co-FAZ). H1, H2 samples were prepared by hydrothermal crystallization and sonication for 15 and 25 minutes, respectively. FH sample is prepared by fusion-hydrothermal activation and 15 minutes sonication and AS sample is prepared by atmospheric crystallization.

The studied fly ash (FA) samples are characterized by a mixed amorphous/crystalline structure evidenced by a well-expressed amorphous hallow and a number of intensive reflections. The following crystalline phases are identified on all the X-ray diffractograms: Quartz (α-SiO_2), Mullite ($Al_6Si_2O_{13}$), Magnetite (Fe_3O_4) and Hematite (α-Fe_2O_3), while Anorthite ($CaAl_2Si_2O_8$) is observed in FA_{AES} and FAcg, and Gypsum ($CaSO_4$) in FAME2. The ratios of amorphous versus crystalline part in FA were computed by deconvolution of the experimental X-ray diffractograms. It was found that the amorphous/crystalline ratio is 0.75 for FA_{ME2}, 1.86 for FA_{AES} and 1.0 for FA_{CG}. FA samples from the three TPPs differ to some extend in their chemical and phase composition despite the fact that the origin of the lignite coal is same field, likely due to the variability in composition of fossil fuels and peculiarities of the incineration systems. A common feature of all the studied FA is that they belong to class F according to ASTM C168 (ASTM C618, Standard Specification for Coal Fly Ash and Raw or Calcined Natural Pozzolan for Use in Concrete, 2018) as SiO_2+Al_2O_3+Fe_2O_3>70 wt.% and CaO << 20 wt.%. The aluminosilicate part SiO_2+Al_2O_3>70 wt.% predominates in the composition of all the FA samples, as the weight ratios of SiO_2/Al_2O_3 are 2.25 for FA_{me2}, 2.00 for FA_{aes} and 1.92 for FA_{CG}, which is equal to molar ratios of 3.8, 3.4 and 3.3, respectively. According to its chemical composition, FA from the three TPPs is suitable starting material for the synthesis of high-silica zeolites of Na-X type, that require optimal molar ratios of SiO_2/Al_2O_3>3 (Querol et al., 2002). Aside from the presence of iron oxides as crystalline phases, iron can also be incorporated in the amorphous matrix of FA. It was established in our previous studies that surface

and bulk transformation of magnetite to hematite takes place under thermal heating above 523 K.
The synthesis conditions of FAZ were summarized in Table 11. The experimental X-ray diffractograms of the FAZ synthesized by different synthesis procedures and the referent zeolite Na-X reveal the main characteristic reflexes of a predominant zeolite phase identified as Na-X for all the samples. The XRD patterns of FAZ_ME2_AA1 and FAZ_ME2_AA2 show reflections at 2 Theta = 35.62°, which are assigned to magnetite, while for the other zeolite samples obtained by applying fusion stage this characteristic line has disappeared, because magnetite most probably transforms to hematite finely dispersed into the zeolite matrix, or it has chemically interacted to sodium ferrite. It could also be expected that part of the iron participates as a compensating cation into the zeolite framework. Initial crystallization of a phase with reflections at 2 Theta = 13.97° and 14.27° typical for Sodalite is registered at FAZ_CG_FHA. The most intensive reflections on the FAZ diffractograms are assigned to Na-X zeolitic phase.

Table 11 Synthesis condition of FAZ prepartation

Samples	raw FA	synthesis procedure	NaOH/FA	NaOH (mol/l)	T_f (K)	T_h (K)	τ
FAZ_ME2_AA 1	FA_{ME2}	AA	0.6	1.5	NA	NA	180 дни
FAZ_ME2_AA 2	FA_{ME2}	AA	0.6	1.5	NA	NA	240 дни
FAZ_ME2_FAC	FA_{ME2}	FAC	1.0	2.5	823	NA	60 дни
FAZ_AES_FHA	FA_{AES}	FHA	2.0	2.5	823	363	21 часа
FAZ_CG_FHA	FA_{CG}	FHA	2.0	2.5	823	363	6 часа

T_f – fusion temperature;
T_h – temperature for hydrothermal activation;
τ - duration of FA activation.

The obtained results for BET surface area (S_{BET}, m^2/g), the specific surface area described by micropores (S_{micro}, m^2/g) and the micropore volume (V_{micro}, m^3/g) calculated applying t-plot model to the experimental isotherms, external surface area of the particles ($S_{external}$, cm^2/g), total pore volume (V_{total}, cm^3/g) and that determined by mesopores are summarized in Table 12, together with the calculated average micro- and mesopores width. The conversion extent of the raw FA into zeolite Na-X was calculated as a ratio of S_{BET} values of the FAZ and the referent Na-X, and was estimated towards the aluminosilicate part of the starting stuff, as was proposed by Kuceba-Majchrzak (Kueba-Majchrzak et al., 2018). The FAZ_AES_FHA, FAZ_ME2_AA2, FAZ_CG_FHA and FAZ_ME2_FAC samples show high surface area and pore volume (Table 12).
The textural parameters are in accordance with the extent of zeolitization determined for the samples. Among them, the FAZ_AES_FHA and FAZ_CG_FHA samples possess the highest surface area and pore volume which is related to their highest extent of zeolitization. N_2-adsorption/desorption isotherms of FAZ obtained by different synthesis procedures are with a similar shape, closest to isotherms of type IV, according to IUPAC classification (1985) (Table 12). Broad hysteresis loops are observed corresponding to a micro-mesoporous texture of the obtained materials. BET surface areas between 116 and 396 m^2/g were measured for FAZ of Na-X type, as the broadest specific surface was established for the FAZ sample obtained from FA_{AES} by a double-stage fusion-hydrothermal synthesis. Despite the fact that S_{BET} values for the studied FAZ are two to seven times lower than those of the referent Na-X, the zeolitization of FA enlarges the surface of the raw materials roughly eleven- to fortyfold. The yield of micropores in FAZ depends on their crystallinity and the synthesis technique, whereas the yield of mesopores is dominant in all the fly ash zeolites. Average mesopore width for FAZ was found in the range between 4.4 and 5.8 nm, as the main part of the porosity is due to pores with size around 4 nm (Table 12). It could be expected that the mesoporosity of FAZ will facilitate the mass transport through the materials, which will be of benefit for their application as catalysts.
Copper modification of FAZ reduces the specific surface parameters (Table 12). The specific surface value drops down to about 70% for Cu_FAZ_ME2_AA2 and about 43% for Cu_FAZ_AES_FHA. Taking into account the changes in the surface parameters it is obvious that part of the copper species fill the micropores of the zeolite structure. The yield of micropores into the framework of the FAZ obtained only by atmospheric aging is higher than when prepared by fusion step.
The extent of copper reduction for the Cu_FAZ_AES_FHA and Cu_FAZ_ME2_AA2 samples is 100% and 85%, respectively. The FAZ_ME2_AA2 synthesized without preliminary fusion stage contains γ-Fe_3O_4, which favours the interaction between copper oxide and magnetite species resulting in formation of finely dispersed spinel copper ferrites possessing lower reducibility. Copper-modified FAZ were subjected to X-ray diffraction studies to clarify the state of Cu in the FAZ matrix. The formation of α-Fe_2O_3, γ-Fe_3O_4 and CuO particles was registered on the Cu_FAZ_ME2_AA2 whereas only α-Fe_2O_3 and CuO was registered on Cu_FAZ_AES_FHA. The higher α-Fe_2O_3 content in FAZ_AES_FHA due to the high iron amount in the raw FA_{AES} and the performed fusion stage results in the formation of α-Fe_2O_3 and CuO on the Cu_FAZ_AES_FHA which can be easily reduced (100% extent of reduction). In addition this sample possesses the highest crystallinity (the highest

extent of zeolitization of FAZ_AES_FHA) which in combination with the reduction properties of Cu_FAZ_AES_FHA are prerequisite for its better catalytic performance.

Table 12 Surface characteristics and porosity of raw FA, FAZ, Cu-FAZ and a referent Na-X

Characteristic	Samples								
	FA_{ME2}	FAZ_ ME2_AA1	FAZ_ ME2_AA2	FAZ_ ME2_FAC	FAZ_ AES_FHA	FAZ_ CG_FHA	Na-X	Cu_FAZ_ ME2_AA2	Cu_FAZ_ AES_FHA_
S_{BET} (m^2/g)	10.40±0. 14	36.96 ±0.08	226.82±0 .28	116.26 ±0.65	395.69 ±0.71	246.58 ±0.27	779.85 ±4.82	70.60 ±0.02	224.41 ±0.54
S_{micro} (m^2/g)	NA	NA	165.68	25.54	270.49	118.34	718.61	8.79	148.30
V_{micro} (cm^3/g)	NA	NA	0.050	0.012	0.108	0.05	0.275	0.004	0.059
$S_{external}$ (cm^2/g)	12.35	37.71	61.25	90.72	125.21	128.34	61.23	61.81	76.11
V_{total} (cm^3/g)	0.012	0.083	0.174	0.162	0.261	0.202	0.330	0.125	0.162
V_{meso} (cm^3/g)	0.024	0.083	0.124	0.150	0.153	0.152	0.055	0.121	0.103
Average mesopore width (nm)	5.853	8.974	5.842	5.286	4.489	4.394	3.526	6.011	4.607
Average micropore width (nm)	NA	NA	1.014	1.203	1.75	1.320	1.349	1.196	1.376
Zeolite conversion extent of (%)	0.00	6.23	38.25	19.61	72.65	43.15	100.00	NA	NA

The catalytic experiments of the conversion of toluene as a model VOCs on FAZ and raw FA_{ME2} are plotted in Fig. 35. The FAZ material obtained from FA_{CG} by combination of fusion and atmospheric aging FAZ_CG_FHA (Fig. 35a) shows the best catalytic performance in total toluene oxidation. The increase of the reaction temperature has a more significant effect on the catalytic activity of FAZ_ME2_AA2 and FAZ_AES_FHA. The increase of the activity from 26.7 to 59.8% and 17.6% to 54.3% was observed for FAZ_ME2_AA2 and FAZ_AES_FHA, respectively.

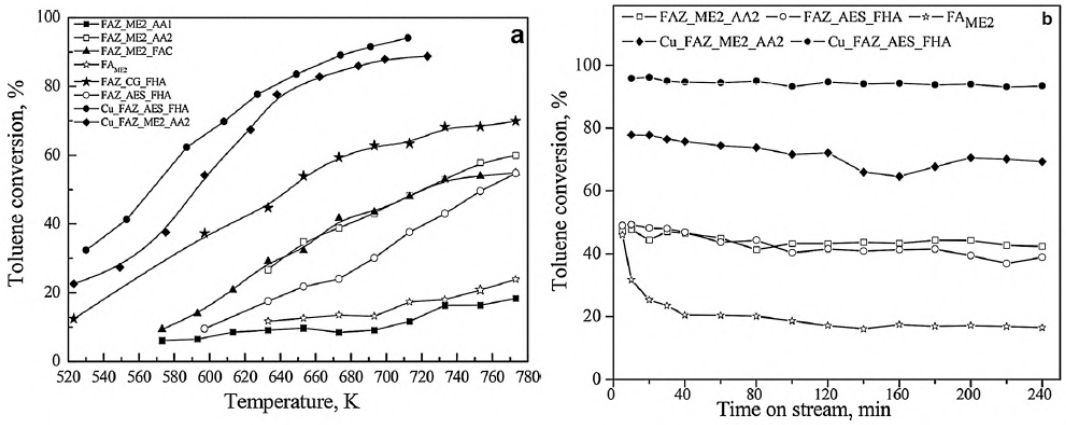

Figure 35 Toluene conversion rate on FA, FAZ and Cu-FAZ: temperature dependence (a) and time dependence at 673 K (b)

Temperature dependencies of toluene conversion for the raw FA_{ME2} and the corresponding FAZs (Fig. 35) reveal low catalytic activity for the unconverted coal ash and for the FAZ with the lowest BET surface value, which confirms the importance of surface parameters for the catalytic performance of solids. Samples FAZ_ME2_FAC and FAZ_ME2_AA2 were prepared from the same starting material by different synthesis approaches, which resulted in a different zeolitization extent and in an almost double S_{BET} value for FAZ_ME2_FAC as compared to FAZ_ME2_AA2.

The formation of different iron oxide species is registered in the FAZ materials. Most probably, the presence of finely dispersed γ-Fe_3O_4 nanoparticles leads to higher catalytic activity. Obviously, the toluene conversion over these two samples differs slightly and increases almost linearly between 633 and 733 K, reaching a value of 50% (Fig. 35). Above these temperatures, the catalytic activity of FAZ_ME2_FAC is kept constant, while that of FAZ_ME2_AA2 exceeds 60% at 773 K but also strives to a steady value. These observations indicate that above some critical value of the S_{BET} parameter, the catalytic activity of FAZs is influenced predominantly by the concentration of the active centers in their matrix. The attendance of finely dispersed γ-Fe_3O_4 species which are available in the FAZ_ME2_AA2 is responsible for its better catalytic performance (Fig. 54). The presence of γ-Fe_3O_4 particles in the FAZ_ME2_AA2 sample is also supported by the registered γ-Fe_3O_4 in the Cu_FAZ_ME2_AA2 sample.

Comparative studies of the catalytic activity for toluene degradation of FAZ obtained from FA containing different amounts of ferrous oxides confirm the observation that the specific surface values are not the dominant parameter above some critical values, as the best toluene conversion rate is established at FAZ_CG_FHA, while the S_{BET} parameter increases in the order FAZ_AES_FHA > FAZ_CG_FHA >

FAZ_ME2_FAC. The concentration of ferrous components in the starting materials grows in the order FA_{AES} > FA_{CG} > FA_{ME2}, which corresponds again to the above order of FAZ. However, the lowest catalytic activity was measured for FAZ_AES_FHA and the highest for FAZ_CG_FHA, which does not correspond to the increase in iron content in the raw materials.

The modification of zeolites with copper oxide species leads to an increase of their catalytic activity in toluene oxidation at a lower reaction temperature (Fig. 35a). Both Cu-modified FAZ possess a similar trend of extremely enhanced catalytic activity for toluene conversion with increase of the temperature, reaching maximal conversion rates of 89% at 723 K and 94% at 713 K for Cu-FAZ_ME2_AA2 and Cu-FAZ_AES_FHA, respectively. The formation of finely dispersed magnetite and copper ferrite oxide species is the most likely reason for the better catalytic performance of Cu_FAZ_ME2_AA2 and Cu_FA- Z_AES_FHA.

Similar dependencies of degradation of four VOCs molecules with different functionality were observed on the initial and Cu-modified samples. The order of catalytic activity of FAZ for the degradation of different VOCs is in good agreement with the order for toluene degradation.

The order for total oxidation of acetone, n-hexane, toluene and 1,2 dichlorobenzene is:

FAZ-CG-FHA > FAZ-AES-FHA > FAZ-ME2-AA2 > FAZ-ME2- FAC > FAZ-ME2-AA1.

Among all the studied samples Cu-modified ones show higher catalytic activity. Total oxidation of acetone and 1,2 dichlorobenze occurs at a lower reaction temperature than that of the other VOCs molecules on all the studied samples, reaching 100% conversion on Cu_FAZ_AES_FHA at 550 K.

The better catalytic performance of the Cu-modified samples can be explained by the simultaneous presence of Fe^{2+}/Fe^{3+} and Cu^{2+}/Fe^{3+} and Cu^{2+}/Cu^{+} species in the catalysts, which is very important for easier oxygen release, essential for Mars-van Krevelen mechanism, accepted for oxidation reaction of the studied VOCs. The FAZ and Cu-FAZ samples were studied in competitive catalytic oxidation of VOCs mixture containing n-hexane, acetone, toluene, 1,2- dichlorobenzene (Fig. 36).

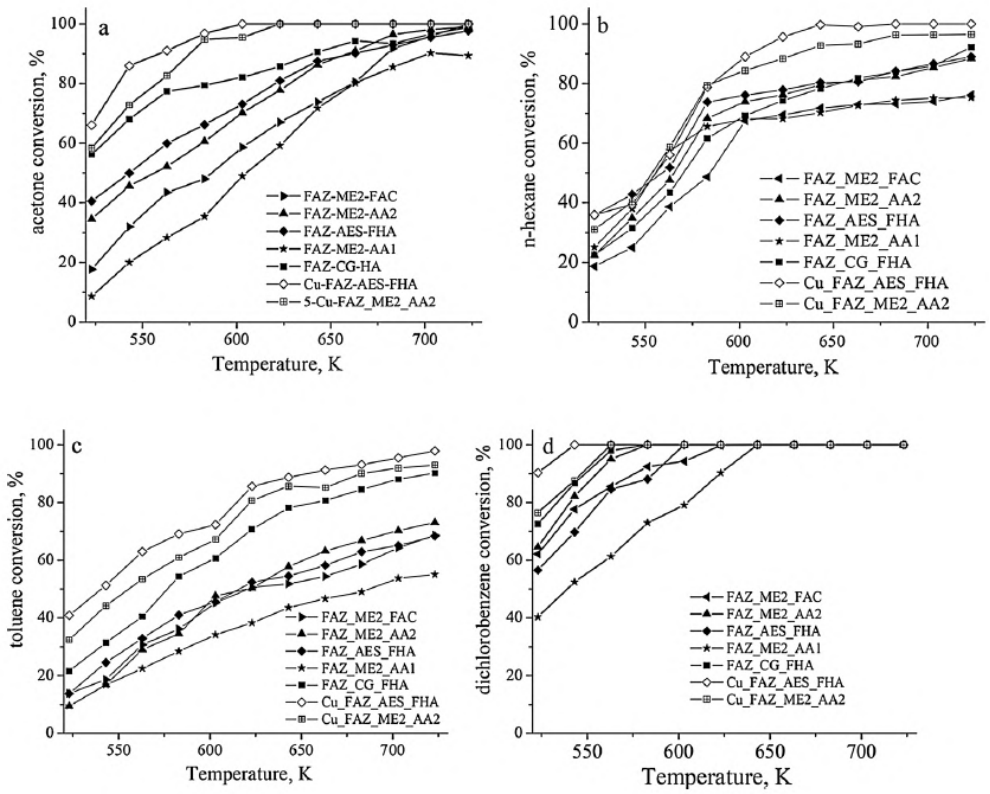

Figure 36 Competitive catalytic oxidation of VOCs mixture containing acetone, n-hexane, toluene, 1,2-dichlorobenzene versus temperature on FAZ and Cu-FAZ: a) acetone; b) n-hexane; c) toluene; d) 1,2-dichlorobenzene

Among the FAZ studied samples FAZ_CG_FHA and FAZ_ME2_AA2 showed the highest catalytic activity for all VOCs molecules. The modification by copper leads to a significant increase of catalytic activity and this effect is more pronounced for the Cu_FAZ_AES_FHA sample. The catalytic stability of Cu_FAZ_AES_FHA in total oxidation of model VOCs mixture was studied at 673 K with TOS in 3 reaction cycles. The studied sample showed negligible deactivation for all the studied volatile organic compounds.

Additionally, samples designated as H1, H2 were prepared by hydrothermal crystallization and sonicated 15 and 25 minutes, respectively; as FH was prepared by fusion-hydrothermal activation and sonicated 15 minutes;

as AS was prepared by atmospheric crystallization of FA in 1.5 mol/l NaOH.
By XRD analysis, the main crystalline component of the obtained fly ash zeolites is faujasite type, NaX. The remaining components are quartz (α-SiO_2), mullite ($Al_6Si_2O_{13}$), magnetite (Fe_3O_4), hematite (α-Fe_2O_3), calcite ($CaCO_3$), dolomite (Ca $Mg(CO_3)_2$) and anorthite type feldspar ($CaAl_2Si_2O_8$). The presence of zeolite A was also detected in sample H2, which was prepared by hydrothermal crystallization and sonication for 25 min. However, FH catalyst, prepared by double-stage fusion hydrothermal activation is composed mainly of NaX zeolite with small amount (~3 wt. %) of quartz and calcite contamination. Separate magnetite (Fe_3O_4) or hematite (α-Fe_2O_3) phases could not be found in it, and the iron content is incorporated into the zeolite lattice occupying ion-exchange positions. As could be expected, the highest extent of zeolitization (94 %) was registered for the latter preparation method, due to the complete homogenization of zeolite constituents. Despite the fact that crystalline iron oxides were not detected in FH catalyst, its iron content was similar to other FAZ samples. By impregnating the zeolite samples by cobalt, formation of Co_3O_4 with high dispersion can be observed. The particle sizes of Co_3O_4 are about 5 nm. The formation of mixed Co-Fe oxides was not observed in any of the studied samples regardless of the applied method of preparation. This result could be due to the stable iron positions on the zeolite matrix which hinder the interaction between the cobalt precursor and iron in the zeolite matrix (iron ions or finely dispersed magnetite/hematite particles). The textural data from nitrogen physisorption measurments are presented in Table 13. N_2-adsorption/desorption isotherms of the fly ash zeolites show similar shape, and can be classified as type IV, according to IUPAC classification (1985) with H3 type hysteresis loop indicating the micro-mesoporous texture of the FAZ materials. The specific surface area of the samples is in the interval between 220 and 486 m^2/g. The mesoporous diameters due to the textural mesoporosity were found in the range of 4.8 and 5.8 nm. It can be expected that the mesoporosity of FAZ facilitates the mass transport, and is beneficial for their application as adsorbent and catalyst. The highest surface area was registered for the FH sample prepared by double stage fusion-hydrothermal activation. Significant differences in the surface area were shown for H1 and H2 materials (268 m^2/g and 220 m^2/g, respectively) prepared by hydrothermal crystallization at different sonication time – 15 and 25 min.

Table 13 Surface characteristics and porosity of FAZ and Co-FAZ

Samples	S_{BET} (m^2/g)	V_{total} (m^3/g)	zeolitization extent (%)	extent of reduction (%)
H1	268	0.25	45	94.0*
H2	220	0.17	50	74.4*
AS	283	0.20	50	93.0*
FH	486	0.31	94	100.0*
CoH1	81	0.13	-	32**
CoH2	69	0.12	-	51**
CoFH	212	0.20	-	72**
CoAS	180	0.18		100**

* reduction of $Fe^{2+/3+}$ to Fe^0 and **reduction of $Co^{2+/3+}$ to Co^0.

SEM images of FH sample prepared by double-stage fusion-hydrothermal activation and characterized with the highest zeolitization extent show that it is composed of agglomerates of 1-2 μm sized octahedral crystallites typical for zeolite NaX crystalline phase.
Mössbauer spectroscopic investigations were performed in order to detect the state of iron in the prepared FAZ. Results are shown in Fig. 37.

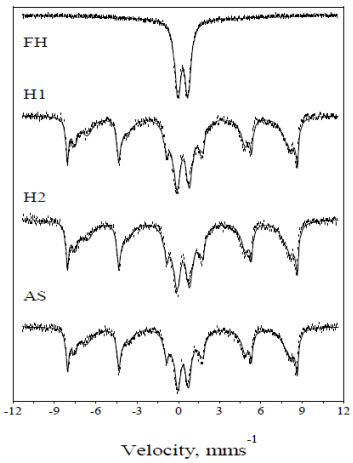

Sample	Comp.	IS* mm/s	QS** mm/s	MHF Tesla	FWHM mm/s	Rel. int. %
H1	α-Fe_2O_3	0.38	0.20	51.8	0.25	16
	γ-$(Fe)_3O_4$(A)	0.33	-	48.9	0.52	23
	γ-$(Fe,x)_3O_4$(B)	0.57	-	44.7	0.98	30
	Fe^{3+} -dubl	0.34	0.89	-	0.62	30
H2	α-Fe_2O_3	0.38	0.20	51.8	0.26	17
	γ-$(Fe)_3O_4$(A)	0.34	-	48.9	0.57	25
	γ-$(Fe,x)_3O_4$(B)	0.57	-	44.7	1.04	30
	Fe^{3+} -dubl	0.35	0.90	-	0.64	28
AS	α-Fe_2O_3	0.38	0.20	51.7	0.26	19
	γ-$(Fe)_3O_4$(A)	0.33	-	48.9	0.49	22
	γ-$(Fe,x)_3O_4$(B)	0.56	-	45.0	0.99	31
	Fe^{3+} -dubl	0.34	0.77	-	0.57	27
FH	Fe^{3+} - dubl	0.31	0.73	-	0.52	93
	Fe^{3+}- dubl	0.51	0.79	-	0.25	7

*δ, isomer shift
**Δ, quadrupole splitting

Figure 37 Mössbauer data of FAZ materials

Room temperature Mössbauer spectra of AS, H1 and H2 fly ash zeolites are practically the same. The spectra can be decomposed to three sextets and a Fe^{3+} doublet. One of these sextets corresponds to hematite (α-Fe_2O_3). The other two sextets may be attributed to the presence of magnetite, characterized by two sextets corresponding to tetrahedral (A) and octahedral (B) siting of iron. Iron is in ferric state in tetrahedral sites, whereas in octahedral sites iron dominantly exhibits Fe^{2+} oxidation state reflected in the $\delta \sim 0.57$ mm/s isomeric shift value. Since other elements may also be incorporated into the oxidic spinel structure, preferably to the octahedral sites, the corresponding line width of the (B) components is rather large (~ 1 mm/s). The appearance of the magnetic fields in the spectra recorded at room temperature indicated that the size of hematite and magnetite particles exceeds ca. 10 nm. The fourth component in these spectra, the central Fe^{3+} doublet, corresponds to small oxide particles or separate Fe^{3+} ions distributed in the zeolite host.

The Mössbauer spectrum of sample FH is distinctly different in accordance with XRD results. It can be described with a dominant doublet accompanied with another doublet of minute intensity. The dominant doublet can be attributed to well dispersed ferric iron ions in the zeolite host, the minor doublet with the 0.51 mm/s isomer shift value is probably related to the presence of Fe^{2+}/Fe^{3+} ions in very small oxidic entities.

The calculated extent of the reduction of iron oxide species is presented in Table 13. TPR curves of the samples show several overlapping peaks in the interval 573-873 K, with the exception of the FH catalyst. The first peak is the most intensive one and it can be associated with the reduction of iron oxides (magnetite (Fe_3O_4), hematite (α-Fe_2O_3)). The FH sample is characterized by two well pronounced peaks at 663 and 793 K. The first one is due to the reduction of a small amount of iron oxide species with high dispersion on the external surface of the zeolite, whereas the second one can be identified as the reduction step of Fe ions incorporated into the zeolite structure as it was shown by XRD and Mössbauer spectroscopy.

TPR-DTG profiles of the CoH1 and CoH2 materials show one intensive peak at 663-673 K and several overlapping peaks up to 873 K. The CoAS sample is characterized by two reduction peaks at 673 and 873 K. The higher temperature peak can probably be associated with the reduction of iron and cobalt species incorporated into the lattice of the zeolite matrix. The overall reduction rates of $Co^{2+/3+}$ to Co^0 (32-100 %, Table 13) are somewhat lower than those theoretically needed, which can be also explained by the formation of hardly reducible cobalt oxide species. According to our former investigations these types of species can be reduced only at much higher temperatures (over 1000 K). The extent of reduction of Co is in the range of 32 to 100 % depending on the applied synthesis procedure for FAZ preparation. The formed nanosized Co_3O_4 is reduced in two steps, first to CoO and then to Co. The highest reduction was detected for the CoAS sample prepared by atmospheric aging. Lower reduction extent was observed for CoH1 and CoH2 catalysts. Significantly lower surface area is also observed for these two samples which could be explained by the pore blocking of the zeolites by cobalt oxides resulting in low reduction extent.

The FAZ materials were studied in static and dynamic conditions for CO_2 adsorption. The results are presented in Fig. 38.

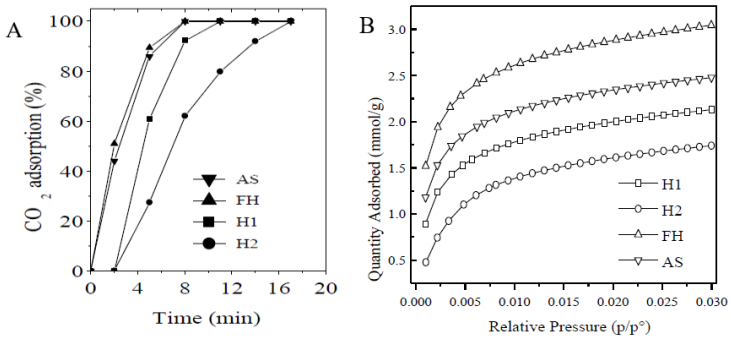

C

Samples	CO_2 ads. (static) mmol/g	CO_2 ads. (dynamic) mmol/g
H1	1.5	1.3
H2	1.7	1.5
AS	2.5	1.8
FH	3.0	2.8

Figure 38 CO_2 breakthrough curves (A), equilibrium CO_2 adsorption isotherms (B) and CO_2 adsorption data for FAZ samples (C)

H1 and H2 show similar adsorption curves and reach the adsorption equilibrium faster compared to other samples. However, the highest adsorption capacity was detected for the FH sample Fig. 38A). Good crystallinity of the latter sample associated with the highest specific surface area and bigger concentration of Na^+ ions in the NaX zeolite phase is a prerequisite for the favorable CO_2 adsorption. Additionally, iron exists predominantly in ion-exchange position in the zeolite, in the form of $Fe^{2+/3+}$ ions, generating more adsorption sites. The presence of

separate, poorly dispersed, crystalline magnetite and hematite phases in H1 and H2 samples together with the low surface area and decreased pore volume can hinder the access of CO_2 molecules to the adsorption sites.
CO_2 adsorption isotherms are presented in Fig. 38B. The determined adsorption capacities for the obtained fly ash zeolites in static conditions are in good accordance with the capacities determined in dynamic conditions (Fig. 38C). The adsorption capacity in equilibrium state is in the interval of 1.5-3.0 mmol/g, whereas in dynamic conditions its values are between 1.3-2.8 mmol/g. The highest CO_2 adsorption capacity is detected for the FH sample (3.0 mmol/g in static conditions vs. 2.8 mmol/g in dynamic conditions).
The experimental adsorption isotherms of FAZs are in good agreement (correlation coefficient values R^2>0.99) with the Langmuir model, described by the following equation:

$$\frac{V}{V_0} = \frac{bP}{bP+1}$$

where V_0, mmol/g and b, kPa^{-1} are adjustable parameters. The equilibrium adsorption capacity C_{ads} of FAZs at 100 kPa, which is a common pressure of exhausted gasses is reported in Fig. 38C.
The conversion of toluene *versus* temperature on the studied catalysts is presented in Fig. 39 A, showing well-pronounced dependence of the catalytic activity on the specific surface areas, and dispersion of metal oxides in the samples.
The best catalytic performance is observed for the FH sample obtained by fusion at 723 K, ultrasonicated for 15 min and hydrothermally activated at 363 K for 4 h. Besides, it shows the highest specific surface area, and the presence of $Fe^{2+/3+}$ ions in it facilitates the redox cycles which are important for the catalytic reaction. Moreover, the uniform and fine distribution of $Fe^{2+/3+}$ centres in the FH sample confirmed by its Mössbauer spectra stipulates its excellent catalytic performance.
Modification by cobalt further increases the catalytic activity, which is more pronounced for CoAS and CoFH in connection with their high reduction ability. Formation of Co_3O_4 nanoparticles with high dispersity is evidenced on Co/FH and Co/AS samples. XRD data for the spent catalysts did not show any change in the crystallite size of the cobalt oxide particles compared to parent ones. The highest and most stable catalytic activity is registered for Co/FH catalyst. The catalytic activity is related mainly to the simultaneous presence of Fe^{2+}/Fe^{3+} species and Co^{3+}/Co^{2+} centers, which is very important for the easier oxygen release, essential for Mars-van-Krevelen mechanism accepted in the literature for VOC oxidation reaction.

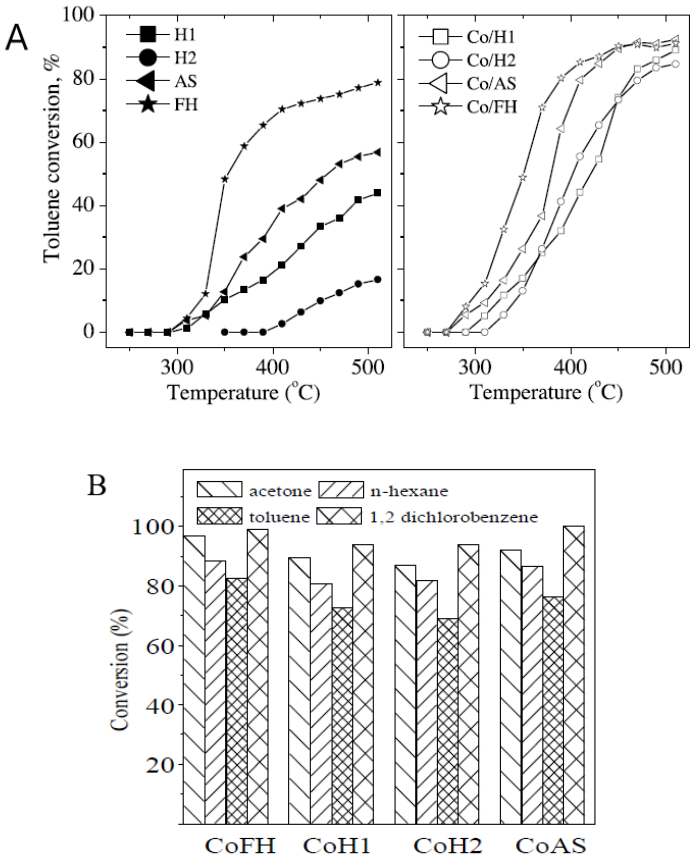

Figure 39 Toluene conversion vs. reaction temperature on the FAZ and Co-FAZ materials (A) and VOC oxidation on Co-modified samples at 663 K (B)

There are a lot of publications on the catalytic oxidation of single VOCs in dry or humid atmosphere. However, the air pollution is always a result of the emission of different types of VOCs. We performed the catalytic tests with four VOCs emitted from many processes and belonging to the most frequently observed pollutants - n-hexane, acetone, toluene, 1,2-dichlorobenzene. Competitive catalytic oxidation of VOCs mixture will reveal the real potential of the developed catalysts in the process of air cleaning. Total oxidation of a mixture containing n-hexane, acetone, toluene, 1,2-dichlorobenzene at 703 K was performed on Co-FAZ samples (Fig. 39 B). Among the studied samples, CoFH and CoAS showed the highest catalytic activity for all VOCs molecules. Compounds more resistible to oxidation are toluene and n-hexane, whereas 1,2 diclorobenzene and acetone can be oxidized easily even at much lower reaction temperature. Total conversion of all VOCs to CO_2 and water was achieved at 723 K.

The catalytic stability of the CoFH sample was studied in 3 reaction cycles and a negligible decrease in the activity was detected, which is a result of its high surface area and the presence of stable Fe^{2+}/Fe^{3+} and Co^{2+}/Co^{3+} active sites. The XRD data of the spent catalyst do not show any change in the dispersion of Co_3O_4 phase, which is a prerequisite for the stable catalytic activity.

The good adsorption and catalytic properties of the obtained fly ash zeolites make them promising materials for the development of a dual system containing two sections, the first one for total oxidation of VOCs to CO_2 and water and the second one – for the CO_2 capture, both based on initial and modified FAZ, ensuring the best environmental impact.

The catalytic activities of the developed catalysts in toluene total oxidation to CO_2 and water are compared and the data are presented in Table 14.

Table 14 Total toluene oxidation on the developed catalysts

Samples	metal content, wt. %	T_{100}^{*} (K)	T_{50}^{**} (K)
Co(N)KIL-2 (SBA-15)	4	650	600
Co/SBA-15(MCM-41) (pH=3)	5.5	625	560
FeKIL-2	1	723	635
TiMCM-41	Si/Ti=10	723	680
Ag/MCM-41 TIE	5.6	723	650
CrCu/SBA-15	3 (Cr); 7 (Cu)	650	580
CuFe/SBA-15	9 (Cu); 4.5 (Fe)	623	580
CuFeKIL-2	5 (Cu); 0.5 (Fe)	713	598
CoFeMCM-41	23CoFe	665	640
Co/TiMCM-41(20)	10 (Co); Si/Ti=20	630	610
Ti/FeMCM-41	Si/Fe=20; Si/Ti=4	680	630
Cu/FAZ	5	723	570
Co/FAZ	5	723	598

* Temperature for 100 % toluene oxidation to CO_2 (K); ** Temperature for 50 % toluene oxidation to CO_2 (K).

The developed catalysts convert toluene totally to CO_2 and water at 600-723 K and 50 % toluene conversion is reached at the interval 550-650 K at comparable reaction conditions (toluene partial pressure, spece velocity). The highest catalytic activity was found for Co/MCM-41 (pH=3), CuFe/SBA-15 and Co/TiMCM-41 (Si/Ti=20). The bicomponent catalysts (CuFe/SBA-15 and Co/TiMCM-41 (Si/Ti=20) also shows stable catalytic activity. Undoubtedly, the cheapest catalyst is 5Cu/FAZ (6Co/FAZ), which solves an additional environmental problem related to the storage of coal ash.

3.2. Drug delivery systems (DDS)

The use of mesoporous silicates is an attractive novel strategy for the development of effective drug delivery systems due to the ability to load a large amount of drug substance and to control its release and delivery to target organs through targeted design of carriers with appropriate pore topology, particle size and morphology. This type of research in Bulgaria started in 2008, and in this thesis the first publication with the participation of Bulgarian authors is presented.

3.2.1. DDS based on mesoporous silicas with different structure and surface functionality

3.2.1.1. Effect of amine functionalization of spherical MCM-41 and SBA-15 on controlled ibuprofen release

The structural characteristics (pore and particle sizes) and the surface modification of the carrier influence the loading and delivery of ibuprofen (Scheme 1) in amino-modified mesoporous spherical MCM-41 and spherical SBA-15 silica materials. The effect of amino functionalization of mesoporous MCM-41 silica with different amounts of aminopropyl triethoxysilane (APTES) on the ibuprofen storage and release was

studied. Besides, a new method for the quantitative determination of the amino groups in the modified materials was developed.

Formation of spherical MCM-41 materials with particle sizes of 100 nm (MCM-41(s)) and 1 μm (MCM-41(l)) was evidenced by TEM measurements (Fig. 40A, B). Spherical SBA-15 with particles of 5 μm (SBA-15(l)) was obtained (Fig. 40 C) and it was applied as a drug carrier for the first time. XRD data of the spherical MCM-41(s), MCM-41(l) and SBA-15(l) samples (not shown) with the intense (100) and higher Miller indices reflections in the low 2 Theta region confirm the formation of the hexagonal structure. However, some broadening and shifting of the diffraction peaks are observed for the amino-modified and ibuprofen loaded mesoporous samples, indicating the decrease in structural order.

The isotherms of the initial MCM-41(s) and MCM-41(l) modifications exhibit a sharp increase at a relative pressure of p/p_0= 0.2-0.4, which is associated with capillary condensation in the channels and narrow pore size distribution. The position of this step can be found at higher relative pressure for the SBA-15(l) sample indicating the presence of larger size pores (Table 15). The isotherms of the MCM-41(s), (l) samples are reversible and do not show any hysteresis loop whereas the isotherms of the SBA-15(l) exhibit a H2 type hysteresis loop, which is a typical feature for this type of mesoporous material. A significant decrease in BET surface area, pore volume and pore size is observed for the amino-modified MCM-41(s), (l) and SBA-15(l) materials (Table 15). This decrease is more significant for the MCM-41(l) sample. The pore structure of the latter sample seems to be more sensitive to amino-modification resulting in partial collapse of the channel system. This can either be due to the different channel systems of the two MCM-41 preparations (see TEM images) or the condensation degree of silanol groups originating from the different preparation procedures (room temperature for MCM-41(l) and 310 K for MCM-41(s) material). MCM-41(s) has straight channels crossing the entire particle and lower amount of hydrogen bonded silanol groups on the surface evidenced by the lower weight loss in TG curve over 773 K (not shown).

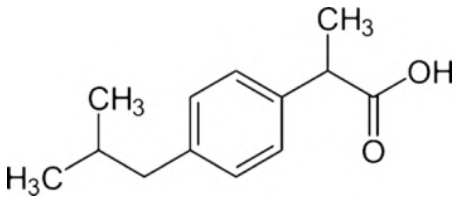

Scheme 1 Ibuprofene molecule

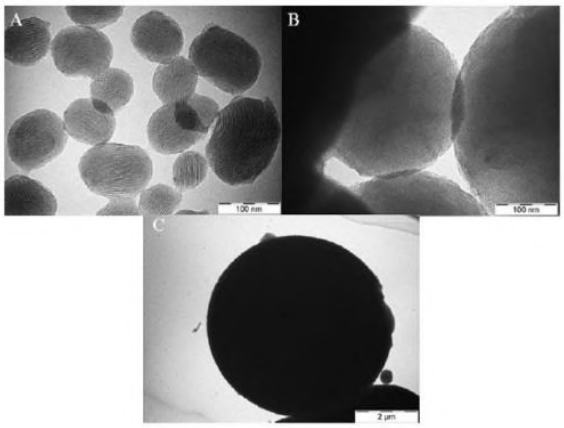

Figure 40 TEM images of (A) MCM(s), (B) MCM-41(l) and (C) SBA-15(l) materials

The particles of the spherical MCM-41(l) are built out of a core with cubic structure and a shell, which consists of channels radially orientated toward the center of the particle (Fig. 40 A) (Lebedev et al., 2001). The structure is built up of domains of parallel short channels separated by thicker walls and the lower condensation of silanol groups is a consequence of the room temperature synthesis method.

Table 15 Physicochemical properties and ibuprofen storage and release capacity of the parent and modified samples

Samples	a_o[a] (nm)	wall thickness (nm)	S_{BET} (m^2/g)	pore diameter (nm)	pore volume (cm^3/g)	adsorbed ibuprofen[b] (mg/g_{ads})	released ibuprofen[c] (mg/g_{ads})
MCM-41(s)	4.43	1.73	1175	2.7	0.987	-	-
MCM-41(s)ibu	4.37	1.87	968	2.5	0.852	151	143
MCM-41(s)NH_2	4.21	2.01	570	2.2	0.468	-	-
MCM-41(s)NH_2ibu	4.32	-	295	n.d.	0.187	368	346
MCM-41(l)	4.16	1.76	1167	2.4	0.825	-	-
MCM-41(l)ibu	4.12	2.02	1049	2.1	0.637	148	139
MCM-41(l)NH_2	4.12	-	202	n.d.	0.147	-	-
MCM-41(l)NH_2ibu	4.12	-	20	n.d.	0.037	314	299
SBA-15	10.22	4.72	878	5.5	1.116	-	-
SBA-15ibu	10.20	6.5	491	3.7	0.659	349	320
SBA-15NH_2	10.09	4.99	477	5.1	0.701	-	-
SBA-15NH_2ibu	9.99	4.59	627	5.4	0.946	177	162

[a] cell parameter ($a_o=2d_{100}(3)^{-1/2}$), [b] calculated from TG analysis, [c] calculated from UV analisis.

The amino-modified MCM-41(s) material exhibits pore filling after the interaction with ibuprofen solution (Table 15). The adsorption of ibuprofen on MCM-41(l) is related to extreme decrease of specific surface area, because of the total pore filling of the disordered pore structure.
Ibuprofen loaded parent SBA-15(l) shows significant decrease of surface area and pore diameter. Ibuprofen adsorption on amino-modified SBA-15 sample results in increased surface area and pore diameter compared to the amino-modified variety. This can be explained by the partial removal of amino-groups from the surface of channels during the ibuprofen loading procedure. Loading the sample with ibuprofen results in the total filling of micropores due to the appropriate size of drug molecule (1 nm x 0.5 nm). The modified SBA-15(l)NH_2 sample does not show any presence of micropores, probably because of the interaction of silanol groups inside the micropores with APTES during the modification. Micropores cannot be detected for the ibuprofen loaded sample, either. The calculated textural parameters for the parent, and modified with different amount of amino groups (MCM-41(1), MCM-41(2), MCM-41(3)) and ibuprofen loaded MCM-41samples are presented in Table 16. The amino modified samples are characterized with lower specific surface area and decreased pore diameter and total pore volume. The textural parameters of the ibuprofen loaded samples show a significant decrease in the surface area and pore volume. The pores are totally filled with drug molecules.
The presence of amino groups was also approved and quantitatively determined by the reaction of ninhydrin with primary amino groups to form the purple dye called Ruhemann's purple (RP). Since its discovery, extensive efforts have been made to apply the ninhydrin reactions for the detection, isolation and analysis of numerous primary amino-compounds e.g. in the field of protein sciences.

Table 16 Physicochemical properties and ibuprofen storage and release capacity of the parent and modified samples

Samples	a_o[a] (nm)	S_{BET} (m^2/g)	pore diameter (nm)	pore volume (cm^3/g)	adsorbed ibuprofen[b] (mg/g_{ads})	released ibuprofen[c] (mg/g_{ads})
MCM-41	4.43	1175	2.7	0.99	-	-
MCM-41ibu	4.37	968	2.5	0.85	151	143
MCM-41(1)	4.40	560	2.15	0.41	-	-
MCM-41(1)ibu	4.38	39	-	0.03	385	380
MCM-41(2)	4.40	544	2.15	0.42	-	-
MCM-41(2)ibu	4.39	98	-	0.09	420	394
MCM-41(3)	4.35	674	2.14	0.50	-	-
MCM-41(3)ibu	4.32	90	-	0.08	549	524

[a] cell parameter ($a_o=2d_{100}(3)^{-1/2}$), [b] calculated from TG analysis, [c] calculated from UV analysis.

To the best of our knowledge, there is no data concerning the determination of amino-groups in surface modified mesoporous silica materials by this method. The rate-determining step in the ninhydrin reaction with α-amino acids (Scheme 2) appears to involve a nucleophilic-type displacement of the OH-groups of ninhydrin hydrate by a non-protonated amino group (the latter is a consequence of the lower pH-value of the reaction medium (pH = 5.5). The reaction of amino acids with ninhydrin entails two molecules of ninhydrin for each molecule of a-amino acid to form Ruhemann's purple (RP) (Scheme 2).

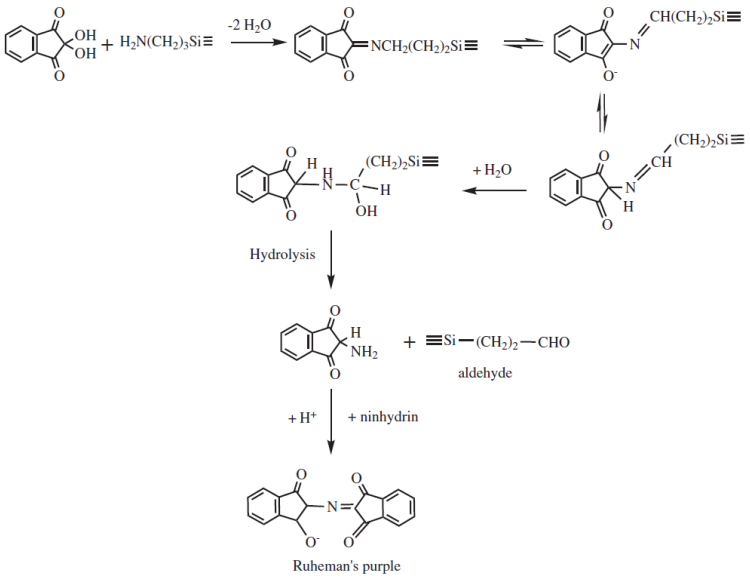

Scheme 2 Reaction mechanism of ninhydrin reaction with amino modified MCM-41 materials

Table 17 Amino and nitrogen contents of the studied materials determined by different methods

Samples	NH_2/N[a] content (wt.%)	NH_2 content[b] (wt. %)	elemental analysis (wt.%)		
			N	H	C
MCM-41(1)	1.40(1.23)	2.33(2.05)	2.1	1.1	7.3
MCM-41(2)	1.60(1.41)	2.36(2.07)	2.3	0.9	6.6
MCM-41(3)	2.65(2.33)	2.66(2.34)	2.2	1.1	8.4

[a] determined by ninhidrin reaction, [b] determioned by TG analysis.

Both polar and steric parameters are involved during the nucleophilic displacement of the OH groups of ninhydrin during the first step of reaction. The products of the reaction of a-amino groups with ninhydrin in our case are only aldehyde (RCHO) and RP in contrast to amino acids whereas CO_2 is also formed. The formed aldehyde is bound to the silica matrix ($RSi(CH2)_2CHO$). The amount of formed RP, released to the solution is proportional to the number of the accessible primary amino groups. Formation of $RSi(CH_2)_2CHO$ can be confirmed by FT-IR detection of carbonyl groups in the solid material.

The number of amino groups was calculated by the following equation, taking into account that one molecule ninhydrin interacts with one molecule glycine:

$$C_{NH_2} = \frac{A_{570} k_d M_m}{tg\alpha g}$$

where $\mathbf{C_{NH2}}$ is the concentration of amino groups (wt%); $\mathbf{A_{570}}$ is absorbance at 570 nm; $\mathbf{k_d}$ is dilution; $\mathbf{M_m}$ is molecular weight of amino group (16); **g** is amount of amino-modified MCM-41 sample and **a** is the calibration coefficient (slope of the calibration curve). Also the amino content of a commercial sample with a known amount of amino groups (3-Aminopropyl-functionalized silica gel (40-63 μm), Aldrich 364258, with ~ 1 mmol/g amino groups) was checked with the above method. The amino contents of the MCM- 41 samples are listed in Table 17.

Our data reveal that the absolute amounts are in the same range as the results of the elemental analysis and the thermogravimetric data of amino-modified MCM-41 samples (Table 17). In elemental analysis the nitrogen content does not correspond directly to the amount of amino groups (2-2.5%,) because other types of nitrogen containing groups can be formed during the surface reaction, such as protonated amino groups (see FT-IR spectra). By TG analysis the total weight loss of amino group containing materials were 8.5, 8.6, and 9.7 wt% for samples MCM-41(1), (2) and (3), respectively. Calculating by the molecular weighs, theoretically 16/58=27.5 wt% of the total weight loss is due to $-NH_2$ groups in $O_3{\equiv}Si\text{-}PrNH_2$ species. Multiplying the total weight loss of amino-modified samples with the above value, we obtain similar values for the amino content as by elemental analysis. Consequently determination of amino groups by the ninhydrin reaction seems to be a more appropriate method to measure the accessible amino content on the surface of the channels or on the outer surface of the silica particles. Assuming 3.6 mmol silanols/g in the parent silica our data from the ninhydrin reaction show that almost all the silanol groups reacted with APTES during the modification. Increasing the amount of APTES the amino group content is also increasing, but to a limited value. MCM-41(2) and (3) has the same amount of surface bound amino groups. This means that the amount of APTES applied for MCM-41(2) is enough to react with all the accessible silanol groups on the surface of channels. However, our ibuprofen loading experiments show that there are significant differences in the distribution of amino groups in these latter two samples. These observations are supported by our FT-IR investigations of adsorbed pyridine on the MCM-41(1) sample. In parent MCM-41 sample one can observe in the OH stretching region the well known intensive band characteristic for terminal silanol groups at 3744 cm^{-1} and the broad band between 3500 and 3600 cm^{-1} for hydrogen bond silanols. Silanol groups react also with adsorbed pyridine with weak hydrogen bond giving a band pair at 1446 and 1598 cm^{-1}. In the spectrum of amino modified sample the amount of terminal and hydrogen bound silanol groups significantly decreased and adsorbed pyridine cannot access the silanol groups on the surface since the typical band pair at 1446 and 1598 cm^{-1} do not appear in the spectrum. Evacuating the sample even at 523 K the characteristic bands of propyl and amino groups appear in the spectrum evidencing the successful amino modification and the stability of covalently bound propyl amino groups on the surface.

The absence of crystalline ibuprofen reflections in the XRD patterns of the loaded mesoporous MCM-41(1), (2) samples demonstrated that washing had removed all the surface loaded ibuprofen. However, in MCM-41(3) sample crystalline ibuprofen could be detected, probably located in secondary mesopores formed by agglomerated small silica particles. The ibuprofen loaded into the mesopores of the MCM-41(1), (2), (3) samples was quantified using TG. The thermogravimetric analysis determines the actual amount of drug in the supports after correcting the curves by water and aminopropyl content. The parent spherical MCM-41 sample shows lower adsorption capacity for ibuprofen than their amino-modified analogs. The highest overall capacity for ibuprofen loading was measured for MCM-41(3) (54.9%). However, about 22% of ibuprofen was evaporated up to 470 K, indicating that a significant part of ibuprofen is physically adsorbed outside the channels, probably in the secondary mesopores.

The amount of loaded ibuprofen in the channels, decomposing above 500 K is relatively lower (33%) than in the other samples.

The mesoporous samples were characterized also by FT-IR (Fig. 41), verifying the presence of functional groups after amino- modification and drug adsorption.

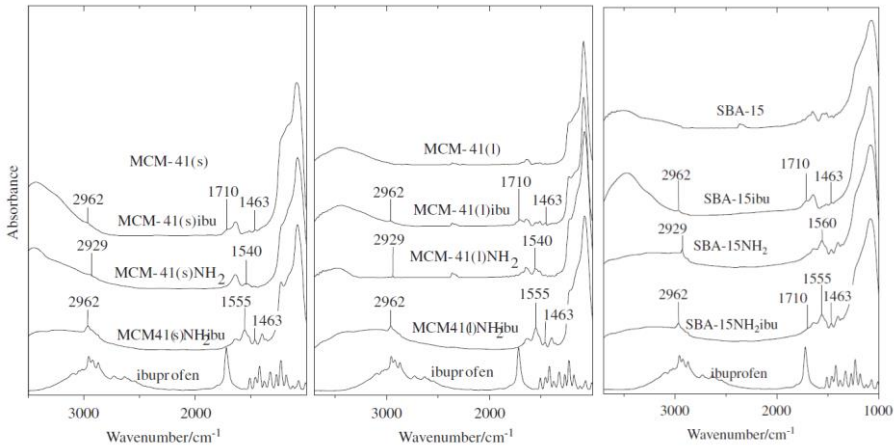

Figure 41 FT-IR spectra of the parent, the amino-modified and ibuprofen loaded MCM-41(s) and SBA-15

The asymmetric stretching vibrations (Si-O-Si) appear at about 1090 cm^{-1} for MCM-41 and at 1075 cm^{-1} for SBA-15. The modification by APTES of MCM-41(s), (l) and SBA-15(l) samples results in the appearance of the bands at 2929 and at 1540 cm^{-1}, which are attributed to C-H and N-H stretching vibrations of aminopropyl anchored on the surface of mesoporous support. The FT-IR spectra of ibuprofen-loaded parent samples (Fig. 41) show the bands at 2962 and 1463 cm^{-1} characteristic for C-H and phenyl bands, respectively. The band at 1710 cm^{-1} registered on ibuprofen loaded parent mesoporous silicas is due to the COOH group of the ibuprofen molecule whereas the presence of the band at 1555 cm^{-1} in the spectra of the amino modified ibuprofen loaded mesoporous silicas (Fig. 83) is indicative for the formation of a COO^{-}-NH_3^{+} bond. Bands at 1463 and 2962 cm^{-1}, typical for C-H and phenyl groups are also registered in the spectra of ibuprofen loaded amino-modified samples.

The absence of crystalline ibuprofen reflections in the XRD patterns of the loaded mesoporous MCM-41(s), (l) and SBA-15(l) samples demonstrated that washing had removed all the surface loaded ibuprofen. The ibuprofen loaded in the mesopores of MCM-41(s), (l), SBA-15(l) samples, and their amino-modified analogs was quantified using TG. The thermogravimetric analysis determines the actual amount of drug in the supports (Table 15), correcting the curves by water and aminopropyl content. The parent spherical MCM-41(s) and MCM-41(l) show lower adsorption capacity for ibuprofen in comparison to their amino-modified analogues. The highest capacity for ibuprofen loading was measured for MCM-41(s)NH_2 (36.8%) and for SBA-15(l) samples (34.9%) (Table 15). It also found (Manzano et al., 2008) an increased adsorption capacity for amino-modified MCM-41 up to 330 mg/g for the mesoporous support with particle size of 615 nm. The amino-modified spherical SBA-15(l) possesses lower capacity for ibuprofen (17.7%). One possible explanation is that amino groups are removed partially from the surface during the ibuprofen loading as it was suggested on the basis of N_2 physisorption data and elemental analysis. The number of possible adsorption sites in mesopores is reduced. On the other hand the low capacity can be related to the distribution of adsorption sites, e.g., the location of silanol groups in the mesoporous support. The micropore fraction in total pore volume of SBA-15 depends on the ratio of the pore wall thickness to the pore diameter and can reach up to 40%, therefore a part of silanols are located in these micropores. As it was shown by nitrogen physisorption, the modification of SBA-15(l) by APTES leads to the blocking of micropores, more probably because of their filling with amino groups. Therefore they are inaccessible for the ibuprofen adsorption. Elemental analysis was applied for the determination of the changes in the C, H and N content of the amino modified and the ibuprofen loaded initial and the amino modified samples (Table 17). The data show more significant increase in the carbon content after ibuprofen loading on the modified ones, which is related to the higher ibuprofen loading. This effect is the opposite for SBA-15(l) which is in good accordance with the TG data.

The results of the ibuprofen release from the parent mesoporous silicas and their amino-modifications are plotted in Fig. 84. The concentration of ibuprofen released in SBF at pH = 7.4 as a function of time was determined by UV-vis spectroscopy by monitoring the changes in absorbance at wavelength of 264 nm at suitable intervals of time. The ibuprofen release equilibrium rates of MCM-41(s), (l) samples are much faster (1 h) than that of the amino-modified MCM-41(s), (l) silicas (Fig. 42 A).

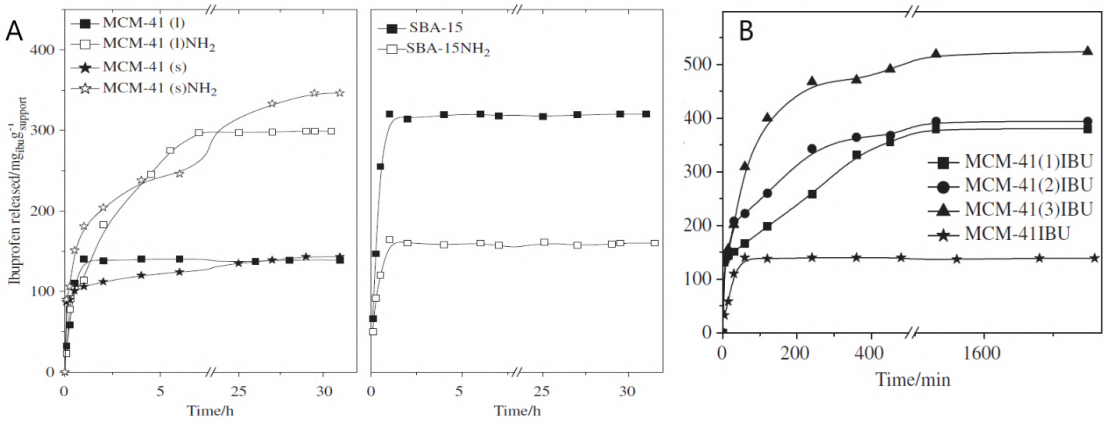

Figure 42 Ibuprofen delivery from the parent and amino-modified spherical MCM-41(s), (l) and spherical SBA-15(l) (A) and from modified with different amounts of amino groups spherical MCM-41 (B)

Hydrogen bonding between ibuprofen and the parent mesoporous silica materials is relatively weak, so the mass transfer of ibuprofen molecules through the channels is controlled by diffusion. However, the formed COO^--NH_3^+ bond between ibuprofen and the functional groups of the amino-modified MCM-41 samples is stronger than that between ibuprofen and silanol groups of the parent silicas. This effect can explain the slower release rates of ibuprofen from both amino-modified MCM-41 samples in comparison to the silica varieties (Fig. 42 A). Moreover, MCM-41(s) shows slower release in comparison to MCM-41(l). Our XRD and N_2 physisorption data show that even the ibuprofen loading procedure made the pore structure of MCM- 41(l) less ordered, which can explain the faster release rate of ibuprofen. The differences between release rates are more pronounced for amino-modified MCM-41 samples. It seems that the partially collapsed pore structure of amino-modified MCM- 41(l) influences the release rate more than the loaded amount of ibuprofen (Table 15). Another possible explanation of lower release rate could be the narrower pore size of the mesoporous carriers after modification (see Table 15).

Parent SBA-15(l) shows higher adsorption capacity of ibuprofen than MCM-41 samples, probably due to the higher pore volume (Table 15). The release rate is fast and similar to MCM-41(l). This high adsorption capacity for SBA-15(l) is unique in literature and probably can be associated with the morphology and special channel system of it, e.g., thin walls (Table 15) with short micropore channels which are easy accessible by ibuprofen or organic molecules. In contrast to MCM-41 samples, the amino-modified SBA-15(l) adsorbed lower amount of ibuprofen and the release rate is as fast as it is in the parent one (Fig. 84A). As nitrogen physisorption data show, modification of SBA-15(l) with APTES results in blocking the micropores where a part of silanol groups is located. Therefore, amino groups in the micropores are inaccessible for ibuprofen and as a result the adsorption capacity of amino modified SBA-15(l)NH_2 is lower. Another aspect is that the mesopore size of SBA-15(l) is larger (about 6 nm) than that of MCM-41 samples, and consequently the modification with amino groups of SBA-15(l) cannot significantly hinder the ibuprofen release by diffusion.

The results of ibuprofen release from the parent mesoporous silica and the modified with different amounts of amino groups varieties are plotted in Fig. 84B. The highest adsorption capacity could be achieved by the MCM-41(3) sample (549 mg/g_{ads}). MCM-41(1) and (2) showed somewhat lower and similar adsorption capacity (385 and 420 mg/g_{ads}). However the high adsorption capacity of MCM-41(3) can be due to the adsorption of ibuprofen on the outer surface or in the secondary mesopores, as formerly evidenced by XRD and TG measurements. The primary amino content of the samples determined by the ninhydrin method can be correlated with their ibuprofen adsorption capacity. The higher the amino content the higher the adsorption capacity is.

All the amino-modified samples show slower release of ibuprofen than the parent silica. The ibuprofen release equilibrium rate of MCM-41(3) sample is faster than that of the amino-modified MCM-41(1), (2) silicas (Fig. 42 B). In accordance with TG and XRD results 50% ibuprofen release was attained in 40 min, whereas in samples (1) and (2) in 120 and 60 min, respectively. The total release of loaded ibuprofen was achieved only for MCM-41(1) in 24 h. About 5-7% of ibuprofen was retained on MCM-41(2) and (3) samples even after 36 h. This can be explained by the strong interaction of the carboxylic groups of ibuprofen molecule with the primary amines on the silica surface. From practical point of view MCM-41(1) has the most advantageous properties, because of its high adsorption capacity, slow and total release of adsorbed ibuprofen.

It was found that the synthesis procedures of mesoporous MCM-41 materials determine their stability in the surface modification procedure. However, the stability differences did not influence the adsorbed amount of ibuprofen but have significant effect on the release rate. Parent MCM-41 with particle size of 100 nm showed a slower release rate. Modification by amino groups had a positive effect on the adsorption capacity of ibuprofen in the case of MCM-41 materials. Amino modified MCM-41 with particle size of 100 nm showed the highest adsorption capacity and slower release rate for ibuprofen in comparison to amino-

modified MCM-41 with larger particles. For the first time, spherical SBA-15 was investigated as a drug carrier. Its adsorption capacity for ibuprofen with 349 mg/g is very close to the highest value of 368 mg/g obtained by amino-modified MCM-41 with 100 nm particle size. The application of a much higher amount of APTES than the stoichiometrically needed results in the development of disadvantageous properties, such as functionalization of outer surface of the silica particles and their detrimental agglomeration. Amino modified MCM-41 with the highest amount of applied APTES showed the highest adsorption capacity but faster release rate for ibuprofen due to the ibuprofen adsorption in the secondary mesopores among the small silica particles. Optimal release properties were achieved when the applied amount of APTES corresponded to the number of surface silanol groups. Ibuprofen loading and release kinetic can be controlled by the proper surface functionalization of mesoporous silicas. We have applied the ninhydrin reaction for the quantitative determination of primary amines in heterogeneous phase and have found good correlation between the amino content of the modified MCM-41 materials and their ibuprofen adsorption capacity.

3.2.1.2. Carboxylic modified spherical mesoporous silicas as drug delivery carriers

We developed a novel route for COOH functionalization of MCM-41 and SBA-15 materials by means of the ring opening reaction with succinic anhydride in toluene. Sulfadiazine was chosen as probe molecule (Scheme 3) because of the available free amine functional group, still taking into account an eventual binding with COOH functional groups of the modified materials. Besides, the drug size was calculated (1.0 nm x 0.5nm) and considered as appropriate for encapsulation in the pores of our novel carboxylic functionalized MCM-41 and SBA-15 mesoporous carriers.

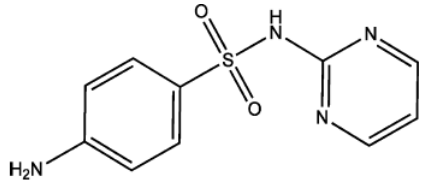

Scheme 3 Sulfadiaine molecule

The present study develops a new method for post-synthetic carboxylic functionalization of spherical MCM-41 and SBA-15 silicas. Thus, the initial step was the modification with 3-amino- propyltriethoxysilane, and the next was the reaction with succinic anhydride in toluene in order to obtain carboxylic modified mesoporous carriers (Scheme 4).

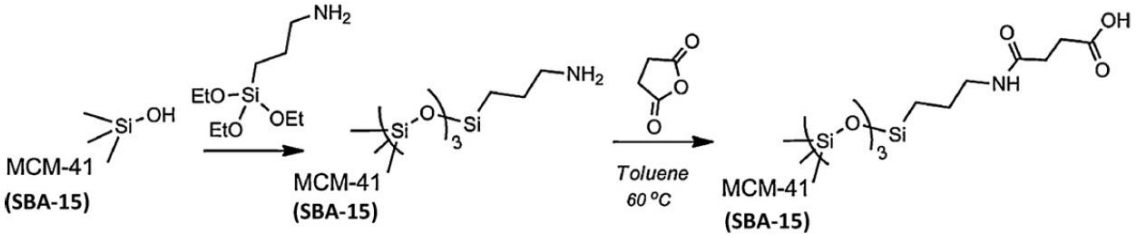

Scheme 4 Process of preparation of the carboxylic functionalized mesoporous silica nanoparticles

XRD patterns of the carboxylic modified MCM-41 and SBA-15 samples at low 2 theta degree region show the preservation of the hexagonal structure (not shown). Compared to the parent materials some broadening, intensity decrease, and structure deterioration can be observed, especially for the modified MCM-41 samples. XRD patterns (not shown) at higher angles show the presence of small amount of separate sulfadiazine phase. These observations were supported also by the N_2 adsorption data (Table 18).

Table 18 Physicochemical properties ofthe parent, amino and the carboxylic modified spherical MCM-41 and SBA-15

Samples	a_o [a] (nm)	S_{BET} (m^2/g)	pore diameter (nm)	zeta-potential (mV)
MCM-41	4.4	1175	2.7	- 12.4 ± 0.4
MCM-41NH_2	4.2	570	2.2	-
MCM-41COOH	3.7	412	1.9	-22.7 ± 0.5
SBA-15	10.2	878	5.5	- 24.9 ± 0.8
SBA-15NH_2	10.1	477	5.1	-
SBA-15COOH	8.2	300	5.1	- 29.1 ± 2.1

[a] cell parameter ($a_o=2d_{100}(3)^{-1/2}$).

The modification by amino and carboxylic groups did not influence the spherical morphology of MCM-41 and SBA-15 materials as evidenced by TEM investigations (Fig. 43).

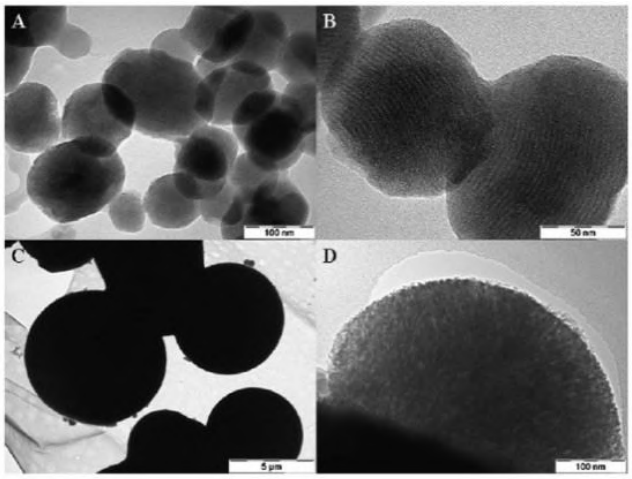

Figure 43 TEM images of carboxylic modified spherical MCM-41 (A and B) and SBA-15 (C and D) samples

The two-step modification procedure resulted in a significant specific surface area decrease for both types of materials. Also, narrower pore sizes were detected. This effect was more pronounced for MCM-41COOH because of the smaller pore size of the parent material. Formation of carboxylic groups was evidenced by ATR FT-IR measurements. Fig. 44 shows the FT-IR spectra of the parent, the amino and the carboxylic modified silica materials. The parent silica materials show only a band at around 1630 cm^{-1} characteristic for adsorbed water in the channels. The modification of MCM-41 and SBA-15 by APTES resulted in the appearance of bands at 1597, 1547 and 1634 cm^{-1}. The first one can be associated with primary amino groups, whereas the two others – with the protonated form of amino groups. The appearance of these bands is the evidence of successful modification of silica materials by amino groups. The symmetric and asymmetric stretching vibration bands characteristic for carboxylate ($-COO^-$) groups can be found at 1555 and 1411 cm^{-1} in both samples, respectively. The band at 1626 cm^{-1} is registered only in the spectrum of MCM-41COOH and it can be associated with the presence of amid groups (-NH-C=O) strongly hydrogen bonded in the network. In the spectrum of the MCM-41COOH sample two additional bands appear. The band at 1697 cm^{-1} can be attributed to the strongly hydrogen bonded -COOH groups. This is an indication of the fact that the number of carboxylic groups is higher, they can be found in close vicinity and can interact with each other or with the neighboring silanol groups. The shoulder at 1717 cm^{-1} is characteristic of non dissociated, "free" carbonyl groups. The weak band at 1770 cm^{-1} can be associated with the unreacted succinic anhydride in the sample. The - CH_2 deformation vibration of hydrocarbon chains can also be detected at the 1350-1450 cm^{-1} region.

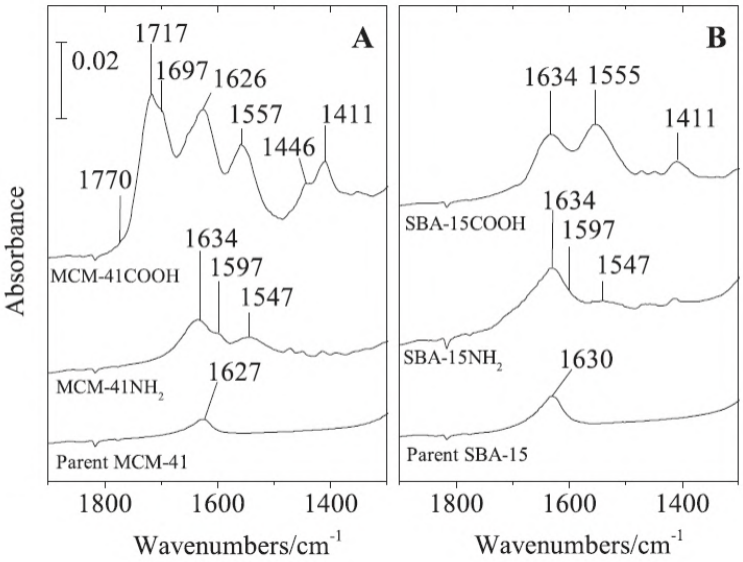

Figure 44 ATR FT-IR spectra of the parent, amino and carboxylic modified MCM-41 and SBA-15 materials

The amount of grafted organic groups was determined by TG analysis. Our results show that the amount of COOH groups corresponds to the total amount of amino groups formed during the modification by APTES. Taking into account the weight loss on TG curve (not shown) between 473 and 773 K we found that the amount of amino groups was 2.3 wt.% and 3.1 wt.% in MCM-41 and in SBA-15, respectively. Considering the theoretical increase of molecular weight due to carboxylic modification the corresponding values were 2.3 and 3.0 wt.%.

The zeta-potential measurements of both types of non-modified and carboxylic modified materials demonstrate negative values (Table 19). As shown, the zeta potential is more negative for the carboxylic modified silicas than the values for the parent ones. This observation can be also considered as an indication for the efficient carboxylic functionalization of the silica carriers. Particle size determination results of sulfadiazine loaded samples showed that the MCM-41 materials are less agglomerated upon carboxylic modification and drug loading procedure than the SBA-15 ones (Table 19). Moreover, the polydispersity index did not increase significantly upon modification of the MCM-41 material, the narrow particle size distribution observed on the parent MCM-41 material was preserved. The average particle size of SBA-15 materials significantly increased after modification, indicating a higher tendency for agglomeration. Polydispersity measurements showed that both SBA-15 materials included size fractions from 0.9 to 5 μm. The polydispersity index for parent SBA-15 is about two times higher than that of for MCM-41 and the modification resulted only in a slight decrease of it.

Table 19 Physico-chemical properties of the sulfadiazine loaded parent and carboxylic modified MCM-41 and SBA-15

Samples	size (nm)	polydispersity index	zeta-potential (mV)	drug loading[a] (%)
MCM-41-SD	480.5	0.43	- 10.4 ± 2.0	39.05
MCM-41COOH-SD	603.9	0.55	+ 3.5 ± 0.1	49.78
SBA-15-SD	938.7	0.97	- 20.3 ± 2.5	53.60
SBA-15COOH-SD	1740.3	0.95	+ 1.8 ± 0.7	52.40

[a] calculated from TG analysis.

Successful modification was also evidenced by our drug adsorption experiments (Table 19). The amount of adsorbed sulfadiazine was measured by TG analysis corrected by the amount of adsorbed water and carboxylic groups. It was found that non-modified MCM-41 can adsorb 39.05 wt.% of sulfadiazine (Table 19). Modification of MCM-41 with carboxylic groups resulted in higher amount of adsorbed sulfadiazine (49.78 wt. %). In contrast, modification by carboxylic groups did not have a positive effect on the adsorption capacity of sulfadiazine in the case of SBA-15 material. The initial and the carboxylic modified SBA-15 possess similar adsorption capacity for sulfadiazine (53.63 wt.% for SBA-15 and 52.40 wt.% for SBA-15COOH). Analyzing the N_2 adsorption isotherms by the as plot method, the microporous volume of the parent SBA-15 sample was 0.05 cm^3/g and practically no micropores were detected for functionalized SBA-15COOH. Hence, the expected higher loading capacity of the functionalized SBA-15COOH was not registered because of the total blocking of the micropores. The close adsorption capacity of both samples (SBA-15 and SBA-15COOH) is due to the presence of micropores in the case of non-functionalized SBA-15 and the stronger adsorption sites in the case of the functionalized SBA-15COOH.
The adsorption capacity of SBA-15COOH for sulfadiazine is higher (52.4 wt.%) compared to MCM-41COOH (49.78 wt.%) (Table 19), but not as much as could be expected owing to the bigger pore size of the SBA-15 carrier. The reason for the high adsorption in the case of MCM-41COOH is the electrostatic binding between sulfadiazine and COOH groups on the outer surface of the MCM-41COOH sample and additional binding in the secondary mesopores between the silica particles. The textural mesoporosity is formed only for MCM-41 silica.
The presence of electrostatically bonded sulfadiazine was also evidenced by the formation of $COO\text{-}NH_3^+$ groups in the ATR FT-IR spectra of sulfadiazine loaded samples at 1545 cm^{-1} (Fig. 45). Non-modified, sulfadiazine loaded MCM-41 silica shows a spectrum, similar to that of free sulfadiazine.

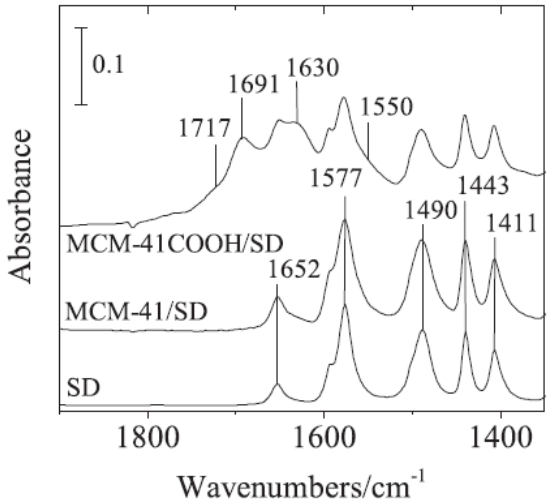

Figure 45 ATR FT-IR spectra of the sulfadiazine loaded MCM-41 and MCM-41COOH samples

Typical bands of sulfadiazine at 1652 (δ_{NH2}), 1577 (υ_{CC} of aromatic ring), 1490 (δ_{CCH} of aromatic ring), and at 1443 and 1411cm^{-1} (δ_{CCH} and δ_{HCN} of pyrimidine ring, respectively) appear, indicating that sulfadiazine can be

found physically adsorbed in the channels or on the outer surface of the MCM-41 material. Bands characteristic for sulfadiazine and surface carboxylic modification appeared also in the spectrum of MCM-41COOH/SD sample. The presence of electrostatically bonded sulfadiazine was evidenced by the formation of $COO\text{-}NH_3^+$ groups at 1550 cm^{-1}. Parallel, the intensive stretching vibration attributed to carbonyl in non dissociated carboxylic groups of MCM-41COOH at 1717 cm^{-1} is almost disappeared upon SD adsorption. The intensity of 1577, 1490 cm^{-1} bands, assigned to aromatic ring vibrations, are also decreased compared to that of free SD, indicating a weak interaction of aromatic ring of SD drug with the narrow channels of MCM-41.
The electrostatic binding of sulfadiazine with carboxylic groups of modified carriers was also proven by zeta-potential measurements. Significant increase of zeta-potential was observed for both types of drug-loaded modified materials, +3.5 and +1.8 mV for MCM-41COOH and SBA-15COOH, respectively (Table 19).
The results of the sulfadiazine release from the parent mesoporous silicas and their carboxylic-modifications are plotted in Fig. 46. As shown, sulfadiazine was rapidly released from non-modified silica carriers (MCM-41 and SBA-15). In particular, in 4 h approximately the whole amount of sulfadiazine was released. This fact could be explained by taking into account that the hydrogen bonding between sulfadiazine and the parent mesoporous silica materials is relatively weak. In contrast, slower release rate was observed from carboxylic-modified samples (MCM-41-COOH and SBA-15-COOH).

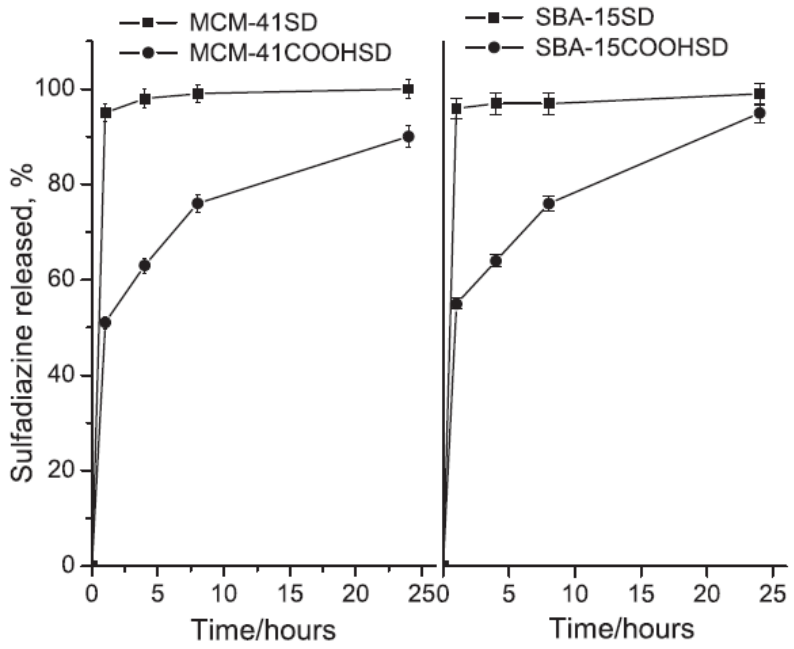

Figure 46 *In vitro* release of sulfadiazine from the parent and the carboxylic modified spherical MCM-41 (A) and spherical SBA-15 (B) in distilled water (mean ± SD, n = 3)

The formed $COO^-\text{-}NH_3^+$ bond between sulfadiazine and the carboxylic groups of the modified mesoporous samples is stronger than that between sulfadiazine and silanol groups of the parent silicas. This effect can explain the slower release rates of sulfadiazine from both carboxylic-modified MCM-41 and SBA-15 samples in comparison to the initial materials. Thus, the drug release process was governed mainly by the functionality of the carrier rather than the pore size.
The cytotoxic activity of the non-modified and the COOH-functionalized carriers was evaluated in Caco-2 cell line after 72 h continuous exposure using the MTT dye-reduction assay. Free sulfadiazine shows low cytotoxicity and the applied mesoporous carriers do not increase the cytotoxic effect of the loaded samples.

We have demonstrated a novel route to synthesizing MCM-41 and SBA-15 mesoporous silica materials functionalized with carboxylic groups. The reaction of ring opening of amino-modified mesoporous silicas with succinic anhydride in toluene was developed. The method allowed the application of mild conditions combined with less toxic reagents. Surface modification with carboxylic groups resulted in a higher degree of sulfadiazine loading for the carboxylic modified MCM-41COOH (~50 wt.% versus 39% for MCM-41), whereas no difference was observed for SBA-15 and SBA-15COOH. In vitro release studies showed that the functionalization of mesoporous appropriate carriers for prolonged release of sulfadiazine. The new method for carboxylic modification of the mesoporous carriers did not increase the cytotoxicity on the Caco-2 cell line, suggesting that the obtained modified carriers were biocompatible.

3.2.1.3. Preparation of resveratrol-loaded nanoporous silica materials with different structures

Bioflavonoids are natural polyphenolic compounds that are potential candidates for drugs due to a number of proven pharmacological effects, such as: antioxidant, anti-inflammatory, anti-tumor and others. Resveratrol (R) is bioflavonoid and a potential natural antioxidant with strong anti-inflammatory and antiproliferative properties, which can be found in grapes, nuts, fruits and red wine (Scheme 5). It is extremely photosensitive compound with low chemical stability, which limits its beneficial therapeutic effects. Thus, loading of resveratrol in nanoporous silica systems can stabilize and protect it from degradation. Solid nanoporous silica-based materials differing in morphology, topology and pore size distribution, such as mesoporous pure silica (spherical MCM-41 and KIL-2) and nanosized silica-alumina zeolite BEA, have been used as carriers of natural resveratrol (Scheme 5). Vibrational ball mill mixer was applied for simultaneous amorphization and loading of the poorly water-soluble drug resveratrol as an alternative to the conventional method of encapsulation in solution. This solid-state procedure for encapsulation has two important advantages. Dry mixing ensures partial amorphization of resveratrol crystallites, expected to increase its water solubility. The other advantage is that the entire amount of added drug substance remains on the carrier without any loss at preparation.

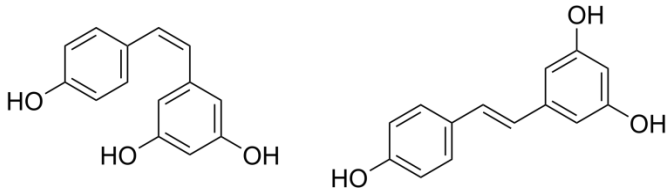

Scheme 5 Cis- and trans-resveratrol

The parent silica nanomaterials as well as their resveratrol-loaded formulations were characterized before and after resveratrol deposition using several techniques.

The low-angle powder XRD patterns of KIL-2 and MCM-41 indicate that KIL-2 has a disordered mesoporous structure, whereas MCM-41 shows an ordered 2D hexagonal (p6mm) pore arrangement (Fig. 47).

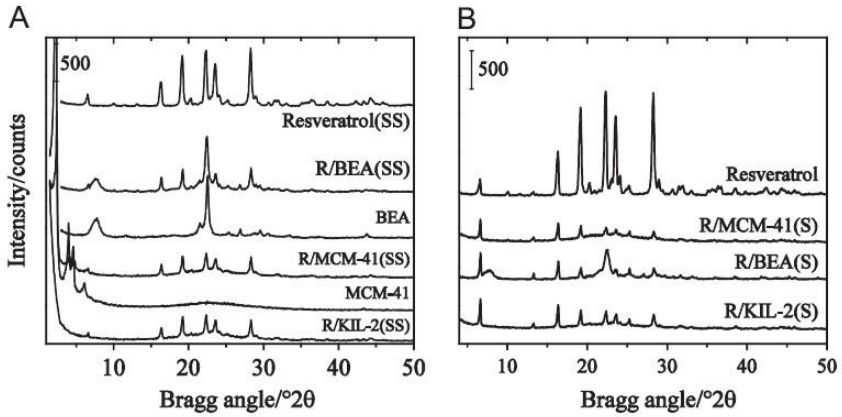

Figure 47 XRD patterns of resveratrol, zeolite BEA and resveratrol loaded systems prepared by solid-state method (A) and in solution (B)

The pattern of calcined nanobeta material in its H-form (Fig. 89) shows the typical diffraction peaks of BEA-type topology with the most intensive reflections at °2Θ = 7.6 and 22.4. In Fig. 47 A the XRD pattern of grinded resveratrol is compared to that of commercial form of the drug. The observed intensity decrease proves that treatment in the vibrational mixer leads to substantial amorphization of the antioxidant, being one of the objectives of solid-state preparation method. The intensity of the reflections of the grinded non-loaded resveratrol is 58% of the pure one. Presence of crystalline resveratrol phase is registered on all loaded samples regardless of the method of drug loading which is an evidence that resveratrol is not only introduced in the pore channels, but can be found on the outer surface of the small nanoparticles or in the voids among the particles. According to SEM analysis (not shown), the size of the Beta zeolite crystallites is about 40-50 nm. Images show that the particles stick together to 100-150 nm agglomerates and mesopores are formed among them. Resveratrol loading resulted in higher intensity decreases than the expected 50% (32% for R/MCM-41(SS), 40% for R/BEA(SS) and 37% for R/KIL-2(SS)). Comparing these data with the loaded amount determined by TG analysis we can conclude that a significant part of resveratrol is in amorphous form, not detectable by XRD.

The calculated textural parameters from nitrogen adsorption and desorption isotherms of the parent and resveratrol loaded MCM-41 and KIL-2 samples are summarized in Table 20A, and for the BEA sampls in Table 20B.

Table 20A Textural and physico-chemical properties of the KIL-2 and MCM-41 silicas and their resveratrol-loaded formulations

Samples	S_{BET} (m^2/g)	pore diameter (nm)	pore volume (cm^3/g)	loaded resveratrol[a] (wt.%)
MCM-41	1175	2.7	0.97	-
RES/MCM-41(S)	320	2.5	0.26	39.8
RES/MCM-41(SS)	306	2.5	0.27	46.6
KIL-2	664	15.2	1.28	-
RES/KIL-2(S)	320	9.8	0.72	35.8
RES/KIL-2(SS)	232	10	0.52	48.3

[a] determined by TG analysis.

Table 20B Textural and physico-chemical properties of the resveratrol-loaded formulations

Samples	S_{BET} (m^2/g)	pore volume (nm)	mesopore volume (cm^3/g)	micropore volume (cm^3/g)	loaded resveratrol[a] (wt.%)
BEA	761	0.46	0.34	0.12	-
R/BEA(S)	34	-	n.d.	-	48.4
R/BEA(SS)	18	0.04	n.d.	-	49.2

[a] determined by TG analysis.

The textural parameters after resveratrol deposition alter significantly. The observed decrease in the surface area and pore volume is indicative for partial pore filling in the case of MCM-41 and KIL-2 after the solid- state loading of the drug (Table 20A). The change of I type isotherm for BEA zeolite support is an indication for micropore filling or rather plugging. The microporosity of this material with much narrower channel system actually disappears and the total pore volume is strongly reduced (Table 20B). For both mesoporous supports loaded with R in ethanol solution, also partial pore filling is observed.

ATR FT-IR method was used to investigate the interaction between the resveratrol molecule and the nanoporous carriers after its deposition (Fig. 48). The FT-IR spectrum of R shows three characteristic strong bands at 1606, 1585 and 1384 cm^{-1}, belonging to double bond C-C stretchings of aromatic and olefinic groups, and of ring C-C stretching, respectively. The bands at 1511, 1443 and 1324 cm^{-1} can be assigned to in plane and out of plane C-H bending, respectively. After encapsulation into the silica/zeolite framework, a slight blueshift of the resveratrol IR bands corresponding to the vinylidene group and a decrease in intensity of the vinylidene C-H in plane bend (1324 cm^{-1}) can be observed. These spectral features due to perturbation at vinylidene dipole moments suggest an interaction of resveratrol C=C with the silica/zeolite framework. The most pronounced changes, witnessed in the case of BEA zeolite (solid-state preparation; shift of 1384 to 1391 cm^{-1} of C-C ring stretching) indicate a nanoconfinement of resveratrol in the micropores/mesopores of BEA. For all cases, the out-of-plane C-H bending of RCH=CHR (965 cm^{-1}, not shown), diagnostic for trans-configuration around the di-substituted double bond, remains unchanged, indicating that the trans-configuration is preserved during encapsulation.

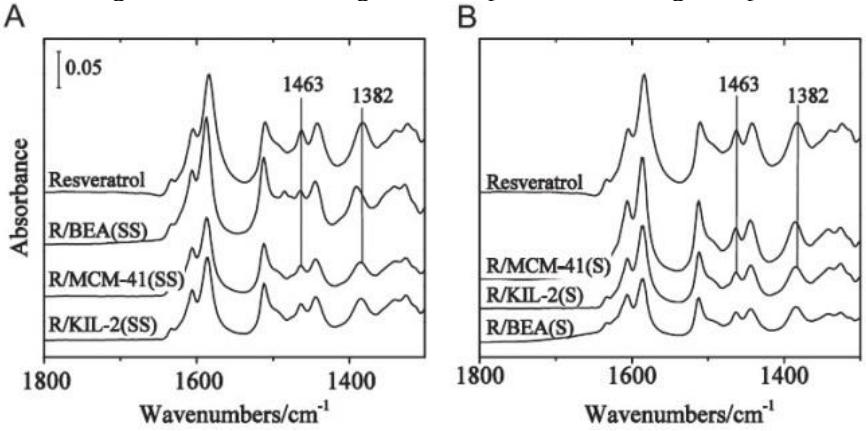

Figure 48 ATR FT-IR spectra of resveratrol, and the resveratrol-loaded samples prepared by solid-state method (A) and in solution (B)

The adsorbed amount of resveratrol was evaluated by thermogravimetric analysis (TGA) considering the weight loss at heating the resveratrol-loaded preparations (Tables 20A and 20B). With the exception of the mesoporous silicas loaded by ethanol solution, almost complete retention is registered for the three studied carriers. This result points to the high effectiveness of the solid-state procedure for preparation of drug delivery systems. As it was expected and the TGA determinations showed, almost the whole amount of added substance has remained on the carrier and evolved upon heating up to 873 K. The lower adsorption capacity for both R/MCM-41(S) and R/KIL-2(S) preparations in comparison to the BEA zeolite can be explained by the difference in their pore size distribution. The much larger size of the mesoporous channels and, respectively, their higher pore volume, suggest more facile diffusion of resveratrol out of the channel system, when the loading is carried out in solution.

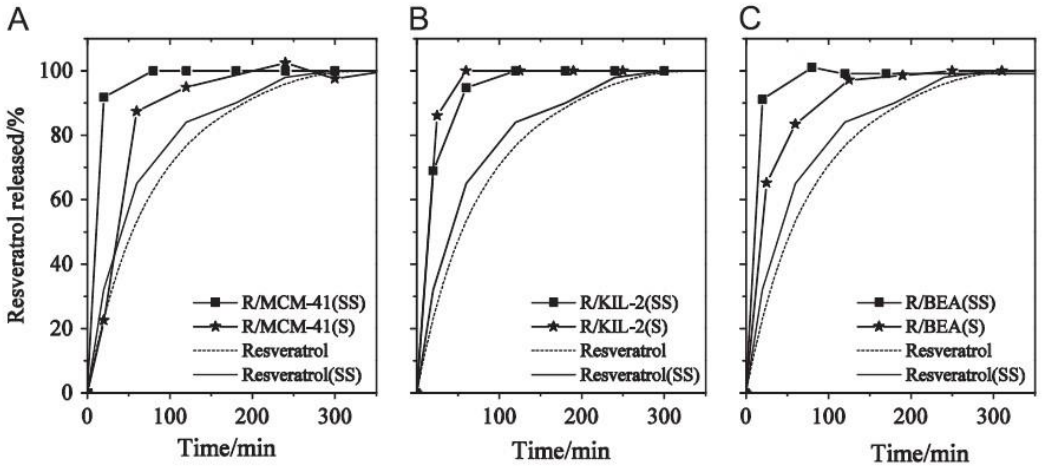

Figure 49 Release profiles of unsupported resveratrol, and the resveratrol-loaded MCM-41 (A), KIL-2 (B) and BEA (C) drug delivery systems prepared in solid state and in solution

Resveratrol release was carried out in phosphate buffer at pH = 7.4 and the kinetics of its evolution were followed by UV-Vis spectroscopy at a wavelength of 306 nm, the characteristic signal of the bioactive trans-resveratrol form. The data showed only this signal in the samples taken from the released solution. The release experiments were repeated 3 times with a period of one week between them and only trans-resveratrol was detected. This result is an indication that the loading on the chosen nanoporous carriers prevents the transformation of the supported bioactive trans-form to the less active cis-form. Thus, deposition of resveratrol on powdered silica-based carriers with mesoporous texture resulted in its stabilization and enhanced solubility. The release profiles of the loaded supports are presented in Fig. 49. Total release in about three hours was achieved for all resveratrol-loaded samples regardless of the preparation method. On the contrary, the free resveratrol and even the resveratrol treated by milling but not loaded on the carriers dissolves more slowly compared to that loaded in nanoporous systems. It indicates that the selected carriers and loading procedures substantially facilitate its dissolution. For the KIL-2 support (Fig. 49 B) almost similar release profiles are observed for both preparation methods. This parity can be explained by the presence of much larger mesopores, vis. the empty voids with the highest adsorption volume (Table 20B), formed among the nanoparticles of the KIL-2 carrier. This specific pore texture presumes equivalent location and surrounding of the supported substance and analogous adsorption characteristics. In the case of MCM-41(Fig. 92A) and the zeolite BEA (Fig. 49 C), the solid state method of loading ensures faster release compared to the analogue formulations prepared in ethanol solution. The presence of multiple pore system (internal and external mesoporosity in MCM-41, and a simultaneous presence of micro- and mesopores in nanosized zeolite) presumes selective access of resveratrol to the pore system of the supports. This can result in diversity in the release kinetics depending on the method used for loading. The solid-state deposition occurs, most probably, on the outer surface of both supports and ensures faster and close release kinetics. The presence of narrower pore channels in the zeolite carrier is the reason for the lower rate of resveratrol delivery from it, compared to MCM-41, when the drug is loaded by the liquid deposition method. Resveratrol amorphization during the grinding procedure upon dry mixing also contributes to the easier release when the substance is loaded in solid-state.

Loading of resveratrol on nanoporous MCM-41, KIL-2 silicas, and on nanosized BEA zeolite by two different methods (in solid- state and from ethanol solution) resulted in similar high loading capacity of the antioxidant. Considering the release profiles, all preparations showed better resveratrol solubility compared to the free resveratrol, regardless of the support structure and the method of loading. *In vitro* release process at pH = 7.4 showed faster resveratrol delivery from MCM-41 and BEA carriers prepared by the solid state method in comparison to that in ethanol solution. Resveratrol release from both KIL-2

preparations was equally fast independently of the loading method. This effect can be associated with the different pore texture of the carriers. The applied solid-state procedure of preparation appears very effective for loading of the medical compound. It ensures preservation of the entire loaded drug amount as well as improves significantly the solubility of the loaded substance due to amorphization upon grinding. Deposition into the powdered mesoporous supports stabilizes the bioactive trans-resveratrol form.

3.2.1.4. Preparation of efficient quercetin delivery system on Zn-modified mesoporous MCM-41, SBA-16 and SBA-15 silica carriers

Quercetin (Scheme 6) is a natural flavonol, which can be isolated from apples, wine, berries and tea. It has been extensively studied because of its biological and pharmaceutical properties and possible medicinal applications. The published data concerning the study of quercetin have been rapidly expanding over the last ten years, owing to its role in the treatment and prevention of many diseases. Flavonols demonstrate wide biological and pharmacological properties such as anti-cancer, anti-inflammatory, anti-diabetic, antiviral, anti-allergic, antimutagenic, lipid peroxidation inhibitory activity, etc. Its use as a health promoting agent is hindered by its low solubility in water and high instability in a neutral and alkaline medium. Different approaches towards the preparation of suitable delivery systems were applied depending on the target place. The formation of complexes between quercetin and pure siliceous or Zn-modified MCM-41, SBA-15 and SBA-16 mesoporous silicas was studied for the first time. *In-vitro* release properties of the obtained delivery systems were studied with respect to their possible application as dermal formulations.

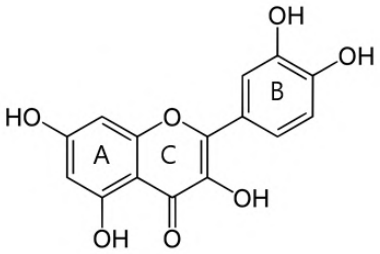

Scheme 6 Molecular structure of quercetin

The low angle XRD pattern of the parent nanoporous silica samples shows the typical intense (100) and (110) reflections for MCM-41 and SBA-16, respectively. The other two weak (110) and (200) lines also appear to confirm the ordered hexagonal structure of MCM-41, however for SBA-16 only the weak (200) reflection can be observed. X-ray powder diffraction pattern of the parent SBA-15 sample at low 2 theta degree region confirms the formation of well-ordered 2D hexagonal mesostructured. Slightly decreased intensity and structure ordering can be observed for samples modified with Zn, however reflections characteristic of crystalline zinc-oxide are not detected at higher angles. A more significant intensity decrease is observed for the functionalized and quercetin loaded mesoporous samples, which can be explained not only by the decreased amount of silica, but with some pore filling effect by quercetin, reducing the scattering contrast between the pores and the silica matrix.
High angle XRD patterns of quercetin loaded non-modified and Zn modified silica carriers are shown in Fig. 50.

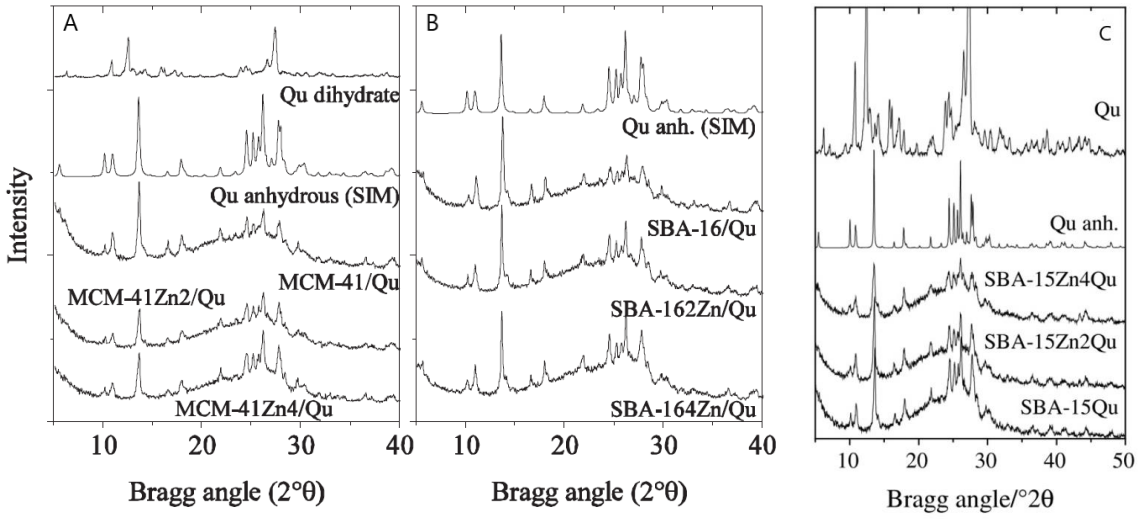

Figure 50 XRD patterns of quercetin loaded pure silica and Zn modified MCM-41, SBA-16 and SBA-15 formulations compared to pure quercetin

Reflections of quercetin can be observed on all samples. This is evidence that quercetin is not only contained in the pore channels, but can be found on the outer surface of the small nanoparticles or in the voids among the particles. Comparing the diffraction patterns of the parent quercetin dihydrate and the silica loaded quercetin samples, non-identical reflections can be found on them. This phenomenon can be associated with the hydration state of quercetin. Single crystal data can be found only on di- and monohydrate forms, however only the powder diffraction pattern generated by the CIF file of dihydrate form (Cambridge Structural Database Fefbex01) is identical with our parent quercetin sample. Thus, we can conclude that recrystallization and crystalline water loss of quercetin upon the loading procedure on silica carrier (dissolution in ethanol and heat treatment at 313 K) and formation of anhydrous form can be observed. The presence of silica carrier strongly influences the crystallization of quercetin, because the heat treatment of bulk quercetin dihydrate does not result consequently in the formation of the above mentioned anhydrous quercetin, but another, yet unidentified polymorph is formed. Loading of Zn on silica carrier did not significantly influence the quercetin loading, also the formation of anhydrous form can be observed.

Quercetin can be found in modified SBA-15 samples in its anhydrous form, regardless of whether it contains Zn or not, as found also in our former study with SBA-16 and MCM-41 support. This is due to the recrystallization process of the drug in ethanol by the loading procedure. This was evidenced by recrystallizing the parent quercetin dihydrate in ethanol, and then in situ heat treating it at different temperatures up to 393K (Fig. 51). It can be seen from the XRD patterns that anhydrous form is crystallized by the evaporation of ethanol at room temperature, and at elevated temperatures only the crystallinity is improved. However, direct heat treatment of the parent quercetin dihydrate results in the formation of another, not yet identified polymorph of anhydrite (Fig. 51A). Careful investigation of the parent quercetin dihydrate reveals that this material is a mixture of real dihydrate and the unknown polymorph formed at 393 K heat treatment. This unknown polymorph is also recrystallized to anhydrous form upon dissolving in ethanol or in methanol. We found as well, that this anhydrous form transforms to mono or dihydrate phase upon longer staying at ambient temperature and humidity.

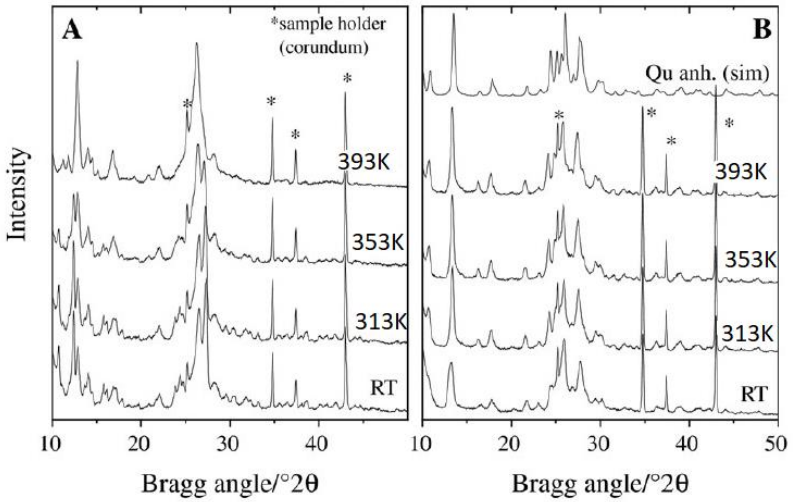

Figure 51 XRD patterns of the parent quercetin dihydrate (A) and the sample recrystallized in ethanol (B) recorded at RT, 313, 353, 393K

Significant decrease of the textural parameters (Table 21A and 21B), such as surface area and total pore volume, of the quercetin loaded samples indicate pore filling by quercetin. Taking into account the mass of nitrogen adsorbing silica in the drug delivery system, we can calculate the ratio of filled pores by the drug. This amounts to ~65% for SBA-15Qu sample and about 25% for Zn containing samples. The modification can lead to the formation of a zinc oxide phase in the chanals of mesoporous silicas. SBA-16 has significantly narrower pore entrances that can be blocked by ZnO nanoparticles, as a result of which Zn or quercetin would be prevented from entering them. The registration of ZnO particles by powder X-ray diffraction is impossible due to their low content in the sample and their small size (below 5 nm). It seems that although Zn modification does not result in pore blocking of SBA-15 channels (Table 21B) it hinders the penetration of quercetin into the channels, probably due to strong interaction of Zn with quercetin at the pore entrances.

Table 21A Textural properties of the non-modified, Zn-functionalized and quercetine loaded mesoporous silicas and the determined amount of quercetin and released Zn

Samples	S_{BET} (m^2/g)	pore volume (cm^3/g)	pore diameter (nm)	quercetin content (wt.%)	released Zn[a] (%)
SBA-16	787	0.49	3.6	-	-
SBA-16Zn2	522	0.36	4.6	-	-
SBA-16Zn4	469	0.34	4.8	-	2.5
SBA-16Qu	276	0.21	3.5	41.1	-
SBA-16Zn2Qu	209	0.16	4.6	43.1	100
SBA-16Zn4Qu	203	0.16	4.6	45.0	43
MCM-41	1175	1.00	2.7	-	-
MCM-41Zn2	1005	0.99	2.7	-	-
MCM-41Zn4	977	0.90	2.7	-	-
MCM-41Qu	249	0.20	-	35.0	-
MCM-41Zn2Qu	222	0.25	-	41.8	95
MCM-41Zn4Qu	278	0.29	2.3	36.6	92

[a] *In vitro* Zn release in buffer at pH=5.5.

Table 21B Textural properties of the studied samples and the quercetin content in the parent and Zn- functionalized samples

Samples	S_{BET} (m^2/g)	pore volume (cm^3/g)	pore diameter (nm)	quercetin content (wt. %)
SBA-15	870	1.10	6.0	-
SBA-15Zn2	849	1.06	5.8	-
SBA-15Zn4	671	0.91	5.9	-
SBA-15Qu	163	0.23	5.8	41.8
SBA-15Zn2Qu	260	0.43	5.5	43.7
SBA-15Zn4Qu	233	0.38	6.0	45.5

Similar phenomena can be observed on the SBA-16 and MCM-41 carriers. Zn modification leads in the reduction of the pore volume, the specific surface area and total pore volume.

All quercetin loaded samples were characterized by ATR FT-IR method (Fig. 52), in order to investigate the interaction between the quercetin molecule and the mesoporous carrier. The parent quercetin material is a mixture of anhydrite and dihydrate form (Fig. 52A), as evidenced also by XRD measurements. The spectra of the dihydrate and anhydrite forms show similarities, however, they can be clearly differentiated. In dihydrate form the carbonyl υC=O vibration, due to the hydrogen bonds, can be found at 1655 cm^{-1}, whereas this band is shifted to 1670 cm^{-1} in the anhydrite form. In the aromatic ring C=C vibration region the bands in anhydrite form (1616, 1594, 1552, 1511, 1456, and 1430 cm^{-1}) seem to shift to upper wavelength (1606, 1558, 1519, 1463 and 1450 cm^{-1}), too. In dihydrate form the δC-OH vibration of phenolic groups is shifted to 1380 cm^{-1} compared to that of in anhydrous quercetin at 1350 cm^{-1}. Also the vibrations of aromatic δC-H (1310 cm^{-1}) and υC-O (1288 cm^{-1}) are more intensive in anhydrite form. The band at 1360 cm^{-1} belongs to -OH bending vibration of the phenols, whereas the band around 1309 cm^{-1} can be assigned as in-plane bending vibration of aromatic C-H (Fig. 52). After quercetin loading on MCM-41, the υ(C=O) at 1655 cm^{-1} and the υ(C=C) at 1600 cm^{-1} show an upshift (Fig. 52B). The splitting of the bands suggests that two types of environment for quercetin are formed. Furthermore, the band intensity of the -OH bending of phenols around 1360 cm^{-1} increased. It seems that an interaction between the -OH groups of the MCM-41 matrix and the phenolic -OH groups of quercetin occurs, which leads to the conjunction loss among the aromatic and pyrone ring in the quercetin molecule. No significant difference was observed for quercetin loaded on pure silica and Zn modified MCM-41 samples. The spectral features of SBA-16Qu spectrum resemble (Fig. 52C) to those of MCM-41Qu. In the presence of Zn, however, the spectra are changed. For detailed analysis of quercetin-Zn interactions, an impregnation procedure by Zn was applied for pure quercetin (Fig. 52D). Regarding the spectrum of Qu:Zn 7%, the slight upwards shift of the υ(C=O) and υ(C=C) bands prove the coordination of Zn to quercetin. Moreover, new bands at 1456 and 1207 cm^{-1} arise, indicating that at least one -OH group is involved in the coordination. For Qu:Zn 1:1 complex, however, the υ(C=O) band is significantly diminished, whereas a new band at 1272 cm^{-1} corresponding to υ(C-O) has increased. This implies that the coordination of the metal ion occurs between the carbonyl group and the -OH group of ring C. The shifts in the C=C aromatic ring vibrations are more pronounced, suggesting a stronger coordination. As for the Zn modified SBA-16 samples, small new bands can be observed in the spectra at 1492,1461 and 1265 cm^{-1} wavenumbers, corresponding to the formation of Zn-quercetin complex involving also both the -OH and the C=O groups.

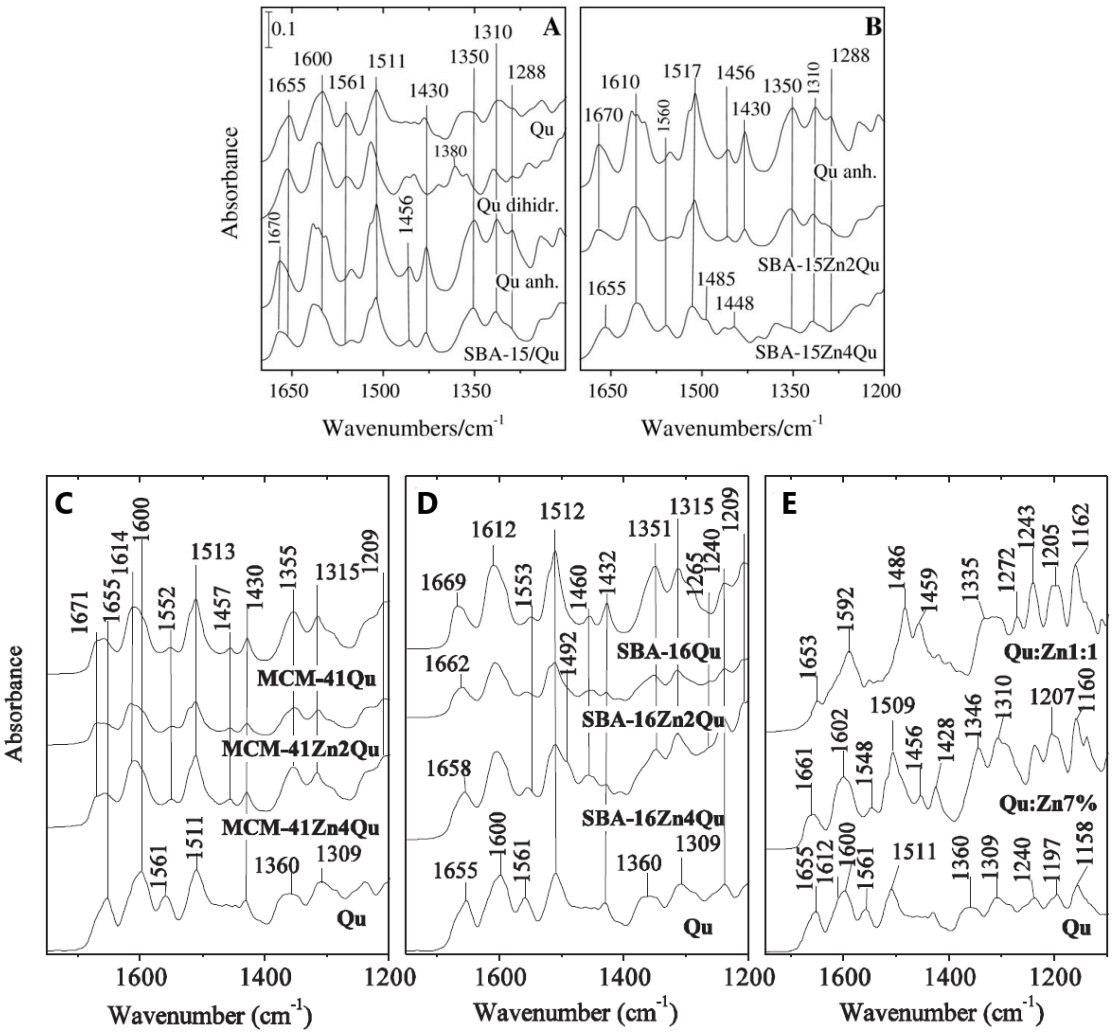

Figure 52 ATR FT-IR spectra of quercetin hydrates and quercetin loaded pure silica and Zn-MCM-41, Zn-SBA-16 and Zn-SBA-15 samples

Observing the spectrum of the SBA-15Qu sample, it rather resembles anhydrous quercetin more than the parent one, which is in accordance with our XRD investigations. However, the intensity decrease of the 1456, 1430 and 1288 cm^{-1} bands supports that physisorbed quercetin interacts with the silanol groups via aromatic rings rather than by phenolic groups. FT-IR spectrum of SBA-15 sample modified with 2% of Zn and loaded with quercetin is quite similar to that of siliceous SBA-15 (Fig. 52E). However, for the 4 wt.% Zn containing sample some changes in the spectrum can be witnessed. The band at 1456 cm^{-1} related to aromatic C =C vibrations is split (into 1462 and 1448 cm^{-1}, respectively) The band at 1430 cm^{-1} (related to C-H deformation of aromatic A-ring) and that of υC-O vibration at 1288 cm^{-1} also diminished. The main spectral change, however, is the disappearance of the broad, medium strong band belonging to OH bending (δC-OH) of phenols at 1350 cm^{-1}. All these changes reveal that mainly the aromatic ring (B-ring) of quercetin is affected by the interaction with the silica carrier. Since the C ring is fixed, probably the conformation of the quercetin molecule also changes (rotation of B-ring along the C-C connecting bond). Taking into consideration all the spectral changes above, it seems that the dominant interaction between Zn and quercetin occurs through the -OH groups of the aromatic B-ring, in contrast to 4% Zn modified SBA-15, where the formation of Zn-quercetin complex involves the C=O group and the -OH groups of C-ring or A-ring.

In conclusion, FT-IR spectroscopic investigations evidenced that on non-modified mesoporous silica quercetin is coordinated via its phenolic OH groups to the silanol groups of the silica matrix by hydrogen bonding. In the presence of zinc, incorporated on the surface of silica walls or as nanoparticles in the channels, a zinc-quercetin complex is formed, mainly by chelating phenolic -OH groups. It is interesting to note that in the case of Zn functionalized SBA-16, the ketonic carbonyl group of the quercetin is also involved in the coordination, presumably resulting in a stronger interaction.

Quercetin was loaded on the mesoporous silica carriers by incipient wetness impregnation from solution. Ethanol was chosen as a solvent, because of the high solubility of the quercetin in it. The loaded amount of quercetin was investigated by thermogravimetric method (Table 21A and 21B). Data show high loading on all samples with 35-45 wt. % quercetin content. The loaded amount of quercetin is higher for zinc containing samples for all supports.

Loading of quercetin on silica carriers slightly influenced its decomposition temperature by shifting it to 298 K lower values. For zinc containing samples this shift is more pronounced, reaching 313 K for SBA-16Zn4 sample. The similar quercetin loading for Zn-modified samples (43.7% for SBA-15Zn2Qu and 45.5% for SBA-15Zn2Qu) and the initial SBA-15 silica (41.6%) is an indication that textural parameters are not significantly changed after the Zn modification (see Table 21B).

Quercetin release (Fig. 53) was investigated in simulated body fluid at pH = 5.5, which is typical for dermal formulations. Quercetin loaded mesoporous MCM-41 and SBA-16 silicas show burst release with 77% of released quercetin in 30 min, whereas for zinc containing silica carriers it was lowered to 40%. Total release was observed in 6 h for non-modified MCM-41 and SBA-16 materials, and also for 4% zinc containing MCM-41 sample. The parent SBA-15 particles are also characterized with initial burst effect, as almost 60% of the drug is released within the first 30 min (Fig. 53). In contrast to the parent silica, Zn modified samples showed slower quercetin release with no initial burst, which is more prominent for SBA-15Zn4 counterparts. However, the complete quercetin release was observed within 4 h for all samples. These differences in release profiles of Zn modified samples could be attributed to the formation of Zn-quercetin complexes, which are temporarily immobilized in the silica structure The formation of water soluble Zn-quercetin complexes is also supported by the fact that under the same experimental conditions hardly any Zn release is observed from SBA-15Zn2 and SBA-15Zn4 samples. After quercetin loading Zn release increased sharply (Table 21A) to 65.5 wt.% for SBA-15Zn4Qu and to 100 wt.% for SBA-15Zn2Qu. This effect can also be associated with the formation of Zn-quercetin complex, making the metal content of the silica carrier soluble.

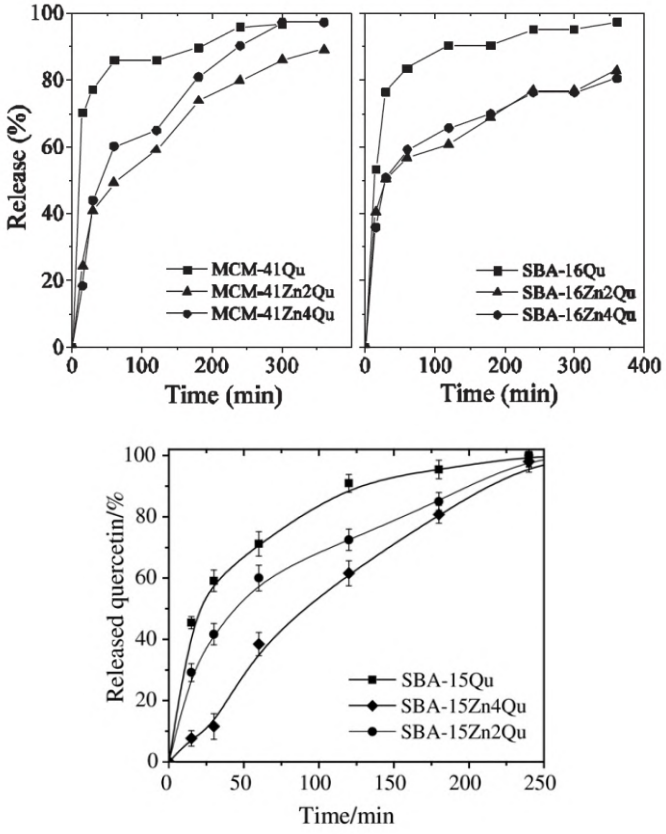

Figure 53 *In-vitro* release profiles of quercetin loaded pure silica and zinc modified SBA-16, MCM-41 and SBA-15 samples at pH = 5.5

Moreover, total release could not be reached with Zn-SBA-16 formulations. The latter can be explained by the bimodal pore structure of SBA-16, consisting of narrower pore entrances and bigger cavities and by the complexation with zinc evidenced by the FT-IR method. Quercetin molecules penetrating into the bigger pores are reacting with the encapsulated zinc nanoparticles and their release is hindered by the narrower entrances.

The release of zinc was also significantly increased with quercetin loading. Zn release of the SBA-16Zn4 sample was 0.05 mg/l, which corresponds to 2.5 wt.% of the total zinc content. However, in the presence of quercetin the released amount of zinc dramatically increased (Table 21A) to 43-100 wt. %. This effect can also be associated with the formation of Zn-quercetin complex, making the metal content of the silica carrier soluble. The dissolution of zinc was higher on Zn-SBA-16 samples than on Zn-MCM-41 ones. This observation is in accordance with FT-IR data suggesting the formation of Zn-quercetin complex predominantly on the SBA-16 structure. This can be explained by the formation of a higher amount of ionic zinc species (=Si-O-Zn-O-Si=) incorporated into the silica framework of MCM-41 evidenced by UV-Vis spectra.

The lack of toxicity is an important requirement for all materials used in preparation of drug delivery systems. The cytotoxicity potential of mesoporous carriers was determined in two human cell lines with different cell types and origin, namely non-malignant HEK-293 and malignant HUT-78. The two cell lines were chosen in order to discriminate between the growth inhibitory potential of tested systems and free drug against non-tumorigenic and malignant cell lines. HEK-293 cells represent non-cancerous epithelial cells, whereas HUT-78 is a suitable model for cutaneous T-cell lymphoma (CTCL). A characteristic feature of CTCL is the constitutive over-activity of JAK-3 kinase, which is selectively inhibited by quercetin, making this polyphenol a potential targeted drug for this condition. The corresponding equieffective IC50 values are summarized in Table 22.

Table 22 Equieffective concentrations of tested quercetin formulations, vs. the free drug

Cell line	IC_{50} (μM)			
	quercetin	**SBA-15Qu**	**SBA-15Zn2Qu**	**SBA-15Zn4Qu**
HEK-293	n.d.	n.d.	n.d.	n.d.
HUT-78	174.8	95.14	91.3	26.5

The non-loaded silica particles failed to induce any significant decrease in cell viability of non-malignant HEK-293 cell line even at the highest dose of 1 mg/ml (not shown). The cytotoxicity of quercetin loaded mesoporous nanoparticles was determined on the same cell lines as empty NPs and compared with the effect on cell proliferation of free drug. As evident from the graphs, quercetin and its SBA-15 and SBA-15Zn2 formulations did not show inhibitory effect on cell proliferation of non-malignant HEK-293 cells. Quercetin loaded SBA-15Zn4 causes eradication of app. 49% of the treated cells, but even at the highest tested concentration IC_{50} values were not reached. In contrast, in malignant HUT-78 cells all tested formulations exerted clear concentration dependent cytotoxic effects. These findings show that the tested quercetin loaded SBA-15 and SBA-15Zn2 formulations are characterized with high selectivity against malignant cells and are non-harmful for normal cells. In addition to their selectivity quercetin loaded mesoporous silica materials were superior in terms of cytotoxic activity as compared to the free quercetin compound. The concentration-response curves were shifted to the lower concentrations and re-spectively the IC_{50} values were app. two folds lower as compared to the effects of quercetin, applied as an ethanol solution. This effect was more pronounced in Zn-modified quercetin loaded particles, causing > 70% eradication of viable cells at the highest concentration 200 μM.

High loading capacities of quercetin on pure silica and Zn-containing mesoporous MCM-41, SBA-15 and SBA-16 materials were achieved by incipient wetness impregnation method. For the first time the formation of more stable Zn quercetin complexes loaded on mesoporous silica materials was evidenced. In-vitro release experiments at pH = 5.5 showed faster quercetin release from initial silica systems in comparison to Zn modified ones due to the stronger interaction of the quercetin molecule with the Zn^{2+} cations than with the silanol groups on the silica surface. Spectroscopic data suggested the formation of Zn-quercetin complex on the zinc modified supports. Our results also showed that the quercetin molecule is bound to the silica surface via different functional groups, depending on the cations available on the surface. Additionally, the comparative cytotoxic experiments show that quercetin encapsulated in Zn-modified silica carrier (2 wt.% Zn) proved to exert superior antineoplastic potential against HUT-29 cells compared to free drug. Thus, it can be concluded that Zn-modified SBA-15 silica particles are promising carriers for dermal delivery of quercetin.

3.2.1.5. Nanostructured silver silica materials as potential propolis carriers

Propolis is a resinous hive product containing beeswax and plant exudates collected by honeybees from certain plant sources. It has well known pharmacological properties as an anti-inflammatory, anticancer, antioxidant, antibacterial, antiviral and antifungal agent. It is used in traditional medicine in the form of alcohol extracts or in combination with other natural products. The composition of propolis is very complex and varies depending on the phytogeographic diversity of the collection area and the season. The main problem restricting propolis diverse application is its very low water solubility. Therefore, there is a pressing need to find a novel approach that can harness the potential of propolis in the clinical practice. Silver nanoparticle containing mesoporous silica Ag-SBA-15 and Ag-MCM-41 carriers were loaded with poplar propolis in order to prepare a drug delivery system possessing high antimicrobial activity and capability of overcoming the disadvantages of propolis related to its poor solubility.

The XRD pattern of pure silica SBA-15 at low 2 Theta region confirms the formation of well-ordered 2D hexagonal structure. Some intensity decrease of the reflections was registered for the Ag-SBA-15 sample compared to the initial SBA-15 material (not shown). Ag-MCM-41 samples prepared by template ion-exchange method also show the typical patterns of highly ordered hexagonal phase with intensive (100) reflection.

Reflections of metallic silver can also be observed at higher angles for both materials, but their intensity is much lower (slightly over the detection limit) on Ag-MCM-41 than on Ag-SBA-15 sample. According to AAS results (Table 23) the silver content of Ag-MCM-41 sample is only slightly lower than that of Ag-SBA-15. The alteration between the two samples can be due to their different preparation methods. By ion-exchange method in Ag-MCM-41 sample probably more ionic silver species connected to silica matrix were formed. The appearance of metallic silver on the pattern is an indication of the formation of silver crystallites bigger than ~ 5 nm, according to the Sherrer equation (Szegedi et al., 2014). These nanoparticles can be found as a separate phase among the silica particles or attached to the outer surface of the silica support.

The N_2 adsorption data are summarized in Table 23. The nitrogen physisorption isotherms of pure silica and silver modified MCM-41 materials show the typical IV type physisorption isotherm with a capillary condensation step of nitrogen between 0.2 and 0.3 relative pressures. Compared to parent silica material the specific surface area and the total pore volume of Ag-MCM-41 sample are somewhat lower which is due to partial structure deterioration. The latter can be explained by effect of template ion-exchange method, i.e. the agitation of mesoporous silica at higher temperature (353 K) in an acidic water solution, resulting in some dissolution of silica.

Table 23 Composition and textural properties of the studied samples

Samples	Ag content[a] (mmol/g)	a_0[b] (nm)	S_{BET} (m^2/g)	pore volume (cm^3/g)	pore diameter (nm)	propolis content (mg/g)	encapsulation efficiency (%)
MCM-41	-	4.4	1175	0.97	2.7	-	-
SBA-15	-	10.2	970	1.20	6.4	-	-
Ag-MCM-41	0.52	4.3	927	0.76	2.6	-	-
Ag-SBA-15	0.66	10.6	698	1.08	6.6	-	-
Ag-MCM-41/Pr	0.48[c]	4.2	301	0.35	2.4	13.6	72
Ag-SBA-15/Pr	0.62[c]	10.2	232	0.59	6.2	17.1	86

[a] determined by AAS method after digestion in HF and HNO_3,
[b] cell parameter ($a_0 = 2d_{1\,0\,0}(3)^{-1/2}$),
[c] release of Ag^+ in 6 h in buffer solution determined by AAS.

The N_2 adsorption isotherms of the Ag-SBA-15 sample are of the type IV with a H1 hysteresis loop, typical for SBA-15 structures. The decrease of specific surface area and pore volume of Ag-SBA-15 sample compared to the silica one is minor and probably cannot only be due to some pore blocking effect of small silver nanoparticles, but to the variation of synthesis method by applying nitric acid instead of hydrochloric acid to avoid the precipitation of silver as AgCl.

Ag-MCM-41 shows the typical 100 nm spherical particles and the channel system is well-preserved. Silver nanoparticles with sizes between 5 and 20 nm can be observed on the images. TEM images of Ag-SBA-15 sample exhibits also the presence of 5-20 nm sized silver nanoparticles on the external surface, and smaller 5 nm particles inside the channels can be observed as well. Formation of metallic silver nanoparticles can be explained by the reducing effect of template decomposition by calcination for both types of silica, i.e. the products of Hoffman degradation can reduce Ag^+ ions weakly bound to the silica matrix during the synthesis procedure. The uniform, nanometer sized pores of silica carriers can hinder only to some extent the migration and agglomeration of metallic silver particles, therefore finely dispersed metallic nanoparticles formed in the channels and on the outer surface of the silica carriers.

Poplar propolis is a bee product which contains around 50 individual compounds. Major compounds of the extract were the flavanones/dihydroflavonols (pinobanksin, pinocembrin, 3-acetylpinobanksin) and flavones/flavonols (galangin, chrysin). Propolis was adsorbed on silver containing samples using ethanol solution (70%) for 24 h. Our preliminary data showed that total encapsulation can be reached by 24 h. Encapsulation efficiency values (Table 23) with 72 and 86% for silver containing MCM-41 and SBA-15 materials supported the successful loading of propolis on the silica carriers.

XRD patterns of the propolis loaded silver silica materials do not show any reflection characteristic for propolis. Dried propolis extract has an amorphous structure, and a broad peak can be observed on the pattern at 2 Theta. Compared to pure propolis the silica loaded varieties do not show the amorphous peaks, only the broad amorphous peak of silica can be observed at ~ 23° 2 Theta.

In contrast to XRD results, N_2 physisorption data showed that compounds of propolis penetrated into the channels of the silica carrier and partial pore filling was achieved (Table 23). Significant decrease of BET surface area, pore volume and pore sizes are registered after the propolis loading on both MCM-41 and SBA-15 silica supports.

The amount of propolis loaded in the Ag-modified mesopores of MCM-41 and SBA-15 was quantified using thermogravimetry. The Ag-MCM-41 sample showed lower adsorption capacity (13.6 wt.%) for propolis in comparison to its AgSBA-15 analogue (17.1 wt.%). About 46% of the pores of Ag-MCM-41 are filled with propolis if we take into account only the amount of adsorbing silica. This value is somewhat lower for Ag-SBA-

15, it amounts to 34%. The lower value can be explained by the more open structure of SBA-15 with wider mesopores releasing a higher amount of propolis during the washing procedure following ethanolic loading (Table 23).

The lower propolis adsorption capacity on Ag-MCM-41 can be explained also by the blocking of pore entrances due to the narrower pores of Ag-MCM-41 carrier. Interaction of propolis compounds with silver ions on the outer surface of MCM-41 can also contribute to this pore blocking effect.

Interaction of loaded propolis with the silica carrier was investigated by the ATR FT-IR method. The ATR FT-IR spectra (Fig. 54) of propolis loaded on Ag-MCM-41 and Ag-SBA-15 show different features compared to pure propolis. The spectrum of propolis is characterized by typical CH_2 stretching vibrations at 2929 and 2855 cm^{-1}, which are clearly recognized also in the spectra of propolis loaded Ag-SBA-15 and Ag-MCM-41 samples (not shown). The most interesting part of the spectra, however, consist of bands between 1800 and 1250 cm^{-1} belonging to the C=O and C=C/C-C vibrations of the flavonoid structure. In the spectrum of the pure propolis, the band at 1690 cm^{-1} belongs to the stretching of C = O group, whereas bands at 1633, 1602, 1587, 1514 and 1450 cm^{-1} are related to C = C and skeletal C-C stretching vibra-tions of flavonoid aromatic rings. The later, however, might be superposed with C-H deformations (Wu et al., 2008). The wavenumber region below 1250 cm^{-1} characteristic for primary and secondary alcohol groups of flavonoids is masked by the strong Si-O-Si vibrations of the silica matrices. After loading on Ag-MCM-41 and Ag-SBA-15, the intensity of C=O stretching of propolis is suppressed, while C=C and C=C/C-C stretching bands of flavonoid aromatic rings are shifted towards higher wavenumber. These spectral features suggest that interactions between the silica matrices and the propolis molecules exist, involving the carbonyl group and the aromatic ring of the latter.

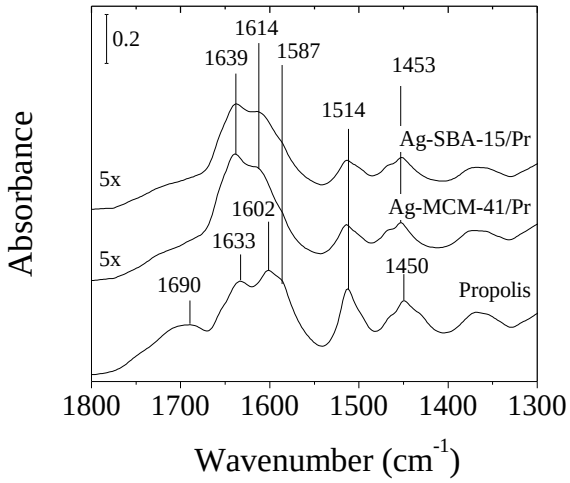

Figure 54 FT-IR spectra of propolis loaded Ag-silica materials

The *in vitro* release of propolis from AgMCM-41 and AgSBA-15 samples was studied in phosphate buffer at pH = 5.5. The latter pH value is widely applied for in vitro experiments for dermatological formulations. As seen in Fig. 55, non-encapsulated propolis is poorly dissolved in the selected medium, which could be expected considering its poor water solubility. In contrast, the loading of propolis on mesoporous carriers resulted in improved dissolution rate (Fig. 55). This can be explained by the higher dispersion of propolis particles confined in the channels of nanoporous silica carriers and the interaction with silver ions deposited on the support surface which is evidenced by ATR FT-IR data. The propolis release from AgMCM-41 is even faster, most probably because of the shorter diffusional route from the small particles. The simultaneous release of Ag is studied as well. The data reveals that together with the release of propolis high release of Ag has been reached in the buffer solution, 77% for the AgMCM-41 sample and 60% for the AgSBA- 15 sample. We can suggest that the released Ag together with the propolis molecules could give evidence for some synergic bioactivity.

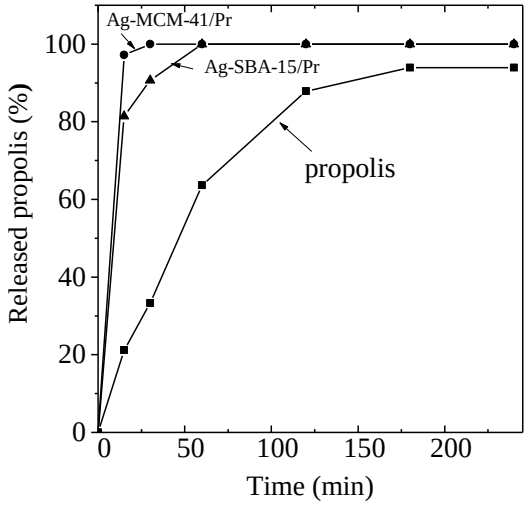

Figure 55 *In vitro* release of propolis from Ag-MCM-41 and Ag-SBA-15 carrier

Our silver and propolis containing samples were tested against the most commonly found bacteria, such as strains of ATCC *Escherichia coli 20* and *Staphylococcus aureus* and fungus *Candida albicans 562I*, and were compared to pure propolis as a control (Table 24).

Table 24 Antimicrobial activity of propolis, Ag-modified mesoporous silicas and their propolis- loaded varieties

	zone of inhibition [mm]		
Samples	**S.aureus 209**	**E. coli wf +**	**C. albicans 562 I**
Ag-SBA-15	5±0.2	8±0.3	5±0.3
Ag-MCM-41	4± 0.1	9±0.5	5±0.4
Propolis	13.7± 0.3	0±0.5	18 ± 1
Ag-SBA-15/Pr	19±0.5	19±0.5	24±1
Ag-MCM-41/Pr	21±0.8	19±1	22±1

Our results show that silver-containing nanoporous silica materials have some inherent antibacterial and antifungal activities, but propolis shows much higher activity, except in the case of *E. coli strain*. Combining silver containing silica materials with propolis showed a synergistic effect by increasing the inhibition zone to somewhat higher value than the sum of the individual components. This is more pronounced in the case of *E. coli*, showing double increase of inhibition zone. These results indicate that propolis-loaded silver nanoporous silica samples are more effective in bacterial and fungal inhibition than pure propolis probably due to the improved solubility of the latter one. Moreover, our experiments supported the well-known fact that ionic silver relesed from silver nanoparticles has positive effect on antibacterial activity. The beneficial effect of silver is so strong that agar plates showed the original in-hibition zones even after 7 days of incubation (Table 24).

It was demonstrated for the first time that silver modified MCM-41 and SBA-15 materials are suitable carriers for propolis to design drug delivery systems with improved solubility and antimicrobial activity. It was found that mesoporous silicas can be easily modified by direct or post-synthesis methods to prepare silver nanoparticles inside the channels or on the outer surface of the particles. The mesoporous channels of the silica support are suitable for the storage of a relatively high amount, 15-17 wt.%, of poplar propolis. Loading of propolis from ethanolic solution on silver containing silica carriers resulted in significantly improved water solubility, probably due to its higher dispersion in the channels of the silica carrier. Antibacterial and antifungal activities investigations showed a synergistic effect of silver and propolis against widespread bacteria strains and fungus.

3.2.1.6. Silver and sulfadiazine loaded nanostructured silica materials as potential replacement of silver sulfadiazine

Silver sulfadiazine (AgSD) (Scheme 7) is an effective and widely used antimicrobial agent to avoid bacterial infections and external contamination. Topical antibiotic therapy is essential for the treatment of burns. Silver sulfadiazine is the leading topical agent to control bacterial infections in second-degree burn wounds. AgSD possesses very low solubility in aqueous systems (3.4 mg L^{-1} at pH = 6.8). However, antibacterial activity develops only by decomposition of AgSD to silver ions and sulfadiazine. The silver ion slowly dissociated from AgSD is the antimicrobially active part of the compound, whereas sulfadiazine has a

supportive effect, but its concentration can be subinhibitory. Silver nanoparticles containing mesoporous silica Ag-SBA-15 and Ag-MCM-41 carriers were loaded with sulfadiazine in order to prepare a drug delivery system, which overcomes the disadvantages of AgSD and possesses improved bioavailability and solubility. The present study is the first attempt to substitute AgSD with silver- and sulfadiazine-loaded nanoporous silica materials, possessing high antibacterial activity.

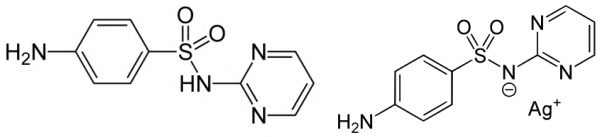

Scheme 7 Sulfadiaine and Ag-sulfadiazine molecules

Low- and high-angle XRD powder patterns of pure silica and silver containing SBA-15 and MCM-41 materials, and their SD and AgSD loaded varieties, are shown in Fig. 56.

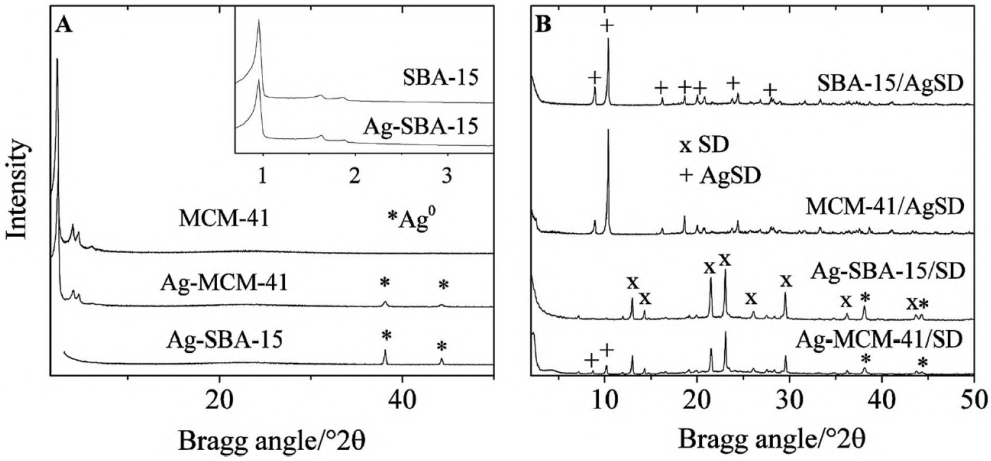

Figure 56 XRD patterns of silver-containing nanoporous pure silica and silver-modified silica samples (A) and their SD- and AgSD-loaded varieties (B)

The XRD patterns of the Ag-SBA-15 sample at low 20° region show the formation of typical, well-ordered 2D hexagonal (p6mm) structure (Fig. 56 inset) with the intense (100) reflection and the appearance of the higher indexed (110) and (200) peaks. Compared to a pure silica SBA-15 some intensity decrease can be observed. XRD patterns at higher angles show the presence of a separate metallic silver phase. Ag-MCM-41 samples prepared by template ion-exchange method also show the typical patterns of highly ordered hexagonal phase. The intensity of (100) reflection is lower than that of parent silica variety. Reflections of metallic silver can also be observed at higher angles, but their intensity is smaller than on Ag-SBA-15 sample. According to AAS results (Table 25), the silver content of Ag-MCM-41 sample is slightly lower than that of Ag-SBA-15.
The appearance of metallic silver on the pattern is an indication of the formation of silver crystallites bigger than ~5 nm, according to the Scherrer equation. These nanoparticles can be found as a separate phase among the silica particles or attached to the outer surface of the silica support.

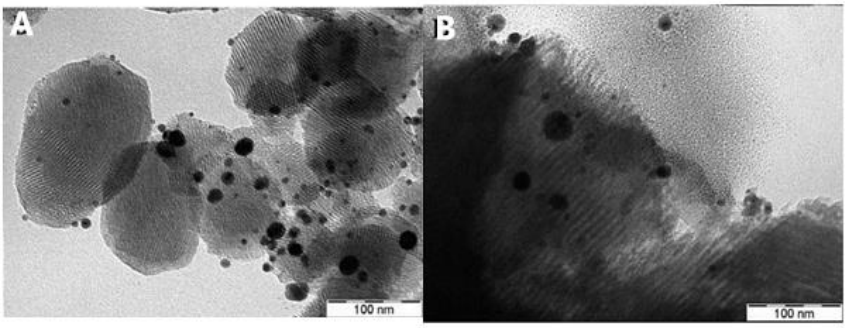

Figure 57 TEM images of Ag-MCM-41 (A) and Ag-SBA-15 (B) samples

No significant changes, only a small decrease can be observed in the unit cell and pore size of the Ag-MCM-41 sample (Table 25) compared to the pure silica variety. This can be due to the deteriorating effect of ion-exchange procedure. Heating the sample in water solution at 353 K for 20 h can result in dissolution of silica and the decrease of ordering of honeycomb-like structure. Incorporation of Ag into the structure of SBA-15 is associated

with more significant changes. The unit cell size and the pore size is increased, which can be either due to the isomorphous substitution of silicon atoms by the bigger silver ions or due to the change of synthesis medium from HCl to HNO_3.

Table 25 Composition and textural properties of the studied samples

Samples	Ag content ($mmol/g_{calc}$)	SD content (mg/g)	a_0[a] (nm)	S_{BET} (m^2/g)	total pore volume (cm^3/g)	pore diameter[b] (nm)
MCM-41	-	-	4.4	1175	0.97	2.7
SBA-15	-	-	10.2	970	1.20	6.4
Ag-MCM-41	0.52	-	4.3	927	0.76	2.6
Ag-SBA-15	0.66	-	10.6	698	1.08	6.6
Ag-MCM-41/SD	0.52	458	4.3	233	0.18	2.3
Ag-SBA-15/SD	0.66	307	10.6	302	0.54	6.3
MCM-41/AgSD	1.03	260	4.4	233	0.18	n.d.
SBA-15/AgSD	1.22	307	10.2	316	0.40	4.1

[a] Unit cell parameter ($a_0 = 2d_{1\,0\,0}(3)^{-1/2}$);
[b] Mean pore diameter calculated by the BJH method.

The above observations were supported also by the N_2 adsorption data (Table 25). The nitrogen physisorption isotherms of pure silica and silver-modified MCM-41 materials show the typical IV type physisorption isotherm with a capillary condensation step of nitrogen between relative pressures of 0.2 and 0.3. Compared to parent silica material the specific surface area and the total pore volume of Ag-MCM-41 sample are slightly lower, supporting the structure deterioration idea. The N_2 adsorption isotherms of Ag-SBA-15 sample belong to the IV type with a H1 type hysteresis loop, typical for SBA-15 structures. The decrease of specific surface area and pore volume of the Ag-SBA-15 sample compared to the silica one is minor and probably can be due to some pore blocking effect of small silver nanoparticles.

Ag-MCM-41 shows the typical 100 nm spherical particles and the channel system is well preserved. Silver nanoparticles with different dispersities between 5 and 20 nm can be observed on the images. These results are in accordance with XRD results showing the presence of separate silver phase on the outer side of the particles. TEM images of Ag-SBA-15 sample exhibits a similar picture. 5-20 nm sized silver nanoparticles on the external surface, and smaller 5 nm particles inside the channels can be observed.

From the antibacterial point of view, the release of Ag^+ ions from the antibacterial material is essential. Silver ions can be released either from silver nanoclusters by their oxidation with H_3O^+ ions in water or by the cleavage of Ag^+ ions connected to the silica wall through oxygen atoms. In this respect, solubility of the silica host also plays an important role. It is well known that due to their thinner walls and lower silica condensation rate MCM-41-type silica materials show less stability towards water dissolution than SBA-15 ones. Therefore, a higher amount of silver release is to be expected from silver-containing MCM-41 materials. The silver ion dissolution capacity of the prepared samples was checked by stirring 0.2 g of Ag-SBA-15 and Ag-MCM-41 in 50 ml water for 24 h at 310 K. By AAS method, for Ag-MCM-41 sample, 4.7 mg Ag^+ g/calc was detected, whereas for Ag-SBA-15 sample, 2.9 mg Ag^+ g/calc was detected. These values correspond to 9% and 4.5% of the total silver content of the samples, respectively. These data support that in MCM-41 material the dissolution of silver is easier, and silver ions and metallic particles are not so strongly bound to the silica host due to the post-synthesis modification method. In SBA-15 support, because of the direct synthesis method, silver can be found embedded in the silica wall in the form of Ag-O-Si_3 ionic species or confined inside the channels as small nanoparticles. These facts can explain the lower amount of released silver ions from Ag-SBA-15, but the higher silver content of the sample can compensate its lower release rate.

Sulfadiazine was adsorbed on silver-containing samples by dissolving SD in the mixture of methanol and acetone. SD penetrated into the channels of silica carrier and partial pore filling was achieved, evidenced by the N_2 physisorption data (Table 25). Correcting the pore volume data by the actual amount of silica carrier, 65-70% pore filling for MCM-41 samples and 10-30% loading can be calculated for SBA-15 support. According to the XRD patterns of the SD loaded silica materials (Fig. 56B), the remaining amount of SD can be found as a separate phase in the sample.

Ag-SBA-15/SD shows similar FT-IR spectral features like free SD (Fig. 58): NH_2 bending of free amino groups (δ_{NH2} at 1652 cm^{-1}), phenyl skeletal vibrations (υ_{CC} at 1574 and δ_{CCH} at 1487 cm^{-1}) and pyrimidine skeletal vibrations (δ_{CCH} at 1439 and δ_{HCN} at 1406 cm^{-1}). The band at 1322 cm^{-1} belongs to the symmetrical stretching of SO_2 groups. However, in the spectrum of Ag-MCM-41/SD, small new bands (shoulders) at 1553 and 1501 cm^{-1} appear. These bands are to be found in the spectrum of AgSD, and they can be assigned to the shifted ring vibrations of pyrimidine due to the presence of Ag^+ ions. Appearance of the latter bands is an indication that a part of adsorbed SD is in the close vicinity of silver nanoparticles or silver ions remained connected to the silica walls

inside the channels of Ag-MCM-41 after the template removal, in accordance with XRD results. It should be noted that no spectral changes can be detected for adsorbed SD in non-modified pure silica MCM-41.
AgSD was also adsorbed on pure silica materials to compare the physicochemical and antimicrobial properties with SD-loaded, silver-modified varieties. N_2 physisorption data (Table 25) show that despite its extremely low solubility, AgSD can penetrate into the channels of silica carriers and almost total pore filling in MCM-41 and partial pore filling for SBA-15 carrier can be detected. However, according to XRD patterns (Fig. 25B), the majority of AgSD can be found outside the channels. This is more pronounced for MCM-41 material, probably due to its lower pore volume and smaller pore size, hindering the penetration of the drug molecules. N_2 physisorption data indicate total pore filling; however, it might be that AgSD blocks only the entrances of pores. Spectra of AgSD-loaded MCM-41 and SBA-15 samples show similar spectral bands like free AgSD, indicating that AgSD is physisorbed on silica carriers. Interaction of adsorbed AgSD with the silica carrier and of SD with Ag-containing mesoporous support was investigated by ^{13}C NMR. Fig. 59 A and B show the ^{13}C spectra of pure AgSD and the AgSD loaded on MCM-41 material, respectively. The two spectra demonstrate similar spectral patterns; however, most of the signals of the AgSD-loaded silica material are shifted downfield. These chemical shift changes are indicative for the new structural and chemical environment of AgSD molecules as a result of their incorporation into the silica matrix. More significant differences between the ^{13}C spectra of the two samples are observed in the spectral region between 156 and 161 ppm, where the two peaks corresponding to C2 and C4 atoms from pyrimidine moiety are shifted upfield; moreover, a broad resonance partially overlapped with these signals appear in the spectrum of AgSD loaded into the silica carrier. The particular spectral pattern in the region between 156 and 161 ppm could be explained by the distribution of AgSD molecules within the pores and on the outer surface.

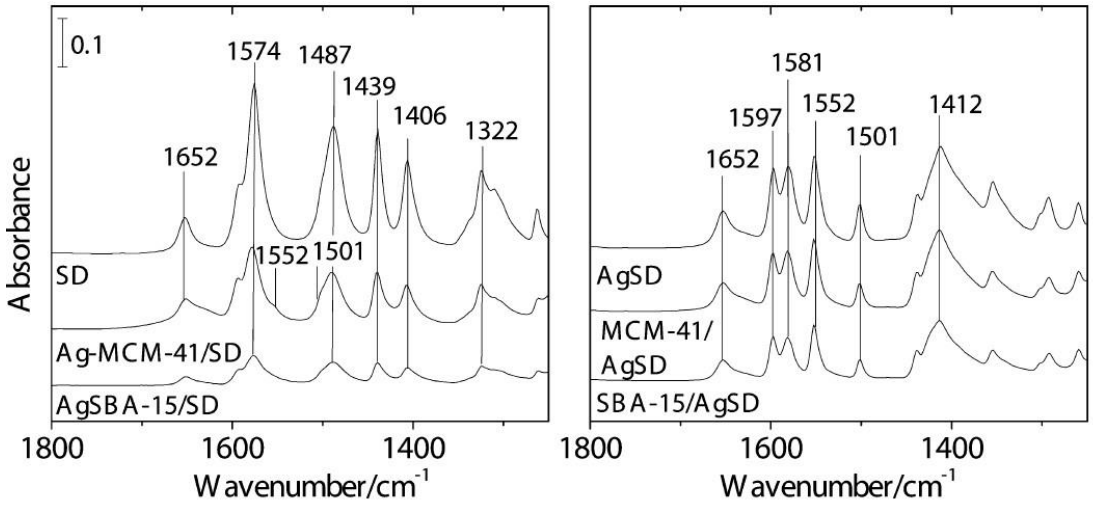

Figure 58 FT-IR spectra of SD-loaded Ag-silica materials and AgSD loaded nanoporous silica samples

Fig. 59 C and D show the ^{13}C NMR spectra of pure SD and SD adsorbed on silver-modified SBA-15 material (Ag-SBA-15). Comparing these spectra, it can be observed that all ^{13}C signals are shifted downfield by an average of 0.32 ppm in SD/Ag-MCM-41 material. This result indicates that SD molecules in silver-modified SBA-15 material are predominantly adsorbed in the pores. ^{13}C NMR investigations are in a good agreement with the XRD and FT-IR data. The amount of sulfadiazine loaded in the mesopores of MCM-41 and SBA-15 and their Ag-modified analogues was quantified using thermogravimetry (TG). The Ag-MCM-41 sample showed lower adsorption capacity (30.5 wt.%) for SD in comparison to its AgSBA-15 analogue (45.8 wt.%) (Table 25). Interaction of SD with silver ions on the outer surface of MCM-41 can also contribute to this pore blocking effect. The loading of AgSD on MCM-41 and SBA-15 silicas resulted in 26.0 wt.% and 30.7 wt.% adsorbed sulfadiazine, respectively (Table 25). Taking into account that in contrast to SD only 70% of AgSD can be decomposed by thermal treatment up to 873 K (metallic silver remains on the surface after decomposition of organic material), the above values correspond to 78% and 92% of the loaded drug. The AgSD content is higher on MCM-41 compared to SD loaded on Ag-MCM-41, and similar to SBA-15 and Ag-SBA-15 carriers. These results show that similarly efficient SD loading can be achieved by the application of Ag-functionalized silica carriers.

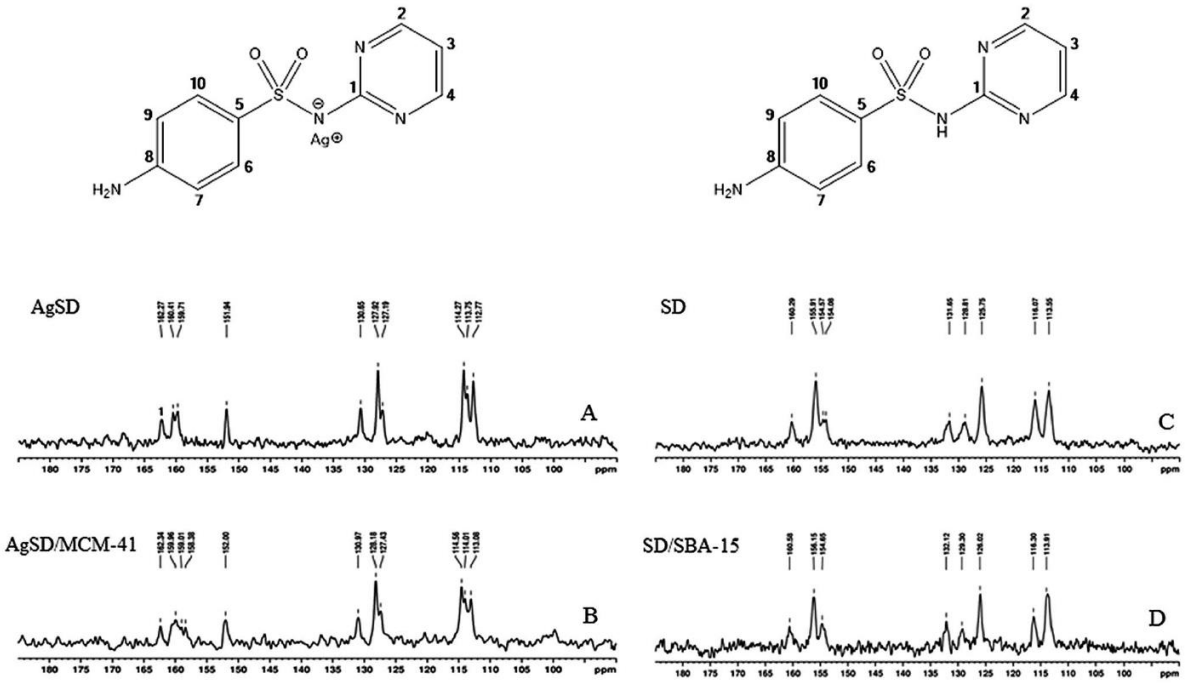

Figure 59 ^{13}C NMR spectra of SD-loaded Ag-SBA-15 and AgSD-loaded MCM-41 sample compared to pure SD and AgSD, respectively

The *in vitro* release of silver sulfadiazine from MCM-41 and SBA- 15 samples and sulfadiazine from silver-modified ones was studied in a phosphate buffer (pH = 5.5). The drug release profiles are presented in Fig. 60. As seen in Fig. 60, non-encapsulated AgSD is poorly dissolved in the selected medium, which could be expected considering its poor water solubility. In contrast, the loading of AgSD on mesoporous carriers resulted in improved dissolution rate (Fig. 60 A). This can be explained by the lower crystallinity of the loaded AgSD, i.e. a part of it can be in nanocrystalline or in amorphous form. The formation of nanocrystalline or amorphous particles is predetermined by the adsorption of AgSD on the high surface of mesoporous silica and by the penetration into the pore system. Comparing the different nanoporous carriers, faster release of AgSD was registered from SBA-15 particles, which can be explained by the larger size of the pores. Note that improvement of AgSD dissolution rate is advantageous because the better solubility of the drug can enhance its antibacterial activity. Similarly, the release of sulfadiazine from Ag-modified SBA-15 carrier was faster compared to MCM-41 one (Fig. 60 B).

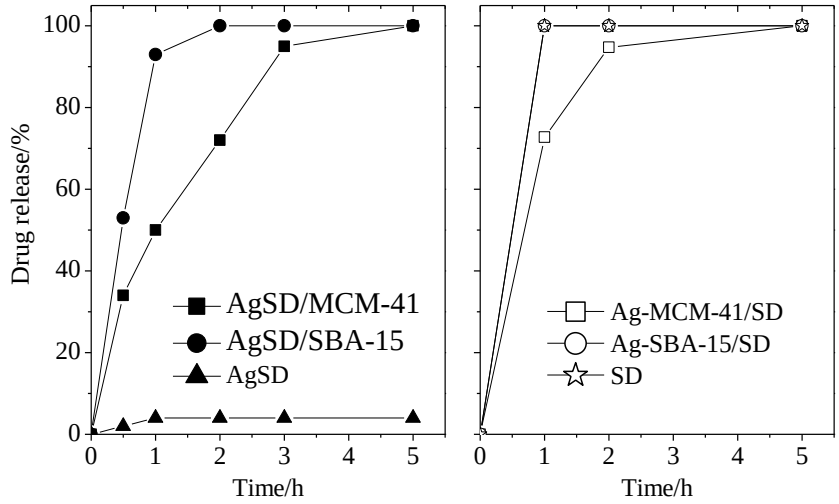

Figure 60 *In vitro* release of SD from Ag-MCM-41 and Ag-SBA-15 carriers and AgSD release from MCM-41 and SBA-15 samples

However, non-loaded sulfadiazine showed similar release profile to that of loaded into Ag-SBA-15 carrier. Adsorption of sulfadiazine on Ag-modified MCM-41 carrier resulted in a prolonged release. The improved solubility of AgSD and the reduced burst release of both SD and AgSD on MCM-41 can be advantageous in the development of topical drug delivery system for wound treatment.

The stability of the drug delivery system was checked by exposing the samples to direct daylight for 5 days. Repeated drug delivery experiments did not show significant differences between the parent and irradiated samples.

Our silver-containing samples were tested against the most commonly found burn wound bacteria such as strains of ATCC *Escherichia coli* 8739, *Staphylococcus aureus* 6538, *Pseudomonas aeruginosa* 9027, *and Streptococcus pyogenes* 19615. Results of antibacterial investigations are summarized in Table 26, and some example photos of agar plates are shown in Fig. 61.

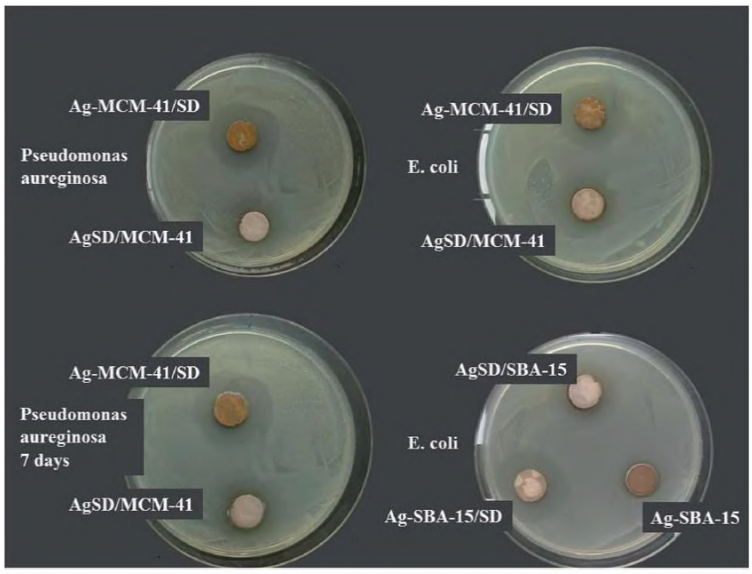

Figure 61 Photos of agar plates inoculated with *Escherichia coli* (ATCC 8739) and *Pseudomonas aeruginosa* (ATCC 9027) illustrating the inhibition zones for Ag-MCM-41/SD, AgSD/MCM-41, Ag-SBA-15/SD and AgSD/SBA-15 samples investigated by the pressed discs method

Silver-containing nanoporous silica materials and SD itself have some inherent antibacterial properties. Therefore, these samples were investigated as control ones. The silver-containing nanoporous silica control samples demonstrated identical or smaller inhibition zones than the SD-loaded varieties. SD-loaded pure silica MCM-41 showed no antimicrobial effect, except for *E. coli*. However, in this case, there was no completely clear inhibition zone, only a less translucent one. Ag-SBA-15 based samples exhibited smaller inhibition zones than Ag-MCM-41 ones, probably in correlation with the higher silver dissolution rate of the latter one (4.7 mg/g for Ag- MCM-41 compared to 2.9 mg/g for Ag-SBA-15).

Table 26 Antibacterial activity of Ag-MCM-41, Ag-SBA-15 and SD loaded MCM-41 samples and SD loaded formulations

Bacterial strains	Zone of inhibition (mm)					
	Ag-MCM-41		Ag-SBA-15		MCM-41/SD	
	pellet	susp.	pellet	susp.	pellet	susp.
Escherichia coli ATCC 8739	1	5	1+1	1	14[a]	14[a]
Staphylococcus aureus ATCC 6538	3	5.5	1	2	0	0
Pseudomonas aeruginosa ATCC 9027	2	2	1+2	2	0	0
Streptococcus pyogenes ATCC 19615 *(PPLO)*	3	7	3.5	6	0	0

Bacterial strains	Zone of inhibition (mm)							
	Ag-MCM-41/SD		Ag-SBA-15/SD		MCM-41/AgSD		SBA-15/AgSD	
	pellet	susp.	pellet	susp.	pellet	susp.	pellet	susp.
Escherichia coli ATCC 8739	1+7	1+6	1+7	1+7	1+7	1+10	1.5+6.5	2+5
Staphylococcus aureus ATCC 6538	1.5	1.5	1	1	1	1	2	2
Pseudomonas aeruginosa ATCC 9027	1+7	1+6	1.5+4.5	1.5+5	1+7	0.5+7.5	1+6	1.5+5
Streptococcus pyogenes ATCC 19615	5	5	3	3.5	4	3	5	5

[a] Not totally clean inhibition zone

SD-loaded Ag-MCM-41 and Ag-SBA-15 samples showed similar inhibition zones, in some cases larger ones than that of AgSD-loaded pure silica. According to the photos of agar plates (not shown), when the diameter of inhibition zones was identical the outer, less transparent zone was much clearer for the Ag-MCM41/SBA-15/ SD samples compared to AgSD-loaded MCM-41 and SBA-15 ones. These results indicate that SD-loaded silver nanoporous silica samples are equally or even more effective in bacterial inhibition than AgSD.

Moreover, our experiments supported the well-known fact that ionic silver, a heavy metal with relatively broad antibacterial spectrum, has stronger effect on antibacterial activity than pure SD. The beneficial effect of silver is so strong that agar plates showed the original inhibition zones even after 7 days of incubation (Fig. 61).

It was shown that silver modified MCM-41 and SBA-15 materials are suitable carriers for drugs such as sulfadiazine to design a drug-delivery system with improved bioavailability and antibacterial activity. It was found that nanoporous silica materials can be easily modified by direct or post-synthesis methods to prepare silver nanoparticles inside the channels or on the outer surface of the particles. By these methods, the amount of incorporated silver can be controlled in a relatively wide concentration range between 0 and 10 wt%. The silica host can stabilize these silver nanoparticles and water-soluble silver ions are released. The empty channels of the silica support are suitable for the storage of a relatively high amount of drug molecules. We demonstrated for the first time that, comparing the SD release and antimicrobial properties, AgSD can be effectively replaced by SD-loaded Ag-MCM-41 or Ag-SBA-15 materials. Adsorbing AgSD on pure nanoporous silica materials significantly improved its water solubility.

3.2.1.7. Solid-state encapsulation of Ag and sulfadiazine on zeolite Y carrier

The usage of zeolites as scaffolds for drug delivery could be based on the presence of charge compensating counter-ions, usually H^+, which impart unique ion-exchange properties. The promising results for AgSD delivery from mesoporous silica provoked us to study the zeolite as a carrier for simultaneous delivery of Ag^+ and SD. A solid dispersion method was developed for the encapsulation of two medical constituents, such as SD and Ag, and it was compared with the more popular solvent deposition approach in AgY and Y zeolite. The physico-chemical properties and the SD release kinetics in pH = 5.5 phosphate buffer over the H- and Ag-form Y zeolite carriers (Scheme 8) were also evaluated.

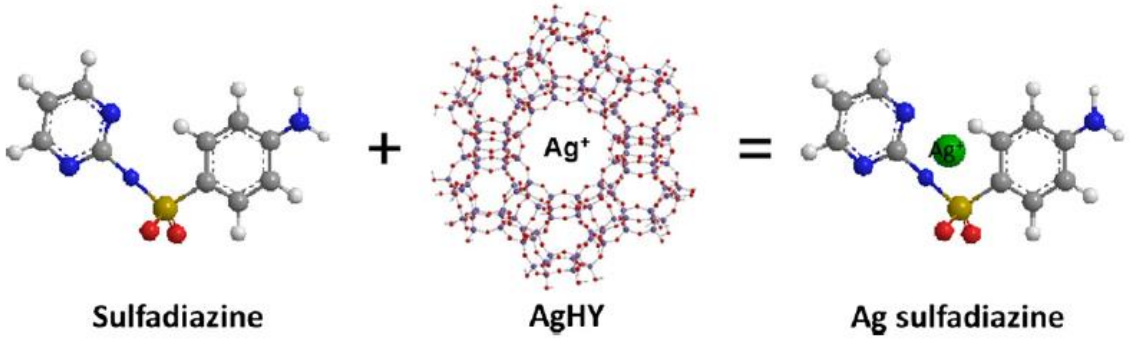

Scheme 8 Ag-sulfadiadine Y zeolite formulation

SEM pictures of the parent zeolite and its SD loaded formulation show the formation of aggregates from smaller zeolite particles as a result of vibrational ball mill mixing of SD with the zeolite. XRD analysis gives more detailed information about the crystallinity of the zeolite and SD structures (Fig. 62). In accordance with the decreased intensity of the strongest SD reflections of the grinded compound (Fig. 62 A), it can be concluded that milling has led to substantial nanosizing of SD. The strongest XRD lines of the drug are clearly visible when it is deposited on the H-form of the zeolite both by solid-state or in solution (Fig. 62 B). The intensity of SD reflections corresponds to the amount of loaded drug (1:0.8 = zeolite:SD ratio). In the case of solid state mixing the intensity of zeolite reflections is proportional with the amount of the zeolite in the delivery system, but it significantly decreases as a result of SD deposition in solution. Such partial crystallinity loss of the parent HY carrier not only takes place when SD is loaded by solution method (Fig. 62 B), but also during the solid-state ion exchange procedure with $AgNO_3$ upon AgY(SS) preparation (Fig. 62 C). The additional solid-state loading with SD over Ag-modified zeolite resulted in further amorphization of the carrier. Obviously, the intense mechanical grinding upon the subsequent solid-state encapsulation of Ag as well as of SD over the parent zeolite, results in loss of crystallinity not only for the drug but also for the zeolite carrier as the decrease of its X-ray reflections reveals (Fig. 62 C).

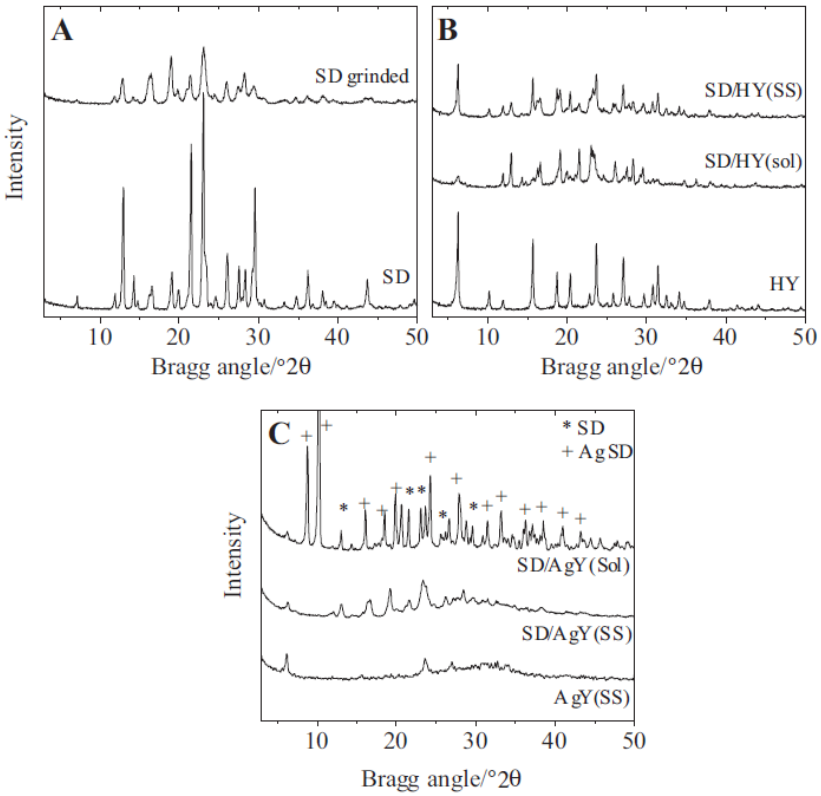

Figure 62 XRD patterns of SD before and after grinding (A), SD/HY(Sol), SD/HY(SS) and parent HY zeolite (B), and SD loaded on AgY in solution and in solid-state (C)

Compared to the zeolite-destructive liquid SD deposition over the unmodified HY carrier, the zeolite structure does not suffer further crystallinity collapse when SD is loaded by the latter method. The almost unchanged reflections of the zeolite support, small amount of SD and formation of higher amount of AgSD can be observed (Fig. 62 C). It is possible that AgSD is also formed in SD/AgY(SS) (and not in such a small amount), but invisible by XRD because of its fine distribution in the pores, in contrast to SD/AgY(Sol), in which AgSD is formed on the AgY crystallite surface.

TEM investigations give some indication about the state of the introduced silver. In Fig. 107 representative TEM images of AgY(SS) and both SD loaded Ag-modifications are presented. According to the picture, metal particles have been formed on the AgY(SS) surface (Fig. 63 A).

This means that after the applied SSIE only part of the silver is kept in exchangeable positions. The remaining Ag^+ has most probably been oxidized to Ag_2O and/or subsequently reduced to Ag^0 upon preparation. The FT-IR and elemental analysis data show 95% Ag exchange level and low crystallinity Ag_2O phase detected by XRD analysis. We assumed the occurrence of the following reverse reaction:

$$2ZO\text{-}H^+ + Ag_2O \leftrightarrow 2ZOAg^+ + H_2O$$

generating simultaneously Ag^+ and Ag_2O nanoparticles depending on the temperature and the environment. Thus, one can conclude that Ag cations and metal/oxide Ag particles exist together over our AgY(SS) formulation prepared by the solid dispersion method. Small Ag nanoparticles with 5-10 nm size as well as larger aggregates (about 50 nm), are visible in Fig. 63 A. Loading the Ag-zeolite with sulfadiazine by the solvent or the solid-state method does not change significantly the TEM image (Fig. 63 B and C).

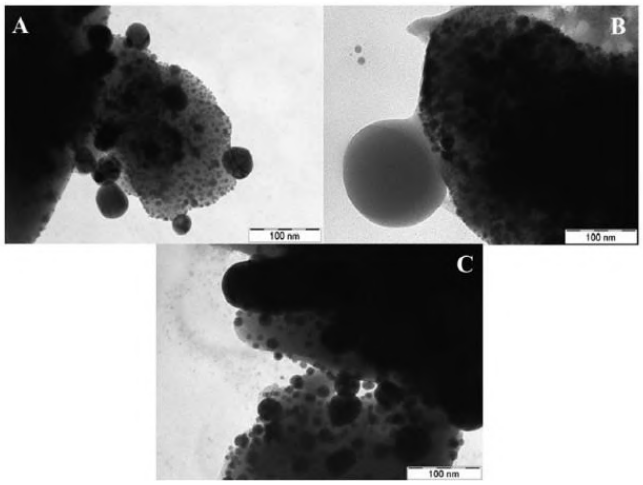

Figure 63 TEM images of AgY(SS) (A), SD/AgY(SS) (B) and SD/AgY(Sol) (C) samples

FT-IR spectra in the hydroxyl stretching region can prove the occurrence of an exchange reaction between the zeolite protons and silver, generating cationic silver upon the SSIE procedure. The observed intensity decrease of the band at 3640 cm^{-1} and the disappearance of the 3540 cm^{-1} band of the AgY(SS) sample, related to the typical low and high frequency υ_{OH} stretching vibrations of Y zeolite framework (Sen et al., 1998), is an indication that such SSIE has occurred upon the high temperature treatment of $AgNO_3$ and HY mixture. It appears that a substantial part of the OH groups of the carrier has been consumed by encapsulation of Ag in cationic positions (Fig. 64).

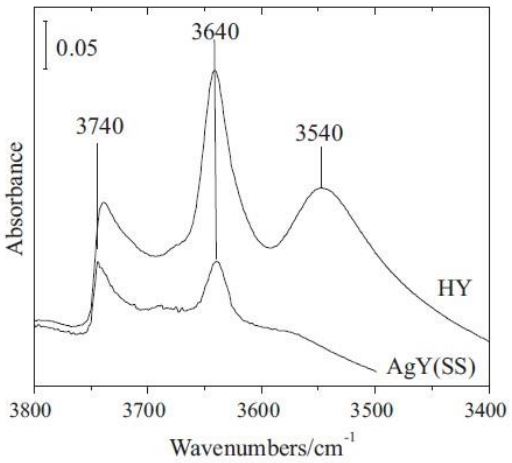

Figure 64 FT-IR spectra of parent HY and Ag modified AgY(SS) sample, prepared by SSIE

ATR FT-IR spectra (Fig. 65) of both HY and AgY supports show the band shift of aromatic ring and pyrimidine moiety vibrations indicates interaction of the benzene (pyrimidine) ring with the zeolite framework.

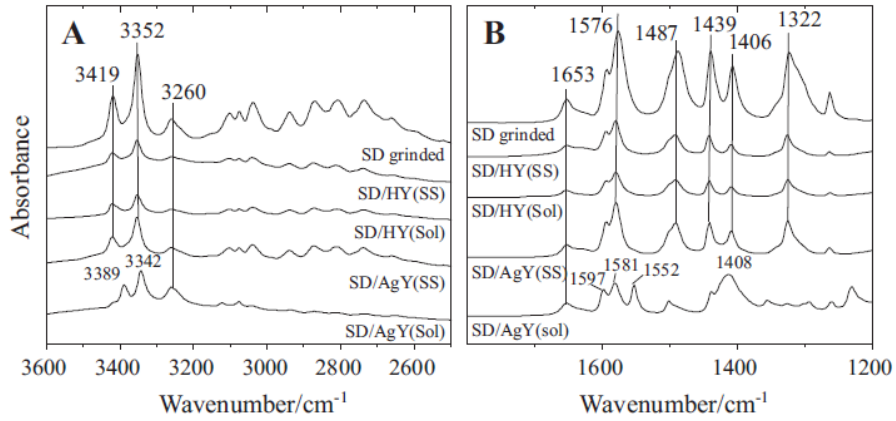

Figure 65 FT-IR spectra of SD supported by solid or by solvent deposition method on unmodified and Ag-modified zeolite carriers in the 3500-3000 cm^{-1} region (amine and sulfonamide groups) (A), and in the NH_2 deformation, aromatic ring vibration and pyrimidine moiety (1200-1700 cm^{-1}) region (B)

For AgY sample loaded with SD by liquid deposition, moreover, bands characteristic for AgSD can be witnessed at around 1597, 1581 and 1552 cm^{-1}. The same phenomenon was observed also in the case of SD loaded AgMCM-41 samples, which is described above. The band at 1552 cm^{-1} is present in the spectra of silver sulfadiazine (AgSD) compound and is assigned to the shifted ring vibrations of pyrimidine by the presence of Ag^+. The appearance of these bands can be due either to the interaction of zeolitic silver cations or metallic silver particles with the adsorbed SD resulting in the formation of AgSD. To derive AgSD was actually our intention and final goal, viz. to test the ability to get AgSD-loaded formulation overcoming the extremely low solubility of this therapeutic compound.

Thermogravimetric analysis (TG) has been used to follow the decomposition of $AgNO_3$ upon the process of silver encapsulation by SSIE (not shown), as well as for quantification of the amount of loaded SD. TG analysis of the SD loaded formulations showed that with the exception of SD/AgY(Sol), the determined amount of the adsorbed drug corresponded roughly to the added amount (in 87-100%) prepared either by solid-state or by solvent method. However, only about 70% of the loaded SD is found to be adsorbed over AgY, when SD was loaded in solution (Fig. 66 A). It should be noted here that comparing the DTG profiles of the drug decomposition, the low temperature peak of this sample is split with T_{max} values of 513 K and 523 K. This also indicates that another compound that could be AgSD has been formed upon the procedure of SD deposition as a result of an ion exchange occurred between the Ag ions of the zeolite and the protons of SD. This Ag-containing product should be eliminated, together with the remaining SD, upon heating.

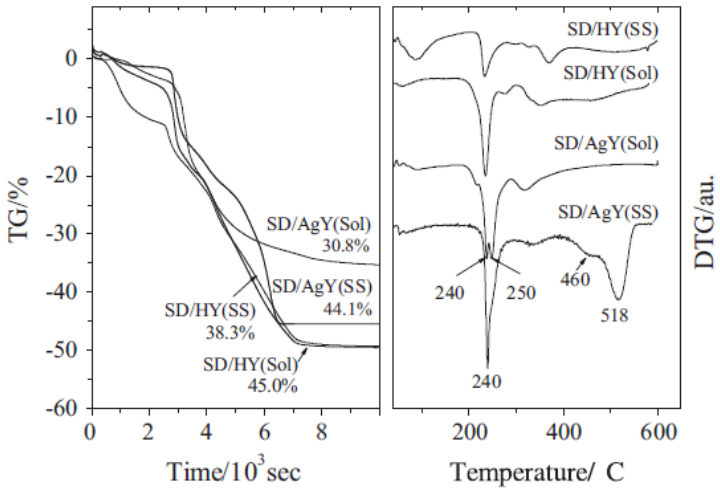

Figure 66 TG (A) and DTG (B) profiles of SD-loaded parent and Ag-modified zeolite Y by solid dispersion and solvent deposition method

The assumption about occurrence of ion exchange phenomena upon SD loading but only in liquid phase over the Ag-modified zeolite is in agreement with the FT-IR data (Fig. 66 B) showing a band at 1552 cm^{-1} indicating formation of AgSD. Considering the TG decomposition profiles of the SD loaded materials it could be inferred that the presence of silver on the support strongly influences the interaction of the drug molecule with the zeolite carrier and respectively its way of decomposition. The TG profiles of the high temperature SD removal from the H-form of the zeolite are similar regardless of the method of its deposition, solvent or solid-state. In the case of Ag-modified carriers, however, they are quite different. When solvent deposition method is applied, the dissolved SD can react with the Ag^+ surface cations or with the Ag^+ released to the solvent. In this latter case superficial precipitation of AgSD occur on the zeolite particles and its decomposition at heating, together with that of SD, would be faster and easier (Fig. 63). Also, the presence of a high amount of finely dispersed silver nanoparticles (see TEM results, Fig. 63) on the surface of the zeolite crystallites may block the entrances of the zeolite pore system and prevent the access of SD into it, thus reducing the adsorption capacity of this preparation. It should be noted here that when zeolite materials are used as carriers, the molecular sieve effect should not be neglected. When Ag has been incorporated into cationic framework positions, a decreased size of the zeolite channels is to be expected as well. The latter will cause, in presence of the solvent molecules in particular, diffusion restrictions for the drug occlusion. Thus, when the drug is loaded by solvent deposition method, only partial SD loading, accompanied by superficial AgSD formation would take place as also the TG curve of SD/AgY(Sol) has indicated.

Upon the first silver deposition step by solid-state ion exchange, a loss of zeolite crystallinity has occurred, which has reduced its further adsorption ability during the solvent method of SD loading. These effects could also be the reason for the observed lower amount of loaded drug (Fig. 66 A), for the weaker interaction with the surface, and for the lower decomposition temperature of the active substance. By applying the solid-state deposition method the above mentioned disadvantages can be overcome.

The concentration of sulfadiazine released in phosphate buffer with pH = 5.5 as a function of time was determined by UV-Vis spectrophotometry at a wavelength of 262 nm. The applied release media simulated the physiological conditions for release of dermatological formulations. In Fig. 67 the delivery profile of the grinded sulfadiazine substance is compared with that of SD loaded (in solid-state or in solution) parent HY zeolite as well as of its Ag-modification. As the results show, the whole amount of the unsupported grinded sulfadiazine is delivered practically immediately. A steep release (over 90% of the loaded drug) for the first hour is registered for the drug encapsulated into both preparations of the unmodified carrier. Complete SD release from the formulations with the H-form of Y zeolite was reached in 2 h.

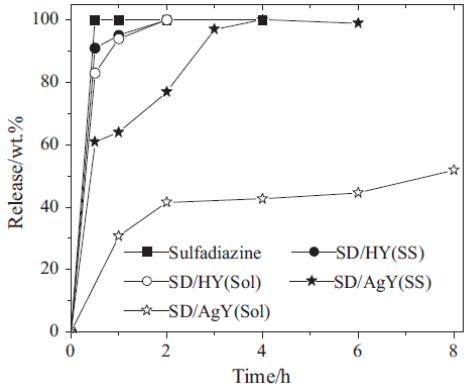

Figure 67 Sulfadiazine release in pH = 5.5 buffer from the parent and the Ag-modified zeolite Y loaded with SD by solid dispersion and by solvent deposition method

The release profile of SD from the silver zeolites is quite different and prolonged (Fig. 67). Almost 3 h are necessary for the gradual delivery of the drug from the sample prepared by solid-state to be completed. This effect is consistent with the TGA result illustrating that much higher temperature is needed for decomposition of the loaded drug by this method. Drug occlusion into the pores of the support and stronger drug-framework silver ions interaction could be the reason for its extended release. By SD solution deposition method over Ag-modified Y zeolite, it can be suggested that part of the silver counterions are released in the solvent and react with the drug. Thus, insoluble AgSD is precipitated on the outer surface of the support as XRD and FT-IR (Figs. 62 and 65) results have indicated and incomplete SD release is observed for the as-prepared formulation.

A successful simplified procedure for the preparation of a dual Ag-sulfadiazine drug delivery system has been developed using zeolite Y as a carrier. To the best of our knowledge this is the first attempt to introduce both Ag and SD in a Y zeolite matrix by combination of solid-state ion exchange with silver and dry mill mixing with sulfadiazine. Silver introduced into the HY carrier by solid-state ion exchange has been encapsulated in both states, viz. as Ag^+ cations and as Ag^0/Ag_2O nanoparticles. The method of subsequent SD loading does not influence its release kinetics when the H-form of the zeolite is used as a carrier and no noticeably sustained release can be achieved compared to pure SD. The amount of deposited SD, the nature of its interaction with the carrier as well as the release kinetics is influenced, however, by the presence of silver. These characteristics depend also on whether the SD loading procedure is performed in solid-state or in liquid. When SD is loaded in solution, a part of the zeolite silver ions is released and interacts with SD, forming AgSD and restricting the bioavailability of the formulation. By solid-state SD deposition, the reaction between the drug and the silver is limited within the limits of an inter-atomic interaction, and total but prolonged drug release occurs, compared to the unmodified zeolite. Thus, perspective drug release systems for topical use in burn injuries can be easily prepared by the latter procedure of solid-state SD encapsulation into Ag-modified zeolite Y.

3.2.2. Development of DDS based on hybrid mesoporous silica-polymer carriers

3.2.2.1.New method for preparation of delivery systems of poorly soluble drugs on the basis of functionalized mesoporous MCM-41

The development of drug delivery systems to specific areas of the GIT (colon) is of great interest, as it is aimed at treating common diseases such as ulcerative colitis, Crohn's disease, some infections and constipation that require local treatment. The application of drugs for administration to the gastrointestinal tract in mesoporous silicates and their coating with a suitable polymeric polyelectrolyte complex can reduce its premature release before reaching the target site and there ensure its controlled release. Mesalazine (Mes) is used to maintain the remission of ulcerative colitis and to treat Crohn's disease. The main problem in its application for the treatment of inflammatory bowel disease is its low solubility and stability under physiological conditions in the stomach. The main task in developing a suitable delivery system is to achieve selective delivery in the intestine in sufficient concentration and to avoid its premature release in the stomach. Solid state reaction is applied for the loading of the poorly soluble drug mesalazine (Scheme 9) in mesoporous MCM-41 silicas functionalized by amino and by amino and carboxylic groups. Alginate coating of the mesalazine loaded MCM-41NH_2COOH was applied in order to modify the release properties of the obtained delivery system.

The two step modification procedure resulted in a significant specific surface area decrease for MCM-41NH_2COOH. Also, narrower pore sizes were detected (Table 27). The modification by amino and amino/carboxylic groups did not influence the spherical morphology of MCM-41 materials.

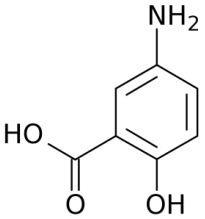

Scheme 9 Mesalazine molecule

Table 27 Physicochemical properties of the parent, functionalized, mesalazine loaded and alginate coated spherical MCM-41 samples

Samples	a_o[a] (nm)	S_{BET} (m^2/g)	pore diameter[b] (nm)
MCM-41	4.3	1175	2.7
MCM-41Mes	4.3	227	2.6
MCM-41NH_2	4.2	1152	2.52
MCM-41NH_2Mes	4.2	315	2.52
MCM-41NH_2MesAlg	4.2	-	-
MCM-41NH_2COOH	4.1	473	1.96
MCM-41NH_2COOHMes	4.1	50	n.d.
MCM-41NH_2COOHMesAlg	4.1	-	-

[a] cell parameter ($a_o=2d_{100}(3)^{-1/2}$), [b] Pore diameter calculated by BJH method

ATR FT-IR method was used to investigate the interaction between the mesalazine molecule and the modified MCM-41 carriers after its deposition. The presence of amino and carboxylic groups was evidenced by ATR FT-IR measurements.

The FT-IR spectrum of mesalazine shows stretching vibration bands characteristic of carboxylate ($-COO^-$) groups at 1573, 1445 and 1350 cm^{-1} and a band at 1555 cm^{-1}, which can be attributed to the protonated form of amino groups, e.g. $-NH^+$. The FT-IR spectra of MCM-41NH_2Mes and MCM-41NH_2COOHMes samples are similar to those of the pure mesalazine indicating no interaction between the functionalized carriers and the mesalazine molecule. Despite the fact that nitrogen physisorption data show that mesalazine is confined in the pores, it seems that it cannot react with the functional groups.

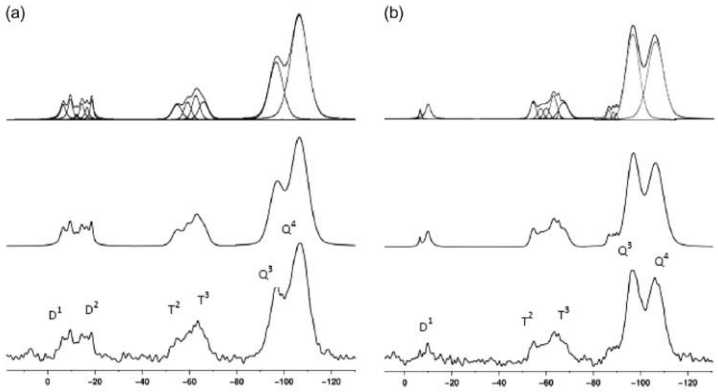

Figure 68 ^{29}Si NMR spectra of MCM-41NH_2COOH (a) and MCM-41NH_2(b).
From bottom to top: experimental spectra, simulated spectra representing the sum of the deconvoluted spectral patterns and individual lines as a result of spectra deconvolution

The incorporation of organic functional groups (NH_2 or NH_2/COOH) was investigated by ^{29}Si NMR (Fig. 68). In the spectra of the modified samples three peaks are registered, at -106, -96 and -89 ppm, which can be ascribed to Q^4, Q^3 and Q^2 species of the silica framework [Q^n = $Si(OSi)_n(OH)_{4-n}$, n =2-4] (Scheme 10).

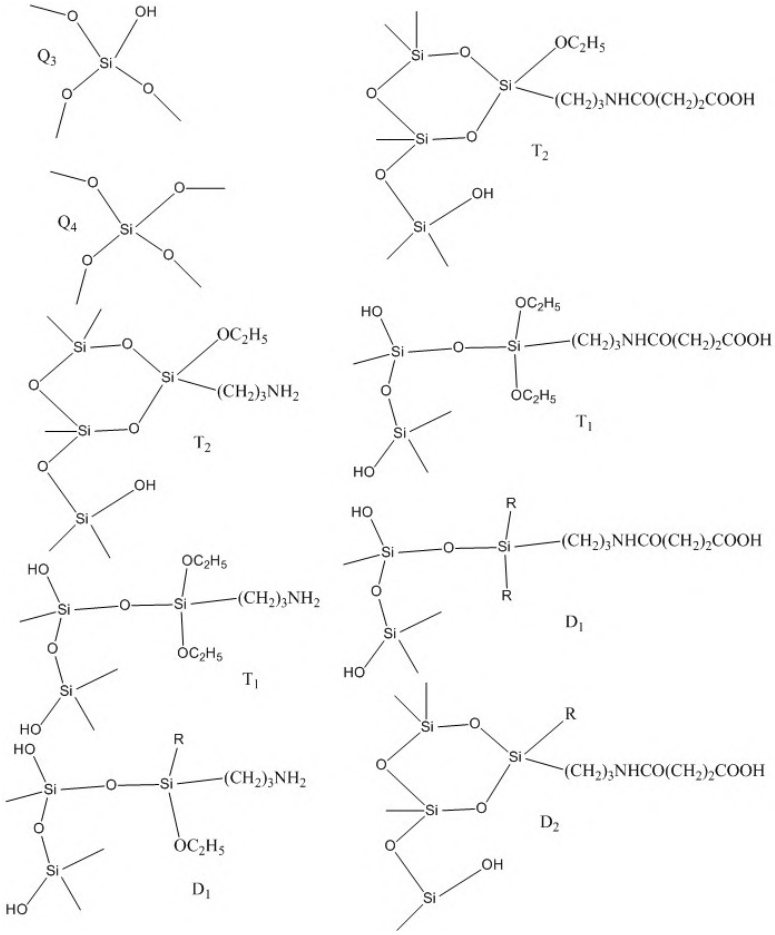

Scheme 10 Structure of different silicon-containing moieties presented on the MCM-41NH_2 and MCM-41NH_2COOH silicas

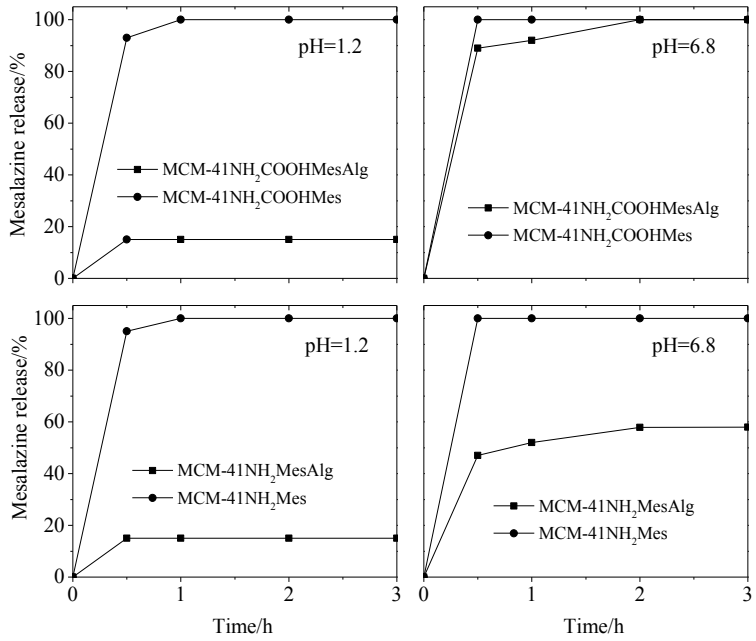

Figure 69 Release profiles of mesalazine loaded MCM-41NH_2 and MCM-41NH_2COOH and alginate coated drug delivery systems

The appearance of the T^2 and T^3 peaks is an indication for the successful modification. The ^{29}Si spectra also display signals in the region between -6 and -19 ppm characteristic for D_1 and D_2 species. The presence of these signals indicates that the incorporation of the organic linker is accompanied by disruption of the silica mesoporous structure. This process is more pronounced in MCM-41NH_2COOH material since the amount of D^1 and D^2 species is higher as evidenced by its ^{29}Si spectrum (Fig. 69). The T/(T+Q) ratio is a quantitative measure of the functionalization level in the modified silica materials (Table 28). Calculations show that the modification is equally successful in both cases, however the fraction of D^1 and D^2 species is much higher in MCM-41NH_2COOH material. The larger extent of silica framework deterioration in MCM-41NH_2COOH material is also in agreement with the observed much lower BET surface area compared to MCM-41NH_2.

Table 28 ^{29}Si NMR data for the functionalized samples

Samples	Q^4	Q^3	Q^2	T^3	T^2	D^2	D^1	T/(Q+T)	D/(Q+D)
MCM-41NH_2	40.3	35.5	2.3	14.8	3.1	-	3.9	18.8	5.0
MCM-41NH_2COOH	48.0	21.4	-	11.2	5.6	7.3	6.5	19.5	16.5

The ^{13}C NMR spectra of MCM-41NH_2 and MCM-41NH_2COOH loaded with mesalazine are compared with the spectrum of pure mesalazine. No chemical shift changes of the mesalazine carboxylic group signal (175 ppm) can be observed in the spectra. These results also support that there is no interaction between the drug molecules and the carrier and are in good accordance with FT-IR results.

The functional groups, mesalazine and alginate content of the samples were quantified using thermogravimetric method. The amount of propylamino and propylamino/carboxylic groups connected on the surface of MCM-41 carrier was 10.7 wt.% and 19.6 wt.%, respectively. The weight losses from alginate layer of MCM-41NH_2Mes and MCM-41NH_2COOHMes was 7 wt% and 5 wt%, respectively.

Drug release was faster from non-coated particles independent of their functionalization. In both buffers the release was completed in 1 h (Fig. 69). However, the process was slower after coating of the particles with sodium alginate. Significant decrease of the released drug amount was achieved in acid buffer that regarding physiological conditions suggested slow release of mesalazine in gastric fluid. This behavior was observed for both types of functionalized coated particles (MCM-41NH_2 and MCM-41NH_2COOH) where approximately 15% of the drug was released for 2h (Fig. 69). This is an important fact, taking into account that for the buffer. In particular, 100% mesalazine was released from MCM- 41NH_2COOHAlg particles in 2 h, and approximately 60% from MCM-41NH2Alg particles for the same time. In both cases, the profiles showed that the release rate from the coated particles was slightly lower compared to non-coated ones. Therefore alginate coating reduced the initial burst release that is frequently observed for mesoporous silica particles. In addition, coating made it possible to achieve specific delivery at the desired region of the gastrointestinal tract, in the present case the small intestine.

The cytotoxicity of free mesalazine and mesalazine loaded nanoparticles was investigated in HT-29 cells. Our study revealed dose dependent cytotoxicity of free mesalazine indicating direct cell damage by free mesalazine even at the lowest applied concentration of 20 μg/ml. Such cytotoxicity may lead to mucosistis, and therefore be at least in part responsible for the appearance of mesalazine frequent adverse drug reactions like diarrhea, stomach pain, nausea and vomiting. The incorporation of the drug into both functionalized mesoporous particles did not

change this effect. However, the post-coating of nanoparticles with sodium alginate led to reduced cytotoxic effect of mesalazine even at the highest concentration (80 μg/ml).

MCM-41 silica with spherical morphology and small particle sizes (100 nm) was synthesized and modified by post-synthesis method with amino and amino/carboxylic groups. Mesalazine, a drug molecule with amino and carboxylic groups, can be successfully introduced into the channels of MCM-41 by solid-state reaction. Appropriate surface functionalization of silica particles provides the opportunity for further polymer coating. The post-coating of the bifunctional (amino and carboxylic) nanoparticles with sodium alginate revealed the capacity to achieve different drug release rates depending on the pH value of the release medium. In addition to that, reduction of the mucosal damage by mesalazine could be achieved after polymer coating of the nanoparticles.

3.2.2.2. pH-dependent delivery of mesalazine from polymer coated and drug-loaded SBA-16 systems

In previous investigations we developed a solid state method for loading of mesalazine into the mesoporous support functionalized by different organic groups. The next step in the development of appropriate delivery system with mesalazine is the optimization of the loaded mesalazine content and its delivery in the target place. For this purpose, a mesalazine delivery system has been developed with two polymer layers, the first layer using a pH sensitive polymer (Eudragit S), and the second polymer layer (Eudragir RL) achieving overall control of the drug release. Wet milling in acidic medium is applied for the loading of different amounts of mesalazine in spherical mesoporous SBA-16 silicas functionalized by amino groups. A single coating with Eudragit S or double coating with Eudragit S and Eudragir RL was performed in order to modify the release properties of the obtained delivery systems.

Fig. 70 shows high angle XRD patterns, where the presence of crystalline mesalazine phase on the SBA-16NH_2 is evidenced. This shows that a part of mesalazine can be found on the outer surface of the silica particles. The amount of mesalazine deposited on the outer surface depends on the applied drug:carrier ratio.

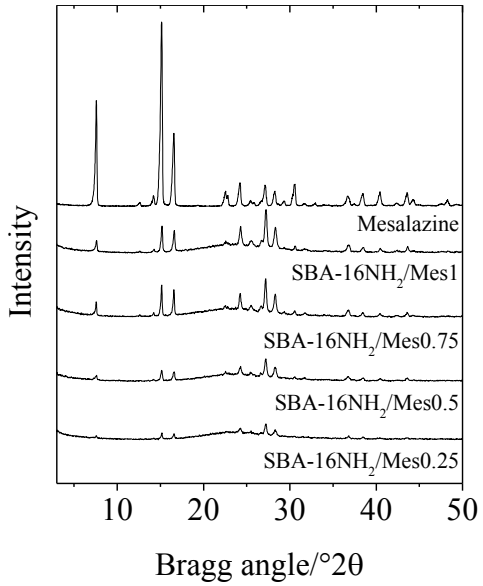

Figure 70 XRD patterns of SBA-16NH_2 carrier and the mesalazine loaded formulations

The highest amount of crystalline mesalazine is registered for SBA-16NH_2Mes0.75 and SBA-16NH_2Mes1 samples. However, even when the drug:carrier ratio is 0.25, a small part of mesalazine is deposited on the outer surface.

The isotherms of the parent and the amino modified SBA-16 are typical IV type ones (IUPAC classification) with steep capillary condensation steps and apparent hysteresis loops that are characteristic for high quality 3D cage-like materials with uniform pore entrances (Table 29). The modification of SBA-16 with amino group resulted in a decrease of specific surface area, pore size and total pore volume, evidencing that organic groups were fastened inside mesopores. It can clearly be observed that the presence of mesalazine in SBA-16NH_2 leads to a marked change in the shape of the hysteresis loops. The hysteresis loop of all loaded samples is closing down at lower relative pressure values in comparison to the parent support (SBA-16), which indicates that the pores are partially narrowed due to the drug loading. The increase of the amount of the deposited drug on SBA-16NH_2 also resulted in a decrease of specific surface area, and total pore volume, confirming the loading of mesalazine within the mesopores. (Table 29). Furthermore, mesalazine is present also on the external surface of the support, which is also evident by XRD data.

Table 29 Textural properties of the parent, functionalized and mesalazine loaded SBA-16 samples

Samples	S_{BET}[a] (m^2/g)	pore diameter[b] (nm)	total pore volume[c] (cm^3/g)
SBA-16	849	5.2	0.56
SBA-16NH_2	755	5.0	0.45
SBA-16NH_2Mes0.25	374	5.0	0.25
SBA-16NH_2Mes0.5	236	5.0	0.16
SBA-16NH_2Mes0.75	144	4.9	0.11
SBA-16NH_2Mes1	68	5.1	0.05

[a]S_{BET}, the BET surface area; [b]Pore diameter mesopore diameters at the maximum of the BJH pore size distribution. [c]V_t, total pore volume evaluated from adsorption isotherm at the relative pressure about 0.96.

ATR FT-IR method was used to investigate the interaction between the mesalazine molecule and the modified SBA-16 carrier after its deposition. The presence of amino groups was evidenced by the appearance of 1540 cm^{-1} band on functionalized SBA-16 carrier (not shown). Crystalline mesalazine is in a zwitterionic form as 5-aminosalicylate (Scheme 11). This is reflected by the dominant carboxylate bands at 1575, 1445 and 1349 cm^{-1} and by the presence of a shoulder of NH_3^+ bending vibration at 1550 cm^{-1} in the spectrum of solid mesalazine (Fig. 71). In the spectrum of SBA16NH2Mes1 sample (Fig. 71) the carboxylate bands are shifted toward higher wavenumbers (from 1575 to 1579 cm^{-1}, from 1445 to 1448 cm^{-1} and from 1349 to 1353 cm^{-1}) and the band belonging to -NH_3^+ deformation is suppressed (shoulder at 1550 cm^{-1}). These spectral variations suggest that the hydrogen bond network in the mesalazine crystal structure might be diminished. Moreover, the wavenumber shift of mesalazine carboxylate bands depend on mesalazine loading: the lower the mesalazine content the higher the wavenumber shift toward higher values. However, the spectrum of SBA16NH_2Mes0.75 sample resembles to that of pure mesalazine regarding the shoulders around 1550 cm^{-1} and 1344 cm^{-1}. It seems that some mesalazine could remain in zwitterionic form with hydrogen bond network. Most probably the use of acid buffer results in a better solubility of mesalazine by diminishing the hydrogen bond network of the zwitterionic structure (Scheme 11). Since no bands for protonated carboxylate (υ(C=O) at 1730-1710 cm^{-1}) can be found in the SBA16NH_2Mes spectra probably new, weak interactions might form between mesalazine COO- and the amino groups of functionalized SBA-16. This effect could be explained by the formation of chloride form of mesalazine during the loading procedure, which prevents the drug-drug interactions. The lack of protonated carboxylate groups indicates also that crystalline chloride (Scheme 11) form of mesalazine is not present. This is confirmed by XRD results showing only the 5-aminosalicylate form in the samples.

The initial SBA-16, SBA-16NH_2 and SBA-16NH_2Mes0.25 and SBA- 16NH_2Mes1 samples were investigated by ^{29}Si NMR (Fig. 72).

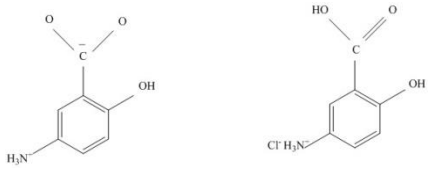

Scheme 11 Chemical structure of 5-ammosalicylate and 5-aminosalicylic chloride

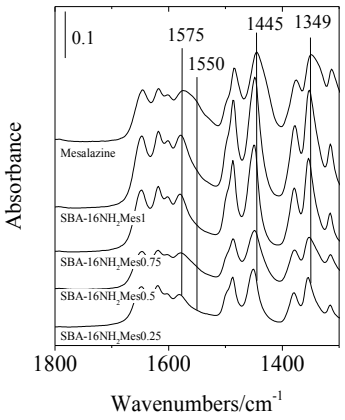

Figure 71 ATR-FTIR spectra of mesalazine-loaded samples

In the spectrum of the spherical nanosized SBA-16 sample three peaks are registered, at -106, - 96 and - 89 ppm, which can be assigned to Q^4, Q^3 and Q^2 species (Skorupska et al., 2014; Popova et al., 2014) of the silica framework [Qn = Si(OSi)n(OH)4_n, n = 2-4]. Upon amino modification the disappearance of the Q^2 band and the increased intensity of Q^3 and Q^4 bands are observed.

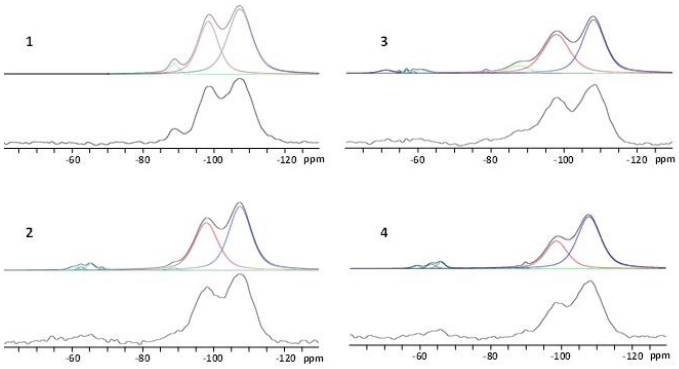

Figure 72 ^{29}Si NMR spectra of initial SBA-16 (curve 1), SBA-16NH_2 (curve 2) and SBA-16NH_2Mes0.25 (curve 3) and SBA-16NH_2Mes1 (curve 4) samples. The deconvoluted spectral patterns and the individual spectral lines are given above each experimental spectrum

Samples	SBA-16	SBA-16NH_2	SBA-16NH_2Mes0.25	SBA-16NH_2Mes1
Q^2+Q^3/Q^4 (%)	40	44	46	33

^{29}Si spectra were subjected to deconvolution in order to quantitatively analyze the relative fractions of the different species Q^2, Q^3, Q^4 after the functionalization and drug loading processes (Fig. 72).
The Q^2+Q^3/Q^4 ratio is 40% for the initial SBA-16 silica and 44% for the functionalized SBA-16NH_2 material. The calculated data are typical for such a type of mesoporous silica materials (Zhao et al., 1998, 2012). The mesalazine loading resulted in an additional increase of this ratio to 46% for the sample, containing the smallest amount of mesalazine (SBA-16NH_2Mes0.25). An opposite tendency was observed for the sample with the highest content of mesalazine (SBA- 16NH_2Mes1), where a significant decrease of Q^2+Q^3/Q^4 ratio to 33% was detected. The larger fraction of Q^4 which is an indication of increased crosslinking could be explained if we assume that the higher amount of mesalazine favors the drug-drug interactions rather than drug-silica carrier interactions. These results are in agreement with the ^{13}C NMR data where larger chemical shift changes are observed for the sample with lower amount of the drug as compared to the spectrum of the pure mesalazine. The NMR findings are in good agreement with ATR FT-IR results as well.
The functional group, mesalazine and polymer content of the samples were quantified using thermogravimetric method. The amount of propylamino groups connected to the surface of SBA-16 support was 8.5 wt.%. The TG analysis determined the actual amount of drug in the carrier after correcting the curves by water and aminopropyl content for SBA-16NH_2Mes samples. The mesalazine contents of the samples are presented in Table 30.

Table 30 Chemical composition of the polymer coated mesalazine loaded SBA-16 samples

Samples	mesalazine[a] (%)	decomposed mesalazine up to 540 K[a] (%)	decomposed mesalazine above 540 K[a] (%)	Eudragit S[a] (wt. %)	Eudragit S+RL[a] (wt. %)
SBA-16NH_2Mes1	42.1	21.8	20.3	10.4	17.1
SBA-16NH_2Mes0.75	36.6	20.0	16.6	11.0	14.6
SBA-16NH_2Mes0.5	23.1	14.5	8.6	12.5	27.1
SBA-16NH_2Mes0.25	17.9	8.8	9.1	10.5	24.3

[a] determined from TG analysis of the samples in air up to 873 K with 5 K/min

The weight loss due to the polymer layer of Eudragit S on SBA-16NH_2Mes0.25-1 was ~10-12 wt.% (Table 30). The polymer content was calculated by correcting the actual weight loss with aminopropyl and mesalazine contents. The applied procedure permits the deposit of a similar amount of the polymer and the formation of an optimal polymer layer.
In order to delay and control the release process a coating of the mesalazine loaded SBA-16NH2 samples with Eudragit type polymers (Eudragit S 100 and Eudragit RL100) was applied. Eudragit S 100 is anionic copolymer based on methacrylic acid and methyl methacrylate whereas Eudragit RL 100 is a copolymer of ethyl acrylate, methyl methacrylate and a low content of methacrylic acid ester with quaternary ammonium groups. A coating procedure by pH dependent polymer Eudragit S resulted in a significant decrease of the released drug amount in acid buffer that regarding physiological conditions suggested slow release of mesalazine in gastric fluid. This behavior was observed for all samples where 10.4-12.5wt.% of polymer layer independently of the amount of loaded drug was formed. Depending on the drug loading no more than 20 % of the drug was released in 2 h in acidic buffer (Fig. 73A).
On the contrary, faster mesalazine release was registered in phosphate buffer (pH = 6.8), where total release was achieved in 1-2 h (Fig. 73B). The total, but slower (about 2 h) mesalazine release was achieved for SBA-16NH2Mes1 formulation coated by Eudragit S in pH = 6.8 buffer, and the total release was observed for the other

samples in 1 h (Fig. 73 B). This is an important fact, taking into account that for the treatment of inflammatory bowel diseases mesalazine should be delivered at the higher pH of intestinal fluids. In order to obtain controlled release also in intestinal fluids coating with a second polymer - Eudragit RL - was applied. As could be expected, the coating by Eudragit RL leads to a controlled release of mesalazine in a buffer with higher pH (6.8) (Fig. 73 D). The pH = 6.8 profiles showed that the release rate from the double coated particles was significantly lower compared to the only Eudragit S coated samples. Therefore Eudragit RL coating reduced the initial burst release, frequently observed for mesoporous silica particles. In pH = 1.2 buffer solution the mesalazine release of double coated samples was lower or identical to that of corresponding single coated ones up to 0.75:1 drug to carrier ratio Fig. 73 C). However in the case of the highest mesalazine content the released amount was slightly higher compared to Eudragit S coating. This can be explained by the higher amount of "free" mesalazine on the outer surface of silica support, and by the dissolution of Eudragit S layer during the deposition of the second polymer in ethanol. The controlled and target release was achieved for double coated SBA-16 loaded with mesalazine up to 23%.

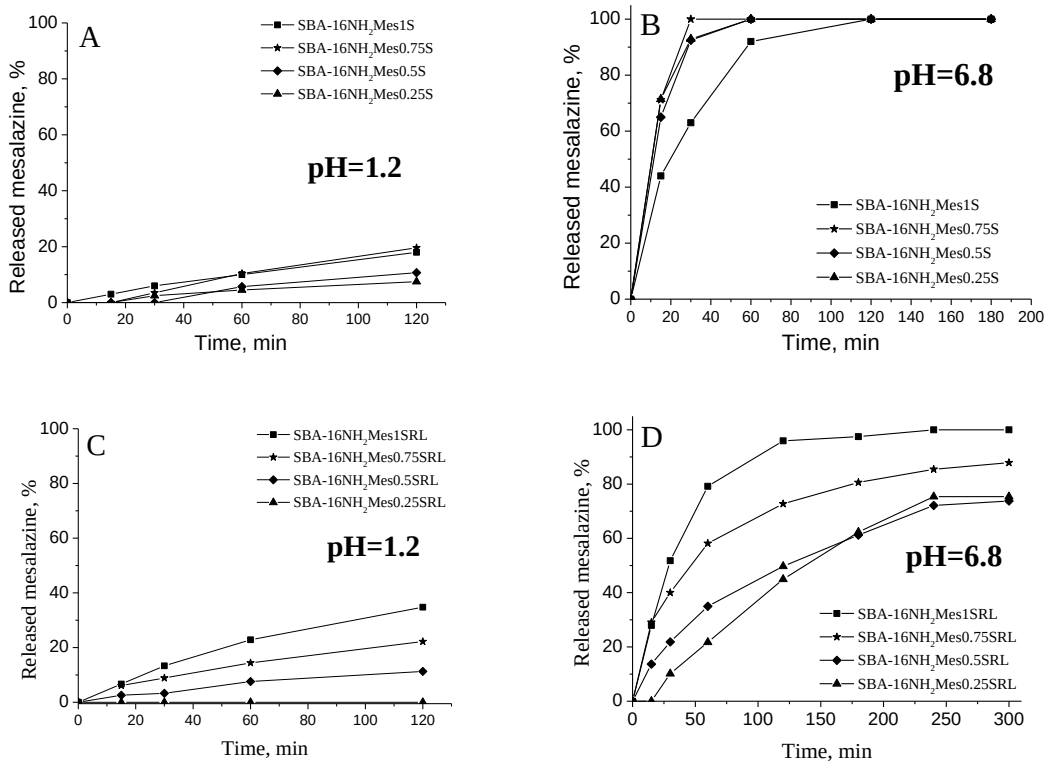

Figure 73 Release profiles of mesalazine loaded SBA-16NH_2 samples and Eudragit coated drug delivery systems at pH=1.2 and pH = 6.8

The cytotoxicity of the obtained formulations was evaluated by treatment with concentrations corresponding to 40 and 80 μg/ml. Free mesalazine demonstrated cytotoxic activity on HT-29 cells that was more pronounced at higher concentration (80 μg/ml). However, mesalazine incorporated in the mesoporous silica (SBA-16NH_2Mes0.5) showed significantly lower cytotoxicity at higher concentration and no cytotoxicity at lower one. These results suggested that encapsulation of mesalazine could provide maintained therapeutic effect with lower cytotoxicity on epithelial cells.

SBA-16 silica was synthesized and modified by post-synthesis method with amino groups. Mesalazine, a drug molecule with amino and carboxylic groups, can be successfully introduced into the silica matrix of amino-modified SBA-16 by wet milling in acidic medium. A weak interaction between drug molecules and the mesoporous SBA-16NH_2 carrier was found. Appropriate surface functionalization of silica particles provides the opportunity for further polymer coating. The post-coating of the nanoparticles with Eudragit S followed by coating of Eudragit RL revealed the capacity to achieve different drug release rates depending on the pH value of the release medium. It was found that the loading of mesalazine on the mesoporous silica carrier in ratio of 0.25:1 and 0.5:1 achieved the best controlled release at the target place. In addition to that, reduction of mesalazine cytotoxicity on epithelial cells could be achieved by its loading into mesoporous silica nanoparticles.

3.2.2.3. Polymer-coated mesoporous silica nanoparticles for controlled release of the prodrug sulfasalazine

Sulfasalazine (Scheme 6) is a prodrug used to treat inflammatory processes in the GIT, as it is metabolized in a column of specific enzymes to its two active metabolites, sulfapyridine and mesalazine. The main task in developing an appropriate delivery system for the prodrug is to deliver it to the intestines in sufficient concentration and to avoid their premature release in the stomach. The approach used for development of mesalazine delivery systems was applied for sulfasalazine as well. The MCM-41 and SBA-15 nanoparticles functionalized with amino groups were used as carriers and after drug loading they were coated by Eudragit polymers (Eudragit S and Eudragit RL) because of their capacity for pH selective release of loaded drug molecules and capacity to influence the bioadhesive properties of the obtained formulations, ensuring prolonged drug residence.

XRD patterns of the parent spherical MCM-41 and nanosized SBA-15 samples with the intense (100) and higher Miller indices reflections in the low 2 Theta region confirm the formation of the hexagonal structure. However, decreased intensity and some broadened reflections are observed for the functionalized, sulfasalazine loaded mesoporous samples, indicating some structural disorder. In addition, the presence of crystalline sulfasalazine phase is registered on the MCM-41NH_2 and SBA-15NH_2 samples. The latter evidence that a part of sulfasalazine loaded on the samples can be found on the outer surface of the small nanoparticles or in the secondary mesopores, e.g. in the voids among the particles.

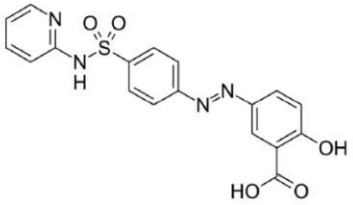

Scheme 12 Sulfasalazine molecule

The isotherms of the parent and the amino modified MCM-41 exhibit a type IV isotherm with sharp, reversible capillary condensation step between relative pressures p/po = 0.2-0.4, typical of MCM-41 materials with well-ordered pore system. By amino modification, the adsorbed volume is decreased and the capillary condensation step is shifted to lower relative pressures (Table 31). This can be associated with the pore blocking and pore narrowing effect of amino propyl molecules connecting to the silanol groups of the channels' walls. The isotherms of the SBA-15 samples are also type IV and show H1 type hysteresis loop. Normalizing textural characteristic to pure SiO_2 base (Table 31) we can calculate that about 80% of the channels of MCMNH_2 sample are filled with sulfasalazine, whereas this amounts only to 60% for SBA15NH_2 formulation.

TEM images of MCM-41 reveal formation of nanoparticles with spherical morphology, the particle sizes being around 100 nm. Scanning microscopic images of SBA-15 sample evidence its nanosized character with disc shaped monodispersed particles around 400 nm.

ATR FT-IR method was used to investigate the interaction between the sulfasalazine molecule and the modified MCM-41 carriers after its deposition. In the region of 1300-1800 cm^{-1} of FT-IR spectrum of sulfasalazine, several bands are observed. The FT-IR spectra of both silica materials loaded by sulfasalazine show a band at 1555 cm^{-1}, which can be attributed to the bending mode of protonated amino groups, e.g. -NH_3^+. In the FT-IR spectra of MCM-41NH_2Ss and SBA-15NH_2Ss samples the 1539 cm^{-1} and 1618 cm^{-1} bands of pure sulfasalazine are shifted to 1525 cm^{-1} and 1600 cm^{-1}, respectively. The former band can be associated with the asymmetric CC ring stretching mode, whereas the latter one with the asymmetric stretching mode of COO^- group. The observed shifts are due to interaction of the above-mentioned functional groups with the amino groups of modified supports. The above observations support that amino modification of silica is an appropriate method to strengthen the interaction between the carrier and the drug molecules.

Table 31 Textural properties of the parent and sulfasalazine-loaded MCM-41NH_2 and SBA-15NH2 samples

Samples	S_{BET} (m^2/g)	pore volume (cm^3/g)	pore diameter[a] (nm)	NH_2 or Ss content (wt. %)
MCM-41	1100	0.90	2.6	-
MCM-41NH_2	421 (455)*	0.36 (0.39)*	2.3	8.3
MCM-41NH_2/Ss	33 (48)*	0.05 (0.07)*	-	37.2
SBA-15	995	1.26	6.1	-
SBA-15NH_2	362 (386)*	0.56 (0.60)*	5.0	6.7
SBA-15NH_2/Ss	82 (109)*	0.18 (0.24)*	-	26.3

[a] Specific surface area and pore volume normalized to pure SiO_2 content.

The calculated sulfasalazine content for MCM-41NH_2/Ss was 37.2 wt. % and for SBA-15NH_2/Ss - 26.3 wt. %. The weight loss from the Eudragit S and Eudragit RL layers in MCM-41NH_2/Ss was 7 wt.% and 5 wt.% for SBA-15NH_2/Ss. The amount of polymers is calculated by correcting the weight loss of the aminopropyl groups and sulfasalazine. To ensure accurate determination of the amount of sulfasalazine, the polymer solutions were checked for possible loss of drug during the prosecution proceedings. The results show that the amount of sulfasalazine after the polymer charge is maintained, as in the uncoated samples, which has been shown that when applying the procedure for building polymer layers does not rise drug from mesoporous carriers.
From non-coated particles no drug release was detected applying buffer with pH = 1.2 (not shown), whereas burst release was observed at pH = 6.8 and the total release completed in 1 h (Fig. 74).

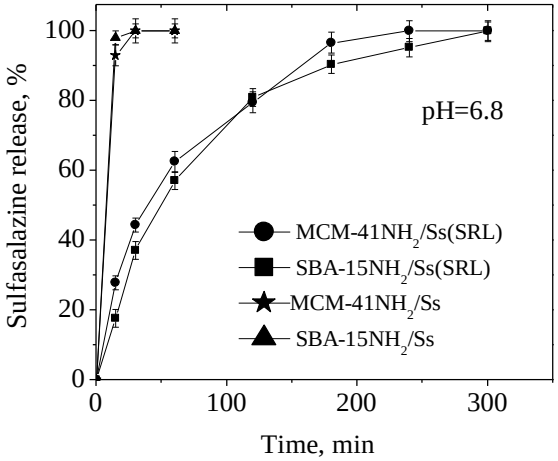

Figure 74 *In-vitro* release of sulfasalazine at pH = 6.8 from the amino modified and polymer coated MCM-41 and SBA-15 silica formulations

Regardless of the fact that almost the entire amount of sulfasalazine was located in the pores of the amino-functionalized carriers, its release at pH = 6.8 was very fast. However, the process was significantly slower after coating of the particles with four successive layers containing Eudragit S and Eudragit RL. In both types of functionalized coated particles (MCM-41NH_2 and SBA-15NH_2), the profiles showed that the release rate was significantly lower compared to non-coated ones. Therefore, polymers coating reduced the initial burst release that is frequently observed for mesoporous silica particles. In addition, coating by two polymer layers differing in pH sensitivity makes it possible to control the delivery rate at the desired region of the gastrointestinal tract, ensuring pH dependent release. No released sulfasalazine was registered in buffer with pH = 1.2 after coating by Eudragit S and Eudragit RL polymers for both carriers - whereas controlled release was obtained in buffer with pH-6.8. As shown in Fig. 74, 100% of the drug was released in 5 h from coated, functionalized nanoparticles. The latter can be explained by the formation of a stable COO^--NH_3^+ bond between carboxyl groups of Eudragit S and the amino groups of the carriers. This stable layer of pH sensitive polymer Eudragit S (excluding drug release at pH = 1.2) and the second layer of Eudragit RL, additionally reducing the release rate, are responsible for the sustained release of sulfasalazine in the target place. The drug loading degree can also influence the release process. However, in this case the particles with different loadings released sulfasalazine at a similar rate (Fig. 74).
Spherical MCM-41 and nanosized SBA-15 silica with particle sizes around 100 and 400 nm, respectively, were synthesized and modified by post-synthesis method with amino groups. Prodrug sulfasalazine was successfully introduced into the channels of MCM-41NH_2 and SBA- 15NH_2 silicas by incipient wetness impregnation. Appropriate surface functionalization of silica particles provides the opportunity for further polymer coating. The formation of polyelectrolite complex by four successive alternating layers of Eudragit S and Eudragit RL revealed the possibility to achieve different drug release rates depending on the pH value of the release medium, and hence regiospecific delivery of sulfasalazine in GIT.

3.2.2.4. Novel quercetin delivery based on amino-modified KIT-6 and KIL-2 mesoporous silica/polymer composites

The possibility for preparation of efficient delivery systems of natural flavonoids based on silica/polymer composites as carriers has been studied. In our research this approach is applied to the natural substances quercetin and curcumine, and in the present thesis the results for the quercetin systems are presented. Two methods for encapsulation of quercetin (Scheme 6) in amino-modified mesoporous KIT-6 nanoparticles have been applied, in particular loading from solution or by solid-state reaction into the pores of the nanosized mesoporous carrier. Afterwards, the loaded particles were coated with a polyelectrolyte complex formed by alternative deposition of κ-carrageenan/chitosan/κ-carrageenan layers.

The low-angle powder XRD patterns of KIT-6 show reflections typical for mesoporous silica with *I3ad* symmetry. For the amino-modified and quercetin loaded silica carriers decreased intensity and some broadened

reflections are observed indicating some structure deterioration and partial pore filling. At higher angles XRD patterns of the quercetin loaded amino-modified samples show the presence of crystalline quercetin, which is more pronounced for the sample prepared by solid state reaction. The latter evidences that a part of quercetin can be found on the outer surface of the silica nanoparticles or in the voids among the particles.
Significant decrease of the textural parameters, such as specific surface area and total pore volume, of the quercetin loaded samples indicates pore filling by quercetin (Table 32). This effect is similar for both quercetin loaded formulations. Despite the smaller amount of loaded quercetin on the KIT-6NH_2/Qu(SS) sample, its partial deposition on the external surface leads to similar decrease in surface area and pore volume as that obtained for the KIT-6NH_2/Qu (IW) sample. Moreover, the milling procedure can additionally decrease the surface area of the KIT-6NH_2/Qu(SS) sample.

Table 32 Textural properties of the parent, amino-functionalized and quercetin loaded mesoporous KIT-6 silicas

Samples	S_{BET} (m^2/g)	pore volume (cm^3/g)	pore diameter[a] (nm)	quercetin amount (wt. %)	loading efficiency[b] (%)
KIT-6	770	1.20	6.1	-	-
KIT-6NH_2	480	0.90	5.5	-	-
KIT-6NH_2/Qu(SS)	208	0.32	4.2	29.1	88
KIT-6NH_2/Qu(IW)	235	0.31	4.6	32.5	98

[a] mean pore diameter calculated by the BJH model; [b] calculated from TG data.

For clarification of the interaction between quercetin molecule and amino groups of mesoporous silica carrier the quercetin loaded samples were characterized by ATR FT-IR method (Fig. 75). No difference in the ATR-FTIR spectra of the KIT-6NH_2/Qu(IW) and KIT-6NH_2/Qu(SS) samples can be observed in the fingerprint region of quercetin regarding the preparation method - solid state reaction or incipient wetness impregnation. Comparing with the spectrum of pure quercetin, again no changes are witnessed referring the stretching vibration of ketonic carbonyl (around 1670 cm^{-1}). This implies that no direct interaction exists between the keto groups of quercetin and the silica matrix. The bands at 1430 and 1289 cm^{-1}, belonging to aromatic C = C stretching and C-O stretching, are suppressed upon loading, suggesting that the interaction, involving the C-O-C moiety and/or the phenolic part of quercetin molecule might happen.

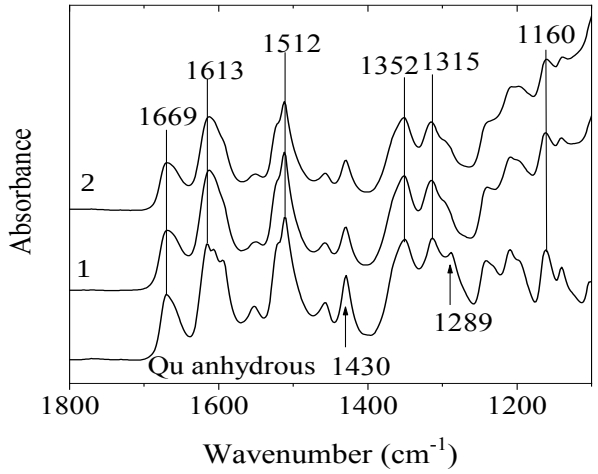

Fig. 75 ATR FT-IR spectra of anhydrous quercetin and quercetin loaded on KIT- 6NH_2 samples: 1 - KIT-6NH_2/Qu(IW) and 2 - KIT-6NH_2/Qu(SS)

Some differences in the morphology of the coated and parent particles are observed (Fig. 76). The first ones possess an outer layer, which can be attributed to the presence of a polymer coating, i.e. built up from different material than the mesoporous silica (Fig. 76). The modification procedures also increased the size of the particles by about 40-50%. The dimensions measured in horizontal distance of the parent KIT-6 species are around 45 nm, while those of the coated species vary from 50 nm to 70 nm. TG data show that the loading of quercetin on KIT-6NH_2 samples by solid state and incipient wetness impregnation is around 29.1 and 32.5 wt.%, respectively (Table 32). The calculated loading efficiency was between 88 and 98% for both samples and it was higher for the KIT-6NH_2/Qu(IW) sample prepared by impregnation. The higher amount of quercetin loaded by impregnation method could be explained by easier penetration of the dissolved drug molecules into the pores of the support. Moreover, the quercetin loaded by solid state reaction is deposited partially on the external surface of KIT-6NH_2 as can be seen from XRD data. The calculated weight loss from TG analysis due to the decomposition of polyelectrolyte complex containing κ-carrageenan-chitosan-κ-carrageenan was 16.2 wt. % for KIT-6NH_2/Qu(SS) and 26.8 wt. % for KIT-6NH_2/Qu(IW). The much lower amount of polymer complex formed on KIT-6NH_2/Qu(SS) is due to the

partial quercetin deposition on the external surface, which shields the amino-propyl groups from interaction with the sulfated polysaccharide and consequently hinder the formation of a compact coating layer.

A B

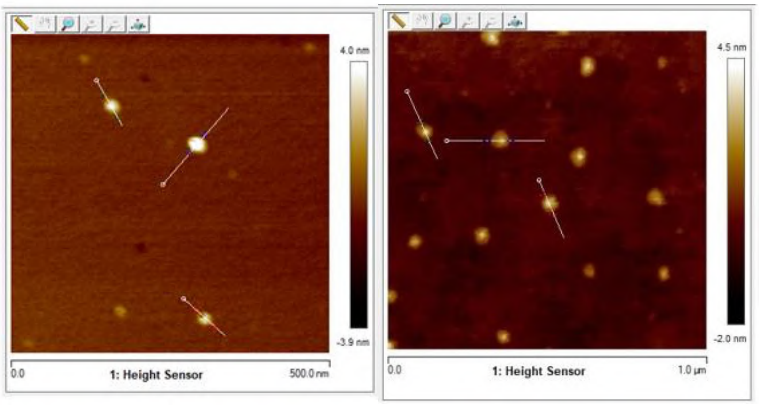

Fig. 76 The AFM cross-section analysis of the parent KIT-6 (A) and KIT-6NH$_2$/Qu(IW)P particles (B)

An *in vitro* quercetin release study from the loaded particles was performed in a phosphate buffer solution with pH = 6.8 at 310 K (Fig. 77). Slightly faster release of quercetin was registered for the KIT-6NH$_2$/Qu(IW) sample compared to its analogue prepared by solid state reaction. Total quercetin release from KIT-6NH$_2$/Qu(IW) at pH = 6.8 was achieved within 3 h whereas KIT-6NH$_2$/Qu(SS) showed maximum drug release reaching 92% in 4 h. This result can be explained by protonation of aminopropyl groups in the buffer solution facilitating the release of quercetin molecule as a result of the competitive adsorption between quercetin and water molecules. Faster release of quercetin from the KIT-6NH$_2$/Qu(IW) sample can be explained with the amorphization of quercetin during its penetration from solution into the pore system of the carrier in comparison to the KIT-6NH$_2$/Qu(SS) material, in which the presence of crystalline quercetin could be observed by XRD. Coating of the particles with a κ-carrageenan/chitosan/κ-carrageenan complex leads to decreased release rate of quercetin for both KIT-6NH$_2$/Qu(IW)P and KIT-6NH$_2$/Qu(SS)P materials (Fig. 77). In our previous papers we found formation of Zn-quercetin complex on zinc modified SBA-15, SBA-16 and MCM-41 silicas which leads to slower *in-vitro* release at pH = 5.5 from Zn-modified SBA-15 samples compared to the parent one. The obtained formulations were suggested as promising for dermal application.

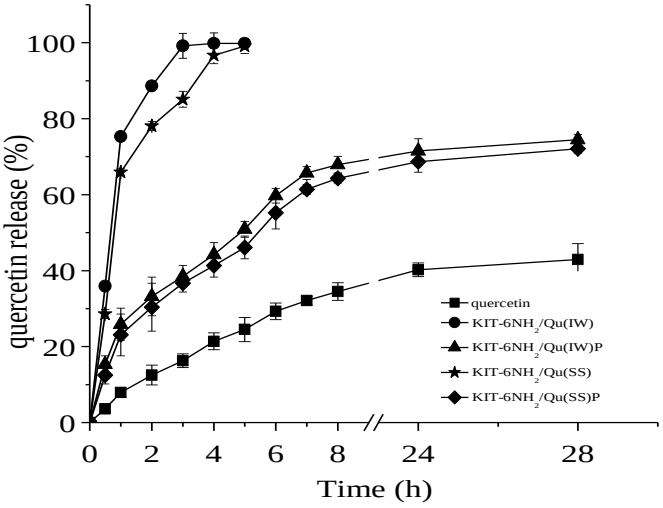

Fig. 77 Release profiles of quercetin loaded parent and amino modified KIT-6 samples

The antiproliferative activity of quercetin loaded in mesoporous carriers was evaluated in a comparative aspect with respect to free quercetin (ethanolic solution) on a HUT-78 human tumor cell line. The cell line was selected as a suitable model for cutaneous T-cell lymphoma (CTCL). JAK-3 kinase overactivity has been found to be selectively inhibited by quercetin, making it a potential target drug for this condition. The obtained results show that the unloaded particles KIT-6 and KIT-6NH2 do not induce a significant decrease in cell viability even at the highest concentration of 200 µM. These effects clearly indicate that the proposed mesoporous silicates are not cytotoxic. In contrast, quercetin-loaded and polymer-coated particles, as well as the free drug, showed dose-dependent cytotoxicity leading to almost 50% eradication of HUT-78 cells. This result unequivocally shows that the inhibitory effect on the cell viability of quercetin-loaded silicate systems is due only to the antiproliferative activity of the drug and not to the carriers themselves. On these grounds, it can be concluded that the tested mesoporous silicate materials are promising nanocarriers for the delivery of the experimental anticancer drug quercetin.

Mesoporous KIT-6 silica nanoparticles with sizes around 45 nm were synthesized and modified with aminopropyl groups by post-synthesis method. Incipient wetness impregnation and solid state reaction methods were used for quercetin loading on the amino-modified KIT-6 samples. High loading capacity (29-33 wt %) was achieved on the KIT- 6NH_2 sample by both methods. Also, high loading efficiency (88-98%) was registered, especially for the formulation prepared by incipient wetness impregnation. The *in-vitro* release process showed faster quercetin release from the KIT-6NH_2 sample prepared by impregnation in comparison to solid state reaction. It was also shown that the release of quercetin loaded on a silica nanocarrier can be additionally controlled by formation of polyelectrolyte polymer complex. ATR-FT-IR spectroscopic data suggested weak interaction of quercetin with the NH_2- modified support involving the C-O-C moiety and/or the phenolic part of the quercetin molecules. The non-loaded KIT-6 and KIT-6NH_2 nanoparticles did not induce a decrease in cell viability of the three tested cell lines (HEK- 293, HL-60 and HUT-78). A comparative study of the cytotoxic potential of free and formulated quercetin shows that quercetin encapsulated into polymer coated, modified silica carriers proved to exert the same cytotoxic potential for HUT-78 cell line as the free drug which proved that modified silica particles are promising carriers for controlled delivery of quercetin.

3.2.2.5.Verapamil delivery systems on the basis of mesoporous ZSM-5/KIT-6 and ZSM-5/SBA-15 polymer nanocomposites as a potential tool to overcome MDR in cancer cells

Verapamil (Scheme 13) is a drug with established use in the clinical practice for the treatment of hypertension. On the other hand, in experimental oncology, verapamil has been found to be a promising modulator of multiple drug resistance. The clinical realization of this potential requires its formulation in appropriate carriers, which on the one hand to provide masking of its main pharmacological effect and on the other hand to allow overcoming the dose-dependent side effects of verapamil. In this regard, verapamil was loaded into two types of modified carriers: ZSM-5/KIT-6SO_3H(COOH) and ZSM-5/SBA-15SO_3H(COOH) and its ability to overcome cellular mechanisms of drug resistance was assessed in vitro on chemosensitive and chemoresistant to doxorubicin cell lines. To demonstrate that verapamil loaded in carriers could block Pgl-efflux pump, cells were treated with doxorubicin at IC_{50} concentrations.

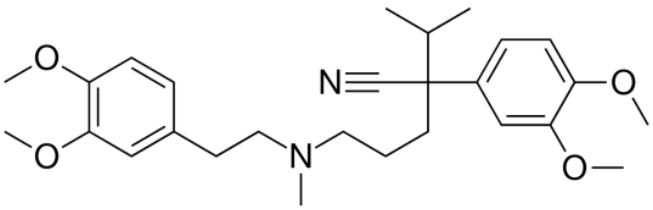

Scheme 13 Verapamil molecule

Verapamil was loaded on zeolite/mesoporous silica carriers by incipient wetness impregnation. The amount of the functional -$CH_3(CH_2)_2SO_3H$ and –$(CH_2)_3NHCO(CH_2)_2COOH$ groups, of the loaded verapamil and of the polymer coating was determined by thermogravimetric method (Table 33). The calculated amount of -$CH_3(CH_2)_2SO_3H$ groups bound to the surface of ZSM-5/KIT-6 and ZSM-5/SBA-15 is 7.3 wt.% and 4.0 wt.%, respectively, whereas the amount of -$(CH_2)_3NHCO(CH_2)_2COOH$ groups connected to the surface of the corresponding nanoparticles is 12.5 wt.% and 11.3 wt.%, respectively (Table 33). The TG analysis determined the actual amount of verapamil in the carriers after correcting the curves for water and functional groups content. TG data show that the amount of verapamil loaded on ZSM-5/KIT-6-SO_3H and ZSM-5/SBA-15-SO_3H samples is 21.3 and 33.6 wt.%, respectively, and on ZSM-5/KIT-6-COOH and ZSM-5/SBA-15-COOH samples is 17.1 and 19.4 wt.%, respectively (Table 33). The lower amount of loaded drug in ZSM-5/KIT-6 material could be explained with its more ordered 3D pore systems with interconnected channels, where the penetration of the drug molecules is hindered within the narrow pore entrances. The long chains with the carboxylic groups at the end (–$(CH_2)_3NHCO(CH_2)_2COOH$) on ZSM-5/KIT-6 additionally restrict the access to the pores. The highest drug adsorption (33.6 wt. %) was achieved for ZSM-5/SBA-15 modified with -$(CH_2)_3SO_3H$ groups due to the more open structure of the nanocarrier and shorter modification segments. The aluminum content determined by elemental analysis is 0.8 wt. % for ZSM-5/KIT-6 and 0.3 wt. % for ZSM-5/SBA-15.

Table 33 Textural properties of the parent, carboxilic-, and sulfonic-functionalized and verapamil loaded materials

Samples	S_{BET} (m^2/g)	pore volume (cm^3/g)	pore diameter[a] (nm)	COOH/SO_3H/verapamil content (wt.%)
ZSM-5/KIT-6	425	1.18	11.0	-
ZSM-5/SBA-15	362	1.20	12.0	-
ZSM-5/KIT-6-COOH	285.4	0.82	9.5	12.5
ZSM-5/SBA-15-COOH	282.1	1.04	11.6	11.3
ZSM-5/KIT-6-SO_3H	399.8	1.10	9.9	7.3
ZSM-5/SBA-15-SO_3H	351.5	1.31	14.6	4.0
Ver/ZSM-5/KIT-6-COOH	46.3	0.19	8.6	17.1
Ver/ZSM-5/SBA-15-COOH	66.4	0.34	11.6	21.3
Ver/ZSM-5/KIT-6-SO_3H	216.2	0.63	7.9	19.4
Ver/ZSM-5/SBA-15-SO_3H	46.0	0.23	12.0	33.6

Parent ZSM-5/KIT-6 and ZSM-5/SBA-15 materials were characterized by solid state ^{27}Al NMR spectroscopy. The ^{27}Al spectrum of the ZSM-5/KIT-6 material shows two resonances at 57 ppm and at around 0 ppm. The intense signal centered at 57 ppm is characteristic for framework Al species in tetrahedral coordination (AlO_4 structural unit), whereas the low intensity broad resonance at 0 ppm indicates the presence of a small amount of six-coordinated aluminum species and defect framework Al sites (AlO_6 structural units). The calculated Al^{IV}/Al^{VI} ratio was 3.8, indicating the presence of predominantly tetra-coordinated Al framework units, which is a proof for the preservation of ZSM-5 structure in the ZSM-5/KIT-6 composites. The ^{27}Al spectrum of the ZSM-5/SBA-15 sample displays a very broad resonance covering the range from 170 to -60 ppm centered at around 30 ppm and overlapped with a sharper signal at around 58 ppm. This observation indicates that during the preparation of ZSM-5/SBA-15 nanocomposite material the ZSM-5 structure was partially disrupted resulting in overall decrease of the Al^{IV} species in tetrahedral positions and formation of other types of Al coordination sites. Successful modification with organic functional groups was confirmed by $^1H \rightarrow ^{13}C$ CP and $^1H \rightarrow ^{29}Si$ CP NMR spectra.

The calculated parameters of the nitrogen physisorption texture of the starting, amino-modified and loaded with verapamil ZSM-5/SBA-15SO_3H(COOH) and ZSM-5/KIT-6SO_3H(COOH) materials are presented in Table 33. Their loading with verapamil leads to a significant reduction in the specific surface area and volume of the pores due to their filling with drug substance. XRD results of verapamil-loaded -$(CH_2)_3SO_3H$ and -$(CH_2)NHCO(CH_2)_2COOH$ modified ZSM-5/KIT-6 and ZSM-5/SBA-15 materials did not indicate the presence of crystalline verapamil, indicating that even the drug a substance that remains on the outer surface is in an amorphous state.

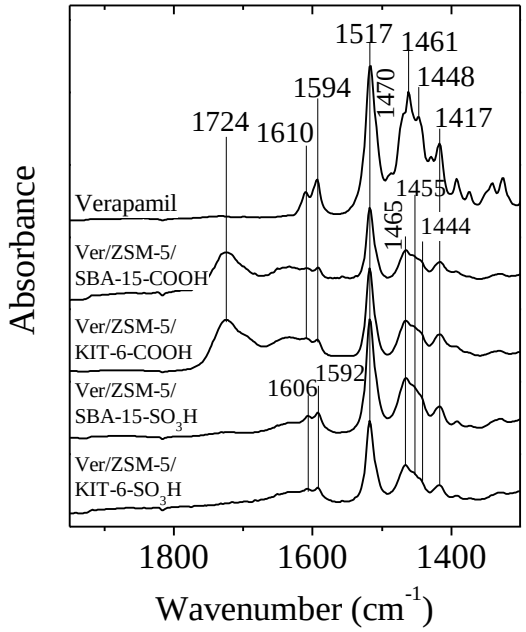

Figure 78 Release profiles of verapamil loaded SO_3H or COOH modified ZSM-5/SBA-15 and ZSM-5/KIT-6 carriers (A) and their polymer coated analogues (B)

In the spectra of COOH-modified nanocomposites the intensive band at 1724 cm^{-1} is an indication that -COOH is in protonated form or that verapamil interacts with the silica matrix via the -C-O- of the carboxyl groups (Fig. 78). Another change in the spectra is that the band at about 1471 cm^{-1} decreases in intensity and new bands appear at 1465, 1455 and 1444 cm^{-1}. A similar trend is observed for materials modified with -SO_3H. In this case, however, there is also some shift in the skeletal ring stretching (C = C) at 1606 and 1592 cm^{-1} (Fig. 78).

The nanocomposite particles contain surface acid groups, -$(CH_2)_3SO_3H$ or -$(CH_2)_3NHCO(CH_2)_2COOH$ groups, therefore the first polymer layer deposited on the nanoparticles is made of chitosan. To obtain the next shell layer an oppositely charged κ-carrageenan was used, forming a polyelectrolyte complex with the chitosan. Polysulfobetaine chain grafted chitosan was applied for the formation of the third layer around the carrier nanoparticles. It is well known that polyzwitteriones are characterized with extremely good biocompatibility and low unspecific protein adsorption, making them suitable materials for biological applications. Therefore, polysulfobetaine with an average molar mass number Mn = 10,000 g/mol and end cyclic carbonate functionality was first synthesed and used for chitosan modification. The PSB chains were grafted on chitosan *via* selective reaction of the cyclic carbonate moieties with the amino groups of the polysaccharide.

The TG analysis data show successful polymer coating around the particles, which is in the range of 22.7-25.0 wt. % i.e. 23.7 wt%, for Ver/ZSM-5/KIT-6-COOH/P; 22.9 wt. %, for Ver/ZSM-5/SBA-15-COOH/P; 24.6 wt. % and for Ver/ZSM-5/SBA-15-SO_3H/P; 24.9 wt. % for Ver/ZSM-5/KIT-6-SO_3H/P.

Atomic force microscopy (AFM) was used for visualization of the modified ZSM-5/KIT-6-SO_3H carrier prior and after polymer coating of the drug loaded particles. ZSM-5/KIT-6-SO_3H material presents quite uniform and spherical particles. Their dimensions measured in the horizontal distance varied from 63 nm to 86 nm with an average value of 78±7 nm. The average size of Ver/ZSM-5/KIT-6-SO_3H/P particles calculated for 15 species is 136±13 nm.

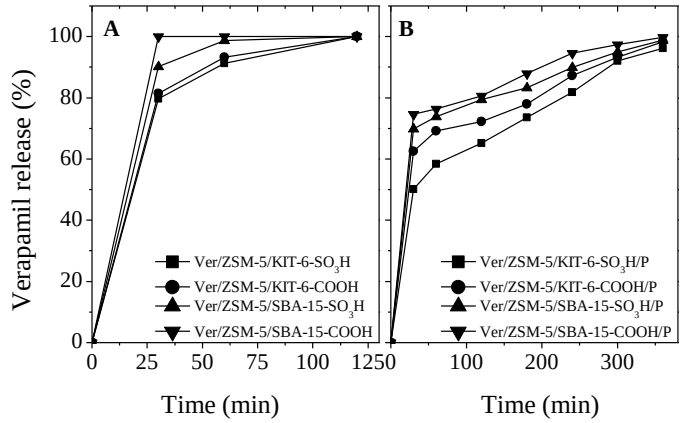

Figure 79 ATR FT-IR spectra of the initial and modified ZSM-5/SBA-15 and ZSM-5/KIT-6 materials and verapamil loaded formulations

In-vitro release study of verapamil was carried out in phosphate buffered saline at pH 7.4, relevant to the physiological pH of the blood. As evident from the results shown in Fig. 79, non coated mesoporous nanocomposites are characterized with initial burst release of verapamil, whereas the total drug release was observed in 60 min for all samples. The high verapamil dispersion in the pore system of ZSM-5/KIT-6 modified by -SO_3H or -COOH groups can be a reason for its slower release from this type carrier in comparison to the ZSM-5/SBA-15 analogs. The polymers coating of particles was associated with decrease in release rate, and this effect was most pronounced for ZSM-5/KIT-6 based formulation, especially for its ZSM-5/KIT-6-SO_3H counterpart. This effect can be associated with the smaller pore size and 3D structure of the ZSM-5/KIT-6 carrier and the presence of polymer coating around the particles, which acts as a diffusion controlling barrier, together with strong adsorption sites. Faster drug release was encountered from uncoated nanocomposite silicas and this tendency was more pronounced for the formulations prepared on ZSM-5/SBA-15 as compared to their ZSM-5/KIT-6 analogues (Fig. 79). Total verapamil release was achieved in 2 hours for all studied samples. The modification by -$(CH_2)_3SO_3H$ groups lead to slower release, most probably because of the stronger interaction of verapamil with stronger acidic groups.

A comparative study of the cytotoxic effect of the resulting formulations on the HL-60 and HL-60/DOX cell lines was performed. Cells were also treated with doxorubicin at IC_{50} concentrations to demonstrate that verapamil loaded in carriers could block Pgl-efflux pump. Doxorubicin concentrations were selected based on experimentally determined IC_{50} values for both cell lines. The concentration of verapamil is ¼ from the experimentally determined IC_{50} to allow easy differentiation of only the cytotoxic effect of doxorubicin and the modulating effect of verapamil on tumor cell resistance. The presented results show that verapamil treatment alone does not inhibit cell proliferation in both cell lines. Unlike verapamil, treatment of cells with doxorubicin results in significant suppression of cell vitality and, as expected, this effect is strongest in the chemosensitive cell line, in which the eradication of tumor cells is above 65%. Concomitant treatment of both cell lines with doxorubicin and verapamil was accompanied by strong inhibition of cell proliferation, especially in doxorubicin-resistant HL60/DOX cells. Therefore, verapamil successfully overcomes the acquired drug resistance. The same dependency is reported for the modulating effect of verapamil loaded in the developed carriers. The obtained results give us reason to conclude that the systems developed by us are promising platforms for systemic delivery of verapamil.

Mesoporous ZSM-5/SBA-15 and ZSM-5/KIT-6 nanoparticles were synthesized and modified by post-synthesis method with -$(CH_2)_3SO_3H$ and -$(CH_2)_3NHCO(CH_2)_2COOH$ groups. Verapamil was loaded by incipient wetness impregnation on the functionalized composite supports. The drug loaded systems were further modified by surface coating with polymer complex layers composed of chitosan-κ-carrageenan-chitosan with grafted polysulfobetaine chains. ATR-FT-IR spectroscopic data suggested weak interaction of verapamil with the functional groups of the modified supports. The *in vitro* release profiles of verapamil from the composite carriers were investigated as a function of time showing modified release of verapamil for a period of 24 hours. The factors influencing the verapamil delivery are the structure of the applied carrier, the chemical nature of functional groups and the presence of a polymer complex around the composite nanoparticles. The bimodal pore structure of the ZSM-5/KIT-6 materials has a positive effect on the verapamil release rate, independently of the nature of surface functional groups. Moreover, the ZSM-5/KIT-6 systems modified with stronger acidic -$(CH_2)_3SO_3H$ groups are characterized by a slower drug release. Additionally, the presence of polymer complex layers further decreased the drug release rate. Based on the CTM comparative study on the MDR reversing capacity of free and nanoformulated verapamil, it can be concluded that loading of the drug into mesoporous nanocomposites drastically augments the antitumor efficacy of doxorubicin. In conclusion, the findings of the conducted synergism study show superior chemosensitizing activity of the experimental verapamil-loaded nanocomposites in HT-29 and HL-60/Dox cells, as compared to free verapamil, presumably as a result of a positive efflux pump modulation.

3.2.3. Development of a twocomponent drug system based on magnetic nanoporous silicate nanoparticles

In cancer therapy anti-inflammatory drugs are often utilized simultaneously with the anticancer drug component in order to treat inflammation side effects of the primary disease. Such a well-accepted and longtime applied glucocorticoid drug is prednisolone (Scheme 14). Prednisolone itself has been used in high doses as an anticancer drug in clinical oncology for more than three decades. The combination of both drugs could be a promising strategy for the treatment of advanced cancer with simultaneous inflammatory problems. Their simultaneous application was approved as a second-line treatment for metastatic hormone-refractory prostate cancer. Thus we designed a drug delivery system, which enables targeted and sustained release of mitoxantrone and prednisolone in order to optimize the therapeutic effect while reducing the severe side effects of both drugs. An additional coating by natural polymers was applied to improve the biocompatibility and drug release behavior of the obtained system. We developed magnetic nanoporous silica materials (MNS) with spherical morphology and particle size around 100 nm. Modification by SO_3H groups was applied to favor the interaction of the silica carrier with mitoxantrone molecules as well as with the polymer layers. A dual drug delivery system carrying mitoxantrone and prednisolone was prepared and coated with chitosan and alginate in connection with its possible application in targeted anti-cancer therapy.

Magnetic silica material was synthesized by template assisted sol-gel method using pre-prepared magnetic nanoparticles put directly into the synthesis gel. Magnetic iron oxide nanoparticles were prepared by co-precipitation of $FeCl_2$ and $FeCl_3$ solution by NaOH. The resulting magnetic nanoparticles were washed chloride free and dried at ambient temperature. Magnetite nanoparticles (Fe_3O_4) can be oxidized to maghemite (γ-Fe_2O_3) by exposing them to air and humidity. The crystalline structure of magnetite and maghemite is very similar, as are their physical properties, but maghemite has somewhat lower bulk saturation magnetization value than magnetite (~92 emu/g for magnetite, ~76 emu/g for maghemite).
The XRD patterns of the nanosized magnetic iron oxide particles, the MNS sample and its sulfonic group modified and mitoxantrone loaded analogues are shown in Fig. 80A.

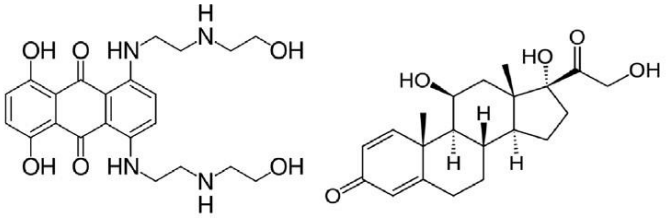

Scheme 14 Structure of mitoxantrone (left) and prednisolone (right)

Iron oxide NP show widened reflections typical of small nanoparticles. The pattern can be identified rather as a maghemite structure than as magnetite. By profile fitting method about 20% of magnetite content could be calculated, however the reflections are fully overlapping due to small particle size. The particle size calculated by the Sherrer equation applying profile fitting method is 11 nm. This value is in good accordance with other published results (Rebodos et al., 2010; Mascolo et al., 2013) for magnetite nanoparticles prepared by the same

method. The XRD pattern of the MNS sample shows the presence of nanosized maghemite with lower intensity but with the same FWHM value (Fig. 80 A). The low angle XRD pattern of the MNS sample exhibits a reflection at d100 = 4.18 nm, typical of ordered mesoporous silica materials, representing a_0 = 4.82 nm unit cell parameter. The (110) and (200) index reflections also appear in the pattern, but with low intensity characteristic of a not perfectly ordered nanoporous structure. By sulfonic group modification no changes in the XRD pattern can be observed at higher angles, but intensity decrease of low angle reflections can be observed by the deterioration of the structure ordering. No reflections of mitoxantrone can be witnessed on the drug loaded system, indicating that MTX has penetrated the channel system, and cannot be detected on the outer surface of the silica carrier.

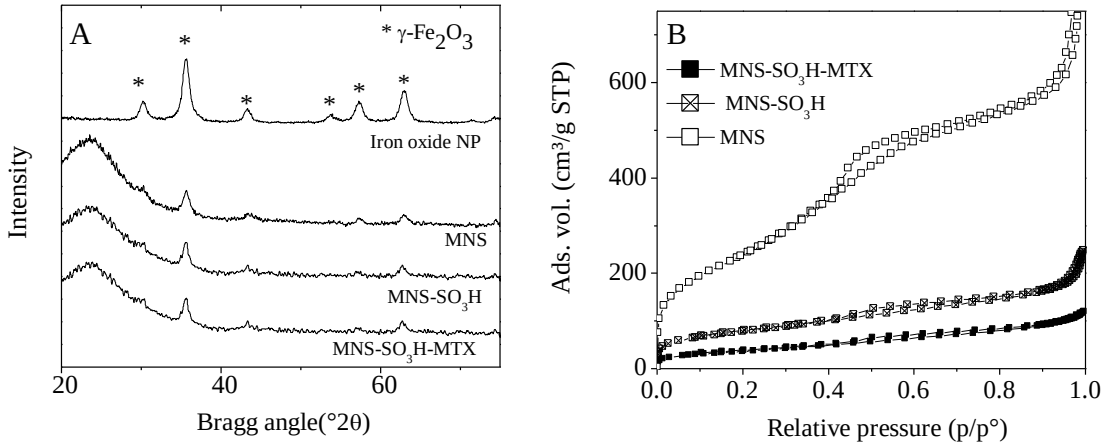

Figure 80 XRD patterns (A) and nitrogen physisorption isotherms (B) of the studied samples

The mesoporous character of the MNS composites was proven by N_2 physisorption measurements and the textural parameters of the parent, the SO_3H modified and drug loaded samples are summarized in Table 34.

Table 34 Textural properties of the parent and drug-loaded MNS and MNS-SO_3H samples

Samples	S_{BET} (m^2/g)	pore volume (cm^3/g)	pore diameter (nm)	SO_3H/drug content (wt.%)
MNS	825	0.94	3.45	-
MNS-SO_3H	285	0.25	1.32	9
MNS-SO_3H-MXT	135	0.13	-	9/6

The obtained materials show type IV isotherms characteristic of mesoporous materials with H2 hysteresis loop. The parent magnetic silica sample has high specific surface area and pore volume, however the capillary condensation step is not so sharp, rather typical of mesoporous silica with non-uniform, wider pore size distribution. In accordance with XRD results, upon modification with sulfonic groups, significant decrease in the surface area and pore volume could be observed. This effect can be explained by pore blocking due to a reaction of (3-mercaptopropyl-trimethoxysilane (MPTMS)) with the surface of the silica walls as evidenced by pore size distribution curves. Furthermore, the deterioration effect of hydrogen peroxide on silica during the second oxidation step in sulfonic group modification resulting in the decrease of the pore structure ordering cannot be excluded. By mitoxantrone loading the pore volume and the surface area also significantly decreased, showing the pore filling by the drug molecules. It can be calculated that in MNS-SO_3H-MTX formulation about 46-50% of the mesopores of the parent MNS-SO_3H sample are filled with the applied amount of MTX if we normalize all the specific surface area and pore volume values to the pure silica base (Table 34). By polymer coating total pore blocking was observed and by nitrogen physisorption only the outer surface area of the particles could be measured, amounting to about 10 m^2/g.
Formation of spherical MNS nanoparticles with sizes around 100 nm was registered by TEM (Fig. 81) investigation.

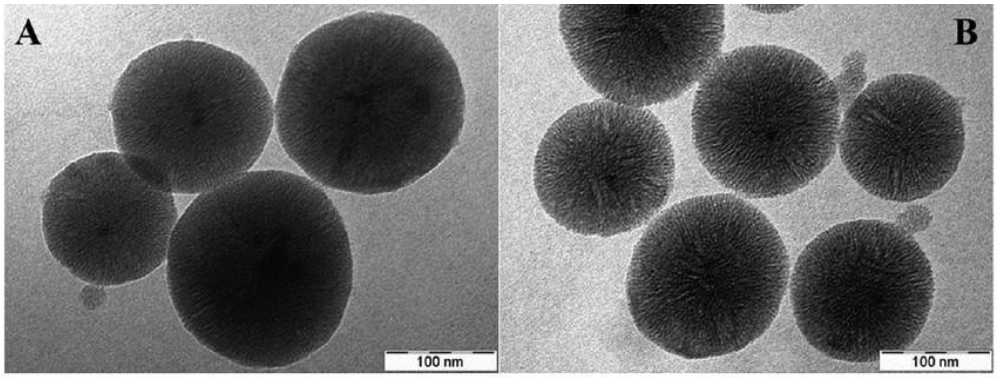

Figure 81 TEM images of the MNS sample (A-B)

TEM images also support the results of nitrogen physisorption measurements, showing the formation of ordered mesopores. Radially arranged channels can be seen in the spherical particles. Some formation of agglomerated iron oxide nanoparticles can also be detected by TEM, and by higher magnification around 10 nm metal oxide nanoparticles can be observed in the core of the silica spheres. The latter observation supports the successful incorporation of finely dispersed magnetic nanoparticles into the mesoporous silica.

Mossbauer spectroscopic investigations also support the presence of maghemite nanoparticles in the silica structure. Comparison of Mössbauer spectra recorded at 300 and 77 K clearly shows the dominant presence of superparamagnetic maghemite nanoparticles (Fig. 82).

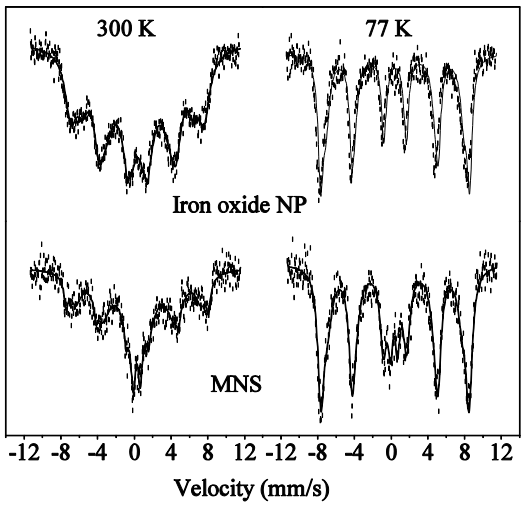

Figure 82 Mössbauer spectra of the parent dried iron oxide nanoparticles and the silica coated MNS material

In the first approach the magnetically split parts of the spectra were decomposed to two sextets in correspondence with the two different possible coordinations of iron ions in maghemite (e.g. tetrahedral and octahedral one - Table 35).

Table 35 Mössbauer parameters of the parent iron oxide nanoparticles and MNS material

Samples		300 K				77 K			
	Comp	IS	QS	MHF	RI	IS	QS	MHF	RI
Iron oxide NP	Sext(1)	0.35	-	45.6	24	0.44	-	50.5	54
	Sext(2)	0.37	-	38.5	76	0.41	-	46.9	46
MNS	Sext(1)	0.34	-	47.7	10	0.42	-	50.1	61
	Sext(2)	0.41	-	42.0	78	0.43	-	45.6	29
	Doubl	0.26	0.73	-	12	0.32	0.76	-	10

The small size of the particles is reflected in the superparamagnetic behavior, i.e. decrease of measuring temperature results in the increase of the extent of magnetic ordering - the presence of antiferromagnetic sextets is more pronounced in the 77 K spectra. In particular, superparamagnetic doublets appear in both 300 K and 77 K spectra of the MNS sample attesting that the size of the magnetic particles is below ca. 8 nm. In the spectra of the latter sample superparamagnetic doublet is present both at 300 and 77 K temperatures. The obtained isomer shift values ($0.35 < IS_{300K} < 0.41$ mm/s) are characteristic of Fe^{3+} oxidation state (Table 35), since the presence of magnetite with Fe^{2+} in 1/3 part of cationic sites would increase the IS_{300K} value of the corresponding sextet to ca. 0.6 mm/s. The "centre of gravity" method (calculation of area weighted mean isomer shift values can also be applied to estimate the proportion of magnetite in our samples. Namely, 21% and 30% magnetite content can be

estimated from the data of Table 35 for the parent iron oxide and for the MNS particles, respectively. This observation is in accordance with the XRD results, determining ~ 20% of magnetite content for the parent iron oxide by profile fitting method.

The interaction between silica, sulfonic groups, and MTX on MNS carriers was studied by ATR FT-IR spectroscopy (Fig. 83 A). The MNS-SO_3H spectrum shows the typical spectral features of silica with a dominant broad Si-O-Si stretching vibration band around 1062 cm^{-1}. The presence of a very weak band characteristic of the stretching vibration of sulfonic acid group (υS=O) can be observed at 1379 cm^{-1} (not shown). The broad and intense -OH absorption band around 3400 cm^{-1} might also comprise the S-OH stretching vibrations. The characteristic S=O and -SO_3H stretching vibration bands around 1160 and 1080 cm^{-1}, respectively, are masked by the strong Si-O-Si stretching feature of the silica matrix. In the same way, weak Fe-O bands of maghemite around 571 cm^{-1} are mantled. Mitoxantrone, being an anthracenedione anticancer drug, shows characteristic IR bands of aromatic rings (3060, 2963, 1608, 1565 cm^{-1}) and of N-H bending and C-O stretchings (1550-1000 cm^{-1}) (Fig. 83B). Weak bands of mitoxantrone can be witnessed in the spectrum of MTX loaded MNS-SO_3H, too. For detailed spectral analysis, subtraction of the MNS-SO_3H spectrum from the spectrum of MTX loaded MNS-SO_3H was investigated and compared with the one of native MTX. For MTX band assignment we used its analogy with quinone and antraquinone. Accordingly, we assigned the band at 1608 cm^{-1} to quinone ketones, the significant wavenumber downshift might be due to the strong inter- and intramolecular H-bonding. Bands at 1565 and 1513 cm^{-1} might belong to skeletal C=C vibrations. The bands at 1446 and 1351 cm^{-1} relate to a combination of C-O stretchings (υC-O) and N-H bendings (δNH). The band around 1204 cm^{-1} can be associated to C-N stretching vibrations. Upon loading of MTX on MNS, no changes of the anthracenedione skeletal vibrations were observed. However, changes in band positions of δN-H and υ(C-O) vibrations, probably originating from the side chains of MTX molecules, suggest that these moieties might be involved in an interaction with the MNS-SO_3H framework.

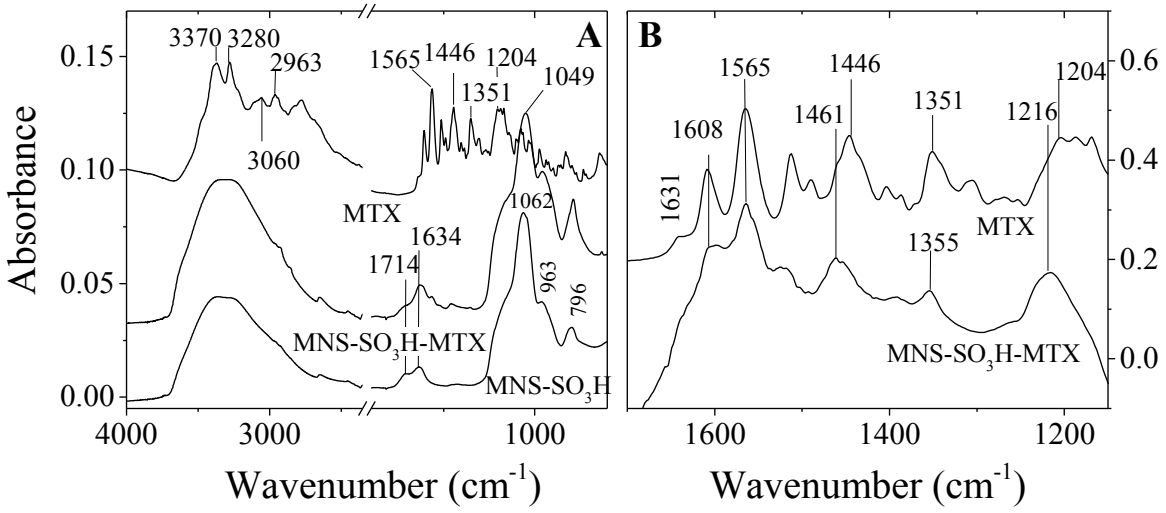

Figure 83 FT-IR spectra of pure sulfonic modified and mitoxantrone loaded MNS samples

TG data show that by the applied method of silica modification the amount of incorporated propyl sulfonic groups is about 9 wt. %, which corresponds to ~0.7 mmol/g of sulfonic functional group on the surface or in the channels of the MNS material. Loading of 7.4 wt% of mitoxantrone resulted in actual 6 wt. % drug on the sulfonic modified silica carrier. The missing excess amount was probably removed by centrifugation of the sample. The therapeutically needed amount of mitoxantron in formulations is around 6 wt. %. TG analysis was also used for quantitative determination of the polymer layers formed around the loaded particles. The first coating was performed via addition of chitosan solution in formic acid to the MNS-SO_3H-MTX followed by solvent evaporation. Both the drug and the silicate material are more or less resistant to mild acidic conditions therefore formic acid was used as a medium for particles coating with chitosan without affecting the drug payload. In addition, the formation of a chitosan coating is favored by the interaction of the oppositely charged polymer and sulfonic acid groups on the surface of the particles. In spite all of our efforts it was not possible to make a chitosan polymer layer on pure MNS particles. It seems that sulfonic functionalization plays a crucial effect on the ability of polymer to connect to the silica surface. The chitosan content in MNS-SO_3H-MTX-CH was calculated to be 6.3 wt.% by correcting the actual weight loss with propylsulfonic groups and mitoxantrone contents. After chitosan coating, 8 wt% prednisolone was loaded on MNS-SO_3H-MTX-CH by incipient wetness impregnation. Subsequent coating by alginate resulted in 6.7 wt. % second polymer layer formation.

Fig. 84A presents the AFM image of the spin-coated MNS particles on a glass wafer. The parent materials are spherical in shape with size calculated to be 105 ± 17 nm after elimination of the tip broadening effect. Spherical in shape and quite uniform particles are preserved after loading of the two drugs and coating by two polymers.

Their dimensions calculated from the AFM images are in the range from 270 nm to 340 nm (Fig. 84B). After application of the deconvolution equation the estimated mean size of the particles is 209±23 nm for MNS-SO_3H-MTX-CH-PRD-ALG nanoparticles. The increased size of the coated particles compared to that of the parent particles is assigned to the modification procedures applied to the particles for introducing functional groups, drugs loading and polymers coating. Additional information on the surface morphology of the particles can be obtained from the 3D AFM image of a single object. The surface has become smooth due to the polymer coating although some roughness is still seen, hinting at the mesoporous structure of the particles.

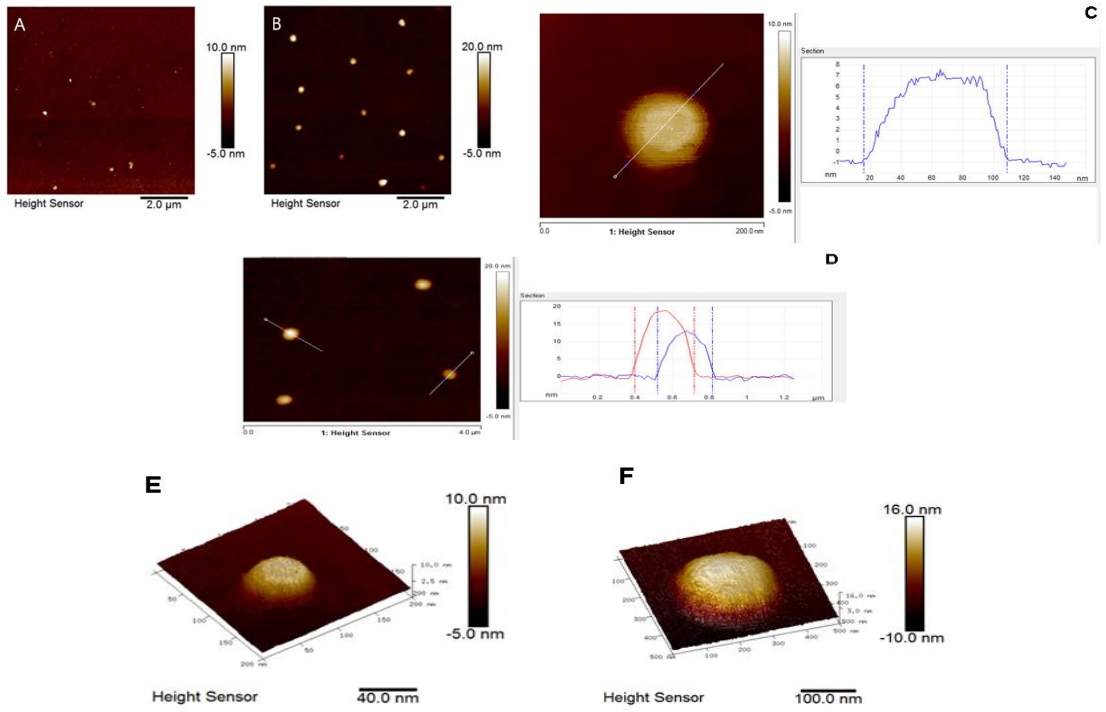

Figure 84 AFM image of the MNS (A) and MNS-SO_3H-MTX-CH-PRD-ALG particles (B), the cross-section analysis of the MNS (C) and MNS-SO_3H-MTX-CH-PRD-ALG (D) particles and 3D images of a single MNS (E) and MNS-SO_3H-MTX-CH-PRD-ALG (F) particle

The *in vitro* release profiles of the mitoxantrone (MTX) and prednisolone (PRD) from the tested formulations in PBS (pH = 7.4) at 310 K are depicted in Fig. 85. As is evident from the data, free drug substances are dissolved almost immediately under the test conditions. The release of the drugs from the tested parent MNS-SO_3H mesoporous silica carrier is slower as compared to the dissolution of free MTX but is characterized by prominent „burst"-effect, as almost 60% of MTX are released within 30 min. By chitosan coating of MTX loaded magnetic/silica nanoparticles, additional control of the release can be witnessed. Because of its polycationic character, the polymer coating under acidic conditions can form a complex with the negatively charged surface of the silica. Chitosan is not soluble at pH=7.4 and the polymer membrane around the particles slows down the drug release (Fig. 85A). As is evident from the data, no burst-effect of MTX is observed from the chitosan coated formulation and more importantly the formulation is able to deliver the cargo in a sustained manner for a period of almost 6 h. Additional coating of the formulation containing both MTX and PRD with alginate resulted in the decreased release rate of mitoxantrone and PRD (Fig. 85A, B).

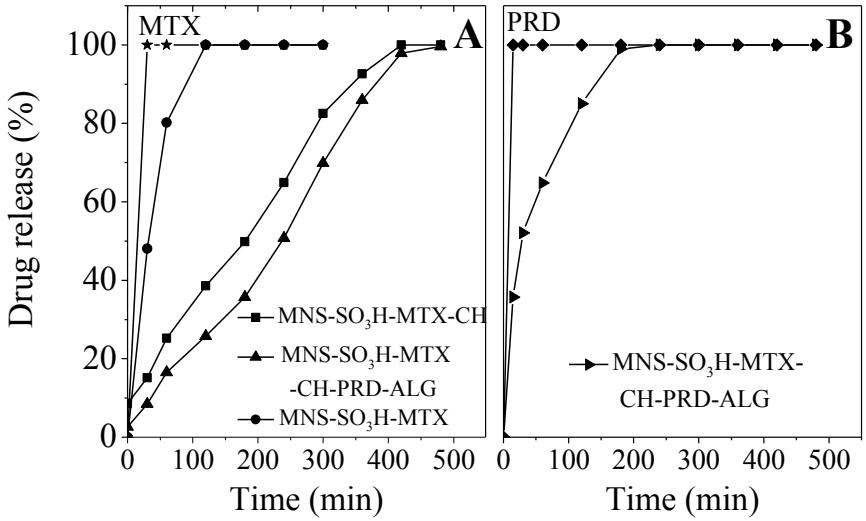

Figure 85 *In-vitro* release of mitoxantrone (A) and prednisolone (B) at pH = 7.4 from the surface functionalized and polymer coated MNS materials

The tumor-inhibiting properties of free or silica-loaded mitoxantrone were evaluated in a panel of human tumor cell lines, following 72 h exposure. Both free drug and its supported and polymer coated forms evoked strong, concentration-dependent inhibition of the growth of cultured tumor cells, which enabled the construction of dose-response curves and the calculation of the equieffective inhibitory concentration - IC_{50} (Table 35).

Table 35 Equieffective concentrations (IC_{50}) of mitoxantrone-loaded magnetic nanoporous silica nanoparticles, vs. the free drug

Cell line	IC_{50} (μg/ml)	
	MTX	MNS-SO_3H-MXT-CH-PRD-ALG
HD-MY-Z	4.4 ± 1.9	5.5 ± 1.8
EJ	3.7 ± 0.5	1.4 ± 0.2
K-562	0.8 ± 0.09	0.87 ± 0.05

The juxtaposition of the concentration-response curves clearly indicates that the encapsulation of the anticancer drug did not compromise its antineoplastic activity - there was minimal modulation of the survival fractions at equivalent exposure data points in HD-MY-Z and EJ cells, whereas in K-562 the inhibitory curves practically overlapped. These findings were further corroborated by the calculated IC_{50} values, which were comparable or identical in the different cell lines.

Magnetic nanoporous silica particles (MNS) with spherical morphology and 100 nm particle with advanced characteristics suitable for nanomedicine purposes were synthesized. The obtained nanoparticles were modified with SO_3H groups in a two-step post synthesis procedure. An anticancer drug, mitoxantrone, and an anti-inflammatory drug, prednisolone, were loaded on the silica support. The mitoxantrone loaded MNS-SO_3H nanoparticles were coated by chitosan and then prednisolone was infused in the chitosan layer. A second layer of alginate was then applied around the prednisolone and mitoxantrone containing formulation (Scheme 15). Alginate coating further improved the release properties by preventing the burst release of mitoxantrone and prednisolone. The cytotoxicity properties of the drugs loaded formulations and their ability to retain the intrinsic pharmacological properties of the encapsulated drugs were investigated on a panel of human tumor cell lines.

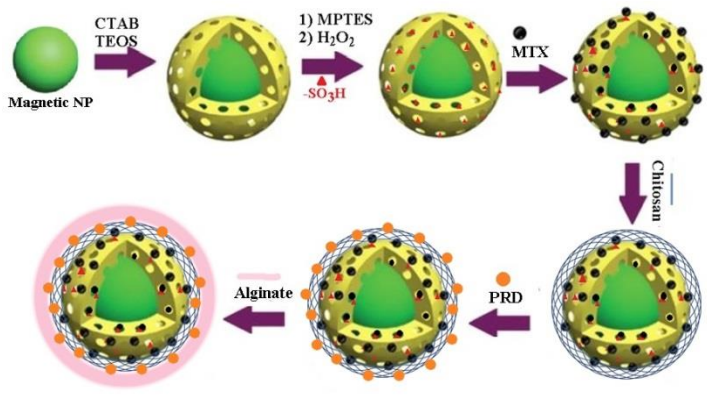

Scheme 15. Dual drug delivery system of mitoxantrone and prednisolone

4. CONCLUSIONS AND CONTRIBUTIONS OF THE DISSERTATION

CONCLUSIONS

EFFICIENT CATALYSTS FOR TOTAL OXIDATION OF VOLATILE ORGANIC CONPOUNDS

- The post synthesis modification with different cobalt salts *via* insipient wetness impregnation of KIL-2, MCM-41 and SBA-15 mesoporous silicas results in the formation of cobalt oxide species with different nature and reducibility (Co_3O_4, Co^{2+} and Co silicate like species). The highest catalytic activity is observed for the catalysts prepared by impregnation with cobalt nitrate at pH=3 pretreated at mild oxidative conditions due to the formation of easily reducible and finely dispersed Co_3O_4 nanoparticles.
- Iron-containing KIL-2, MCM-41 and SBA-15 are highly active adsorbents and catalysts for toluene removal from polluted air. The iron content influences the nature of the metal species in the silica matrix. The highest catalytic activity is observed for the 01FeKIL-2 sample with a Fe/Si molar ratio of 0.01 due to the predominant incorporation of isolated Fe^{3+} ions into the silica matrix.
- The method of modification of mesoporous silica materials strongly influences the state of the incorporated titanium species in MCM-41. In contrast to the wet impregnation procedure, the direct synthesis of titanium modified MCM-41 material facilitates the formation of titanium ions incorporated into the silica host matrix, providing higher catalytic activity in total toluene oxidation. This effect is more pronounced when the preparation procedure is carried out in propan-2-ol medium.
- Silver nanoparticles are loaded on SBA-15 support by using the ultra-short pulsed laser ablation for the first time and it was found that smaller and more homogeneously dispersed nanoparticles can be fabricated. It is shown that nanostructured silica supporting metallic silver nanoparticles are suitable catalysts for total oxidation of toluene.
- It was found that the post-synthesis modification with chromium and copper via wet impregnation of SiO_2 and SBA-15 materials depends on the type of support used. The formation of copper chromate and bichromate species is responsible for the higher catalytic activity of the bi-component SBA-15-supported modifications in comparison to SiO_2-supported ones. The optimum metal oxide content is 3 wt.% chromium and 7 wt.% copper supported on SBA-15 to achieve high catalytic activity.
- It was found that SBA-15 and SBA-16 are suitable supports for the preparation of copper and iron containing catalysts, possessing high activity in total toluene oxidation. The variation of the pore structure of the support has notable influence on the nature and dispersion of the formed metal oxide species as well as on their catalytic activity. In contrast to the bimodal pore structure of SBA-16 during the impregnation process, metal salt can penetrate into the more open channels of the SBA-15 support and finely dispersed copper oxide and copper ferrite phases, which are more active in toluene oxidation and can resist agglomeration during the catalytic test, are formed. It was also found that bi-component systems possess higher catalytic activity. The addition of iron resulted in more stable catalytic behavior for both supports and for both iron concentrations. This result is related with the formation of bicomponent oxide phases (copper ferrite), more pronounced on SBA-15 catalyst.
- Catalytic toluene oxidation results show that the performance of the bicomponent CuFe KIL-2 catalysts greatly depends on the Fe loading in the silica matrix. A slight addition of iron (Fe/Si = 0.005) induces formation of CuO nanocrystals and Cu-oxo-Fe clusters and significantly improves the catalytic performance compared to monometallic copper containing samples. The catalytic activity for oxidation of toluene is positively influenced by a synergistic effect between CuO nanocrystals (size 30 nm and 22 % fraction) and Cu-oxo-Fe clusters (78 % fraction).
- It was found that MCM-41 and SBA-15 are suitable supports for the preparation of cobalt ferrite-containing catalysts, which showed high activity in total toluene oxidation. The variation of the calcination temperature for precursor decomposition has notable influence on the nature and dispersion of the formed metal oxide species as well as on their catalytic activity. This can be explained by the different confinement effects of the different supports. The most active catalyst was the 23CoFe/MCM-41 sample calcined at 773 K, where simultaneous presence of Co^{2+}/Co^{3+} and Co^{2+}/Fe^{3+} species was detected.
- The method of MCM-41 modification with iron and/or titanium influences the state of the metal species in the silica matrix. Formation of Fe^{3+} and Ti^{4+} ions in tetrahedral position is registered for all materials prepared by direct sol-gel synthesis, whereas the introduction of titanium in the iron-modified MCM-41 by impregnation technique leads to additional formation of finely dispersed anatase nanoparticles. The highest catalytic activity is observed for the sample obtained by impregnation procedure. Bicomponent materials obtained by direct sol-gel synthesis possess lower catalytic activity, but higher stability in total toluene oxidation in comparison with the mono-substituted iron material.

- Cobalt and iron containing Ti-MCM-41 materials showed high activity in total toluene oxidation. The high and stable catalytic activity of Co/Ti-MCM-41 samples is due to the formation of finely dispersed Co_3O_4 nanoparticles by pretreatment in air and subsequently in hydrogen at 773 K and to the lower amount of titanium incorporated into the mesoporous support. Formation of finely dispersed cobalt ferrites particles on CoFe/Ti-MCM-41 samples was found to be responsible for the significant increase of catalytic activity after pretreatment in air and subsequently in hydrogen at 773 K.
- Fly ash zeolites (FAZ) were prepared by alkaline conversion of ash residues collected from the electrostatic precipitators of one of the biggest Thermal Power Plants, "AES Galabovo", supplied with lignite coal from the "Maritza-East" basin in Bulgaria, by hydrothermal activation, double stage fusion-hydrothermal activation, and atmospheric aging. The obtained FAZ materials were with micron and submicron dimensions and mixed micro-mesoporous structure of the Na-X zeolites. The cobalt- or copper-modified FAZ show high activity for the degradation of VOCs molecules with different functionality (acetone, n-hexane, toluene and 1,2 dichlorobenzene) and the specific surface area of FAZ is a critical parameter for their catalytic activity. Fly ash zeolites also show high capacity for CO_2 adsorption depending on their specific surface area and the state of iron. The good adsorption and catalytic properties of the obtained fly ash zeolites make them promising materials for the development of a dual catalytic/adsorption system.

DRUG DELIVERY SYSTEMS

- Spherical amino modified MCM-41 with particle size of 100 nm and spherical amino modified SBA-15 with particle size of 5 μm showed high adsorption capacity and modified release rate for model drug ibuprofen. For the first time, spherical SBA-15 was investigated as a drug carrier. Its adsorption capacity for ibuprofen with 349 mg/g is very close to the highest value of 368 mg/g obtained by amino-modified MCM-41 with 100 nm particle size. Optimal release properties were achieved when the applied amount of aminopropyltriethoxy silane corresponded to the number of surface silanol groups. We have applied the ninhydrin reaction for the quantitative determination of primary amines in heterogeneous phase and have found good correlation between the amino content of the modified MCM-41 materials and their ibuprofen adsorption capacity.
- We have demonstrated a novel route to modify the mesoporous MCM-41 and SBA-15 materials with carboxylic groups. The method allowed applying mild conditions combined with less toxic reagents. *In vitro* release studies showed that the functionalization of mesoporous MCM-41 and SBA-15 silicas with carboxylic groups makes them appropriate carriers for prolonged release of sulfadiazine. The new method for carboxylic modification of the mesoporous carriers did not increase cytotoxicity on Caco-2 cell line, indicating that the obtained modified carriers were biocompatible.
- Loading of resveratrol on nanoporous MCM-41, KIL-2 silicas, and on nanosized BEA zeolite by two different methods (in solid state and from ethanol solution) resulted in similar high loading capacity of the antioxidant. Better resveratrol solubility compared to the free resveratrol, regardless of the support structure and the method of loading, was shown. The applied solid-state procedure of preparation appears very effective for loading of the medical compound and for stabilization of bioactive trans-resveratrol form.
- The delivery systems of the drug mesalazine were developed on the basis of SBA-16 and MCM-41 silica carriers modified by post-synthesis method with amino and/or carboxylic groups. The post-coating of the nanoparticles with Eudragit S/Eudragit RL or sodium alginate revealed the capacity to achieve different drug release rates depending on the pH value of the release medium. It was found that the loading of mesalazine on the mesoporous silica carrier in ratio of 0.25:1 and 0.5:1 ensures the best controlled release at the target place. In addition to that, reduction of mesalazine cytotoxicity on epithelial cells could be achieved by its loading into mesoporous silica nanoparticles.
- For the first time the formation of stable Zn quercetin complexes loaded on mesoporous materials was evidenced. High quercetin loading on mesoporous MCM-41, SBA-15 and SBA-16 materials and controlled release make them promising as carriers for dermal application. Stability against light sensitivity was also significantly improved by loading quercetin on the nanostructured silica carriers. Additionally, the comparative cytotoxic experiments of quercetin encapsulated in a Zn-modified SBA-15 carrier (2 wt.% Zn) prove its superior antineoplastic potential against HUT-29 cells compared to the free drug.
- It was demonstrated for the first time that silver modified MCM-41 and SBA-15 materials are suitable carriers for propolis to improve its solubility and antimicrobial activity. Loading of poplar propolis from ethanolic solution (15-17 wt.%) on silver containing silica carriers resulted in significantly improved water solubility, probably due to its higher dispersion in the channels of the silica carrier. Antibacterial

and antifungal activities investigations showed a synergistic effect of silver and propolis against widespread bacteria strains and fungus.

- We demonstrated for the first time that Ag sulfadiazine can be effectively replaced by sulfadiazine-loaded Ag-MCM-41, Ag-SBA-15, and AgY materials. Adsorbing Ag sulfadiazine on pure nanoporous silica and zeolite materials significantly improved its water solubility.
- Prodrug sulfasalazine was successfully introduced into the channels of spherical MCM-41 (100 nm) and nanosized SBA-15 silica (400 nm) modified with amino groups. Appropriate surface functionalization of silica particles provides the opportunity for further polymer coating. The formation of polyelectrolite complex by four successive alternating layers of Eudragit S and Eudragit RL revealed the possibility to achieve different drug release rates depending on the pH value of the release medium, and hence regiospecific delivery of sulfasalazine in GIT.
- The successful loading of quercetin by solid state and incipient wetness method in mesoporous KIL-2 and KIT-6 nanoparticles with sizes around 40 and 60 nm, respectively, and modified with amino groups was achieved. The further modification by surface coating with an oppositely charged pair of polyelectrolytes, i.e. k-carrageenan and chitosan, leads to a controlled release of the loaded quercetin. The main factors that influence the rate of drug delivery are the method of drug loading and the presence of polyelectrolyte complex around the mesoporous nanoparticles.
- Verapamil delivery systems were developed on the basis of mesoporous ZSM-5/SBA-15 and ZSM-5/KIT-6 nanocomposites modified with $-SO_3H$ and -COOH groups. The drug loaded systems were further successfully modified by surface coating with polymer complex layers composed of chitosan-κ-carrageenan-chitosan with grafted polysulfobetaine chains, ensuring modified release of verapamil for a period of 24 h. The factors influencing the verapamil delivery are the structure of the applied carrier, the chemical nature of functional groups and the presence of a polymer complex around the composite nanoparticles. The bimodal pore structure of the ZSM-5/KIT-6 materials has a positive effect on the verapamil release rate, independently of the nature of surface functional groups. The findings of the conducted synergism study show superior chemosensitizing activity of the experimental verapamil loaded nanocomposites in HT-29 and HL-60/Dox cells, as compared to free verapamil, presumably as a result of a positive efflux pump modulation.
- The dual delivery system on the antitumor agent mitoxantrone and prednisolone loaded in magnetic nanoporous silica nanoparticles with spherical morphology, small particle sizes (around 100 nm) and high surface area (> 800 m^2/g) and functionalized by sulfonic groups was successfully developed. Prednisolone loading on the chitosan coated formulation and a second polymer coating with alginate beneficially affected the release rate of mitoxantrone and prednisolone as well. The cytotoxicity assessment showed that the polymer formulated mitoxantrone is characterized by activity, similar to that of the free drug.

CONTRIBUTIONS

EFFICIENT CATALYSTS FOR TOTAL OXIDATION OF VOLATILE ORGANIC COMPOUNDS

- The role of the modification procedure and the support peculiarities for the preparation of the monocomponent Co-, Fe-, Ti-, Ag-, Cr-, Cu- and bicomponent Cr/Cu-, Cu/Fe-, Co/Fe-, Co/Ti-mesoporous KIL-2, MCM-41, SBA-16 and SBA-15 and fly ash zeolite catalysts with high catalytic activity, selectivity and stability in the process of total oxidation of VOC and VOC mixture was found.
- The optimal ratio for the modification with different metal oxides in bicomponent catalytic systems (Cu-Cr, Cu-Fe, Co-Fe, Fe-Ti, Co-Ti) in order to obtain high catalytic activity in total toluene oxidation, with toluene as a model VOC, was found.
- By choice of appropriate pretreatment procedure (temperature and gas medium), the catalytic properties of the metal oxides modified catalysts can be optimized and high activity can be achieved in the total oxidation of toluene.
- A dual adsorption/catalytic system for VOC oxidation and CO_2 adsorption was developed on the basis of cheap fly ash zeolites for maximum environmental effect.

DRUG DELIVERY SYSTEMS

- Spherical amino modified MCM-41 with particle size of 100 nm and spherical SBA-15 with particle size of 5 μm were developed as ibuprofen carriers, showing high drug capacity and modified release properties.
- The ninhydrin reaction was applied for the quantitative determination of primary amines in heterogeneous phase, which allows us to optimize the extent of modification of mesoporous silicas with amino groups.
- A novel route to modify the mesoporous MCM-41 and SBA-15 materials with carboxylic groups was developed, applying mild conditions combined with less toxic reagents.
- A solid-state procedure was suggested as very effective for loading of the medical compounds with low solubility and for stabilization of their bioactive form.
- Delivery systems based on composite carriers containing mesoporous silica and stimuli-responsive polymers were developed for controlled and targeted delivery of an anti-inflammatory drug (mesalazine, sulfasalazine, quercetine)
- We demonstrated for the first time that Ag sulfadiazine can be effectively replaced by sulfadiazine-loaded Ag-MCM-41, Ag-SBA-15, and AgY materials, significantly improving its water solubility and antimicrobial properties.
- We designed verapamil delivery systems based on bimodal mesoporous ZSM-5/SBA-15 and ZSM-5/KIT-6 nanocomposites modified with -SO_3H and -COOH groups possessing positive efflux pump modulation.
- We developed magnetic nanoporous silica nanoparticles with spherical morphology, small particle sizes (around 100 nm) and high surface area (> 800 m^2/g) as efficient carriers in dual delivery systems containing anti-tumor and anti-inflammatory drugs, the combination of which is frequently used in antitumor therapy.

5. APPENDIX

PUBLICATIONS

EFFICIENT CATALYSTS FOR TOTAL OXIDATION OF VOLATILE ORGANIC COMPOUNDS

1. **M. Popova***, Á. Szegedi, P. Németh, N. Kostova, T. Tsoncheva, Titanium modified MCM-41 as a catalyst for toluene oxidation, Catalysis Communications, 10 (2008) 304, **IF=2.80, Q1**

16 цитата

2. **M. Popova***, Á. Szegedi, Z. Cherkezova-Zheleva, I. Mitov, N. Kostova, T. Tsoncheva, Toluene oxidation on titanium and iron modified MCM-41 materials, Journal of Hazardous Materials, 168(1) (2009) 226, **IF=4.66, Q1**

52 цитата

3. Á. Szegedi, **M. Popova**, Ch. Minchev, Catalytic activity of Co/MCM-41 and Co/SBA-15 materials in toluene oxidation, Journal of Material Science, 44 (2009) 6710, **IF=2.0, Q1**

71 цитата

4. Á. Szegedi, **M. Popova**, Z. Cherkezova-Zheleva, A. Dimitrova, I. Mitov, Effect of the pretreatment procedure on the physico-chemical and catalytical properties of cobalt and iron containing TiMCM-41 materials, Microporous and Mesoporous Materials, 136 (2010) 106, **IF=3.67 Q1**

22 цитата

5. **M. Popova*,** Á. Szegedi, Z. Cherkezova-Zheleva, A. Dimitrova, I. Mitov, Toluene oxidation on chromium and copper modified SiO_2 and SBA-15, Applied Catalysis A, 381 (1-2) (2010) 26, **IF=3.82, Q1**

31 цитата

6. **M. Popova***, Á. Szegedi, K. Lázár and Z. Károly, The physico-chemical and catalytical properties of cobalt ferrite-containing MCM-41 and SBA-15 materials, Microporous and Mesoporous Materials, 151 (2012) 180, **IF=3.60, Q1**

11 цитата

7. **M. Popova***, A. Ristić, K. Lazar, D. Maučec, M. Vassileva, N. Novak Tušar, Iron-Functionalized Silica Nanoparticles as a Highly Efficient Adsorbent and Catalyst for Toluene Oxidation in Gas-Phase, ChemCatChem, 5(4) (2013) 986, **IF=5.37, Q1**

19 цитата

8. Á. Szegedi, **M. Popova**, K. Lázár E. Drotára, Impact of silica structure of copper and iron-containing SBA-15 and SBA-16 materials on toluene oxidation, Microporous and Mesoporous Materials, 177 (2013) 97, **IF=3.55, Q1**

27 цитата

9. **M. Popova***, A. Ristić, V. Mavrodinova, D. Maučec, L. Mindizova, N. Novak Tušar, Design of Cobalt Functionalized Silica with Interparticle Mesoporosity as a Promising Catalyst for VOCs Decomposition, Catalysis Letters, 144 (6) (2014) 1096, **IF=2.31, Q1**

5 цитата

10. Á. Szegedi, **M. Popova**, J. Valyon, A. Guarnaccio, A. De Stefanis, A. De Bonis, S. Orlando, M. Sansone, R. Teghil, A. Santagata, Comparison of silver nanoparticles confined in nanoporous silica prepared by chemical synthesis and by ultra-short pulsed laser ablation in liquid, Applied Physics A, 117 (1) (2014) 55, **IF=1.87, Q2**

5 цитата

11. **M. Popova***, A. Ristić, M. Mazaj, D. Maučec, M. Dimitrov, N. Novak Tušar, Autoreduction of Copper on Silica and Iron-Functionalized Silica Nanoparticles with Interparticle Mesoporosity, ChemCatChem, 6 (1) (2014) 271, **IF= 4.75, Q1**

8 цитата

12. S. Boycheva, D. Zgureva, M. Václavíková, Y. Kalvachev, H. Lazarova, **M. Popova***, Studies on non-modified and copper-modified coal ash zeolites as heterogeneous catalysts for VOCs oxidation, Journal of Hazardous Materials, 361 (5) (2019) 374, **IF=9.04, Q1**

20 цитата

13. **M. Popova***, S. Boycheva, H. Lazarova, D. Zgureva, K. Lázár, Á. Szegedi, VOC oxidation and CO_2 adsorption on dual adsorption/catalytic system based on fly ash zeolites, Catalysis Today, 357 (2020) 518, **IF=5.83, Q1**

4 цитата

14. P. Djinović, A. Ristić, T. Žumbar, V. D.B.C.Dasireddy, M. Rangus, G. Dražić, **M. Popova**, B. Likozar, N. Zabukovec Logar, N. Novak Tušar, Synergistic effect of CuO nanocrystals and Cu-oxo-Fe clusters on silica support in promotion of total catalytic oxidation of toluene as a model volatile organic air pollutant, Applied Catalysis B, 268 (2020) 118749, **IF=16.68, Q1**

6 цитата

DRUG DELIVERY SYSTEMS (DDS)

15. Á. Szegedi, **M. Popova**, I. Goshev, J. Mihály, Effect of amine functionalization of spherical MCM-41 and SBA-15 on controlled drug release, Journal of Solid State Chemistry, 184 (2011) 1201, **IF=2.33, Q1**

122 цитата

16. Á. Szegedi, **M. Popova**, I. Goshev, Controlled drug release on amine functionalized spherical MCM-41, Journal of Solid State Chemistry, 194 (2012) 257, **IF=2.24, Q1**

53 цитата

17. **M.D. Popova***, Á. Szegedi, I. N. Kolev, J. Mihály, B. S. Tzankov, K. P. Yoncheva, N. G. Lambov, Carboxylic Modified Spherical Mesoporous Silicas as Drug Delivery Carriers, International Journal of Pharmaceutics, 436 (2012) 778, **IF=4.20, Q1**

64 цитата

18. **M. Popova***, Á. Szegedi, V. Mavrodinova, N. Novak Tušar, J. Mihály, S. Klébert, K. Yoncheva, Preparation of resveratrol-loaded nanoporous silica materials with different structures, Journal of Solid State Chemistry, 219 (2014) 37, **IF=2.27, Q1**

23 цитата

19. Á. Szegedi, **M. Popova**, K. Yoncheva, J. Makk, J. Mihály, P. Shestakova, Silver and sulfadiazine loaded nanostructured silica materials as potential replacement of silver sulfadiazine, Journal of Materials Chemistry B, 2 (2014) 6283, **IF=5.04, Q1**

26 цитата

20. **M. Popova***, Á. Szegedi, K. Yoncheva, S. Konstantinov, G. P. Petrova, H. A. Aleksandrov, G. N. Vayssilov, New method for preparation of delivery systems of poorly soluble drugs on the basis of functionalized mesoporous MCM-41, P. Shestakova, Microporous and Mesoporous Materials, 198 (2014) 247, **IF=3.71, Q1**

29 цитата

21. V. Mavrodinova, **M. Popova**, K Yoncheva, J. Mihály, Á. Szegedi, Solid-state encapsulation of Ag and sulfadiazine on zeolite Y carrier, Journal of Colloid and Interface Science, 458 (2015) 32, **IF=4.04, Q1**

10 цитата

22. **M. Popova***, I. Trendafilova, Á. Szegedi, J. Mihaly, P. Nemeth, S. G. Marinova, H. A. Aleksandrov, G. N. Vayssilov, Experimental and theoretical study of quercetin complexes formed on pure silica and Zn-modified mesoporous MCM-41 and SBA-16 materials, Microporous and Mesoporous Materials, 228 (2016) 256, **IF=3.86, Q1**

9 цитата

23. I. Trendafilova, Á. Szegedi, K. Yoncheva, P. Shestakova, J. Mihály, A. Ristić, S. Konstantinov, **M. Popova***, pH dependent delivery of mesalazine from polymer coated and drug-loaded SBA-16 systems, European Journal of Pharmaceutical Sciences, 81 (2016) 75, **IF=4.18, Q1**

11 цитата

24. I. Trendafilova, Á. Szegedi, J. Mihály, G. Momekov, N. Lihareva, **M. Popova***, Preparation of efficient quercetin delivery system on Zn-modified mesoporous SBA-15 silica carrier, Materials Science and Engineering C, 73 (2017) 285, **IF=5.56, Q1**

10 цитата

25. **M. Popova***, H. Lazarova, B. Trusheva, M. Popova, V. Bankova, J. Mihály, H. Najdenski, H. Tsvetkova, Á. Szegedi, Nanostructured silver silica materials as potential propolis carriers, Microporous and Mesoporous Materials, 263 (2018) 28, **IF=4.55, Q1**

7 цитата

26. **M. Popova***, I. Trendafilova, I. Tsacheva, V. Mitova, M. Kyulavska, N. Koseva, J. Mihály, D. Momekova, G. Momekov, H. A. Aleksandrov, S. G. Marinova, P.St Petkov, G. N. Vayssilov, Á. Szegedi, Amino-modified KIT-6 mesoporous silica/polymer composites for quercetin delivery: Experimental and theoretical approaches, Microporous and Mesoporous Materials, 270 (2018) 40, **IF=4.55, Q1**

7 цитата

27. **M. Popova*,** I. Trendafilova, Á. Szegedi, D. Momekova, J. Mihály, G. Momekov, L. Kiss, K. Lázár, N. Koseva, Novel SO_3H functionalized magnetic nanoporous silica/polymer nanocomposite as a carrier in a dual-drug delivery system for anticancer therapy, Microporous and Mesoporous Materials, 263 (2018) 96, **IF=4.55, Q1**

6 цитата

28. **M. Popova***, Á. Szegedi, R. Mihaylova, G. Momekov, D. Momekova, H. Lazarova, V. Mitova, N. Koseva, J. Mihályi, P. St. Petkov, H. A. Aleksandrov, G. N. Vayssilov, Verapamil delivery systems on the basis of mesoporous ZSM-5/KIT-6 and ZSM-5/SBA-15 polymer nanocomposites as a potential tool to overcome MDR in cancer cells, European Journal of Pharmaceutics and Biopharmaceutics, 142 (2019) 460, **IF=4.60, Q1**

4 цитата

***corresponding author**

Total number of papers: 28
Q1, top ranking: 1
Q1: 27
Q2: 1
Total IF: 125.63
Avarage IF: 4.5

In 18 out of 28 papers Margarita Popova is author for correspondence

PARTICIPATIONS IN CONFERENCES

1. M. Popova, M. Vassileva, A. Ristić, M. Dimitrov, K. Lazar, D. Maučec, N. Novak Tušar Copper modified FeKIL-2 nanoparticles as highly active catalysts for toluene elimination in gas-phase, 14th International Workshop Nanoscience & Nanotechnology, 22-23 November 2012 - Sofia, Bulgaria, poster.
2. M. Popova, V. Mavrodinova, A. Ristić, D. Maučec, M. Vassileva, N. Novak Tušar, Functionalisation of mesoporous silicates by cobalt and their catalytic evaluation for the decomposition of VOCs, 11th European Congress on Catalysis – EuropaCat-XI, Lyon, France, 1-6 September 2013, oral presentation
3. M. Popova, A. Ristić, K. Lazar, D. Maučec, M. Vassileva, N. Novak Tušar Iron-functionalized silica nanoparticles: synthesis, characterization and catalytic activity in total toluene oxidation in gas-phase, Moscow, Russia, 17th International Zeolite Conference, 2013, oral.
4. L. Mindizova, M. Popova, V. Mavrodinova, A. Ristić, N. Novak Tušar, Total toluene oxidation on the novel cobalt functionalized KIL-2, 15 International Workshop Nanoscience & Nanotechnology, 20-23 November 2013, Sofia, Bulgaria, poster.
5. Á. Szegedi, M. Popova, K. Lázár, S. Klébert, E. Drotár, Impact of silica structure of copper and iron-containing SBA-15 and SBA-16 materials on toluene oxidation, International Conference on Advanced Complex Inorganic Nanomaterials, ACIN 2013, 15-19 July 2013, Namur, Belgium.
6. Á. Szegedi, M. Vassileva, M. Popova, K. Yoncheva, P. Shestakova, Preparation of new mesalazine delivery systems based on nanoporous silica particles, International Conference on Advanced Complex Inorganic Nanomaterials, ACIN 2013, 15-19 July 2013, Namur, Belgium, P081.
7. M. Popova, A. Szegedi, K. Yoncheva, P. Shestakova, New method for preparation of delivery systems of porely-soluble drugs supported on functionalized mesoporous MCM-41, 6th FEZA Conference: Porous Systems: From novel materials to sustainable solutions, 8-11 September 2014, Leipzig, poster.
8. I. Trendafilova, A. Szegedi, K. Yoncheva, V. Mavrodinova, M. Popova, Preparation of mesalazine delivery systems based on mesoporous amino-functionalized SBA-16 silica, 16 International Workshop on Nanoscience and Nanotechnology, 06-08 November 2014, Sofia, poster.
9. M. Rangus, M. Mazaj, M. Popova, A. Ristić, N. Novak Tušar, Structural properties of highly efficient bimetal catalyst for catalytic oxidation of VOCs, 6th International FEZA Conference, 08-11 September, Leipzig, Germany, poster.
10. C. Gorinova, B. Tzankov, K. Yoncheva, V. Tzankova, M. Popova, A. Szegedi, N. Lambov, Development of sulfadiazine loaded mesoporous silica MCM-41 nanoparticles and evaluation of their biocompatibility, 17 International Workshop Nanoscience & Nanotechnology, 20-23 November 2013, София, България, poster.
11. A. Szegedi, M. Popova, K. Yoncheva, J. Makk, J. Mihali, Ag- and sulfadiazine loaded nanostructured silica materials, 6th International FEZA Conference, 6th FEZA Conference: Porous Systems: From novel materials to sustainable solutions, 8-11 Sept. 2014, Leipzig, poster.
12. I. Trendafilova, A. Szegedi, J. Mihály, N. Lihareva, M. Popova, Preparation of quercetin delivery systems on the basis of Zn-modified mesoporous SBA-15 carriers, 17 International Workshop Nanoscience and Nanotechnology, 27 – 28 November 2015, Sofia, Bulgaria, poster.
13. I. Trendafilova, M. Popova, A. Szegedi, J. Mihály, D. Momekova, G. Momekov, I. Nikolova, L. Marinov, Design of mesoporous Fe3O4/MS nanoparticles as drug delivery platform of prednisolone, International Conference on Nanomedicine And Nanobiotechnology, 28 – 30 September 2016, Paris, France, poster.
14. A. Szegedi, M. Popova, K. Lazar, SBA-15 supported copper and iron catalysts for total oxidation of toluene, 13 Pannonian International Symposium on Catalysis, 19-23 September 2016, Siofok, Hundary, poster.
15. I. Trendafilova, M. Popova, A. Szegedi, J. Mihaly, D. Momekova, G. Momekov, Prednisolone Loaded Mesoporous Fe_3O_4/MS Nanoparticles, 18 International Workshop on Nanoscience and anotechnology, NANO 2016, 17 – 19 November 2016, Sofia, Bulgaria, poster.
16. M. Popova, Дизайн на нови лекарство-доставящи системи на основата на мезопорести нанокомпозити, 10 Пролетен семинар на докторантите и младите учени „Интердисциплинарна химия“, 21-23 април 2016, oral.
17. I. Trendafilova, M. Popova, Quercetin complexes formed on initial silica and Zn-modified mesoporous materials, First International Conference on Bioantioxidants entitled: "Natural Bioantioxidants - as a base of new synthetic drugs and food additives/supplements", 25 – 29 June 2017, Sofia, Bulgaria, poster.
18. A. Szegedi, M. Popova, K. Lazar, SBA-15 supported copper and iron oxide catalysts for total oxidation of toluene, 7th FEZA Conference "The ZEOLITES: Materials with Engineered Properties", 03 – 07 July 2017, Sofia, Bulgaria, poster.
19. I. Trendafilova, M. Popova, A. Szegedi, D. Momekova, G. Momekov, Mesoporous silica/polymer composites as carriers in delivery systems for biological active molecules, International Meeting on Medicinal and Bio(in)organic Chemistry, 26 – 31 August 2017, Vrnjačka Banja, Serbia, доклад

20. M. Popova, I. Trendafilova, A. Szegedi, J. Mihály, D. Momekova, G. Momekov, N. Koseva, Design of magnetic/mesoporous silica nanocomposites as a delivery platform of antineoplastic drugs, International Conference On Nanomedicine And Nanobiotechnology – ICONAN 2017, 24 – 28 September 2017, Barcelona, Spain, oral.
21. I. Trendafilova, M. Popova, P. Shestakova, J. Mihály, A. Szegedi, Modified Mesoporous Silica Type SBA-16 as a Carrier in Delivery Systems of Bioflavonoids, ACIN 2018, 16 – 20 July 2018, Namur, Belgium, poster.
22. H. Lazarova, S. Boycheva, D. Zgureva, M. Popova, Copper-modified coal ash zeolites as heterogeneous catalysts for VOCs oxidation, Twelfth International Symposium on Heterogeneous Catalysis, 26 – 29 Aug. 2018, Sofia, Bulgaria, постер
23. A. Szegedi, M. Popova, K. Lazar, Total oxidation of toluene over bimetallic (Cu, Fe) nanoporous silica catalysts, Twelfth International Symposium on Heterogeneous Catalysis, 26 – 29 Aug. 2018, Sofia, Bulgaria, oral.
24. S. Boycheva, D. Zgureva, H. Lazarova, M. Popova, Coal ash zeolites as heterogeneous catalysts for VOCs oxidation, Twelfth International Symposium on Heterogeneous Catalysis, 26 – 29 Aug. 2018, Sofia, Bulgaria, постер.
25. P. Shestakova, V. D. Kancheva, M. Popova, I. Trendafilova, A. Michelotti, Ch. Martineau, Advanced NMR methods for structural characterization of systems with antioxidant properties: Diffusion NMR and Magic Angle Spinning (MAS) NMR spectroscopy, Second International Conference on Bio-antioxidants:"Natural Bio-antioxidants and their Synthetic Analogues - Beneficial Effect of Human Health", 07 – 10 Sept. 2018, Varna, Bulgaria, oral.
26. H. Lazarova, S. Boycheva, D. Zgureva, M. Popova, Copper modified fly ash zeolite catalysts for VOCs oxidation: Effect of preparation procedure, 20 International Workshop Nanoscience and Nanotechnology, 08 – 10 November 2018, Sofia, Bulgaria, poster.
27. A. Szegedi, H. Lazarova, M. Popova, SBA-15 Supported Copper Ferrite Catalysts for Total Oxidation of Toluene, An international conference in chemistry, 20 – 21 Dec. 2018, Assam, India, oral.
28. M. Popova, S. Boycheva, H. Lazarova, D. Zgureva, A. Szegedi, VOCs oxidation and CO_2 adsorption on dual adsorption/catalytic system based of fly ash zeolites, 4th Euro Asia Zeolite Congress, 27 – 30 Jan. 2019, Taormina, Italy, oral.
29. P. Shestakova, Ch. Martineau-Corcos, A. Szegedi, I. Trendafilova, A. Michelotti, M. Popova, Al and SO_3H modified SBA-15 mesoporous silicas as drug delivery carriers of verapamil hydrochloride and diclofenac sodium: solid state nmr characterization, 4th Euro Asia Zeolite Congress, 27 – 30 Jan. 2019, Taormina, Italy, oral.
30. D. Zgureva, S. Boycheva, M. Popova, H. Lazarova, S. Miteva, I. Marinov, Utilization of coal fly ash via synthesis of adsorbents carbon capture applications, 4th Green and Sustainable Chemistry Conference, 05 – 08 May 2019, Dresden, Germany, oral.
31. S. Boycheva, D. Zgureva, K. Lazarova, T. Babeva, C. Popov, H. Lazarova, M. Popova, Synthesis of zeolites from coal fly ash with applications in environmental protection systems, 4th Green and Sustainable Chemistry Conference, 05 – 08 May 2019, Dresden, Germany, poster.
32. S. Boycheva, I. Marinov, H. Lazarova, D. Zgureva, M. Václavíková, M. Popova, Cobalt- and copper-modified fly ash nanozeolites for environmental protection systems, 16th International Conference on Environmental Science and Technology, 04 – 07 September 2019, Rhodes, Greece, oral.
33. D. Zgureva, S. Boycheva, S. Miteva, H. Lazarova, I. Marinov, M. Popova, Thermal Swing Adsorption in a Carbon Capture System, 16th International Conference on Environmental Science and Technology, 04 – 07 September 2019, Rhodes, Greece, oral.
34. S. Boycheva, S. Miteva, I. Trendafilova, D. Zgureva, M. Václavíková, M. Popova, Magnetite nanoparticles activated coal fly ash zeolites with application in wastewater remediation, 16th International Conference on Environmental Science and Technology, 04 – 07 September 2019, Rhodes, Greece, oral.
35. N. Koseva, M. Popova, I. Tsacheva, I. Trendafilova, P. Shestakova, A. Szegedi, G. Momekov, D. Momekova, Design of drug delivery systems based on hybrid mesoporous nanocarriers, 19 симпозиум с международно участие "Полимери 2019", 09 – 11 September 2019, Pomorie, Bulgaria, oral.
36. M. Popova, R. Mihaylova, G. Momekov, D. Momekova, H. Lazarova, I. Trendafilova, V. Mitova, N. Koseva, J. Mihalyi, P. Shestakova, A. Szegedi, Verapamil delivery systems based on hybrid mesoporous silica nanocomposites, 19-и симпозиум с международно участие "Полимери 2019", 09 – 11 September 2019, Pomorie, Bulgaria, poster.
37. S. Boycheva, D. Zgureva, H. Lazarova, K.Lazarova, T. Babeva, M. Popova, Processing of high-grade zeolite composites from solid state combustion by-products as critical raw materials substitutes, 2nd International conference on Emmerging Tehnologies in Materials Engereering, EmergeMAT, 6-8.10.2019, Bucharest, Romania, oral.

PROJECTS RELATED TO THE THESIS' TOPIC

I. Projects funded by the Bulgarian Science Fund

1. Oxide nanocomposite catalysts for the oxidation of toxic organic pollutants emitted in formalin production and other industrial processes, ВУ–Х–305/07, Coordinator: Prof. Krasimir Ivanov, 2007-2010.
2. Development of new materials including metals in mixed valence state and their utilization as catalysts for environmental protection, DO 02-295 2008, Competition "IDEAS" - 2009 г., Coordinator: Prof. Ivan Mitov, 2009-2012.
3. Adsorption and catalytic elimination of VOCs over porous materials, Bilateral project between Bulgaria and Slovenia, ДНТС/Словения 01/6 from 28.11.2011 г., Coordinator: Prof. Margarita Popova, 2011-2014.
4. Design of novel mesoporous nanocomposite drug delivery systems for antineoplastic and multi-drug resistance-reversal agents, ДН 09/18, Coordinator: Prof. Margarita Popova, 2016-2020.
5. Synthesis of zeolites from coal ashes for adsorption, catalytic degradation and detection of atmospheric pollutants, ДН 17/18, Coordinator: Assoc Prof. Dr. Silvia Boycheva, Coordinator for IOCCP: Prof. Margarita Popova, 2018-present.

II. Project Center of excellence „National Centre for Mechatronics and Clean Technologies"; BG05M2OP001-1.001-0008, Coordinator: Prof. Plamen Stefanov, Coordinator for IOCCP: Prof. Margarita Popova, 2018-2023

III. National Scientific Program „Low-carbon energy for transport and domestic use" (E+), with a leading scientific organization Bulgarian Academy of Sciences. Coordinator: Prof. K. Hadjiivanov, Coordinator for IOCCP: Prof. Margarita Popova, 2018-2021

IV. Projects supported by Bulgarian-Hungarian Inter-Academic Exchange Agreement:

1. Preparation and chemical modification of porous silica materials and their catalytic and biological applications, Coordinator: Assoc Prof. Dr. Vesselina Mavrodinova, 2010-2012.
2. Synthesis of novel nanoporous silica materials and their application as drug carriers and catalysts Coordinator: Prof. Margarita Popova, 2013-2015.
3. Development of new nanosized mesoporous composites for biomass valorization and preparation of delivery systems of bioactive compounds, Coordinator: Prof. Margarita Popova, 2016-2019.